Computational Biology Group

Department of Computer Science

University of Oxford

Vasculature Reconstruction from 3D Cryomicrotome Images

Ayush Goyal

Balliol College, Oxford





Supervisors:

Professor Nicolas Smith

Dr. Vicente Grau

Thesis submitted in partial fulfilment of the requirements for

the degree of Doctor of Philosophy at the University of Oxford

Hilary 2013

Thesis Title: Vasculature Reconstruction from 3D Cryomicrotome Images

Name: Ayush Goyal

College: Balliol College

Degree: D.Phil. Computer Science

Term: Hilary 2013

Contact Information: aja.govinda@gmail.com (email), 07505727193 (mobile)

Executive Abstract

Background: Research in heart disease can be aided by modelling myocardial hemodynamics with knowledge of coronary pressure and vascular resistance measured from the geometry and morphometry of coronary vasculature. This study presents methods to automatically reconstruct accurate detailed coronary vascular anatomical models from high-resolution three-dimensional optical fluorescence cryomicrotomography image volumes for simulating blood flow in coronary arterial trees.

Methods: Images of fluorescent cast and bead particles perfused into the same heart comprise the vasculature and microsphere datasets, employed in a novel combined approach to measure vasculature and simulate a flow model on the extracted coronary vascular tree for estimating regional myocardial perfusion. The microspheres are used in two capacities - as fiducial biomarker point sources for measuring the image formation in order to accurately measure the vasculature dataset and as flowing particles for measuring regional myocardial perfusion through the reconstructed vasculature. A new model-based template-matching method of vascular radius estimation is proposed that incorporates a model of the optical fluorescent image formation measured from the microspheres and a template of the vessels' tubular geometry.

Results: The new method reduced the error in vessel radius estimation from 42.9% to 0.6% in a 170-μm vessel as compared to the Full-Width Half Maximum method. Whole-organ porcine coronary vascular trees, automatically reconstructed with the proposed method, contained on the order of 92,000+ vessel segments in the range 0.03 – 1.9 mm radius. Discrepancy between the microsphere perfusion measurements and regional flow estimated with a 1-D steady state linear static blood flow simulation on the reconstructed vasculature was modelled with daughter-to-parent area ratio and branching angle as the parameters. Correcting the flow simulation by incorporating this model of disproportionate distribution of microspheres reduced the error from 24% to 7.4% in the estimation of fractional microsphere distribution in oblique branches with angles of 100°-120°.

Acknowledgements

I would like to express my sincerest appreciation to Professor Sir Mike Brady for his critical review of this work. His expert recommendations gave this work the solid scientific rigor expected of an Oxford D.Phil. dissertation. I would like to express my sincerest appreciation to Professor David Gavaghan for his continued advice from the start to the end. Additionally, I would like to thank Dr. Julia Schnabel at the University of Oxford Biomedical Image Analysis Laboratory and Dr. Graeme Penney of King's College London Department of Imaging Sciences for their valuable feedback in improving the presentation of the thesis. I would like to especially thank Pepijn van Horssen, Dr. Jeroen van den Wijngaard, and Professor Jos A.E. Spaan of the University of Amsterdam, Academic Medical Center for providing the cryomicrotome data and highly useful insight into the entire project. Many people at the University of Oxford Computational Biology Group and the King's College London Department of Imaging Sciences have facilitated the research in this work, specifically Dr. Martin Bishop of the Computational Biology Group at the University of Oxford for running the Monte Carlo simulation of photon transport in tissue, Dr. Jeyarajan Thiyagalingam of the Oxford e-Research Centre for his facilitating the research into optimization and parallel MATLAB programming, Dr. Pablo Lamata of the Computational Physiology Group at University of Oxford for the generic cubic hermite mesh template of the heart, and Dr. Jack Lee of the Computational Physiology Group at University of Oxford for the cubic-hermite spline-fitting code for smoothing the coronary vasculature and extremely valuable advice on vessel segmentation. I would like to express my deepest gratitude to my supervisor Dr. Vicente Grau, who not only educated me in the technical aspects of the research, but also was always there as a guide whenever I was confounded. Finally, but most importantly I would like to express my deepest heartfelt gratitude to my primary supervisor Professor Nic Smith, who with utmost patience taught me to grow from an inexperienced undergraduate to a critical thinker who could learn to ask the right questions and find the answers independently with a good starting point of research. I am deeply indebted to my parents Dr. Sudhir Goyal and Sulekha Goyal, and also to my sister Shatakshi Goyal, for without their love and support this thesis would not have been possible.

Abstract

The purpose of this project is to reconstruct accurate vasculature models from three-dimensional optical fluorescence cryomicrotomography images to facilitate blood flow simulations in whole organ arterial coronary trees, which in turn, can augment research in to hemodynamics and cardiovascular autoregulation. Simulations of coronary blood flow and vascular resistance are highly dependent on accurate models of vascular geometry and morphometry. Recent developments in high-resolution imaging of whole-organ vasculature now facilitate extraction and reconstruction of detailed coronary vascular anatomical models. Among these new advances, the optical fluorescence cryomicrotome method, employed in this study, in particular offers automated imaging and 3D visualization of whole-organ vascular networks in large extended tissue volumes of animal and human models.

This imaging system creates a digital volume of a tomographic series of images captured with a camera each time a micrometer-scale thin slice is sectioned off of the tissue block containing the organ. The organs are perfused with fluorescent cast and micrometer-size beads, both of which are separately imaged with different filter settings to obtain two distinct sets of images, namely the vasculature and microsphere datasets, respectively. Both these datasets are employed in a novel combined approach to measure and extract vasculature and simulate a flow model on the reconstruction of this extracted coronary vascular tree to measure regional myocardial perfusion distribution. The microsphere dataset is not only used to measure the regional myocardial perfusion but also to measure the image formation in order to accurately extract the vasculature dataset.

The image formation is modelled because in the optical fluorescence cryomicrotome images, the extraction of vascular geometry is impeded by the broadening of vessel cross-sections due to the scattering of light emitted by the vascular fluorescent cast in the non-opaque myocardial tissue. The image formation can be represented mathematically as the imaging system's impulse response. The imaging modality response function can be approximated and modelled as the point spread function (PSF). The PSF implemented in this work incorporates the transport of light inside the scattering tissue and the lens blur. Since the PSF models the intensity distribution produced by a point

source embedded in tissue, parameters of this analytical PSF model can be obtained by fitting the PSF model to the experimental images of fluorescent microspheres, which are effectively point sources embedded in the cardiovascular tissue. In this study, optimal values of tissue excitation and emission attenuation coefficients (PSF parameters measuring how much light intensity is attenuated in tissue per distance), are obtained by minimizing the mean square error between the mathematical PSF model and the experimental microsphere image with nonlinear optimization. The optical attenuation coefficients are then mapped onto the myocardial geometry to characterise spatial variations, which affect the estimation of vessel radii. These parameters are then applied within a new model-based method for vessel radius estimation that inherently accounts for light scattering in optical fluorescence microtomography images. This method incorporates a model of the vessels' tubular geometry and calculates the optimal vessel radius by minimizing the mean square error between the actual image of the vessel cross-section and a simulated image synthesized by convolving a cylindrical model of a vessel segment with the PSF. Since the model-based radius estimation incorporates vessel orientation information in its cylindrical model of each vessel segment, skeletonization was employed to provide the vessel centrelines, and the radius was estimated for each vessel segment of the vasculature.

In a phantom validation study, state-of-the-art radius estimation methods and the proposed model-based method developed in this project were used to measure radii of vessel phantoms of various sizes orientated at different angles with respect to the cutting plane. Compared to other methods, the model-based algorithm is shown to be robust to the vessel angle and estimated the radii more accurately for any vessel orientated at any angle. In images of artificial vessel-mimicking tubes embedded in gel and imaged with the cryomicrotome, using microscope measurements as ground truth, the extracted results show more accurate radius estimation than the compared methods. The Full-Width Half Maximum (FWHM) method of radius estimation, when performed on the raw data without correcting for the optical blurring, resulted in 42.9% error on average for the 170μm vessel. In comparison, the model-based method resulted in 0.6% error on average for the same phantom. This proposed model-based approach was subsequently applied to automatically reconstruct whole-organ

porcine coronary vasculatures. The extracted trees contained on the order of 92,000+ vessel segments and the range of vessel radii extracted was 0.03 – 1.9 mm.

In order to obtain perfusion models on the coronary arterial network, a 1D steady state Poiseuille model of blood flow was simulated on the reconstructed porcine coronary vasculature to estimate pressure and flow rate at each branch in the arterial tree. The results of the 1D blood flow simulations on the reconstructed vascular model were validated by comparison with the regional distribution of microspheres, used as a surrogate for local perfusion. In bifurcating branches coming off at a large branching angle from the parent branch and in branches whose cross-sectional area is much smaller than the cross-sectional area of the parent branch, the fraction of microspheres deviated from the fractional flow (i.e. regional flow in daughter divided by the regional flow in the parent branch). This discrepancy is due to the disproportionate distribution of microspheres at junctions. This effect was modelled and parameterised with the branching angle and cross-sectional area ratio of the daughter to parent branch to correct the flow-predicted microsphere distribution. This two-parameter model increased the agreement accuracy of the 1D flow estimation in simulating microsphere distribution in the coronary tree. The error between the fraction of flow predicted by the 1-D Poiseuille model and the fraction of microspheres was reduced from 24% to 7.4% error by incorporating the disproportionate microsphere distribution model for bifurcating segments with the largest branch angles, ranging from 100˚ - 120˚.

Table of Contents

Chapter 1 2

Introduction 2

1.1 Background 2

1.1.1 Coronary Vasculature 2

1.1.2 Myocardial Infarction 3

1.2 Vascular Morphometry 4

1.2.1 The History of Coronary Vasculature Morphometry Studies 4

1.2.2 Overview of Research in Vascular Imaging 7

1.3 Image Modelling 14

1.3.1 Limitations of Cryomicrotome Image Acquisition 14

1.3.2 Cryomicrotome Image Formation 16

1.4 Vasculature Extraction 18

1.4.1 Filtering 18

1.4.2 Segmentation 19

1.4.3 Voxel Classification 22

1.4.4 Skeletonization 23

1.4.5 Summary of Vessel Extraction 25

1.4.6 Image Restoration 26

1.5 Objectives 36

1.6 Materials 37

1.6. 1 Image Data 37

1.6. 2 Phantom Data 38

1.7 Contents 41

1.8 Contributions 42

1.9 Publications 43

Chapter 2 44

Cryomicrotome Point Spread Function 44

2.1 Background 44

2.2 Point Spread Function Modelling 44

2.2.1 Point Spread Function Model 45

2.2.2 Parameters of the Point Spread Function Model 47

2.2.3 PSF Model Validation with Monte Carlo Simulation 48

Chapter 3 60

Measuring Optical Tissue Properties 60

3.1 Background 60

3.1.1 Tissue Optics 61

3.1.2 Effect of Optical Blur on Vessel Diameter Estimation 61

3.1.3 Measuring the Total Optical Tissue Attenuation Coefficient 66

3.2 Methods 68

3.2.1 Fluorescence Microsphere Images 68

3.2.2 Optical Parameter Estimation from Microspheres 69

3.2.3 Microsphere Slice Depth Parameter 71

3.2.4 Parameter Estimation Algorithm 72

3.3 Results 74

3.3.1 Slice Depth Uniform Distribution 74

3.3.2 Optical Parameter Distributions 75

3.3.3 Shape of the Objective Function 77

3.3.4 Optical Parameter Validation with Published Values 79

3.3.5 Optical Parameter Spatial Variation Map 79

3.4 Discussion 87

Chapter 4 90
Vessel Radius Estimation 90
4.1 Introduction 91
4.1.1 Vessel Radius Estimation 91
4.1.2 Vessel Image Restoration 92
4.2 Methods 93
4.2.1 Image Processing Pipeline 94
4.2.2 Vessel Enhancement and Binarization 97
4.2.3 Segmentation and Skeletonization 100
4.2.4 Model-based Template-matching Radius Measurement 101
4.3 Results 106
4.3.1 Validation Against Previous Vessel Detection Method 107
4.3.2 Simulated Phantom Validation of Radius estimation 110
4.3.3 Ground Truth Validation of Radius estimation 114
4.3.4 Preciseness of Radius estimation 119
4.3.5 Sensitivity Analysis of Radius estimation 121
4.3.6 Comparison of Radius estimation Methods 129
4.3.7 Agreement with Murray's Law for Vasculature 135
4.3.8 Training Data - Reconstructed Vasculature Models 141
4.3.9 Test Data - Reconstructed Vasculature Models 146
4.3.10 Extension Data - Reconstructed Vasculature from CT Images 149
4.4 Discussion 153
Chapter 5 158
Myocardial Perfusion Flow Modelling 158
5.1 Introduction 159
5.2 Methods 163

5.2.1 Image Acquisition 164
5.2.2 Microsphere Detection 165
5.2.3 Myocardial Segmentation 165
5.2.4 Vasculature Reconstruction 165
5.2.5 1-D Blood Flow Simulation 166
5.2.6 Boundary Conditions 167
5.2.7 Nodal Voxel Count 169
5.2.8 Nodal Microsphere Count 170
5.2.9 Parameterised Model Fitting 171
5.2.10 Poisson Process Modelling of Error in Microsphere Distribution 174
5.3 Results 175
5.3.1 Perfusion Territories 175
5.3.2 Pressure and Flow Measurements 176
5.3.3 Comparison of 1-D Blood Flow and Microsphere Distribution 177
5.3.4 The Effect of Boundary Conditions on Flow Simulations 179
5.3.5 Model Correction of Predicted Microsphere Distributions 183
5.3.6 Poisson Fits to Binned Microsphere Distributions 187
5.3.7 Radius Measure Accuracy 191
5.4 Discussion 195
Chapter 6 198
Conclusions 198
6.1 Summary 199
6.2 Methods 200
6.2.1 Optical parameter estimation 200
6.2.2 Vascular extraction 201
6.2.3 Coronary Perfusion Flow Estimation 202

6.3 Contributions 202
6.3.1 Methodological 202
6.3.2 Anatomical 203
6.4 Limitations and Future Research 204
6.4.1 Data Dependency Requirements 204
6.4.2 Data Acquisition Experimental Improvements 205
6.4.3 Future Research in Optical Parameter Estimation 206
6.4.4 Future Research in Vessel Radius Estimation 208
6.4.5 Future Research in Myocardial Perfusion Measurements 209
6.4.6 Future Research in Coupled Vascular-Ventricular Modelling 212
References 214
Appendix A: Monte Carlo Simulations 247
A.1 Comparison of Monte Carlo and PSF Models at Shallow Depths 247
A.2 Phantom Based Evaluation of PSF Model Validity 249
Appendix B: Optical Parameter Estimates 250
B.1 Unconstrained Unbounded Variable Estimates 250
B.2 Partial Volume Effect on Microsphere Optical Parameter Estimation 251
Appendix C: Deconvolution Tests 252
C.1 Phantom Based Evaluation of Deconvolution 252
C.2 Ground Truth Based Evaluation of Deconvolution 257
Appendix D: Comparison of Image Processing Algorithms 263
D.1 Constant Versus Variable Step Size Multi-scale Filtering 263
D.2 Comparison of Local Adaptive Otsu and Sauvola Thresholding 265
Appendix E: Unconstrained Unbounded Radius Estimation 268

Chapter 1

Introduction

Cardiovascular disease (CVD) is the number one cause of death worldwide. Europeans (48% of all deaths in Europe) die of heart disease every day (Lloyd-Jones et al. 2010, Allender et al. 2008). Annually, more than four million Europeans are expected to undergo a new or recurrent heart attack or other coronary event. Annually heart disease costs the European economy an estimated €192 billion. However, with recent medical advances in coronary therapies and changes in health habits, heart disease death rates declined by 20% in Europe from 1994 to 2004. Certain countries have a much better improvement in the heart disease death rates: in the United Kingdom, heart disease death rates (patients under the age of 65) have decreased by more than 40% from 1994 to 2004 (Lloyd-Jones et al. 2010, Allender et al. 2008).

For preventing and treating heart attacks and other cardiac problems, understanding of the blood perfusion patterns and branching structures of arteries in the coronary vasculature is essential. This thesis proposes new methods to extract coronary vasculatures from high resolution cardiac images and reconstruct the vasculatures such that they can be used in 3D computer models. These models in turn, provide a foundation for studying arterial branching patterns, blood flow simulations, and analysis of regional perfusion of blood and oxygen in the cardiac muscle.

1.1 Background

1.1.1 Coronary Vasculature

The heart is the organ that pumps venous blood to the lungs for oxygenation and then pumps the oxygenated blood to the rest of the body. The average heart pumps more than 7500 litres of blood a day throughout the body in an estimated 100,000 cycles of expansions and

contractions, approximately 70 beats a minute. The myocardium, or cardiac muscle, consists of striated cardiac muscle, which is perfused by the coronary vasculature. The main coronary arteries (shown in Fig. 1.1) branch out of the aorta into the myocardium and divide out into arterioles, which further branch out into capillary beds to perfuse cardiac muscle cells.

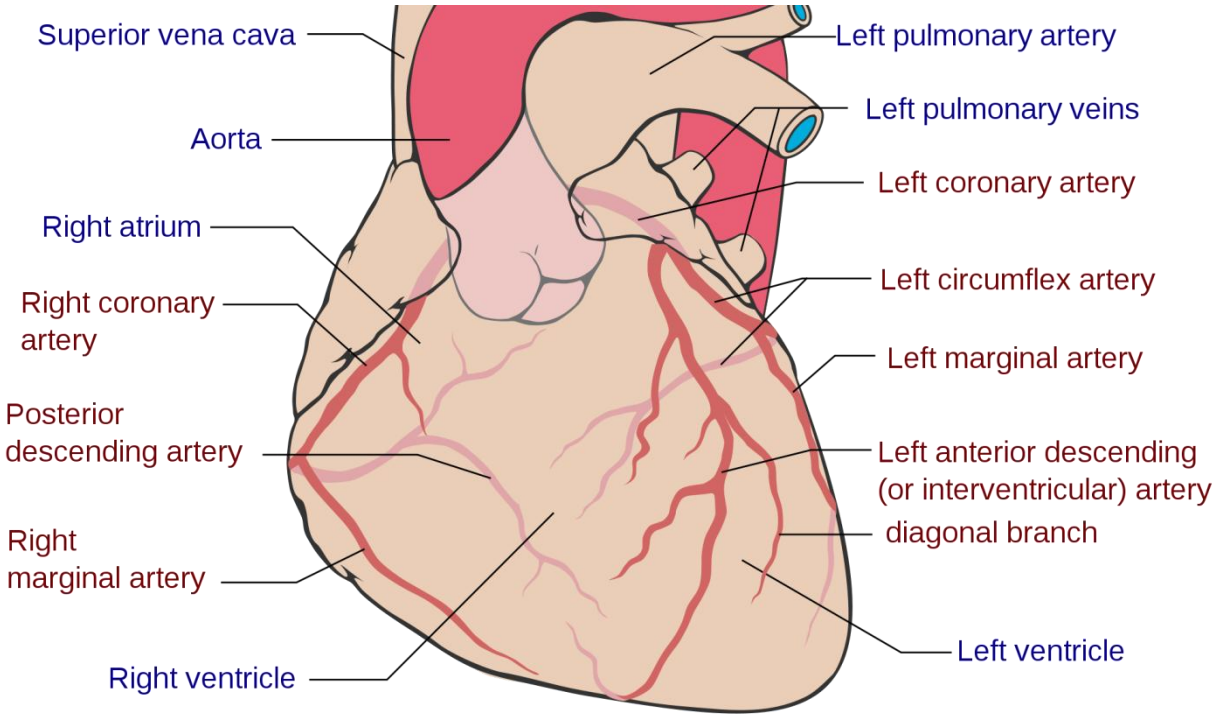


Figure 1.1: Coronary arteries perfuse blood and oxygen throughout the heart muscle. [Source: Patrick J. Lynch and Mikael Häggström.]

1.1.2 Myocardial Infarction

If the passage of blood in any artery or arteriole of the coronary vasculature is blocked, the areas of the myocardial muscle that are perfused by the blocked artery no longer receive nutrients and oxygen and thus die (see Fig. 1.2), i.e. suffer infarction. Furthermore, cardiac muscle areas perfused by narrowed arteries (stenosis) also are at risk of infarction. For developing better clinical models of myocardial infarctions which can be used for prevention and treatment, an understanding of the morphological and topological structure and branching patterns of the coronary vasculature, and myocardial perfusion regions in sub-arterial-trees is

necessary. Hence, as discussed next, visualization and imaging of the coronary vasculature has been the subject of ongoing studies in cardiovascular research.

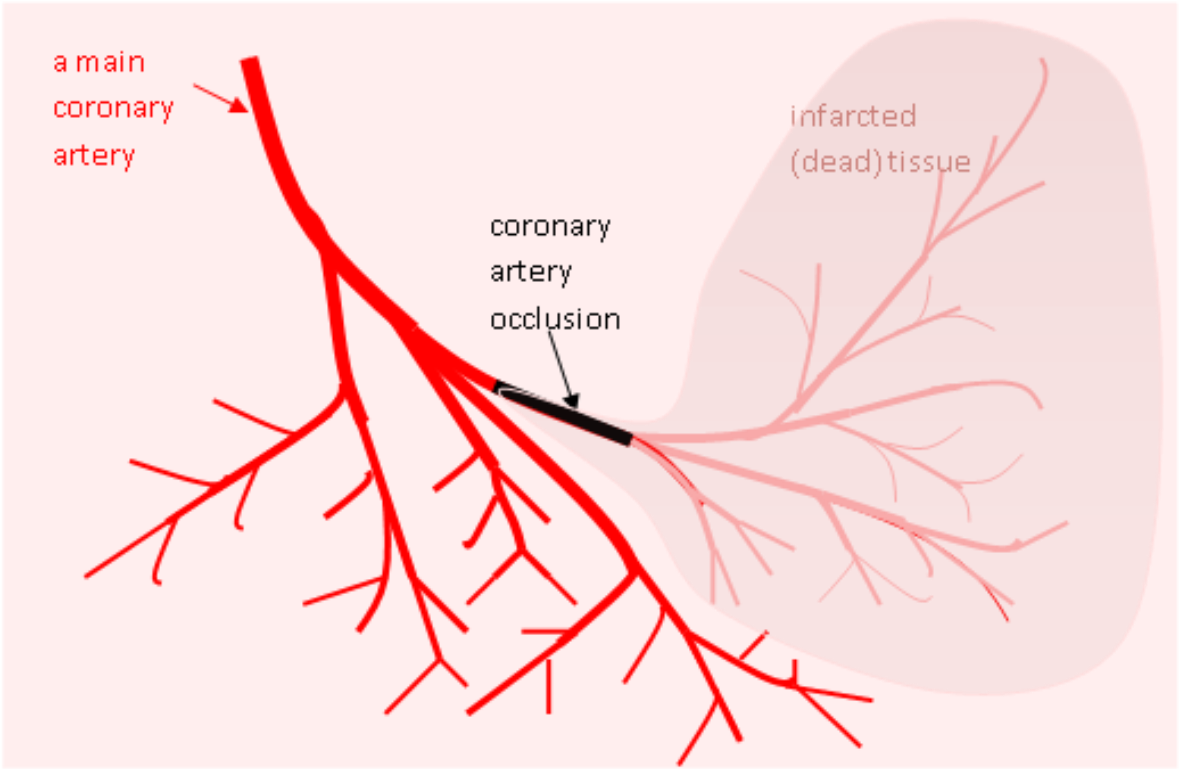


Figure 1.2: Death of cardiac muscle tissue after occlusion of a coronary artery in myocardial infraction. The darker colored tissue represents oxygen deprived infarcted tissue.

1.2 Vascular Morphometry

This section surveys past research focused on visualization of the entire vasculature over a whole organ as an image volume from which the vasculature can be extracted and reconstructed in a 3D model. The techniques for vessel segmentation and extraction in the literature applicable to this work are also discussed.

1.2.1 The History of Coronary Vasculature Morphometry Studies

The study of the coronary vasculature morphometry dates back to the early 1900s, when European researchers investigated the coronary capillaries (Spalteholz 1907, Nussbaum 1912). Light microscopy of capillaries and muscle fibers subsequent to ink injections was performed

in the 1920s (Wearn 1928), and the method was further advanced by researchers in the 1960s and 1970s for analysis of branching patterns and lengths of arterioles, capillaries, and venules in several animal models (Brown 1965, Ludwig 1971). In the 1970s, cardiovascular researchers developed the Microfil method in which a liquid polymer is inserted into the arteries where it solidifies and the tissue is corroded away leaving a hard cast of the vasculature geometry. The vascular corrosion casts were used to analyze anastomoses or the rejoining of arterial branches descended from the same parent artery (Grayson et al. 1974) and to measure the lengths, diameters, density, and intercapillary distances of ventricular capillaries (Bassingthwaighte et al. 1974). In the 1980s, scanning electron microscopy allowed imaging of vascular corrosion casts (Anderson et al. 1978, Anderson et al. 1988). In the 1990s, cardiovascular researchers fixed coronary arteries with glutaraldehyde / formaldehyde to preserve their morphology and natural original shape for extensive study of the microvascular coronary networks (Rakusan et al. 1990, Rakusan et al. 1994).

The studies described above have enhanced quantitative and qualitative knowledge of the coronary vasculature structure. They provided insight into the structural organisation of the coronary arterial network and the myocardial capillary bed. However, none provided a complete morphometric data set of the coronary vasculature, and they also could not fully detail the branching patterns of the coronary arterial tree. A mathematical model representation of the full porcine coronary vasculature was reported by Kassab et al. from porcine vascular corrosion casts (Kassab et al. 1993). Porcine vascular corrosion casts featuring details of the coronary arterial tree (van Bavel et al. 1992) and capillary bed (Kassab et al. 1994) were extracted. Whereas Grayson et al. (1974) studied corrosion casts of dog hearts, which contain extensive preformed collateral circulation (Sjöquist et al. 1984), Kassab et al. (1993-4) analyzed pig hearts, which contain few native collateral arteries (Millard et al. 1981). It is

interesting to note that previous research suggests that pig coronary anatomy, collateralization, and myocardial perfusion are very similar to their human counterparts (White et al. 1981, Weaver et al. 1986) and pig hearts are anatomically more similar to human hearts than dog hearts (Crick et al. 1998). The present study thus also uses pig coronary vasculature images. Kassab's pig coronary vascular corrosion casts offered statistical descriptions of the morphology of the coronary tree and an accurate representation of vascular geometry that facilitated vascular morphometry (vessel diameters, length, and connectivity), mathematical modelling of the arterial tree, hemodynamic analysis, and blood perfusion distribution (Cornelissen et al. 2000, Cornelissen et al. 2002). However, information on the vessel segments' and branches' spatial locations and connections in three dimensions could not be gathered from the corrosion casts.

In the early 1990s and 2000s, cardiac modellers simulated the growth of arterial model trees with constrained optimization, in which the arterial tree was modelled as a network of bifurcating cylindrical tubes. Such stochastically generated vascular trees corresponded well morphologically and morphometrically with experimental measurements of vasculatures (Wang et al. 1992, Karch et al. 2000). Statistical measurements from histological sections of ventricular vessels in the vascular corrosion casts were also used as lumped parameters for vascular network generation, assuming homogeneity in the morphometry of several diameter-defined Strahler orders of microvessels and vessels in the coronary vasculature (van Bavel et al. 1992, Kassab et al. 1993, Jiang et al. 1994, Kassab et al. 1994, Kassab et al. 1997). Vascular network topology in 3D distribution algorithms were stochastically generated from published anatomical data measured from corrosion casts, and the vascular vessels were spatially arranged incorporating global network geometry and optimal regional branch angles (Beard et al. 2000, Smith et al. 2000, Kaimovitz et al. 2005). However, in terms of

representing the vascular anatomy and physiology in actual animal models, image-based 3D computational models directly extracted from real vascular images are more representative than the aforementioned stochastically generated models. Recent advances in medical image acquisition and processing now facilitate direct extraction, measurement, and representation of the original and whole-organ coronary vascular structure from entire hearts as 3D computer reconstruction models, instead of stochastic generation of vascular networks with cast derived parameters. This is the fundamental motivation of this study. The direct extraction of the vasculature and its morphometry, topology, and structure from vascular images is discussed next.

1.2.2 Overview of Research in Vascular Imaging

1.2.2.1 Whole Organ Vasculature Imaging

For reconstruction and modelling of the coronary vasculature and whole-organ blood flow simulation in the entire myocardium, the objective of cardiovascular researchers has been to image the entire coronary vasculature from the major coronary arteries down to the capillaries, measure or extract the morphometry of each vessel, and represent the whole-organ coronary tree as a 3D computational network. Recent advances in medical image acquisition and analysis have enabled the direct, and in some cases automated, extraction of whole-organ 3D vascular structures (Lorigo et al. 2001, Aylward et al. 2002, Chen et al. 2003, Krissian et al. 2000, Fetita et al. 2005, Wischgoll et al. 2008, Wischgoll et al. 2009, Wu et al. 2011, Shingrani et al. 2010). More recently, high resolution images have facilitated the visualization of whole-organ models of vascular networks and both segmentation and reconstruction from 3D volumes using both magnetic resonance imaging and computed microtomography (Marxen et al. 2004, Burton et al. 2006, Lee et al. 2007). Furthermore, developments in 3D micro-CT now feature the resolution required to capture images of microvessels (Beighley et al. 1997,

Jorgensen et al. 1998, Plouraboue et al. 2004, Heinzer et al. 2006). The very high resolution of computed micro-tomography (known as 3D micro-CT), in some cases as fine as 1 μm isotropic spatial voxel resolution, has been exploited to visualise image vessels down to the microvasculature in small animal hearts at the whole-organ level or small samples of larger hearts (Garcia-Sanz et al. 1998, Bentley et al. 2002, Lee et al. 2007). However, so far, micro CT or other X-ray techniques are limited to small animal model hearts (Mohlenkamp et al. 2002, Toyota et al. 2002, Holdsworth et al. 2002, Schambach et al. 2010). Though able to acquire whole organ data, magnetic resonance and computed tomography angiography have been limited in their acquisition times due to short transits of contrast agents (Roditi et al. 2009, Kauczor 1998). Additionally, these modalities have a trade-off between spatial resolution and field of view (Prokop 2000, Randoux et al. 2001, Ofer et al. 2003).

Optical modalities have also been used for whole organ vascular imaging. Optical fluorescence microtomography, or cryomicrotome imaging, is a method that overcomes many of the limitations associated with resolution and acquisition in the above mentioned modalities. In this technique, the tissue sample is serially sectioned and the fluorescence from the tissue block surface is captured in high resolution optical images each time a section is removed. This microtome sectioning obviates the issue of image registration and facilitates fast 3D reconstruction of a 2D image stack. Despite the requirement of a specialised set up of experimental microscopes or digital cameras, this potential means that the cryomicrotome modality is now an increasingly established imaging technique with several variations of the microtome set-up published in literature. Rosenthal et al. (2004) and Roy et al. (2006) implemented fluorescence and brightfield (Wilson et al. 2008, Roy et al. 2009, Steyer et al. 2009) microtome sectioning, respectively. A similar methodology has been employed by LeGrice et al. (2004) to capture serial confocal microscope images over large tissue areas

(Sands et al. 2005, Annese et al. 2006, Gerneke et al. 2007, Pope et al. 2008, Sands et al. 2008). The imaged blocks stacked together can form an extended 3D volume image of the entire specimen. To overcome the penetration limit of light in tissue, extended volume confocal microscopy separately images resin-embedded transmural blocks sliced off progressively with a microtome. This has been used for imaging myocardial tissue, fibres, myocytes, extracellular collagen matrix, and blood vessel networks (Young et al. 1998, Hanley et al. 1999, Hooks et al. 2002, Arribas et al. 2007). Ultra high-resolution applications of microtome imaging have been reported by Denk and Hortsmann (2004) who reconstructed 3D tissue nanostructure using scanning electron microscopy and Ragan et al. (2007) who employed a high-speed multi-photon approach to cover a wide range of imaging length scales. Most recently the modality has been further extended by Sarantopoulos et al. (2011) to customize multispectral epi-illumination cryoslicing to image the distribution of fluorescent probes in small animal models.

1.2.2.2 Imaging Modality of the Current Study

As such, these high-resolution cryomicrotome datasets are now providing rich sets of information for developing detailed whole-organ models with a significantly enhanced level of anatomical detail. This is particularly true in the case of the vascular models as demonstrated by Spaan et al. (2005), who have shown automatic imaging of whole organ (heart, lung, kidney, etc.) vasculatures of larger animal models such as pig, dog, and human with the high voxel resolution of 50x50x50 microns. Of specific relevance to the current work and the development of the coronary vascular models outlined above are recent studies that have successfully been employed for ex-vivo visualization of whole-organ vascular trees (Lagerveld et al. 2007, van den Wijngaard et al. 2008, van Horssen et al. 2009, van Horssen et al. 2010, Lagerveld et al. 2010, van den Wijngaard et al. 2010, van den Wijngaard et al. 2011).

Cryomicrotome images have been used by Kelly et al. (2000), Spaan et al. (2005), Wee et al. (2006), Lagerveld et al. (2007), van Wijngaard et al. (2008), van Horssen et al. (2009), and several others to investigate vasculature, myocardial perfusion, and regional blood flow. Detection of micro-vessels and accurate vessel radii measurement are essential for correct coronary vascular reconstructions and blood flow simulations, which thus require high resolution images of the vasculature network in the heart. The cryomicrotome provides both the acquisition volume and the micrometer resolution required to image the whole-organ vasculature in the coronary tree over the entire heart down to microvessels (see Fig. 1.3).

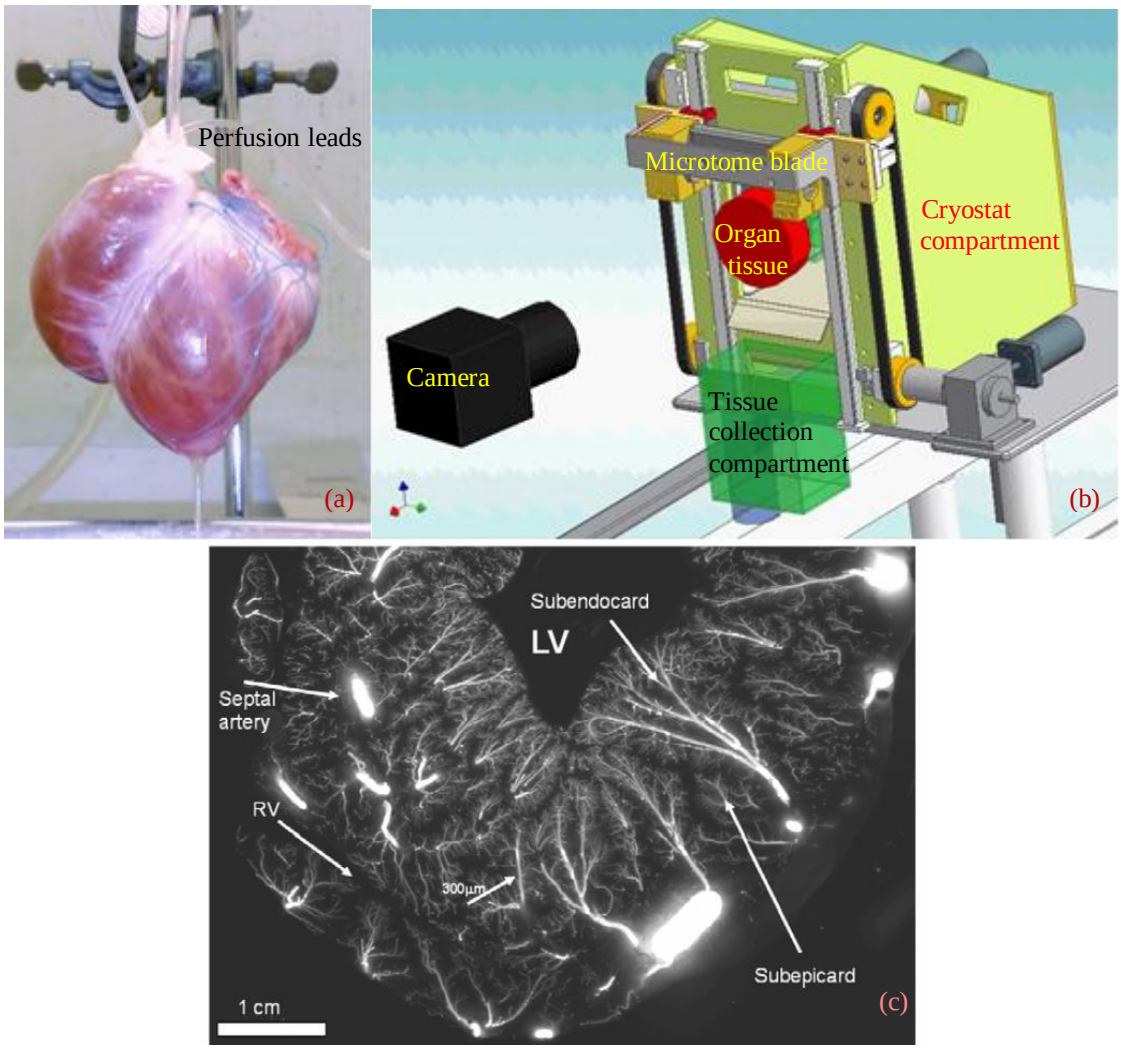


Figure 1.3: The cryomicrotome image acquisition procedure is shown chronologically in a-c. (a) First, coronary vasculature in the extracted heart is perfused with a fluorescent cast and frozen. (b) A diagram of the cryomicrotome, in which the frozen organ is placed in the cryostat compartment and serially sectioned by the microtome blade, while the camera captures a picture of the organ tissue surface each time a slice of tissue is sectioned off. (c) Digital camera-captured optical fluorescence cryomicrotome image (maximum intensity projection of image volume of a tissue slab of 2mm thickness) detailing vasculature down to the micro-vessels in the ventricular myocardial tissue. Voxel resolution: $(50\mu m)^3$. [Source: Spaan et al. 2005, van den Wijngaard et al. 2011].

1.2.2.3 Cryomicrotome Data Acquisition Protocol

Cryomicrotome data is obtained from experiments in accordance with the Institutional Animal Care and Use Committee (IACUC) of the University of Amsterdam and the Maastricht University in the Netherlands.

Microsphere Perfusion – While the heart is still inside the animal (animal models defined in Table 1.1) and is still functioning normally, i.e. beating and pumping blood, infusion catheters are used to selectively deliver a dose of approximately 100,000 15μm FluoSpheres (Invitrogen, Netherlands) microspheres (colours specified in Table 1.1). The microspheres are allowed to mix with the blood as they flow down the coronary arteries to ensure their distribution resembles real blood perfusion patterns (van Horssen et al. 2009).

Vasculature Cast Perfusion – Subsequent to the microsphere perfusion, the heart is surgically extracted out of the animal and flushed with adenosine (100 μg/L) loaded phosphate buffered saline. Subsequently, perfusion is switched to a fluorescent cast replica material comprised of Batson #17 solution (Polysciences, Germany) consisting of a monomer base solution, a catalyst and a promoter, which is infused throughout the coronary arterial tree at the average arterial pressure, i.e. 90 mmHg, and allowed to harden over a 24 hour period at ambient temperature. The perfused organ is immersed in a carboxymethylcellulose sodium solvent (Brunschwig Chemie, Netherlands) and Indian ink (Royal Talens, Netherlands) solution and frozen at -20° C.

Cryomicrotome Image Acquisition – The frozen organ, positioned inside the cryomicrotome, is serially sectioned by the cryostat microtome. The slices are cut across the transverse (axial) plane. The fluorescent cast (colour specified in Table 1.1) in the organ is illuminated by filtered light in a specific frequency bandwidth and its fluorescence emission at the surface is filtered again and captured by a digital camera (Nikon Lens 70-180mm fitted to a Kodak Megaplus 4.2i CCD Camera) each time the microtome removes an ultra-thin (≤ 50μm) layer of tissue and advances the bulk material (refer to Fig. 1.3). The heart processing and imaging in the cryomicrotome is according to the standard procedure developed at the

Department of Biomedical Engineering and Physics, Academic Medical Center, University of Amsterdam (Spaan et al. 2005, van den Wijngaard et al. 2011).

The resulting image data stack is a 3D volume of the vasculature network over the entire organ (maximum intensity projection shown in Fig. 1.4). Microsphere data is obtained by imaging the fluorescent bead particles embedded in the same heart of the vascular data (see Fig. 1.4 bottom). The voxel resolution of the 3D images used in this study is $(50\ \mu m)^3$, but this resolution is adjustable. In the optical axis or *z*-dimension, the resolution can be adjusted in the cryomicrotome by setting the slice thickness in the range of tens of micrometers. The pixel resolution in the cutting plane depends upon the number of pixel sensors in the digital camera. In this work, the imaging parameters are adjusted so that dimensions are 2000x2000 pixels. A limitation of the image acquisition is the camera's limited 8-bit pixel depth, which results in pixel saturation in the centre of large vessels due to over-exposure of the CCD sensors.

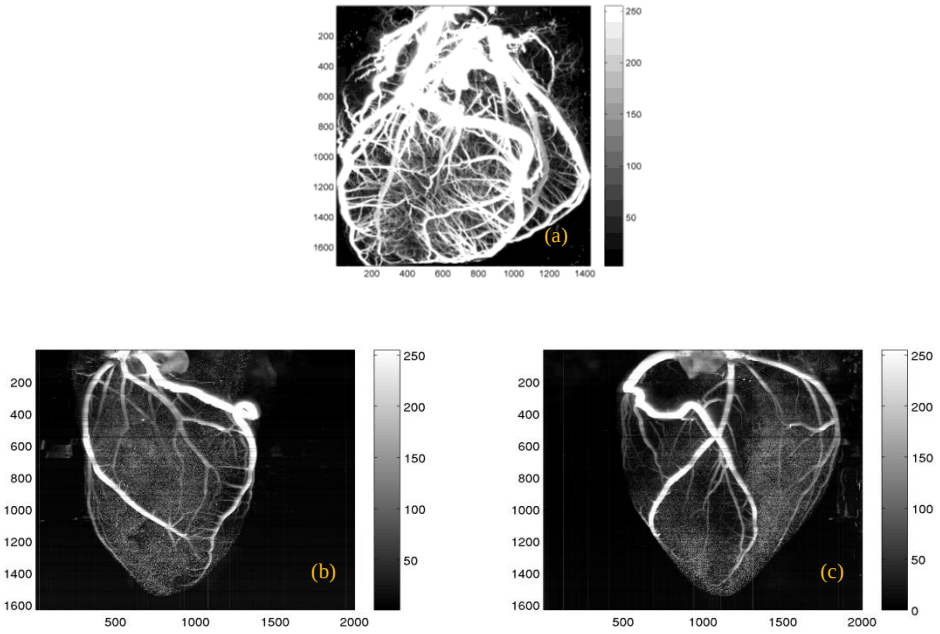


Figure 1.4: (a) maximum intensity projection (MIP) along y-dimension of cropped image volume of a porcine coronary vascular volume (1432x1461x1723 voxels) obtained with the cryomicrotome. Maximum intensity projections (MIPs) along x- (b) and y- (c) dimensions of cropped image volume of another porcine coronary vascular volume (2000x2000x1600 voxels) with both vessels and microsphere beads visible. The image data is shown at its original full resolution and includes the full imaged vasculature. The 8-bit grayscale image data has intensity ranging from 0–255 with voxel size $(50\text{-}\mu m)^3$.

1.3 Image Modelling

1.3.1 Limitations of Cryomicrotome Image Acquisition

Though the cryomicrotome approach can image the vasculature of a whole organ with 50-micrometer resolution, the images of the vessels are still suboptimal for accurate quantification. While the fluorescent pigment creates a marked contrast between the vessels and the surrounding tissue, there are three difficulties in extracting morphology from this data, as graphically illustrated in Fig. 1.5:

1) Pixel saturation due to over-exposure of the CCD sensors results in loss of data regarding the vessel size. This issue is dealt with by simulating pixel saturation as the CCD sensor blooming effect in the simulated images, which are fitted to the observed raw images in the proposed vessel radius estimation method.
2) Intensity is not consistent over vessel size, and the variation in intensity over vessel size hampers segmentation of all vessels with a single threshold. This issue is resolved by using multi-scale vesselness filtering combined with local adaptive thresholding for segmenting the vessels across all scales and sizes and incorporating a model of the cryomicrotome vessel image formation in the vessel measurement.
3) Vessel boundaries are affected by scattered out-of-focus light, resulting in a blurred gradient between the bright lumen and surrounding tissue, an artefact caused by tissue transparency which allows light from fluorescent sources embedded deep in the tissue to reach the camera's CCD sensor. This issue is tackled by computational modelling of the light scattering in tissue in an optical fluorescence image formation model that is simulated in the vessel radius estimation technique proposed in this study.

The combination of pixel saturation, intensity variation, and blurred gradients creates a challenge for both intensity- and gradient-based segmentation methods. Thus for accurate segmentation of network morphology, the saturation, tissue transparency effects, and out-of-focus blur in vessels need to be modelled and incorporated into the image processing for accurate quantification. To address the image artefacts of this modality, a model-based template-matching radii extraction method has been developed in this study. In this method, a vessel phantom image is simulated by convolving a tubular template with a point spread function (PSF) model of light transport in tissue and the optical fluorescence image formation. An additional novel element to the method is that the regional intramural variation of the optical tissue parameters for this PSF are measured with known markers (in this case 15-micron fluorescent microsphere beads) embedded throughout the myocardium. The radius of each vessel branch is estimated by fitting the simulated phantom image generated with the tubular template model to the original vessel in the image data. The advantage of this radius estimation method is that it inherently accounts for the vessel's tubular morphology, its orientation, and optical blurring. Since the microspheres are imaged in the same tissue as the perfused vasculature, the model-based template-matching method implements the classical method of modelling the image acquisition with known markers (in our case – 15 μm microspheres) and using the model to estimate what is not known (in our case – vessels).

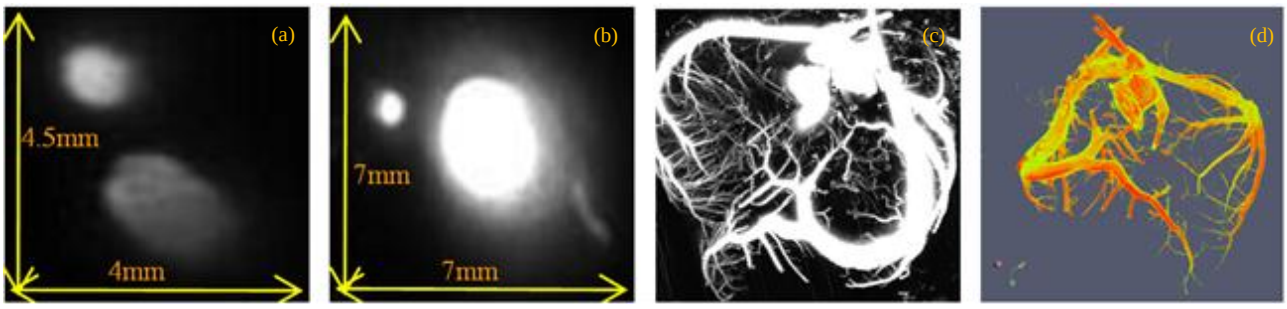


Figure 1.5: Cryomicrotome images (8-bit grayscale, intensity ranges from 0-255) with voxel size $(50\mu m)^3$ of a serially sectioned slice of porcine heart showing small (a) and large (b) vessels. Maximum intensity projection (c) and 3D volume rendering (d) of a 500x500x548 [$voxel^3$] region of a cryomicrotome image data stack.

1.3.2 Cryomicrotome Image Formation

For extracting data from images, information about the image formation is necessary. The image formation of the optical fluorescence cryomicrotome images in this study can be categorized in two stages. Each part of the cryomicrotome imaging system, from the illumination, excitation, emission, lens projection, and the CCD sensor detection in the digital camera is modeled as described below.

The first stage is the illumination of the tissue block with filtered light at a particular wavelength, the excitation of fluorophores in the fluorescent cast, and the subsequent emission of light at a different wavelength from the fluorophores. The intensity distribution at the tissue block surface is composed of the light emitted by the surface and sub-surface fluorescent sources. As they are travelling to the imaged tissue block surface, scattering and absorption in the tissue diffuses and attenuates the photons radiated by the fluorochrome sources. Light scattering and distribution in tissue is a non-linear process (Jermyn et al. 2012) but with certain assumptions it has been approximated with a linear model of photon transport and scattering in tissue in the literature (Ishimaru 1997, Wang et al. 2007). Previous research (Shimizu et al. 2005, Rolf 2005, Rolf et al. 2008) has used a linear point spread function to model the image formation in the cryomicrotome modality, which is setup in a reflection measurement geometry (i.e. the illumination source and image capturing device are on the same side of the tissue block) that performs transillumination imaging of transcutaneous intramural fluorescent objects. Chapter 2 of this thesis discusses the validity of using a linear point spread function to model the scattering of light in tissue at relatively shallow depths in the cryomicrotome setup.

The second stage is the capture of a digital image of the tissue block surface. The filtered excitation light is first imaged through a lens. The effect of the lens blur on the tissue block surface's intensity distribution is represented by the non-linear Airy pattern, but it can be

adequately modelled as a linear Gaussian blur function (van Vliet et al. 1994). After the lens system projects the incoming radiation flux onto the sensor plane, the CCD detectors convert the radiation flux to electronic signals corresponding to the grayscale levels of the generated image. The digital camera's CCD sensor is a highly sensitive photon detector, divided up into a large number (2000x2000 in the image data of this study) of light-sensitive small areas (pixels), which converts the photons that fall within the area defined by each of the pixels into electrons. The digital image intensity at each pixel is directly proportional to the number of electrons in that pixel. Previous researchers (Ientilucci et al. 1998, Ientilucci 2000, Bonnot et al. 2003) have modelled the digital image capture and pixel saturation as the non-linear blooming effect of the CCD sensor. When overexposed, the bright fluorescent sources in the field of view emit an overabundance of photons hitting the CCD plane. If the intensity of illumination exceeds the dynamic range of the sensor, the pixel wells saturate which causes the CCD potential wells to respond non-linearly and overfill and spill the electrons over to adjacent pixels. Furthermore, the finer resolution CCDs (50 micron pixels in the image data of this study) are more susceptible to this blooming and smearing phenomena because of their reduced dynamic range due to the smaller pixel and smaller electron well capacities. Chapter 4 describes the blooming simulation (presented in Ientilucci 2000) of this saturation effect that has been implemented in this work.

In the above steps in the cryomicrotome image formation, the final stage of CCD detection is non-linear at luminosities greater than the dynamic range of the pixel and thus in this study, pixel saturation is accounted for by a computer simulation of blooming performed on the computer generated image of a vessel cylindrical model convolved with the tissue point spread function model. On the other hand, as discussed earlier, the mathematical representation of scattering and attenuation of the photons in tissue light transport with a linear point spread

function model is well-established in the literature for over two decades (van der Zee et al. 1987, van der Zee et al. 1988, Grinvald et al. 1994, Brukilacchio 2001, Akcay et al. 2003, Dong et al. 2003, van Leeuwen et al. 2003, Watanabe et al. 2003, Pilz et al. 2008). The PSF has been used as a mathematical model in optical imaging of tissues extensively in the literature (van der Zee 1992, Izatt et al. 1994, Schmitt 1998, Fujimoto et al. 1999, Kim 2004, Wang et al. 2012). Thus, in this thesis, the tissue scattering and distribution of the fluorescent light of the image formation is modelled with a linear point spread function. Therefore, discussed in section 1.5.6 is the functional use of the point spread function in image restoration.

1.4 Vasculature Extraction

Extracting the vasculature requires filtering of the input images for vessel enhancement and detection, segmentation of the vasculature from the images, and skeletonization of the segmented vasculature to define vessel centrelines.

1.4.1 Filtering

As a pre-processing step, vessel segmentation first requires detecting and enhancing the vasculature in the images and filtering out noise and non-vessel structures. Morphology schemes can be used to enhance vascular images. Since vessels have a tubular shape, morphological operators such as dilation and erosion can be applied to the images to remove noise structures and enhance the shape of the vessels (Eiho et al. 1997, Thackray et al. 1993). However, the risk associated with dilation and erosion is the loss of anatomical vessel detail along with the removal of noise.

In another filtering approach, the matched-filters technique, the image is convolved with multiple filters to detect vessels of different sizes and orientations. A subset of this approach is

known as line filtering, which can enhance and detect, at multiple scales, curvilinear objects (Sato et al. 1998, Hoover et al. 2000). A concern regarding line filtering is that other curvilinear objects such as catheter leads, ribs, organ boundaries, or image outlines, i.e. structures in the images apart from the vessels can also sometimes be enhanced, and hence the line filtering may not be adequate enough for separating the vessels from other linear structures enhanced in the images. In order to avoid extracting non-vessel and noise line structures, a vesselness measure can be calculated as done by Frangi et al. 1998 in his multi-scale vesselness filtering approach.

Multi-scale filtering, enhances vessels at several resolutions since the size of the vessel determines what specific resolution it is most clearly visible at (smaller vessels are extracted from the finer resolution scale image and larger vessels are extracted from the coarser resolution version of the same image). In this way all the vessels from the microvascular to the macrovascular range of a coronary tree can be extracted at multiple image scales (Sarwal et al. 1994, Chwialkowski et al. 1996, Frangi et al. 1998). Multi-scale filtering on its own does not segment but only enhances the vessels since it does not define the voxel as vessel as opposed to background, but rather it labels each voxel with a vesselness value related to the probability of its being vessel in the range from 0-1. The vesselness filtering output requires further processing to be binarized into vessel and background with a threshold method. Hence, in this study, multi-scale vesselness filtering followed by local adaptive thresholding (as discussed in section 1.3.5.3) is employed for vessel segmentation.

1.4.2 Segmentation

Segmentation requires classifying the image into vessel and non-vessel regions. Deformable model methods can be used to segment the vasculature. Active contours are parametric curves that evolve under a balloon force (contour inflation) towards edges with smoothness

constraints until they delineate vessel boundaries or contours (Kass et al. 1988, Acharya et al. 2000, Toledo et al. 2000). In the level sets framework, the deformable curve propagates towards the lowest potential of a cost function, with imposed smoothness constraints by embedding the contour in a higher-dimensional signed distance function, the zero level of which represents the actual curve that will delineate the vessel boundary (Lorigo et al. 2001, Nain et al. 2004). However, deformable model methods are not well suited for the optical fluorescence image data employed in this study since the boundaries between the vessel cross-sections and the background are blurred by out-of-focus light excited from below the surface and the optical lens blur. For this reason there is no clear segregation of the intensities of the vessel voxels and the background, but rather a slow gradual decrease in pixel intensity from the vessel boundary to the background. So both gradient-based and intensity-based approaches to deformable model methods typically result in imprecise vessel boundary delineation in the optical fluorescence data because the final evolution of the active contour and / or level sets would be affected by the blurred out-of-focus halo surrounding the vessel cross-sections.

Vessels can also be segmented as parametric models, i.e. shape based modelling of the vessels as either a collection of overlapping ellipsoids, bifurcating tubular structures, cylindrical structures (Krissian et al. 2000), circular contours (Chan et al. 2000), or generalized cylinders (Agin et al. 1976). An important consideration in the shape based modelling of vessels is where the radii are defined. If only a single radius is defined for each vessel branch, then the vessel model misses the information of the change in radius from the start to the end. If the radius is defined for each start and end node of the vessel, then the vessel is modelled as a tapering cylinder. However, if the radius is only measured at the far endpoints of a vessel, the sharp intermediate changes of radius that can be important for clinical detection of stenoses or aneurysms can be lost. Rather than two endpoints, a more accurate representation of the vessel

branch is as a set of several consecutively connected node points defined by their coordinates and radius. Another commonly used model in literature that addresses this issue is the generalized cylinders, wherein a vessel is modelled as a three dimensional cylindrical volume consisting of circular contours connected by a cubic spline representing the spine of the volume (O'Donnel et al. 1994). A three dimensional vascular reconstruction requires the position, orientation, and diameter of each circular contour (Sato et al. 1998).

Researchers have also applied rules that define general blood vessel appearance in images, such as high-intensity centrelines, circular contours, segment intersections, etc. (Smets et al. 1988). However, one prominent limitation with the method in Smets et al. (1988) is that the intersection models do not incorporate trifurcations and quadrifications a rare but still observed branching type. Additionally, assuming high-intensity centrelines as a general blood vessel heuristic could miss small vessels in the optical fluorescence image data of this study since not all vessels have high-intensity centrelines as the intensity varies with vessel size. Also in some vessels the centrelines are of the same intensity as the rest of the vessel voxels. Finally, vessels in the cross-sectional images of the data in this study are often more elliptical than circular in their shape. Geometric contours can also be evolved to extract tubular structures in 2D or 3D from intensity images. The vessel cylinder models can be localized with detected contours and defined by a cross-sectional element swept along the long axis to optimally fit the contours (Huang et al. 1993). However, the matching filter approach in Huang et al. 1993 assumes smoothness constraints between adjacent vessel branches and may not work well for matching highly tortuous blood vessels.

Another approach, template matching, deforms an *a priori* template of vessels, represented as a network of nodes connected by segments, to optimally and stochastically fit to the arteries in vascular images (Petrocelli et al. 1992, Petrocelli et al. 1993). However, this template-

matching approach cannot be applied for simultaneous whole-organ vascular extraction because the template is limited to only matching branching arteries and lacks the global structure and computational complexity needed to match the entire coronary tree. Template-matching can be augmented with a priori information about the anatomy and morphology of the object to be detected (in this case vascular morphology) and also information about the imaging modality's point spread function (PSF) or degradation model, which describes the modality's degradation influence on how the object appears in the image as opposed to how the object is in reality. This is what is done in the current study, in which a cylindrical template blurred with the imaging modality's measured PSF is matched to the real vessel image volumes for successively performing morphometry of all the individual vessel branches for the full vasculature extraction from the optical fluorescence images.

1.4.3 Voxel Classification

Region growing and connected component labelling are two voxel-based image segmentation methods that are commonly applied for vascular extraction. Region-growing starts from a seed point, and the region grows out by encompassing voxels that are within a certain distance or within a certain intensity or brightness range until it delineates the whole vascular tree (Masutani et al. 1998, Yi et al. 2003). One danger associated with region growing is that if at any point any of the vessels come very close to other structures in the images, such as bones or other organs, with similar pixel intensities, then the region growing may expand out to include these other objects in the images. In connected component labelling, voxels are labelled and grouped into connected components to separate non-vessel or noise structures and segment the vasculature from the background (as used in Jiang et al. 2003). Connected component analysis is very useful for removing smaller noise structures disconnected from the vasculature but it requires the input image to be binary. This technique is used in the vascular extraction pipeline

proposed in this study for removing blobs, caused by leakage of fluorescent cast in the tissue, from the images of the vessels after they are binarized by local adaptive thresholding for segmenting the data following multi-scale vesselness filtering.

1.4.4 Skeletonization

Skeletonization delineates the connected vessel centrelines, which form the basis of a 3D reconstruction model of the vascular network. The centrelines can be traced or detected by one of two main categories of methods.

In the first category, ridge-tracking, the images are considered as topographical maps in which the vessel centrelines are located at ridges, i.e. points at the peaks of the intensity map that can be reached by travelling along the direction of steepest ascent from any arbitrary position on the image. Thus the vessel centreline points can be determined by ascending in the direction of maximal surface gradient (Aylward et al. 1996, Aylward et al. 2002). The differential-geometry approach delineates vessel centrelines with crest points, which are local maxima of maximum surface curvature in the parametric surface image (Prinet et al. 1997, Armande et al. 1999). Generally, vessel-tracking begins from a seed point, and traces vessel centrelines by examining the voxels lying orthogonal to the centreline axis using edge detection (Lu et al. 1993), intensity ridge detection (Aylward et al. 1996), fuzzy clustering (Tolias et al. 1998), or graph representation (Lecornu et al. 1994).

The second category of these methods is thinning (Lam et al. 1992). Topological thinning iteratively peels away voxels at the border of the vessel until just a single-voxel-thick line remains (Chen et al. 2003). Simple points, i.e. voxels that are not fundamental to the preservation of the topology of the vessels, are removed (Lee et al. 1994). Distance-ordered homotopic thinning examines each vessel voxel sequentially (following the order of increasing

distance to the vessel surface) and removes it if it is a simple point (Pudney 1998). Voxel coding identifies centrelines by stepping through voxels, coding each with a unique label, and returning to them to identify the medial centrelines according to the labels which specify the distance of the voxel from the vessel boundary (Lee 2009, Zhou et al. 1999). A point to note is that the accuracy of the vessel centreline delineation in the above-mentioned topological thinning and distance transform based methods is limited to the discrete voxel resolution of the images because these methods only identify the centremost voxels as the centrelines.

The aforementioned ridge, crest, and edge tracking approaches assume that the vessel centrelines lie at the local intensity maxima or gradient maxima points, but this may not be true in the case of clipped pixel intensities in saturated images due to over-exposure, which may result in a flat rather than an ascending-descending intensity profile across the vessel cross-section. Since the image data in this study has over-exposed saturated pixel intensities in the centres of larger vessel cross-sections, ridge tracking would not be ideal for tracing the vessel centrelines across large vessel sizes. The local maxima approach (Krissian et al. 2000) for delineating intensity ridges, which assumes that the local maxima points will always occur at the vessel medial axis or centreline, would work well if the local maxima points' intensity across all the vessel centrelines would not vary much and would be higher than the rest of the vessel's pixel intensities. But in vessels in the image data of this study, these conditions are not always met. In large saturated vessels of this study's images, there may be no local maxima points in the vessel centre with intensity higher than the surrounding voxels, i.e. local maxima might not exist because the intensity at the centre is not higher but the same as the rest of the vessel's pixel intensities (e.g. as in clipped saturated vessel pixels). In small vessels of this study's images, the intensity of the local maxima points varies greatly. The large variation in the local maxima intensities across the vessel sizes in the data of this study would complicate

the selection of a threshold. Hence, the vessel centrelines in this study's images traced with the local maxima method would be susceptible to broken disjointed skeletons after the threshold segmentation of the local maxima output. Finally, with regards to the image data of this study, due to out of focus light from below the surface, the halo surrounding the vessel cross-section that obscures the vessel boundary may skew the local maxima off the actual vessel centrelines. Therefore, the work in this study applies the second category discussed, i.e. the distance transform based topological thinning approach for delineating vessel centrelines.

1.4.5 Summary of Vessel Extraction

There are many methods for segmenting vasculature in the literature. Lesage et al. 2009 and Dehkordi et al. 2011 offer recent comprehensive reviews of vessel segmentation methods. Kirbas et al. (2004) also contains more comprehensive descriptions of the above-mentioned methods.

It is important to note the particular segmentation and skeletonization methods applied to extract vasculature from images depend on the particular imaging modality and application. In the images of this study, blob structures (caused by leakage of fluorescent cast into tissue) can degrade the images and thus multi-scale vesselness filtering with a vesselness measure is applied for vessel enhancement and non-vessel structure suppression. The intensity of vessel voxels in this study is not consistent over vessel size, and so local adaptive thresholding is employed to make the vessel detection robust to the large intensity variation. Connected component labelling is utilized for segmenting the fully connected tree from noise structures. Medial axis thinning is performed for tracing the vessel centrelines in the binarized segmented vasculature images. A model-based template-matching approach incorporating a model of the image acquisition is used to measure vessel radius in the optically blurred images.

Pre-processing may be necessary to correct for noise or imaging artifacts before the vessel extraction can be performed. Restoring the images by deblurring, removing artifacts, deconvolution, maximum likelihood estimation, and model-based iterative restoration is discussed in the next section. Since this thesis deals with digital optical fluorescence images, the image restoration review discusses the out-of-focus halation caused by the tissue scattering and diffusion of the fluorescence, the lens blurring of the intensity distribution, and the pixel saturation in the conversion of the luminosity into 8-bit grayscale pixel intensity levels by the CCD (charge coupled device) sensors.

1.4.6 Image Restoration

Various techniques have been developed to restore images of 3D samples, acquired as a series of parallel 2D slices. Primarily, in the literature, the major approaches to deblurring and image restoration are 1) no neighbours, 2) nearest neighbours, 3) linear inverse filtering, 4) regularized constrained iterative filtering, 5) Wiener filtering, 6) constrained least squares filtering, 7) maximum likelihood restoration, 8) blind deconvolution, and 9) model-based restoration.

1.4.6.1 No-neighbour Deblurring

No-neighbour deblurring algorithms operate on a single 2D image at a time by amplifying higher spatial frequencies and thus augmenting the specimen of interest, while reducing out-of-focus light caused by lower spatial frequencies. The primary limitation of this method is it does not account for image slices below and above the current image. Additionally, if the specimens imaged are a complex mixture of low and high spatial frequencies, 2D filtering methods might remove objects of interest within the specimen (Monck et al. 1992).

1.4.6.2 Nearest -neighbour Deblurring

The *nearest-neighbour algorithm* takes into account the influence of the neighbouring planes above and below the current plane. The neighbour planes are blurred with a digital filter and then subtracted from the plane in the middle or the current plane of interest. A better approximation of the haze can be obtained by taking into account more than just the two adjacent neighbours. Multiple neighbours can be blurred and subtracted from the current plane of interest to de-blur each slice of an entire 3D stack (Castleman 1979, Agard 1984). Though these 2D deblurring algorithms are computationally efficient, they run the risk of removing components of interest in the specimen and sharpening irrelevant features originating from neighbouring planes in the *z*-direction.

1.4.6.3 Linear Inverse Filtering

Linear inverse filtering, a 3D deconvolution method, attempts to find the inverse to the convolution operation inherent in an imaging system; the application of this inverse operation repositions out-of-focus light back into focus. This approach assumes that the raw image data produced from an imaging system can be modelled as the result of a convolution of the original specimen with the point spread function of the imaging system. In restoring out-of-focus light to its origin, deconvolution is limited by the uncertainty factor caused by noise, a fundamental limitation inherent in any image-formation system. In practice, an estimate of the point spread or degradation function of the imaging system is used to restore the original specimen. The point spread function (PSF) is a model of the imaging system's response to a point source.

The observed image can be represented as the convolution ($\otimes$) of the imaging system's PSF with the specimen being imaged:

$$Observed = PSF \otimes Specimen \tag{1.1}$$

Since spatial convolution is equivalent to multiplication in the Fourier domain, the Fourier transform of the observed image is equal to the multiplication of the PSF's Fourier transform with the imaged specimen's Fourier transform:

$$\Im\{Observed\} = \Im\{PSF\} \bullet \Im\{Specimen\} \tag{1.2}$$

Deconvolution, or image restoration, is the process of estimating the original object. The Fourier transform of the original specimen can be achieved by dividing the observed image's Fourier transform by the PSF's Fourier transform (also known as the optical transfer function or OTF):

$$\Im\{Specimen\} = \frac{\Im\{Observed\}}{\Im\{PSF\}} = \frac{\Im\{Observed\}}{OTF} \tag{1.3}$$

Thus in linear inverse filtering, the deconvolution operation can be efficiently computed in the Fourier domain as the division of the observed image's Fourier transform by the PSF's Fourier transform. With the inverse Fourier transform, the original specimen's Fourier transform can be inverted back into the spatial domain to get the restored spatial image of the original object:

$$Specimen = \Im^{-1}\{\Im\{Specimen\}\} \tag{1.4}$$

This method is computationally efficient, but does not account for the noise amplified by the Fourier division operation (Erhardt et al. 1985, Tommasi et al. 1993). In practice, the observed image cannot be modelled as just a convolution of the PSF with the specimen, because the imaging system also adds noise to the image, i.e.:

$$Observed = PSF \otimes Specimen + Noise \tag{1.5}$$

Due to this unknown random noise component, the original specimen cannot be recovered exactly even if the optical transfer function is known precisely. Restoring a 3D biological specimen from optically sectioned images is thus an ill-posed inverse problem. For this reason, the deconvolution restored image is only a noise-distorted estimate, at best, of the original. Inverse filtering is unfeasible due to noise amplification during division in Fourier space, as shown in the equations below in which we first take the Fourier transform of both sides of equation (1.5) and then divide all terms of the equation by the PSF's Fourier transform:

$$\begin{aligned} \Im\{Observed\} &= \Im\{PSF\} \bullet \Im\{Specimen\} + \Im\{Noise\} \\ Deblurred &= \frac{\Im\{Observed\}}{\Im\{PSF\}} = \Im\{Specimen\} + \frac{\Im\{Noise\}}{\Im\{PSF\}} \end{aligned} \quad (1.6)$$

Deblurring is offset by noise gain, which can induce ringing artifacts in the image. Ringing effects near steep intensity gradients (Lagendijk et al. 1988) and stripe noise (Wang et al. 2007) can be eliminated with a priori knowledge of the original specimen. Specifically, a *regularized inverse filter* which uses an object's attributes, such as smoothness or brightness, as constraints for statistically determining the best restored estimate can be applied (Biemond et al. 1990).

1.4.6.4 Regularized Constrained Iterative Filtering

The *constrained iterative* approach to image restoration is a method of successive approximations, which iteratively seeks to refine the restored estimate. The operator is not only based on the degradation or distortion function, but also includes constraint terms to steer the restored estimate as close as possible to the original specimen. The end goal of this constrained iterative restoration approach is to converge to a reasonable approximation for a finite number of iterations. The imaging process is simulated by convolving the estimate of the original specimen with the PSF of the imaging modality. Iterations are ended with certain

stopping criterion such as when the difference between the simulated image and the observed one is lower than or equal to a specified threshold. The restored image is the estimate at the final iteration (Schafer et al. 1981, Kundur et al. 1998, Sezan et al. 1990, Verveer et al. 1999, Zhang 1993).

1.4.6.5 Wiener Filtering

A further category of iterative algorithms endeavour to minimize a statistical error criterion. *Minimum mean square error or least square error filtering* produces a restoration estimate of the original specimen by spatially convolving an optimal filter with the degraded observed image. As explained above (eq. 1.5), the degraded observed image is the original specimen convolved with the distortion or impulse response (optical transfer or point spread function) inherent in any imaging modality (assumed to be a linear time-invariant system) with unknown added noise. The least square error to be minimized is the mean square error between the restoration estimate and original specimen. The solution to the least square error minimization is called a Wiener filter, which is a function of the optical transfer function and power spectrums of the original specimen and noise. In the ideal case of a noiseless system (wherein the signal-to-noise ratio is infinite), the Wiener filter reduces to the inverse of the optical transfer function or inverse filtering (Wiener 1949, Gonzalez et al. 2002). The Wiener filter works on the principle that frequencies at which noise predominates are attenuated by the filter because at these frequencies, the signal to noise ratio is small. Wiener deconvolution relies on information about the noise in the imaging system, such as noise covariance and signal-to-noise ratio, which can be estimated from the power spectrum of the noise. Due to noise amplification during division in Fourier space, Wiener deconvolution is susceptible to ringing artefacts at sharp intensity gradients at image boundaries, which result in high frequencies in the Fourier domain. Deconvolution in the Fourier domain amplifies these high frequencies,

thus introducing the ringing phenomenon in the image when it is inverted back to the spatial domain.

1.4.6.6 Constrained Least Squares Filtering

On the other hand, noise mean and variance are the only prerequisites for *constrained least squares filtering*. These parameters can generally be determined from the Fourier or power spectrum of the image. Uniformly distributed white noise can be estimated from the Fourier spectrum. If the noise is periodic, it will spike at certain frequencies corresponding to the primary components of the noise signal's Fourier series. The constrained least squares filter replaces the signal to noise ratio in the Wiener filter with a frequency variant function. Whereas the Wiener filter deconvolution minimizes an error criterion between the restored and original specimen, constrained least squares restoration minimizes a criterion function that also satisfies a smoothness constraint (e.g., the Laplacian of an image, which quantifies the edges or intensity transitions), thus minimizing the ringing or wavelike oscillation artifact caused by Wiener filtering. The restored estimate of the original specimen is restricted by the constraint that the expected Euclidean vector norm of the difference between the raw observed image and the estimate obtained by convolution with the PSF should be equal to the Euclidean vector norm of the expected noise (this is to ensure that the difference between the degraded or observed image and the estimate is purely due to noise). The restored estimate obtained through Lagrangian minimization is given in the Fourier domain as a function of the observed image, the optical transfer function, and the Fourier transform of the Laplacian mask (Umbaugh 2007, Bilgen et al. 1994, Hunt 1973, Lang 1973, Bertsekas 1982). By calculating the inverse Fourier transform, the restored 3D image in the spatial domain can be recovered.

1.4.6.7 Maximum Likelihood Restoration

Maximum likelihood restoration methods model image pixel values with a statistical probability distribution to optimize the restored estimate. A log-likelihood function (a function of the raw observed image and the PSF-blurred estimate of the original specimen) is maximized in order to obtain the best restored estimate of the original specimen. The original specimen can be restored with the estimate that maximizes the likelihood function (Kay 1993, Lehmann et al. 1998, Aldrich 1997, Markham et al. 2001). Expectation-maximization is a common method for determining a maximum likelihood estimate of a parameter in statistical models, depending on unknown hypothetical variables. Expectation-maximization iteratively calculates the expected value of the likelihood function and updates the estimate of the parameter that maximizes the expected likelihood. Statistical maximum likelihood produces higher quality restoration results at the expense of a higher computational cost than linear and constrained image deconvolution methods because it integrates Poisson or Gaussian noise statistics into the formulation. This additional feature of incorporating a statistical model of the noise in the maximum likelihood method augments the distinction between noise and out-of-focus light. With the right noise statistic, this statistical technique can more precisely retrieve image data lost or degraded by the lens and noise.

1.4.6.8 Blind Deconvolution

Finally, *blind deconvolution* is similar to statistical maximum likelihood estimation method, but a significant difference is that the PSF is also estimated along with the restoration of the original specimen. An initial estimate of the original specimen is convolved with a PSF, which is calculated theoretically from the imaging modality optics. The image produced from the convolution is compared with the observed image. After the comparison, the algorithm updates the estimates of both the image restoration and the PSF. The process continues

iteratively until the difference between the estimated and observed images has been minimized (Katsaggelos et al. 1990, Katsaggelos et al. 1991, Kundur et al. 1996). In classical linear image restoration, the blurring or degradation function is predetermined, and its Fourier version, the optical transfer function, is inverted and convolved with the observed image to obtain an estimate of the original. However, for cases where limited or no information about the imaging modality's PSF and the original specimen is available, blind image restoration offers PSF identification along with image restoration.

1.4.6.9 Model-Based Restoration

The image data in this study has voxels saturated at the larger sizes of vessels, a non-linear effect. Since deconvolution assumes a linear model of image degradation, it typically only works well for restoring unsaturated vessel image volumes. Due to the non-linearity introduced by the saturation in the vessel data, model-based iterative optimization approaches to image restoration are more applicable than linear deconvolution, since non-linearity can be explicitly incorporated in the models. In the literature, several researchers have published the application of model-based methods for restoring or directly segmenting the image data.

One approach to restoration is maximum probability estimation. Chen et al. (2011) restored and reconstructed optical images with a model-based statistical optimization algorithm based on Bayesian estimation theory known as maximum *a posteriori* estimation, which obtains the maximally optimal estimate of the original image. Assuming additive noise, the observed measured image, and the original unknown image as stochastic signals, estimation of the original unknown image is done by maximizing the conditional probability density function (PDF) of the observed measured image given the original unknown image. The PDF is mathematically represented as a function of the point spread function, original unknown image, and the observed measured image (Elad et al. 1997). The proposed method

performed better than traditional blind deconvolution. Olofsson (2005) also used this maximum *a posteriori* approach to recover pixel data clipped at the maximum saturation level by explicitly accounting for the signal clipping in a signal generation model. A similar approach of simulating pixel saturation as the blooming effect is employed in the modelling of the image formation in the proposed vessel extraction method of this thesis.

Several authors have explored restoration with Markov random fields (MRF), which are models for image intensity. Among other methods, maximum probability estimation can be used to fit the MRF model to the images. Geman et al. (1984) obtained the highest probability estimates of the original image as the lowest energy states of a Markov random field model of the image. The lowest energy states in the Markov random field model of the image are identified by simulated annealing, in which each point of the search space is analogous to a state of a physical system, and the energy function, analogous to the internal energy of the system, is brought from an arbitrary initial state to a state with the minimum possible energy (i.e. the most probable state and most likely estimate of the original image). Rajagopalan et al. (1999) modelled the space-variant blur parameter and the focused image as Markov random fields and recovered the depth and the focused image of a scene from two defocused images with simulated annealing. Chalmond 1988 restored grey level images corrupted by additive independent Gaussian noise by modelling the spatial interaction as a Markov random field whose energy was parameterised and edge-preserving parameter estimation was performed. Likewise, minimization of a parameterised energy function representing the difference between the observed measured and a simulated image is used in the model-based vessel extraction method proposed in this thesis.

Another approach found in the literature is parameterised model-based restoration. Motion estimation (Martinez 1986), turbulence (Lemaitre et al. 2005), vibration (Jakubik 1998), haze, fog, smoke (Tarel et al. 2009), and lens defocus (Hasinoff et al. 2007) have been

simulated with models parameterised by variable parameters measured from the images. In this thesis, the tissue scattering and diffusion of fluorescent light is simulated with a parameterised model of the point spread function. Optical tissue attenuation coefficients are the model parameters that are measured by fitting the model to images of the microsphere fluorescent bead markers embedded throughout the tissue.

Of particular relevance to the work in this study is the spatially-variant model restoration approach. Tekalp et al. (1988) performed model-based segmentation of blurred images representing the space-variant blur as a collection of a number of distinct point spread functions. Ozkan et al. (1994) performed space-varying image restoration by using a different blurring function at each pixel of a real-life image with unknown space-varying out-of-focus blur. The approach proposed in this thesis incorporates the spatial variation in the point spread function parameters by measuring them from microsphere fluorescent bead markers embedded throughout the tissue.

The vessel measurement approach proposed in this thesis is inspired by the approaches discussed above that represent the image restoration, segmentation, and reconstruction problem as a parameterized energy function to be minimized. The optimal parameter estimates are obtained at the minimal energy states. The model-based template-matching method proposed in this thesis optimizes vessel radius by minimizing the error between the observed and simulated images of the vessels. Every aspect of the cryomicrotome vessel image formation from illumination, excitation of the fluorescent dye in the vessels, reflection of the wavelength-altered emitted light, optical blurring in the lens, pixel intensity quantification, saturation, and blooming is simulated. Though the vascular reconstruction method proposed in this thesis is primarily model-based, this section's earlier review of deconvolution is still useful for initialization in the model-based template-matching radius estimation method developed in this thesis (refer to Chapter 4 for details on how the

deconvolved image is used for initializing the radius estimate that is then iteratively optimized).

1.5 Objectives

Modelling myocardial blood flow on accurate computational reconstructions of the morphology and topology of the coronary arterial network presents significant opportunities for understanding the anatomy and physiology underlying cardiac ischemia and myocardial infarction (Lee & Smith 2012). Specifically, detailed three-dimensional (3D) models of the coronary vasculature provide the potential to analyse the functional implications of the organisation of intramural coronary vessels across a range of normal and pathophysiological states. Among other factors, the branching pattern and 3D geometry of the coronary vasculature have a direct influence on coronary blood flow and pressure distributions (Kaimovitz et al. 2005). Hence, the morphometry and reconstruction of the coronary arterial network down to the level of microvasculature is fundamental in blood flow simulations to model hemodynamics in the myocardium (Mittal et al. 2005). This is important for the understanding of flow and oxygen distribution within the myocardium and the location and extent of areas at risk of infarction in the case of a vascular occlusion or stenosis (Spaan et al. 2005). With enhanced knowledge of the coronary arterial tree and its hemodynamics in the presence of heart diseases and an anatomically based understanding of vessel remodelling and collateralization, future diagnosis and treatment of coronary artery disease may be further advanced. Since coronary blood flow is highly sensitive to vessel cross-sectional area (vascular conductance is proportional to the fourth power of radius), accurate detection of micro-vessels and vessel morphometry is essential for computational fluid flow simulations on 3D reconstructions of coronary vessels (Beard et al. 2000, Smith and Kassab 2001, Boutsianis et al. 2004, Huo et al. 2007, Huo et al. 2009). Thus the motivation of this work is the

development of techniques to segment and reconstruct computational models of myocardial vessels with accurate vessel measurements from imaging data that is now becoming available with significantly improved spatial resolution. In this study our objective is to extract vasculature down to 0.5 voxel = 25μm radius vessels with sub-voxel accuracy (error of ± 0.25 voxel = 12.5 μm) of vessel radii measurements from the 50μm isotropic voxel resolution 8-bit grayscale cryomicrotome images. Then our goal is to obtain a coronary pressure and regional flow distribution model across the reconstructed vasculature with a 1D steady-state blood flow simulation, which can be compared to the regional microsphere perfusion in the same vasculature. Section 5.3.7 in chapter 5 demonstrates that the model-based vascular extraction method presented in this study sufficiently improves the accuracy in radius estimation for application to blood flow simulations such that radius error is no longer the limiting factor for estimating accurate models of coronary perfusion with the reconstructed vasculature. As illustrated in section 5.3.7, an error of 0.25 voxel standard deviation in the radii estimates results in negligible error in the coronary flow simulation as compared to the error between the flow model and microsphere perfusion measurements.

1.6 Materials

1.6. 1 Image Data

Table 1.1 below lists all the cryomicrotome image datasets that were processed in this work. The acquisition of cryomicrotome vasculature and microsphere image datasets is described in section 1.2.2.3. Datasets 1-2 were employed in chapter 3 section 3.3.2 for measuring optical attenuation parameter variation in the myocardium.

Dataset	Figure no.	Organ	Animal model	Dimensions	Vasculature	Microspheres	Myocardium
1	3.3	Heart	Pig	67x77x73 mm^3	--	Yellow-green	☑
2	3.6	Heart	Rabbit	30x30x56 mm^3	--	Carmine-red	☑
3	4.23	Heart	Pig	70x70x70 mm^3	Green + red	--	--
4	4.24	Heart	Pig	70x70x70 mm^3	Red	--	--
5	4.27	Kidney	Pig	50x50x70 mm^3	Yellow	--	--
6	4.28	Heart	Pig	73x67x64 mm^3	Yellow	Yellow	☑
7	4.29	Heart	Pig	72x62x98 mm^3	Yellow	Yellow	☑

Table 1.1: The cryomicrotome datasets processed in this study along with figures in which they are shown.

The vascular reconstruction methods in this study were trained / developed on datasets 3-5 and tested / demonstrated on datasets 6-7 (refer to Chapter 4 sections 4.3.8-9). In the final two pig heart datasets, microsopheres are embedded in the same pig heart tissue and are of the same color as the fluorescent cast perfused in the vasculature. Therefore, this allows estimation from the microsphere images of the optical tissue attenuation parameters (which are dependent on and specific to tissue material and light wavelength) in the PSF model that can be employed in the model-based vessel radius measurement. Chapter 3 implements the microsphere extraction and PSF measurement and chapter 4 implements the radius measurement using the image modality PSF measured with the microspheres.

1.6. 2 Phantom Data

Artificial Cylinder Phantoms – For phantom validation, three fluorescent cylinders (Rolf et al. 2008) of known diameter (measured through a microscope), were embedded in tissue-mimicking gel and imaged with the cryomicrotome. Three glass micrometer-size cylinders were filled with the same fluorescent cast that is used in imaging coronary vasculature. After the cast hardened, the fluorescent cores were extruded out of the glass and two independent observers measured 3 sections of each of the artificial vessels on a transparent stage graticule ruler with an optical microscope of numerical aperture NA = 0.5 and lateral resolution in the order of the wavelength of the fluorescent light (0.5 μm = 500 nm), which is much finer than

the 50 μm resolution of the cryomicrotome (Rolf 2005, Rolf et al. 2008). The fluorescent phantoms were measured by the microscope to be 510 ± 10 μm (5.1 ± 0.1 voxels), 300 ± 40 μm (3.0 ± 0.4 voxels), and 170 ± 10 μm (1.7 ± 0.1 voxels) in diameter. The phantoms were then embedded in a gel with scattering and absorption properties similar to biological tissue. The gel was frozen and the sample containing the artificial vessels was sliced and imaged with the cryomicrotome at 50-μm voxel resolution. Since the microscope measurements are achieved at a much higher resolution and are not biased by the optical blurring that occurs in the cryomicrotome imaging, they are considered the gold standard measurements for radius estimation validation in this study.

Computer-Generated Data – Cylinders of varying radii and length oriented at varying angles to the image plane were generated as 3D image volumes to be used for simulating optical blurring.

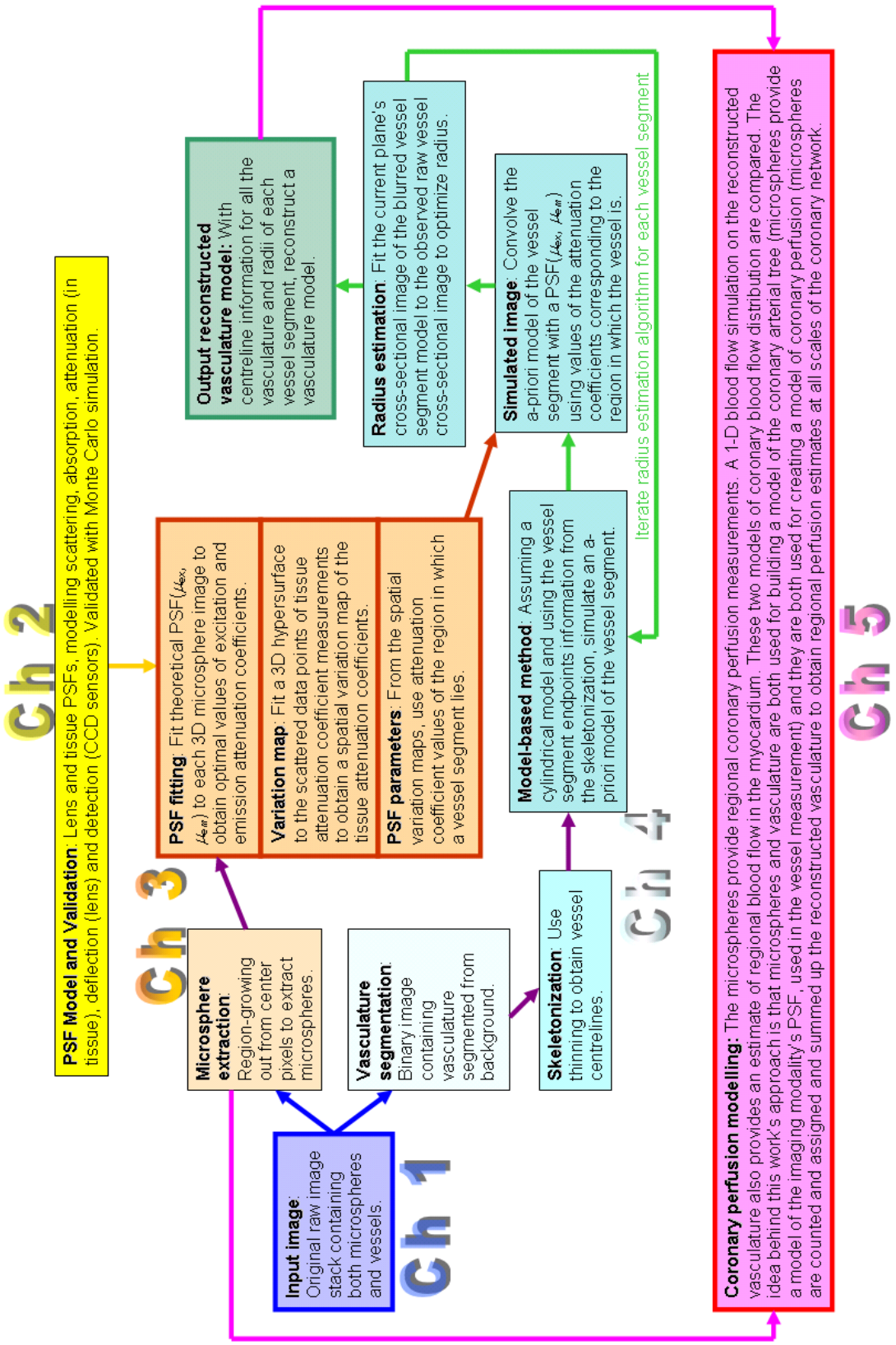


Figure 1.6: Flow diagram of the overall project.

1.7 Contents

Below is the project's research covered in the individual chapters of this report and graphically illustrated in Fig. 1.6:

- **PSF Model** – chapter 2 presents the analytical model of the PSF, which is based on radiative transfer theory (Shimizu et al. 2005, Ishimaru et al. 1997) of wave propagation and scattering in media. It also validates the analytical model with the rigorous numerical Monte Carlo simulations of photon scattering, absorption, attenuation, and transport in tissue media, which is considered gold standard in light transport modelling (according to Bishop et al. 2009).
- **PSF Parameter Optimization** – chapter 3 describes the methods of obtaining the PSF parameters (excitation and emission optical tissue attenuation coefficient) values by fitting the PSF model to the real experimental image data of 15-micron diameter fluorescent microspheres embedded in tissue, applying the point source approximation. The optical attenuation parameter is mapped onto a mesh of the heart geometry as a continuous spatially-varying field to analyse patterns of spatial variation in the myocardial tissue.
- **Vessel Radius Estimation** – chapter 4 first tests deconvolution techniques (McNally et al. 1999) on the vascular cryomicrotome data for evaluating image restoration to correct the optical blurring prior to vessel measurement. The restoration fails to improve vessel boundary delineation, and also leaves the images darkened. A novel model-based radius estimation algorithm incorporating vessel orientation and optical blurring caused by light propagation through tissue is proposed. This proposed method optimizes for vessel radius by minimizing the mean square error between FWHM measurements (in an interpolated plane perpendicular to the vessel axis) of the raw

observed cross-sectional image of a vessel and the simulated cross-sectional image of a cylindrical model of the vessel segment convolved with the PSF. To test the accuracy of radius estimation, the method developed in this study is validated on artificial vessel phantoms of a priori known radii and its measurements compared with current state-of-the-art methods of vessel radius estimation. Cryomicrotome datasets were segmented, skeletonised, extracted, and measured with the new vessel radius estimation method to render 3D model reconstructions of the whole-organ vasculatures.

- **Blood Flow Simulation** – chapter 5 simulates a 1D steady-state Poiseuille flow model on the reconstructed porcine vasculature. The regional flow normalized to the total flow in the heart is compared to the regional microsphere distribution data in the same heart. The discrepancy between the 1D flow and microsphere regional distributions is modelled and parameterised by the branching angle and cross-sectional area ratio of daughter to parent branch. The model corrects the 1D flow to more accurately predict the regional microsphere perfusion.
- **Conclusions** – chapter 6 reiterates the main research objectives and defines what goals have been achieved and what the contributions were.

1.8 Contributions

Listed below are the primary contributions of this thesis:

- The cryomicrotome modality's image acquisition has been modelled.
- The pattern of spatial variation of optical properties in intramural myocardial tissue and its potential relation to underlying cardiac anatomy has been analyzed.
- A novel methodological combined approach using microspheres for measuring the imaging modality's point spread function and measuring regional coronary perfusion

has been implemented. Vasculature and microsphere data are both employed in modelling the coronary arterial tree and regional perfusion within it.

- A new model-based template-matching method for cryomicrotome vascular morphometry has been proposed.
- The proposed vascular extraction image processing pipeline has been trained, tested, and coded into an automatic customizable program.
- The disproportionate distribution of microspheres at arterial bifurcations has been modelled to correct predictions of microsphere distribution with a 1-D flow model.

1.9 Publications

Listed below are studys published as part of this research:

[1] A. Goyal, J. Lee, P. Lamata, J. van den Wijngaard, P. van Horssen, J. Spaan, M. Siebes, V. Grau, and N. Smith, "Model-based Vasculature Extraction from Optical Fluorescence Cryomicrotome Images", *IEEE Transactions on Medical Imaging*, In press (accepted), 2012.

[2] A. Goyal, J. van den Wijngaard, P. van Horssen, V. Grau, J. Spaan, and N. Smith, "Intramural spatial variation of optical tissue properties measured with fluorescence microsphere images of porcine cardiac tissue," in *Annual International Conference of the IEEE Engineering in Medicine and Biology Society. IEEE Engineering in Medicine and Biology Society*, 2009, vol. 2009, pp. 1408–11.

Chapter 2

Cryomicrotome Point Spread Function

2.1 Background

The cryomicrotome imaging modality has been presented in Chapter 1, the Introduction, sections 1.2-3. Spaan et al. (2005) observed qualitatively that the PSF of the cryomicrotome is anisotropic, longer in the direction of the optical axis than in the cutting plane. Bennink (2007) attempted to correct the halo and remove the haze by deconvolution through convolution with an enhanced Gaussian derivative kernel consisting of an embedded transparency cancelling function. However, the results showed only a small improvement because the model only incorporated the tissue transparency in the direction of the optical axis, excluding the effect of a point source's intensity distribution in the cutting plane. This work also lacked a model for the lens blurring, which plays a crucial role in the image formation process.

Rolf et al. (2008) applied the theory of spatial distribution of a point source's light intensity, presented by Shimizu et al. (2005), to model and validate a cryomicrotome PSF due to scattering and absorption of light in tissue. Rolf et al. (2008) modeled the lens distortion as a Gaussian kernel, an approximation justified by van Vliet et al. (1994). The research described herein further expands the PSF presented by Rolf et al. (2008) as explained later in this section. This study extends Rolf's research further by proposing a model-based radius estimation algorithm that applies the PSF to measure radii of vessels in cryomicrotome images, as explained in the chapter 4 of this thesis.

2.2 Point Spread Function Modelling

Transparency artifacts arise due to illumination from the lamp penetrating the transparent tissue and exciting fluorochrome molecules beneath the current image plane or cutting surface.

The light emitted from excited fluorescent cast below the surface appears on the surface as out-of-focus light. If a fluorochrome perfused vessel is modelled as a cylinder filled with fluorophore point sources, the intensity distribution on the cutting surface is mathematically determined by convolving (represented by the symbol $\otimes$) the tubular collection of point sources with the PSF due to the scattering and attenuation of light in the tissue (PSF_{tissue}). The lens blurring, simulated as the PSF of the digital camera's lens (PSF_{lens}), further distorts the intensity distribution on the cutting surface in the image captured by the camera:

$$Image = PSF_{lens} \otimes PSF_{tissue} \otimes I_{vessel} = PSF_{effective} \otimes I_{vessel} \quad (2.1)$$

The observed image (*Image*) can be modelled as a convolution between the effective PSF ($PSF_{effective}$) and the original intensity of the light emitted by fluorophores embedded in the vessel (I_{vessel}).

The original image data can be estimated, given the observed image and the PSF. To estimate the original vessel data, the cryomicrotome image stack can be processed with the effective PSF that models the image acquisition accounting for the transparency artifacts, haloes, and out-of-focus light caused by tissue translucency and lens blurring.

2.2.1 Point Spread Function Model

At a radial distance *r*, the intensity *I* of the light from a point source embedded in a medium with power I_0 radiating or emitting light is given by Shimizu et al. (2005):

$$I(r) = I_0 \frac{e^{-\mu_t r}}{4\pi r^2} \quad (2.2)$$

The light radiated by the point source is absorbed and scattered by the tissue media, which is accounted for by the total (scattering + absorption) attenuation coefficient μ_t [1/μm] in equation (2.2). At any point in the medium, the intensity of the light emitted by the point

source is attenuated depending upon the radial distance r (illustrated in Fig. 2.1). Assuming homogeneous excitation and assuming that the excitation light travels primarily in the z direction (as illustrated in the left diagram of Fig. 2.1), the attenuation of the excitation light can be accounted for with an additional depth-dependent exponential factor in the tissue PSF model (Rolf et al. 2008):

$$PSF_{tissue}(x, y, z) = I_0 \frac{e^{-\mu_t z} e^{-\mu_t r}}{4\pi r^2} \tag{2.3}$$

The PSF of the camera lens is modeled by the Airy pattern, which can be approximated by a Gaussian in the x-y plane with a lens scale σ[μm], variance σ^2 [μm^2] (van Vliet et al. 1994):

$$PSF_{lens}(x, y) \propto e^{\frac{-(x^2+y^2)}{2\sigma^2}} \tag{2.4}$$

A 2D convolution (represented by the symbol $\otimes$) in the plane of the cutting surface of the lens and tissue PSFs yields the effective PSF for the imaging cryomicrotome (Rolf et al. 2008):

$$PSF_{effective}(x, y, z) = I_0 \frac{e^{-\mu_t z} e^{-\mu_t r}}{4\pi r^2} \otimes e^{\frac{-(x^2+y^2)}{2\sigma^2}} \tag{2.5}$$

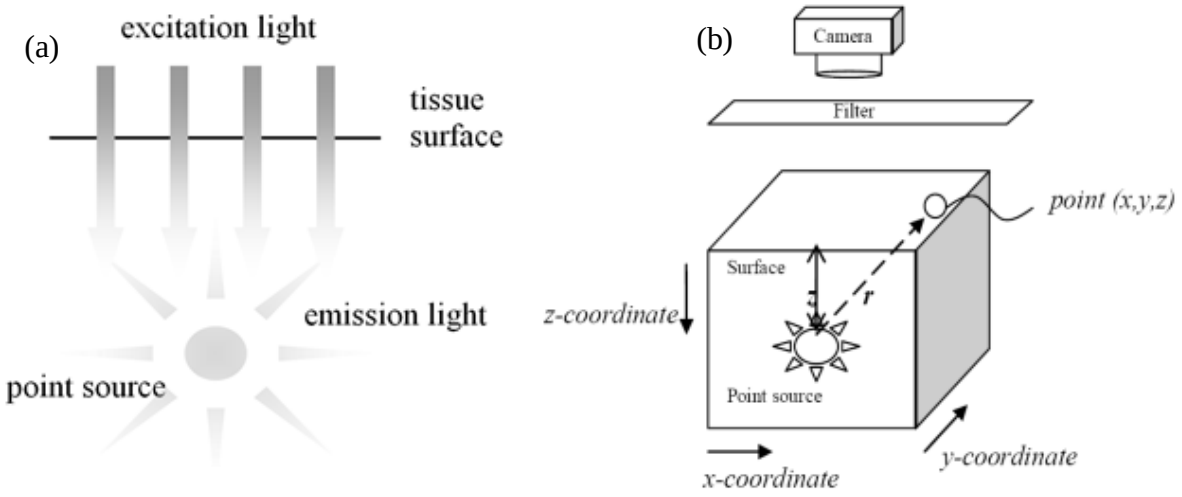


Figure 2.1: Homogeneous excitation light, attenuated by the tissue, excites the fluorescent point source and the point source in turn emits fluorescence light, which is also attenuated in the tissue. The excitation light is directional, along the *z* direction (a). The camera captures images of the emitted fluorescence light on the surface of the tissue sample. The attenuation of the excitation light depends on depth *z* of the point source. The attenuation of the fluorescence light emitted by the excited point source depends upon the distance *r* from the point source to any arbitrary point *(x,y,z)* at the tissue surface. At the point *(x,y,z)* on the tissue surface, the intensity of the light emitted by the point source is attenuated by the tissue in relation to the radial distance *r* from the fluorescent source to the point (b).

2.2.2 Parameters of the Point Spread Function Model

Rolf et al. (2008) assumed that the total tissue attenuation coefficient (which is the sum of the absorption and scattering coefficients) is identical for excitation and emission. However, according to measurements recorded by Ding et al. (2001), the coefficients have differing values for excitation and emission (see Table 2.1 in the next section), i.e. light attenuates differently when entering and exiting the tissue. This is because attenuation is dependent on the wavelength of light, which is increased when it is emitted by the excited fluorochrome molecule. After absorbing a photon, a fluorophore enters an excited state for a finite duration (generally less than 10 nanoseconds), during which the fluorophore interacts with its molecular environment and changes conformationally. The energy of the fluorophore's excited state is partially dissipated, yielding a relaxed state from which fluorescence photon emission occurs, subsequently returning the fluorophore to its ground state. Due to energy dissipation during the excited-state lifetime, the energy of the emitted photon is lower and therefore of longer

wavelength than the excitation photon, and this difference in the photon's energy or wavelength is known as the Stokes shift (Guilbault 1990). In the research, we test the significance of the difference in optical tissue properties and models of light attenuation when it is exciting the fluorescent point sources versus when it is being emitted by the point sources. We thus implement a double optical attenuation parameter model with two separate attenuation coefficients, one for excitation (μ_{ex}) and the second for emission (μ_{em}):

$$PSF_{improved}(x,y,z) = I_0 \frac{e^{-\mu_{ex} z} e^{-\mu_{em} r}}{4\pi r^2} \otimes e^{\frac{-(x^2+y^2)}{2\sigma^2}} \qquad (2.6)$$

In this model, the lens scale was measured by Rolf et al. 2008 to be 68 μm and the two parameters that are to be estimated are the excitation and emission attenuation coefficients.

2.2.3 PSF Model Validation with Monte Carlo Simulation

Photon transport in tissue can be modeled either numerically with Monte Carlo simulations or analytically by an equation of radiative transfer (electromagnetic energy transport through a media). Whereas the PSF equation is only an approximate analytical model of light attenuation in tissue, Monte Carlo simulation is considered the gold-standard of light scattering simulation (Bishop et al. 2009). Thus in order to validate the tissue PSF model of equation (2.6), a numerical simulation of light transport through tissue using the Monte Carlo method was performed wherein a single fluorescent point source was placed inside a simulated tissue slab (see Fig. 2.2) at progressively larger depths below the tissue surface, to visualize the distribution of fluorescence emitted by the point source at the tissue surface.

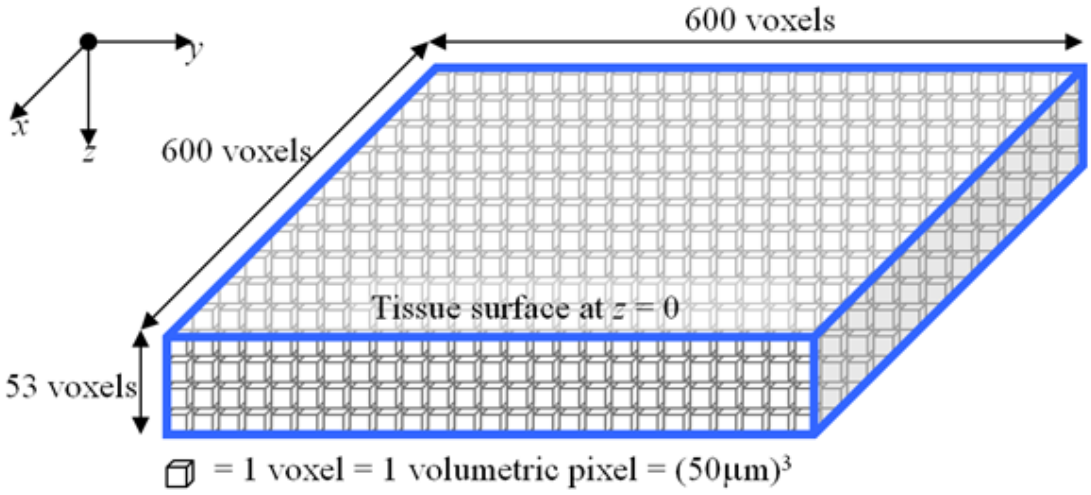


Figure 2.2: Diagram of the simulated tissue slab of dimensions 600x600x53 voxels, where each voxel is a cube of volume $(50\mu m)^3$. Note that the figure is not drawn to scale.

The simulated tissue slab was divided-up into equal cubic voxels of side-length 50 μm (Fig. 2.2). Photon packets of illumination light were simulated to uniformly enter the tissue from the surface at an angle of incidence $\theta = 0°$ relative to the depth axis. Each photon packet started travelling with a weight $W = 1.0$, which decreased over the photon packet's journey to represent the attenuation of the photons due to tissue scattering and absorption events. Photon packet motion was determined by directional cosines μ_x, μ_y, μ_z, defined as the cosine of the angles between the photon packet and the 3 Cartesian unit vectors in the *x*-, *y*- and *z*-directions, respectively.

In the numerical simulation of photons propagating through the slab of tissue during illumination and fluorescent emission, the distance each photon packet travels between scattering events is represented as a step-size *s* [μm]. The step-size of individual packets is determined by sampling a random number ξ from a standard uniform distribution ($0 \leq \xi \leq 1$), where *s* is calculated as (Wang et al. 1995, Bishop et al. 2009):

$$s = \frac{-\ln(\xi)}{\mu_a + \mu_s} \tag{2.7}$$

The parameters μ_a and μ_s [μm] are the optical tissue absorption and scattering coefficients, respectively. The scattering and absorption coefficients measure how far light can penetrate into a particular medium before it is scattered or absorbed, respectively. Both the scattering and absorption coefficients depend on the material properties of the medium and also on the wavelength of light which is being transmitted. In this work, the excitation and emission fluorescence light is specified by a mean wavelength ± a standard deviation (see chapter 3). Measurement of the optical tissue attenuation coefficients is discussed in the next chapter 3.

After each step, photon absorption within the tissue was simulated by reducing a photon packet's weight by δW. The fraction of absorption to the total attenuation (scattering and absorption combined) is the factor that is multiplied to the current packet weight W to derive the fraction of weight δW that is to be deducted from the photon packet for simulating photon absorption in the tissue (Wang et al. 1995, Bishop et al. 2009), as given by:

$$\delta W = W \frac{\mu_a}{\mu_a + \mu_s} \tag{2.8}$$

For representing photon absorption during illumination, as each photon packet propagated through the tissue, fractions of its weight (δW) were subtracted from the photon packet's weight W and deposited in the voxel elements of a simulated 3D array, representing the 3D voxelated tissue slab, subsequent to which each of those photon packets was simulated to be scattered into a new direction with its remaining packet weight. After the fluorescent point source excitation, subsequent photon emission by the fluorescent point source was simulated. The amount of fluorescence emitted by the point source depended on the number and weights of photon packets that reached and excited it. The intensity of the fluorescent light emitted by

the point source is related to the amount of photons it absorbed, which is quantified by the total of all fractions of weight δW deposited by photon packets at the voxel where the point source is located. Isotropic fluorescent emission from the point source was simulated by fluorescent packets emitted at randomly distributed angles. Each of these fluorescent packets also underwent absorption and scattering. The scattering angles of the photon packets, which defined the directional motion of each packet, were calculated using the Henyey–Greenstein equations (Wang et al. 1995, Jacques 1998) and depended on sampling randomly distributed variables ξ, the direction of the packet's motion, and the anisotropy factor g. The factor g is representative of the directionality of the scattering of light incident on a material, and hence differentiates isotropy (g = 0) from anisotropy (g = 1) of the light scattering. A transparent material will result in anisotropy (light continues propagating in the same or within 90 degrees of the direction it started transmission from the source), whereas an opaque diffusive material will result in isotropy (light scattered in all directions). Photons travelling through tissue will be attenuated both by being absorbed and scattered, and thus it is important to account all these effects for modelling light transport in tissue. In the images of the intensity distribution on the tissue surface, the value at each voxel, i.e. the voxel intensity, was the summed weight of all photon packets reaching that voxel on the tissue surface.

Four numerical simulations of photon transport were performed. For comparative analysis of the tissue PSF model in equation (2.6) with the random walk Monte Carlo model of light transport in tissue, two simulations (first with 50 million and the second with 100 million photon packets to demonstrate statistical convergence of the simulation) were run where the attenuation of excitation or illumination light was modelled with the above-mentioned random walk Monte Carlo model of photon transport (Wang et al. 1995). In order to assess the effect of assuming light attenuation as exponential decay for comparative analysis of the tissue PSF

model with the diffusion theory of light transport in tissue, in a further two more simulations (first with 1 million and the second with 50 million photon packets), the random walk Monte Carlo method was used to numerically simulate the attenuation of the fluorescence emitted by the excited point source, but an exponential decay function was used instead of random walk Monte Carlo to model the attenuation of incoming illumination light entering the tissue according to the diffusion theory model presented by Wilson et al. (1990):

$$N(z) = N_0 e^{-z/\delta} = N_0 e^{-\mu_{eff} z} \qquad (2.9)$$

where z is the depth into the tissue [mm]; δ is the penetration depth [mm], i.e. the depth into the tissue at which the intensity of incoming light is reduced to 37% of the original intensity; μ_{eff} is the effective attenuation coefficient or the rate of decay of the fluence (a measure of particle flux) in the tissue [mm^{-1}]; N_0 is the initial number of photon packets entering the tissue at the surface; and $N(z)$ is the approximate number of photon packets that reach depth z. According to Wang et al. (1995), for $z > \delta$ (i.e. at depths greater than the penetration depth), the diffusion theory model is valid and has been shown by Bishop et al. (2009) to closely agree with Monte Carlo simulations of incoming illumination light attenuation as it enters the tissue.

	g	μ_s	μ_a	μ_{eff}	μ_t
Excitation	0.94	23.0 mm^{-1}	0.52 mm^{-1}	1.72 mm^{-1}	23.52 mm^{-1}
Emission	0.96	21.8 mm^{-1}	0.10 mm^{-1}	0.54 mm^{-1}	21.90 mm^{-1}

Table 2.1: Values (Ding et al. 2001) of the anisotropy factor, scattering, absorption, effective, and total attenuation coefficients for rabbit cardiac tissue at excitation and emission wavelengths of 488 nm and 669 nm, respectively.

Rabbit cardiac tissue optical parameters as specified by Ding et al. (2001) and used in Bishop et al. (2009) were used to provide a basis for the comparison between the Monte Carlo and PSF models. Table 2.1 specifies the values for the anisotropy factor g and the absorption and scattering coefficients, μ_a and μ_s, respectively, for excitation and emission. These values are

for rabbit cardiac tissue at illumination and fluorescence emission wavelengths of 488 nm and 669 nm, respectively (note: in the optical cardiac tissue parameter estimation study detailed in chapter 3 of this thesis, the animal model is also rabbit and the wavelengths are 515 nm and 534 nm at excitation and emission, respectively). Equations from Wang et al. (1995) and Wilson et al. (1990) were used to calculate the effective attenuation coefficient, the inverse of the penetration depth δ, for the diffusion theory simulations:

$$\delta_{ex} = \left.\frac{1}{\sqrt{3\mu_a(\mu_a + \mu_s(1-g))}}\right|_{ex} \qquad \delta_{em} = \left.\frac{1}{\sqrt{3\mu_a(\mu_a + \mu_s(1-g))}}\right|_{em}$$
$$\mu_{eff}\big|_{ex} = \frac{1}{\delta_{ex}} \qquad \mu_{eff}\big|_{em} = \frac{1}{\delta_{em}} \tag{2.10}$$

For comparing the Monte Carlo simulations to the tissue PSF model, the PSF parameter total attenuation coefficient μ_t at excitation ($\mu_t = \mu_{ex}$) and at emission ($\mu_t = \mu_{em}$) was calculated from the absorption and scattering coefficients, μ_a and μ_s, respectively, at excitation and emission. Table 2.1 tabulates the values of μ_t at excitation and emission derived from parameters specified in Ding et al. (2001). The total attenuation coefficient is the sum of the absorption and scattering coefficients (Rolf et al. 2008, Cheong et al. 1990):

$$\mu_t\big|_{ex} = \mu_{ex} = [\mu_a + \mu_s]_{ex} \qquad \mu_t\big|_{em} = \mu_{em} = [\mu_a + \mu_s]_{em} \tag{2.11}$$

The results of the Monte Carlo simulation and the tissue PSF model are compared in Figs. 2.3-5. Fig. 2.3 plots the normalized intensity at the *(x,y)* coordinates of the point source, plotted against the depth of the point source for the Monte Carlo simulations and the tissue PSF model. The intensity at the surface drops drastically as the point source is located deeper in the tissue.

When the diffusion theory approximation (Wilson et al. 1990) is used to calculate the attenuation of incoming light entering the tissue, the simulations are not as detailed as when

using the random walk Monte Carlo model. This is because the diffusion theory model uses the diffusion approximation to obtain an approximate simplified version of the transport equation used in radiative transfer theory to model photon transport in tissue (Cheong et al. 1990). The diffusion approximation assumes that relative to scattering events, there are very few absorption events, and the radiance is nearly isotropic. On the other hand, the random walk model is a rigorous numerical analogue of the analytical radiative transfer theory for wave propagation in media (Ishimaru 1997, Arridge et al. 1997).

The diffusion theory model (Wang et al. 1995, Wilson et al. 1990) is valid for depths greater than the penetration depth (when the diffuse component of light is prominent). In Fig. 2.3, if we use the Monte Carlo random walk simulation as the reference gold standard, at larger depths (depths greater than the excitation penetration depth $\mu_{ex} = 1/\mu_{eff\backslash ex} = 1/[1.72\ \text{mm}^{-1}] \approx 0.58$ mm ≈ 580 μm ≈ 11.6 voxels), the diffusion theory light distribution model is more accurate than the tissue PSF model. This is because at larger depths, the light is more scattered and diffused, but the tissue PSF only accounts for the unscattered direct component of light. This approximation is justified at shallow depths at which the photons have undergone less scattering events. The tissue PSF models unscattered collimated transmission of light (Rolf et al. 2008). Thus it is only valid for depths where the mean free path (*mfp*, i.e. average distance traversed by photons before they collide with surrounding atoms, which disperse and diffuse the light transmission) of the photons is much larger than the depths of the fluorescent sources at which the image is acquired (Shimizu et al. 2005), i.e. the tissue PSF is a valid model of light transport only for fluorescent sources located at shallow depths (depths << *mfp*), for which scattering is less significant. If the light source is located closer to the surface (at shallow depths << *mfp*) rather than deeper, there will be less scattering (due to less interaction with atoms in the tissue) and the light emitted by the source will remain mostly unscattered

collimated transmission as it exits the surface and is captured by the camera. This is the case for an imaging cryomicrotome setup according to Rolf et al. (2008). In Rolf et al. (2008), the mean free path presented is *mfp* = 500 μm, whereas the largest depth at which a fluorescent source is visible on the surface image is much less than 200 μm, so *mfp* >> depth of imaged light source, i.e. the depths of the sources imaged are much less than the average distance after travelling which a photon is scattered.

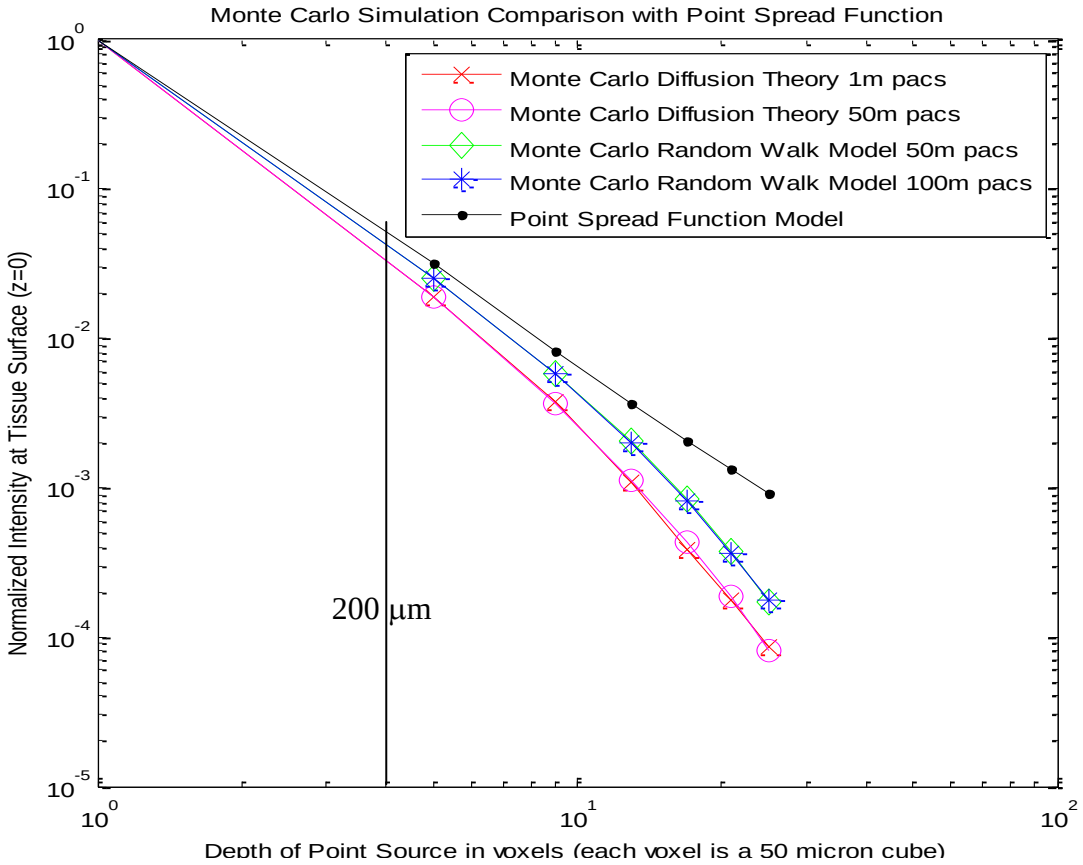


Figure 2.3: Log-log plot of the normalized intensity at the center of the tissue surface plotted against the depth of the point source for both Monte Carlo and the PSF models. As observed by the negligible difference between the 50 million versus 100 million photon packet simulations, 50 million photon packets are sufficient for the Monte Carlo simulation.

In Fig. 2.3, the tissue PSF model presented in sections 2.2.1-2 (Rolf et al. 2008) overestimates intensity of the fluorescence emitted from the point source, when compared to the Monte Carlo random walk simulation. The PSF is closer in agreement with the Monte Carlo random walk

simulation at shallower depths (depth < 5 voxels or 250 micrometers, at which the difference between the PSF and Monte Carlo models in normalized intensity at the centre of the tissue surface is 0.008, an error that when normalized to the original intensity is a relatively negligible 0.8% of the starting intensity of 1). At larger depths though, the Rolf PSF model does lose validity. However, since the cryomicrotome can only image fluorescent objects embedded in tissue at shallow depths (less than 200 micrometers), the PSF is an approximate but valid model for this study. This is because in a phantom validation study (see Appendix A), error in vessel radius estimation due to using a PSF versus the Monte Carlo model of light transport was found to be 0.08 ± 0.01 voxels, which is negligible for blood flow simulations. To give some perspective to the effect of radius error, section 5.3.7 in chapter 5 perturbs vessel radii estimates in the reconstructed vasculature model with the much larger error of 0.25 voxel (0.25 voxel >> 0.01 voxel) standard deviation, and the error in blood flow simulations due to this 0.25 voxel uncertainty in radii is shown to be negligible compared to the error between the flow model and microsphere perfusion measurements.

Figs. 2.4 and 2.5 offer a visual and quantitative comparison of the two models, respectively. Fig. 2.4 shows the image on the tissue surface of the intensity distribution emitted from the point source placed at progressively larger depths in the tissue (see Appendix A for comparison of the tissue PSF model and Monte Carlo simulation performed at shallow depth ranging from 25 – 225 micrometers). As the depth increases, the photons simulated by Monte Carlo reaching those depths become more and more sparsely scattered and the fluorescent photons barely reach the surface. As expected, the intensity distribution on the surface is thus quite low in intensity when the point source is deep in tissue. As explained earlier, unscattered direct light from the point source is observed when the point source is at shallow depths, but when the point source is located at larger depths, its emitted fluorescence reaching the surface

is primarily diffused having undergone much more scattering. Thus the intensity of light observed at the surface drops rapidly as the point source is placed progressively deeper in the tissue.

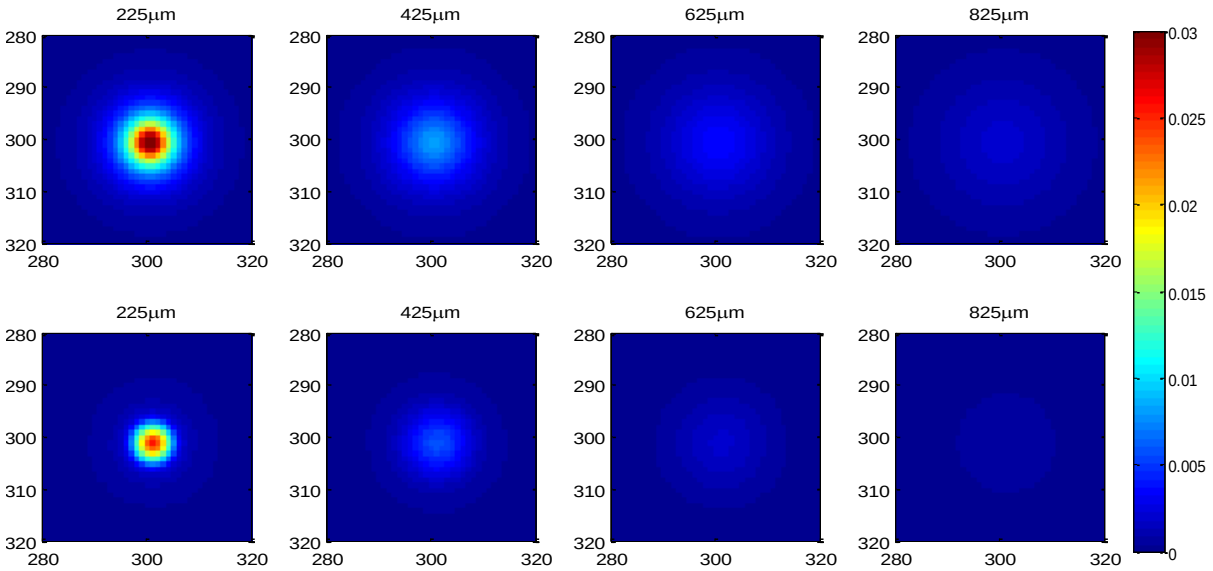


Figure 2.4: Intensity distribution images at the tissue surface from fluorescence emitted by a point source placed at progressively larger depths (depths are printed in each plot's title). The tissue PSF model surface images are in the top row and Monte Carlo random walk (50 million photon packets) simulation surface images are in the bottom row. These images show that as depth increases, the light distribution is broadened and the intensity sharply decreased. Colormap is the same for all the images. The intensity range is 0 – 1. The depths start at 225 μm which is where differences between Monte Carlo and the PSF start to appear. The colour only gives values up to 0.03, so the difference is small relative to the starting intensity of 1.

Fig. 2.5 shows the line intensity profiles across the centre of each surface image intensity distribution emitted from the point source placed at progressively larger depths in the tissue. It can be observed from the Monte Carlo simulation that as the depth decreases, that is as the point source is moved increasingly closer to the surface (see Appendix A for simulation of point source at shallow depths ranging from 25 – 225 micrometers), the line profile of the intensity distribution of the point source at the tissue surface approaches the Dirac delta impulse response (smaller standard deviation σ), but as the depth increases, the light distribution is broadened (larger standard deviation σ) and the intensity sharply decreased.

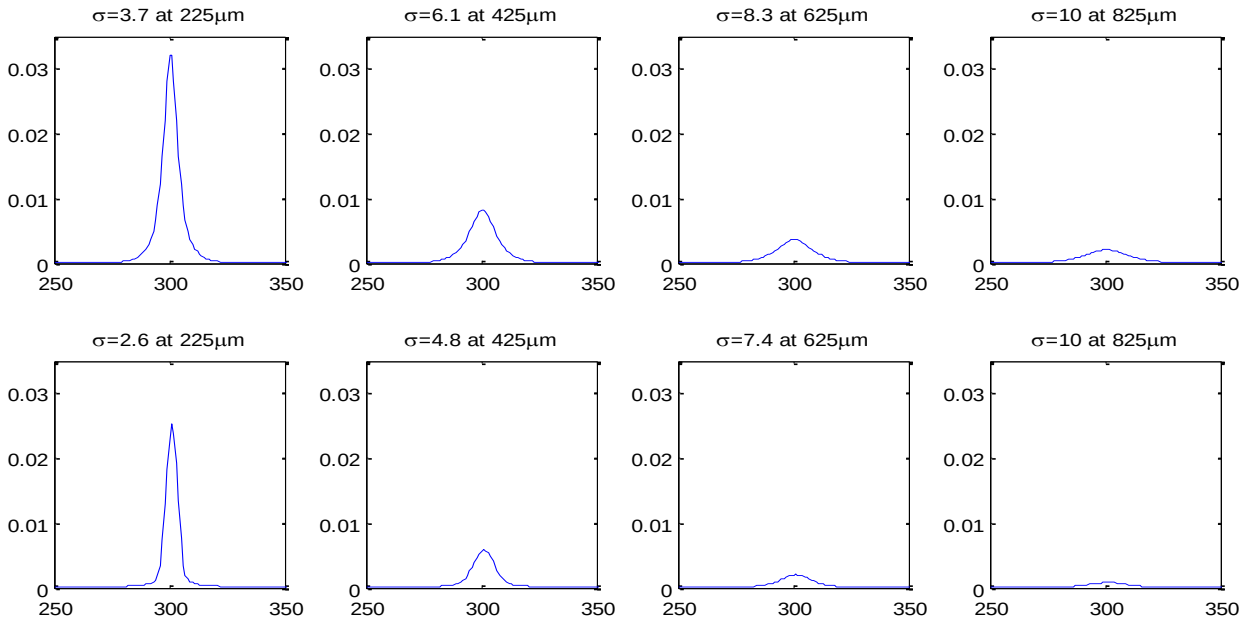


Figure 2.5: Line intensity profiles across the centre of each surface image intensity distribution emitted from the point source at each progressively larger depths in tissue (depth is printed in plot titles). The tissue PSF model's line intensity profiles are in the top row, and Monte Carlo random walk (50 million photon packets) simulation's line intensity profiles are in the bottom row. The intensity distribution of light emitted by the point source at the tissue surface when it is very near the surface approaches the Dirac delta function, but as the depth of the point source increases, the distribution broadens (σincreases) and there is a steep drop in intensity. The intensity ranges from 0–1. At 225 μm depth, the absolute difference between the PSF and Monte Carlo models in normalized intensity at the centre of the tissue surface is 0.032-0.024 = 0.008, an error that when normalized to the original intensity is a relatively negligible 0.8% of the starting intensity of 1.

In summary, the differences between the Monte Carlo and the PSF model are because the PSF model does not account for the diffusion of photons, which is negligible for imaging point sources located at shallow depths. Rolf et al. (2008) have stated this assumption to be valid for the cryomicrotome imaging modality, and our Monte Carlo study corroborates it. The PSF model overestimates the intensity of the fluorescence emitted by the point source because it only considers the unscattered collimated transmission and does not account for the diffusion of the photons; thus it is only valid for shallow depths. Diffuse light from sources deep below the tissue surface (at depths greater than the penetration depth, which is δ = 11.6 voxels in this study) has trivial signal intensity at the surface – less than 0.1% of the original incoming illumination (refer to Fig. 2.3 to observe that according to the diffusion theory simulations, at

the surface the normalized intensity of the light emitted by a point source located at depths larger than the penetration depth, which is primarily diffused when it reaches the surface, drops to below 10^{-3} = 0.001 = 0.1% of 1, the original intensity of incoming illumination). As such, diffuse light from deep below the tissue surface hardly influences the intensity distribution image on the tissue surface. Thus neglecting the diffusion of light is a reasonable approximation for modelling light transport in tissue from shallow objects (the case for the cryomicrotome) because light emitted by fluorescent objects at shallow depths remains non-diffuse and the intensity of diffuse light emitted by fluorescent objects embedded deep below the surface is negligible on the surface, as detailed earlier.

Our study suggests that the PSF model suffices as a valid model of attenuation of light in tissue in the cryomicrotome setup. The Monte Carlo is a computationally expensive but highly rigorous numerical simulation, whereas the tissue PSF is a computationally efficient but simplified analytical model. The phantom validation study in Appendix A shows that the error in model-based radius estimates between simulating a vessel with the Monte Carlo and PSF models is negligible for blood flow simulations. Henceforth in this thesis, the tissue PSF is used for modelling light transport in tissue. The current work uses the PSF as a first approximation model of light transmission in tissue to measure optical tissue parameters from several thousand point sources embedded in cardiac tissue (the task covered in the next chapter), which would be infeasible with the computationally expensive Monte Carlo simulation.

Chapter 3

Measuring Optical Tissue Properties

3.1 Background

In order to extract vasculature from cryomicrotome images, the centrelines of the blood vessels need to be detected and their radii need to be measured. For this, the tissue transparency effects in the form of haloes surrounding large bright vessels, caused by the scattering and distribution of light from fluorescent cast filled in vessels underlying the cutting surface need to be modeled and corrected. Modeling the out-of-focus fluorescence firstly requires knowledge of the optical properties of the tissue in which the vasculature is embedded. Essentially, radius estimation of vessels in the cryomicrotome image data requires a model of the tissue PSF model (equation 2.6), parameterized by attenuation coefficients. Accurate values of these parameters are essential for a reliable PSF model, which is crucial for precise radius estimation (see chapter 4 for radius estimation). Previous studies (Rolf et al. 2008, Bishop et al. 2009) assumed homogeneity in optical tissue properties, but we herein investigate intramural variation of these parameters across an entire heart to gain insight into how differences in optical properties in distinct regions influence light transport. To produce the images used this chapter, data from 15μm diameter fluorescent microsphere beads perfused throughout the vasculature of rabbit and pig hearts is used. Using the microspheres as an approximation of fluorescent point sources, cryomicrotome images of these tissue-embedded microspheres are used to measure optical parameters, and their intramural variation, in *in vitro* cardiac tissue. Our approach can be summarized as using the *known* markers (microspheres) embedded in tissue to measure tissue properties, which in turn can be used to measure *unknown* objects (vessels) embedded in the same tissue.

3.1.1 Tissue Optics

In optical bioimaging, the propagation of light in tissue is affected by the scattering and absorption of photons in tissue. The propagation and attenuation of light through tissue is modelled in this study by the PSF, which is parameterized by the total attenuation coefficient μ_t [1/microns], the sum of the absorption μ_a [1/microns] and scattering μ_s [1/microns] coefficients:

$$\mu_a+\mu_s=\mu_t \tag{3.1}$$

Knowledge of these parameters is essential for modeling transport of light in tissue (Cheong et al. 1990).

3.1.2 Effect of Optical Blur on Vessel Diameter Estimation

In order to show how optical blur due to light transport in tissue affects the radius estimation of a vessel embedded in that tissue from the vessel's cross-sectional image, we used a phantom to simulate three vessels, whose line intensity profiles are shown in Fig. 3.1. Using the tissue PSF of equation (2.6) as the model of light transport in tissue, the simulated vessels were blurred with three versions of the PSF, each with a different set of values for the excitation and emission coefficients (Table 3.1). Fig. 3.1 shows the cross-sectional line intensity profiles across each of the three vessels (20, 40, and 80 voxel diameter) for the simulated vessels both original and blurred with the PSF of three different sets of attenuation coefficient values (specified in Table 3.1). This tests the full range of total optical tissue attenuation coefficient for cardiovascular cryomicrotome images (according to Rolf 2005, the range is 0.004 - 0.020 μm^{-1} for cardiac tissue for light with wavelength ranging from 450 - 700 nm).

Diameter estimation of the vessels was performed with the full-width half-maximum (FWHM) calculation. FWHM is used as a measure of the extent of the vessel

intensity across a cross-section, given by the distance between the two extreme points of the vessel cross-sectional profile at which the intensity is equal to half of its maximum value. A Gaussian profile is fitted to the vessel cross-section, and the FWHM = $2\sqrt{2\ln 2}\sigma$, where σ is the standard deviation or scale of the Gaussian. FWHM has been used extensively for defining vessel boundaries for measurement of vessel radii in medical images (Zhou et al. 1994, Hoogeveen et al. 1998, Botnar et al. 1999, Pedersen et al. 2000, Marxen et al. 2004, Rolf et al. 2008). Table 3.1 tabulates the values of the diameter calculated as the full-width half-maximum or the distance across the points where the vessel intensity is half of its maximum (shown in Fig. 3.1 as dotted cyan line). The images are saturated (saturation point is 255) to simulate the situation with our acquired images, where the bit depth is only 8-bit, and the fluorescent emission from the vessels often saturates the pixel intensity recorded by the CCD sensors. As can be observed in the Fig. 3.1, the PSFs enlarge the original vessels.

As simulated in Fig. 3.1, the light distribution from vessels embedded in tissue is broadened on the cutting surface (simulated by the convolution with the PSFs) and so the measure of vessel diameter using FWHM results in significantly different values, which in turn produce hugely different measures of flow (up to 170% error in the worst case).

FWHM works in the absence of a model of image acquisition accounting for pixel saturation and was tested herein as it is the state-of-the-art vessel radii estimation for optical fluorescence modalities, and is applied in the literature on unsaturated images. The error in FWHM is due to the vessel broadening caused by optical blurring and also due partly to information loss caused by pixel saturation, which results in non-Gaussian plateau-like profiles of vessel cross-sections in the images (discussed earlier in the introduction section 1.3.2). If the camera could record higher intensities with a higher bit depth or larger CCD sensor dynamic range, the vessel cross-sectional profiles would not be saturated in the center, allowing the vessel's full profile to be fit to a Gaussian. However, there is a trade-off to

increasing the dynamic range to avoid saturation, as this would decrease the ability to detect lower intensity vessels. In unsaturated images captured with higher bit-depth sensors (a future experimental improvement), the FWHM would give better radii estimates, but would still not be completely accurate, because it does not account for the optical blurring degradation (see Chapter 4 for FWHM tested on unsaturated vessel images). Since FWHM is not applicable to situations in which intensities are saturated (i.e. nonlinear), Chapter 4 of this thesis proposes a new method that incorporates these nonlinear effects in vessel radii measurement.

		PSF1	PSF2	PSF3	Original
Excitation atten. coef	μ_{ex} (1/micron)	0.005	0.009	0.05	--
Emission atten. coef	μ_{em} (1/micron)	0.001	0.005	0.01	--
FWHM as a measure of diameter (voxel)	Small vessel	25.7812	24.6381	23.2175	20
	Medium vessel	46.1624	44.9599	43.4901	40
	Large vessel	86.2248	85.0319	83.5738	80
% Error in diameter estimation	Small vessel	28.9061	23.1907	16.0873	0
	Medium vessel	15.4059	12.3997	8.7253	0
	Large vessel	7.781	6.2898	4.4673	0
% Error in blood flow	Small vessel	176.1173	130.3092	81.6097	0
	Medium vessel	77.3832	59.61	39.7408	0
	Large vessel	34.9487	27.6342	19.1027	0

Table 3.1: Diameter (FWHM) and the error in diameter and blood flow estimation for each of the three vessels in the phantom both original and blurred with three PSFs (each with different parameter values). The PSF parameter values are based in the range of optical attenuation coefficients for myocardial tissue given by Rolf 2005.

Since the error in diameter measure with FWHM is unsystematic and inconsistent over each vessel size and orientation and each set of optical tissue attenuation values, no single factor can correct the FWHM measure of vessel diameter. The errors in FWHM measure of diameter and blood flow measure increase as the attenuation coefficients decrease in value because for less attenuation in the tissue, more out-of-focus fluorescent emission from vessels embedded in the tissue can reach the cutting surface and obscure the vessel cross-sectional boundaries (see blurred vessel phantom boundaries in Fig. 3.1). Smaller vessels result in larger relative errors in both the diameter and blood flow estimation than larger vessels. Calculating the

radius of smaller vessels is more challenging as their cross-sectional intensity distributions are much more obscured by the imaging modality's optical blurring degradation (modeled by the tissue PSF). From the above figures, it is evident that vessel radius measurements (and even more so blood flow) from vessel images are strongly sensitive to changes in optical tissue parameter values. Therefore, it is essential to obtain accurate measurements of the attenuation coefficients to obtain an accurate model of the tissue PSF to be incorporated into the radius estimation, covered in chapter 4.

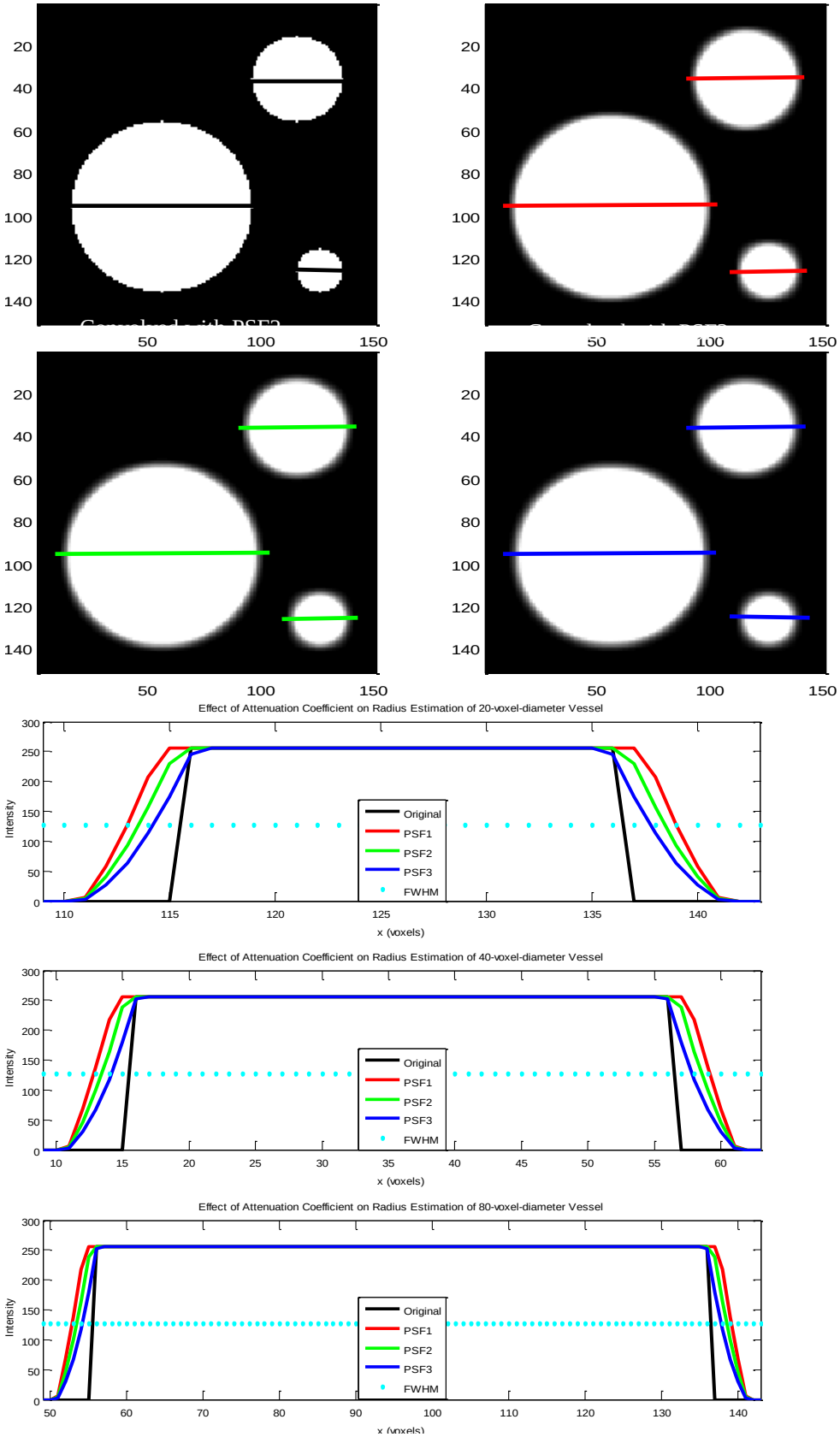


Figure 3.1: Cross-sectional line intensity profiles across (shown as colored lines across center of vessels in phantom images) each of the three simulated vessels, for original and blurred (see legend). Images are 8-bit grayscale.

3.1.3 Measuring the Total Optical Tissue Attenuation Coefficient

In optics, the Beer–Lambert law, also known as Beer's law relates the attenuation of light to the properties of the media through which the light travels. Given unscattered collimated transmission T_c, which is the ratio of the intensity I of light exiting a slab of tissue of thickness t and the intensity I_0 of the light when it was first incident on the tissue slab, Beer's law can be used for calculating the attenuation coefficient μ (Cheong et al. 1990):

$$T_c = \frac{I}{I_0} = e^{-\mu t} \Rightarrow \mu = -\frac{1}{t}\ln(T_c) = -\frac{1}{t}\ln\left(\frac{I}{I_0}\right) \qquad (3.2)$$

The above scenario works only for a transmission geometry, wherein light enters and exits, without changing direction, through a slab of homogeneous media. However, the cryomicrotome setup is in part a transmission geometry, but it also includes reflection, in which filtered excitation light is incident upon tissue and is reflected back as emission from the excited fluorophores embedded in the tissue (Rolf et al. 2008), as shown in Fig. 3.2.

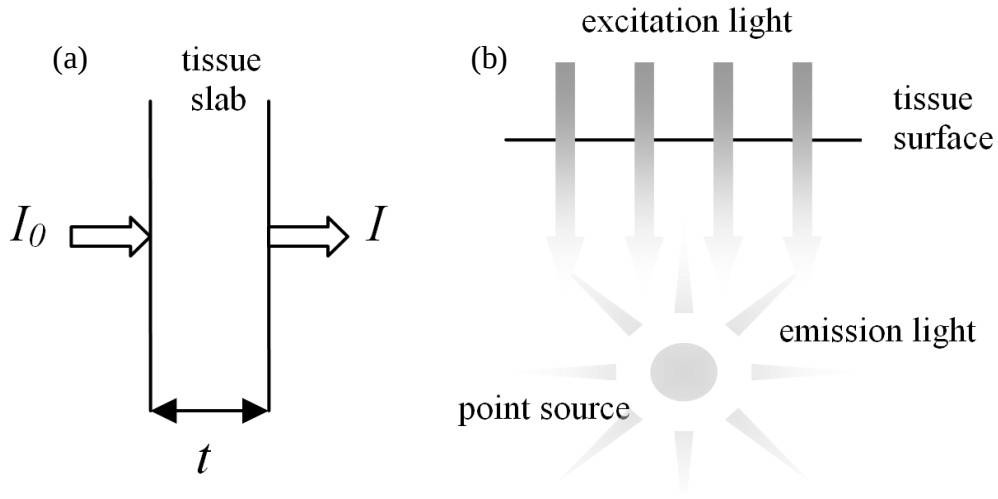


Figure 3.2: (a) Transmission geometry showing a slab of tissue of thickness t on which light incident with intensity I_0 exits with reduced intensity I. (b) Reflection geometry of the cryomicrotome in which the excitation light is attenuated as it enters the tissue and the emission light reflected by the fluorescent point source is also attenuated.

A second method for measuring the total attenuation coefficient of tissue is OCT or optical coherence tomography (Faber et al. 2004), an optical signal acquisition and interferometric technology that can achieve a signal penetration depth of a few millimeters into scattering media (Wang et al. 2001), e.g. biological tissue, which is much larger than the penetration depths (in the range of hundreds of micrometers) of confocal and multi photon microscopy (Centonze et al. 1998). The attenuation coefficient μ_t estimate is optimized by least-squares fitting the measured backscattered OCT signal to a model $I(z) \propto \sqrt{\exp(-2\mu_t z)}$ of the simulated OCT signal $I(z)$, where z is the probing depth into the tissue sample (Kholodnykh et al. 2003). Even though the attenuation coefficient can be locally measured at the surface of a tissue sample, since OCT cannot slice off sections from an organ and can only achieve a limited penetration depth (1-2 mm) caused by the highly scattering properties of biological tissue, it cannot be used to visualize patterns of spatial variation of optical tissue properties across an entire organ.

Due to the penetration depth limit of optical coherence tomography and the differing geometry of Beer's law (see Fig. 3.2), neither Beer's law nor OCT can be used for whole-organ spatially-localized measurements of the total attenuation coefficient. Instead, we use the method of fitting a theoretical PSF to the experimental images of fluorescent microspheres embedded in tissue. This method of PSF determination from microspheres has been employed recently in several optical imaging modalities – fluorescence microscopy (Beverage et al. 2002, Haver et al. 2008, Pankajakshan et al. 2009), epifluorescence microscopy (Hiraoka et al. 1990), confocal microscopy (Cole et al. 2011), differential interference contrast microscopy (Azucena et al. 2010), raster image correlation spectroscopy (Vendelin et al. 2008), and optical coherence tomography (Agrawal et al. 2010, Woolliams et

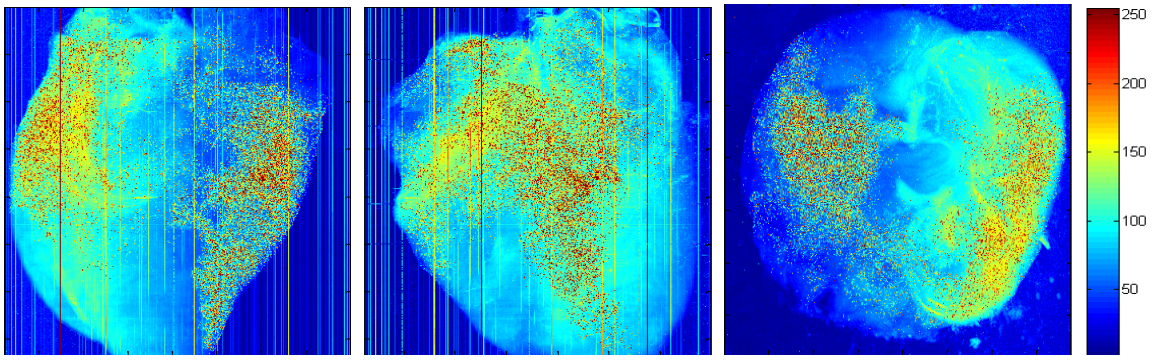
al. 2010). The parameter estimation work in this thesis follows on from Rolf et al. (2008) in PSF measurement from microspheres in cryomicrotome imaging.

3.2 Methods

3.2.1 Fluorescence Microsphere Images

Fluorescent microsphere images of a rabbit heart and a porcine heart were obtained by first preparing the hearts for the cryomicrotome by perfusing their arteries with 15-micron diameter FluoSpheres® fluorescent microspheres (detailed earlier in the Introduction). For PSF determination, the microspheres need to be modeled as point sources, i.e. they need to be significantly smaller than the minimum size of an object that can be resolved by the imaging system (one third of the resolution is the size suggested in McNally et al. 1999). The 15 micron microsphere size is thus appropriate for the 50 micron voxel resolution. The rabbit heart was perfused with yellow-green microspheres with excitation and emission wavelengths of 515 nm and 534 nm, respectively. The pig heart was perfused with carmine-red (excitation at 580 nm and emission at 620 nm) fluorescent microspheres. Subsequently, the hearts were immersed in a sodium solvent and thickening agent mixture, and frozen. They were imaged by the cryomicrotome separately. Excitation light was filtered with a 510±20 nm bandpass filter for the yellow-green microspheres in the rabbit heart and with a 560±20 nm bandpass filter for the carmine-red microspheres in the pig heart. The filtered illumination was reflected off a mirror onto the frozen heart sample (placed in the cryomicrotome) to excite the fluorescent microspheres embedded in the cardiac tissue. The fluorescence emitted by the microspheres was filtered with a 555±30 nm bandpass filter for the yellow-green microspheres in the rabbit heart, and filtered with a 635±30 nm bandpass filter for the carmine-red microspheres in the pig heart. A digital camera captured an image of the fluorescent emission coming from the cutting surface each time a slice of precise micrometer thickness was serially sectioned off

from the frozen heart sample. The resulting image data stack is a 3D volume of microspheres embedded in tissue all over the entire heart (see Fig. 3.3). The image acquisition procedure is covered in more detail in the Introduction chapter 1 section 1.2.2.3.



(a) (b) (c)

Figure 3.3: Maximum intensity projections (across *x*-axis in (a), across *y*-axis in (b), and across *z*-axis in (c), where z-axis is depth axis or long axis from the base to the apex of the heart) of the 3D image volume of microspheres perfused in a pig heart. The pig heart volume has dimensions of 1351 (*x*) x 1551 (*y*) x1464 (*z*) voxel^3, with voxel size of (50μm)^3. The 8-bit image intensity ranges from 0 (blue) to 255 (red), as shown in the colorbar. The vertical lines in the left and middle figures are cutting artifacts of the cryostat microtome blade.

3.2.2 Optical Parameter Estimation from Microspheres

All the microsphere centerpoints in the heart image data were detected by finding local maximum intensity voxels, and each microsphere was extracted with 3D region growing. The stopping condition for region growing to neighboring voxels was the property that the intensity of the voxel should be between two thresholds: a user-defined lower noise threshold and an upper threshold equal to the intensity of the centerpoint. Each microsphere was extracted by region growing out in all three dimensions from the detected centerpoint voxel to next neighbor voxels (the embedded microspheres imaged are all of the same 15μm diameter, but they appear of different sizes in the images dependent upon their depth relative to the imaging surface and the tissue optical properties in that region). Dark current noise (detection of electrons instead of photons by CCD sensors – caused by electrons freed up by thermal energy), hot voxels (CCD sensors gone awry and always recording a high intensity), and microsphere clusters (more than one microsphere embedded close together in the tissue) were

precluded from being selected by only extracting microspheres which met certain conditions: 1) the centerpoint voxel of the microsphere should be above a certain intensity threshold (to avoid dark current noise), 2) the centerpoint should not be a voxel with an $i_a > 100$ (the maximum intensity in the 8-bit image is 255) where i_a is that *(x,y)* voxel's intensity averaged across the entire *z* or depth direction (to avoid hot voxels), and 3) the total detected volume of the microsphere should be less than 14 voxels in each dimension (to avoid microsphere clusters). Microspheres containing voxels with saturated intensity (255 in 8-bit images) were also avoided because part of the PSF information of these microspheres is lost. The 3D size, breadth, width, and depth [B, W, D] of the analytical theoretical $PSF(\mu_{ex}, \mu_{em})$ model presented in equation (2.6) was, for each microsphere, set to match the size of the 3D extracted microsphere image (e.g., if the microsphere extracted was 11x11x11 voxels, the theoretical PSF would be of the matching size). Constrained nonlinear multivariate optimization was used to obtain the optimal parameter values for the excitation and emission attenuation coefficients (μ_{ex}, μ_{em}) for each microsphere by fitting a computer-generated simulated microsphere convolved with the analytical theoretical $PSF(\mu_{ex}, \mu_{em})$ model to each 3D microsphere image. The 3D extracted images were used for the fitting because they captured the microsphere's light distribution in tissue (we assumed that the microsphere behaves as a point source, as proposed by Rolf et al. 2008). This method of optical tissue parameter estimation from microspheres is shown to be robust to partial volume effects (in Appendix B). The cost function minimized was the mean square error between the extracted microsphere image volume I_m and the simulated image I_s, which is the computer-generated phantom microsphere *M* convolved ($\otimes$) with the *PSF*:

$$I_s = M\{s\} \otimes PSF\{\mu_{ex}, \mu_{em}\}$$
$$\hat{o} = \arg\min_{o} \frac{1}{BWD} \sum_{i=1}^{B} \sum_{j=1}^{W} \sum_{k=1}^{D} [I_m(i,j,k) - I_s(i,j,k)]^2 \quad (3.3)$$
$$where \quad \hat{o} = \{\mu_{ex}, \mu_{em}, s\}, \quad image\ size\ [B,W,D]$$

For each microsphere, the simulated image I_s that models the distribution of a microsphere's light in tissue is parameterised by the coefficients of excitation and emission tissue attenuation, μ_{ex} and μ_{em}, respectively, and a third parameter – distance of the microsphere to the cutting plane (denoted by *s*) in the slice, which affects the detected intensity of the microsphere. The next section further explains this third parameter.

3.2.3 Microsphere Slice Depth Parameter

The slice depth (parameterized as *s*) or location of the microsphere (with respect to slicing) is calculated as the depth of the microsphere from the tissue surface in the range of 0 - 50 micrometers, because 50 micrometers is the slice thickness. Fig. 3.4 illustrates the slice depth parameter.

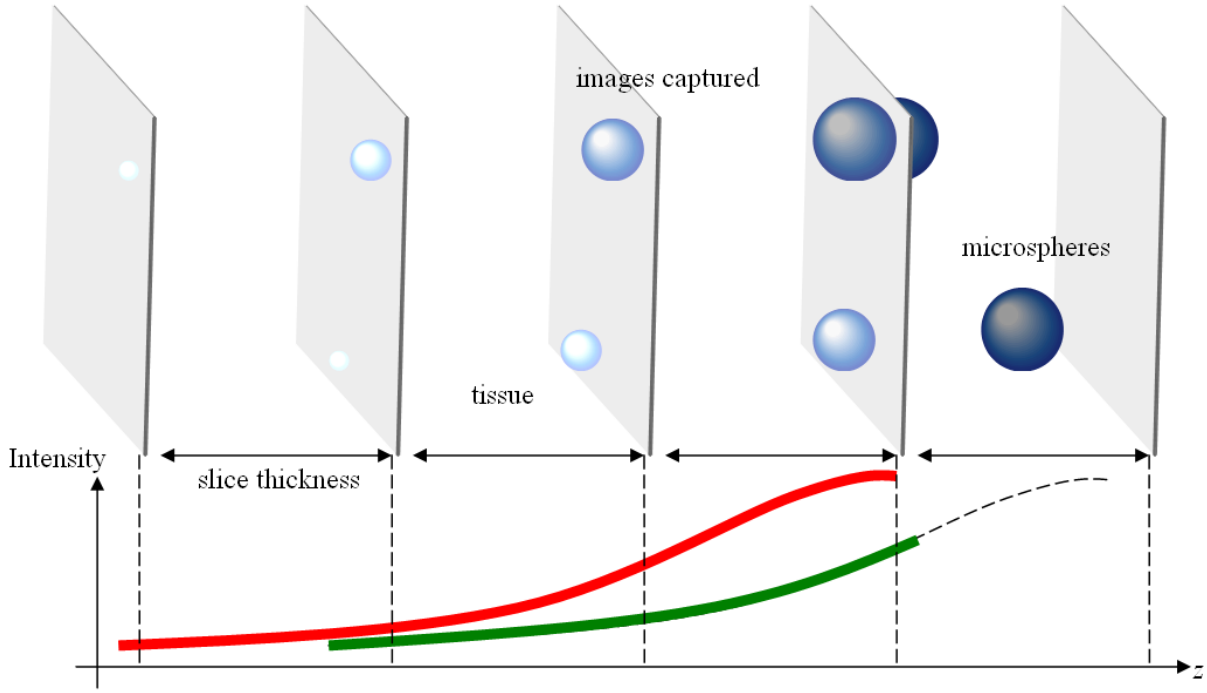


Figure 3.4: The effect of the microsphere's slice depth (location of the microsphere with respect to slicing) on the light intensity distribution of the captured microsphere images. The position of the microsphere affects the intensity of light that is recorded in each image slice. The dark blue spheres represent the microspheres and the lighter ones represent the images of the microspheres in successive slices.

3.2.4 Parameter Estimation Algorithm

The parameter estimation represents a fitting problem, where a simulated image is synthetically generated by convolving a simulated microsphere with the tissue PSF model and the PSFparameters are adjusted such that the difference between the simulated image and the observed image of the microsphere (embedded in tissue) is minimized in a least squares sense. The algorithm is iterative, starting with initial parameter values and updating them (and thus generating a new simulated microsphere image every time) until the least squares difference is minimised. The complete algorithm is listed in Table 3.2. The search is bounded such that parameters μ_{ex}, μ_{em}, and s can vary only within the following permissible ranges: $0 \leq s \leq 50$ µm because in a single slice, the imaged microsphere can only be located at a maximum depth of 50 µm from the surface (the slice thickness is 50 µm); $0.001\ \mu m^{-1} \leq \mu_{ex} \leq 0.050\ \mu m^{-1}$ and $0.001\ \mu m^{-1} \leq \mu_{em} \leq 0.050\ \mu m^{-1}$ is the domain in order to cover the entire range of attenuation

coefficient values for all visible wavelengths of light in cardiac tissue (published as 0.004 - 0.020 μm^{-1} in Rolf 2005). All three parameters vary continuously within the bounds given and are not restricted to integral or discrete values, so a discrete exhaustive search is unviable. The coefficients are constrained by the condition $\mu_{ex} > \mu_{em}$, since the emitted fluorescence is of a longer wavelength than the excitation illumination (Guilbault 1990) and light is less attenuated in tissue at longer rather than shorter wavelengths (Morgner et al. 2000). Thus this problem becomes a constrained bounded optimization problem (refer to Appendix B for unconstrained and unbounded optimization of the PSF parameters, which resulted in closely agreeing mean values of the optical tissue attenuation coefficients).

In the computational algorithm depicted in Table 3.2, in the function *Extract()*, the specified microsphere's image volume V_i is extracted by region growing out from the location index *loc* from the list *L*, which specifies the location index of all microspheres in the entire dataset. *Initialize()* sets μ'_{ex} and μ'_{em}, the optical tissue parameters being estimated, with initial values midway between lower and upper boundaries, and the location of the simulated microsphere with respect to slicing, parameterized by *s'*, is initialized to be midway between two slices. *GeneratePSF()* creates a PSF model of the tissue with the parameters μ'_{ex} and μ'_{em}. *CreateMicrosphere()* generates a simulated microsphere volume *M* with the microsphere centrepoint situated at the location specified by *s'*. The simulated microsphere *M* is convolved by *Convolve()* with the PSF model to obtain a simulated volume V_s of a convolved microsphere, i.e. the simulated light distribution of a microsphere embedded in tissue. The mean square error, *err*, is calculated by *MSE()* between the simulated image volume V_s and the original image volume V_i of the microsphere extracted from the image dataset. The *Optimizer()* updates the parameter values in its search for the minimum of the error and continues until the cost function *err* is less than a user-specified error threshold ε. The

Optimizer() function optimizes the value of the cost function by altering the parameters under constraints. After each iteration of the *while* loop, the newly updated values become the current parameter values, until the minimum of the error is reached. The *Optimizer()* function uses the Newton-Raphson gradient descent algorithm with a quasi-Newton approximation to the Hessian matrix of second-order partial derivatives (Waltz et al. 2006). Using a global multi-start approach, the optimization starts searches from several points in the specified parameter space range. After the minimum of the error function is reached, the optimized parameters are declared for that microsphere, and the process continues to the next microsphere.

```
for loc ∈ L
        V_i ← Extract(loc)
        [μ'_ex, μ'_em, s'] ← Initialize()
        while (err > ε)
                PSF ← GeneratePSF(μ'_ex, μ'_em)
                M ← CreateMicrosphere(s')
                V_s ← Convolve(M, PSF)
                err ← MSE(V_i, V_s)
                [μ'_ex, μ'_em, s'] ← Optimizer(err, μ'_ex, μ'_em, s')
        end while
        params(μ_ex, μ_em, s) ← Final(μ'_ex, μ'_em, s')
end for
```

Table 3.2: Computational algorithm for estimating optical parameters from microspheres.

3.3 Results

3.3.1 Slice Depth Uniform Distribution

Over the entire 3D image stack of the rabbit and porcine hearts, excitation and emission attenuation coefficients μ_{ex} and μ_{em} and slice depth s were estimated for the extracted microspheres. We expect that the microspheres are uniformly distributed across slices, and thus the slice depth parameter should be uniformly distributed. A Chi-square goodness of fit uniformity test on the distribution of slice depths calculated for each of the microspheres (see Fig. 3.5) showed that the slice depth parameter was uniformly distributed as expected.

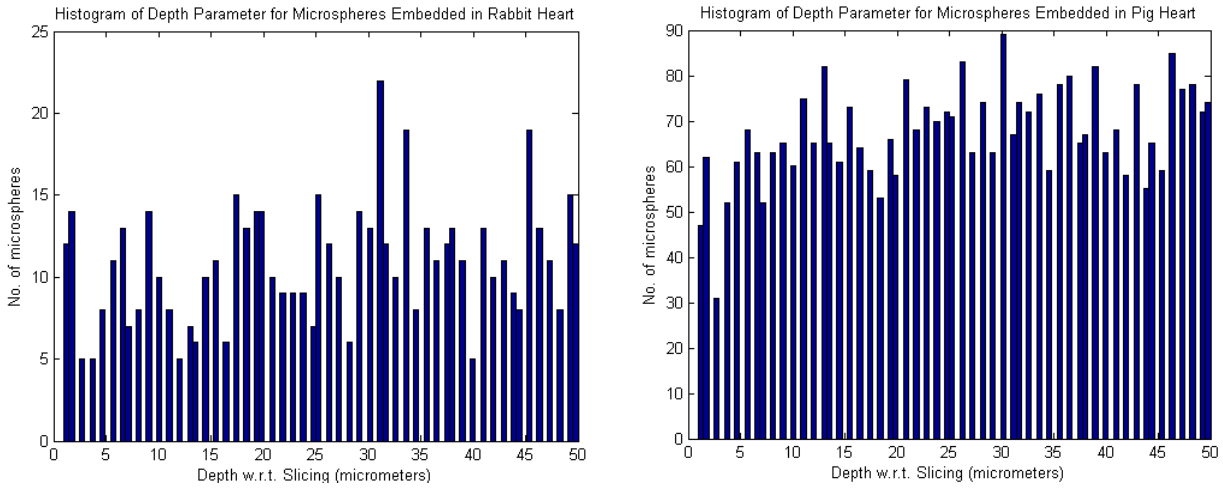


Figure 3.5: Distributions of the microsphere slice depth (location of the microsphere with respect to slicing) parameter. The distributions' uniformity was confirmed by performing a chi-square goodness-of-fit test of the null hypothesis that the sample data in the slice depth histogram is from a uniform distribution against the alternative that the data is not uniformly distributed. The result was that the null hypothesis (the hypothesis that the distribution is uniform) cannot be rejected and the probability, under assumption of the null hypothesis, of observing the given statistic is 27%.

3.3.2 Optical Parameter Distributions

Fig. 3.6 shows the microsphere image data slices across the rabbit and porcine hearts. Fig. 3.7 shows the histograms of the attenuation coefficients estimated from the microspheres. These plots show variation in optical tissue attenuation across the heart.

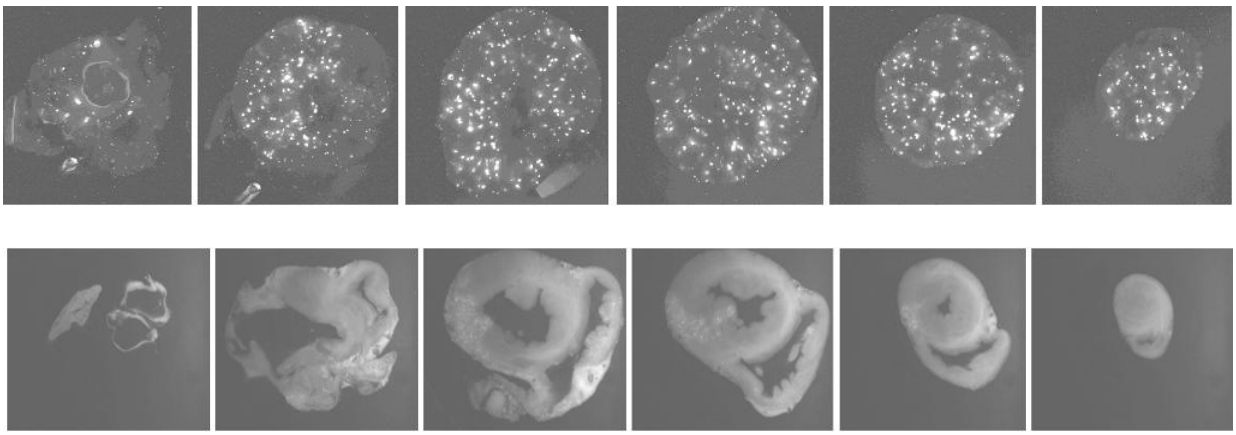


Figure 3.6: Short-axis images of rabbit (upper row) and porcine (lower row) hearts perfused with microspheres. Slices are shown at intervals equal to 5 mm (for rabbit heart slices) or 12 mm (for porcine heart slices) from base to apex (starting at left and ending at the right). Image dimensions: 3x3 cm^2 (rabbit heart) and 7x8 cm^2 (porcine heart). Images are 8-bit gray-scale with intensity range 0-255.

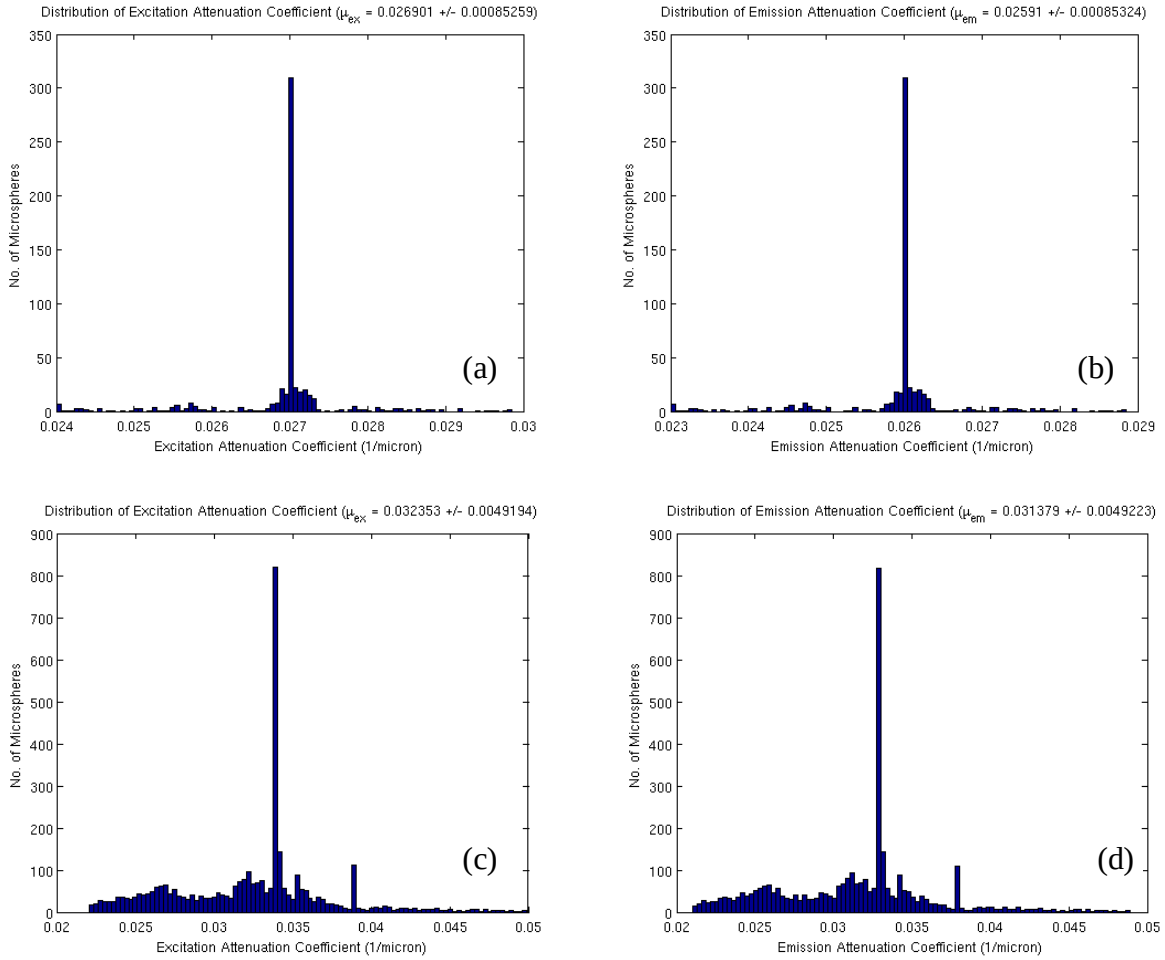


Figure 3.7: Probability distributions (approximated with histograms) of μ_{ex} and μ_{em} [1/μm] for the rabbit ((a) & (b)) and pig ((c) & (d)) hearts. These optical parameter distributions are for constrained bounded optimization (see Appendix B for unconstrained unbounded optical parameter estimation from microspheres). The microspheres are excited by and emit fluorescence at a mean wavelength ± a narrow standard deviation. While the attenuation coefficient for most of the microspheres lies within a narrow band, the large number of samples means there are a number of recordings away from this peak. The two peaks in (c)-(d) are discussed in 3.3.5.

In the histograms in Fig. 3.7 showing the probability distributions of the porcine myocardial optical attenuation coefficients, a narrow Gaussian distribution is expected because the microspheres are excited by and emit fluorescence at a mean wavelength ± a narrow standard deviation. However, the spatial pattern in the intramural optical tissue attenuation correlated to regional tissue is discussed further in section 3.3.5. To investigate if the two peaks in Fig. 3.7 (c)-(d) could potentially have any anatomical basis, section 3.3.5 discusses the possible underlying relationship between the fibre orientation and the attenuation coefficient.

3.3.3 Shape of the Objective Function

Fig. 3.8 shows for one microsphere image volume, from the porcine cardiac images, the shape of the objective function near the minimum and across a larger domain in the parameter search space. To test the sensitivity of the final minimum detected in the objective function to discretization in the parameter search space, we tested discrete exhaustive searches with varying numbers of evaluation points in both optical parameters across the range $\mu_{ex} \in [0.01 \ldots 0.05]$ μm^{-1} and $\mu_{em} \in [0.01 \ldots 0.05]$ μm^{-1}.

However, this discrete optimization can fail to detect the minimum at the correct location (see plot (b) in Fig. 3.8) depending on the number of points at which the objective function is evaluated. In other words, in a discrete exhaustive search, the minimum found is sensitive to the number of evaluation points and can often be far from the actual minimum of the objective function. This is because a discrete search space potentially misses evaluating the objective function at lower values at very specific non-discrete combinations of the multiple parameters, whereas a gradient search algorithm will evaluate the function progressing down towards the minimum. For this reason we preferred continuous optimization (where the variables can assume any real continuous value within their range), specifically gradient descent minimization, which robustly detected the minimum (μ_{ex} at the minimum of the objective

function in Fig. 3.8 *b* very closely matches the mean of μ_{ex} in Fig. 3.7 *c*).

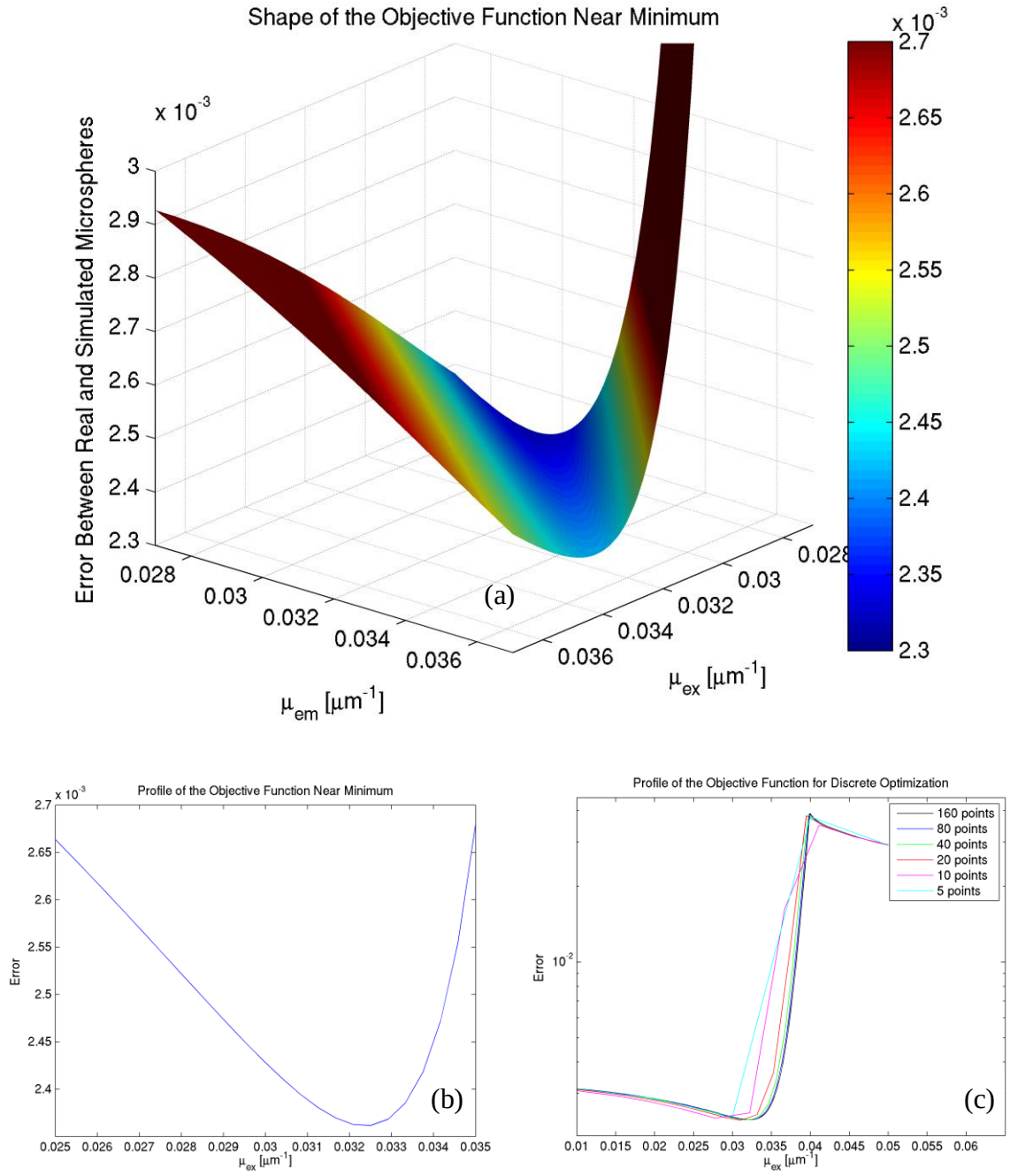


Figure 3.8: The shape and profile of the objective function are shown near the minimum in (a) and (b) plots, respectively. The profile is shown in (c) across a wider domain in the parameter search space calculated with a varying number of evaluation points. The discrete optimization approaches convergence as the number of points (listed in legend) at which the objective function is evaluated is increased. In (b)-(c), the parameter estimation is for μ_{ex} (μ_{em} is omitted because its minimum is of the same shape) for a single carmine microsphere image volume in the porcine myocardium.

3.3.4 Optical Parameter Validation with Published Values

The values measured in our study closely matched previously published values of myocardial optical parameters in the literature. The mean values of the attenuation coefficients μ_{ex} = 0.027 μm^{-1} and μ_{em} = 0.026 μm^{-1} measured from microspheres in our rabbit heart closely match literature values given for total optical tissue attenuation coefficient μ_t = 0.0267 μm^{-1} (Steyer et al. 2009) for rat heart tissue estimated from green fluorescent labelled microspheres (wavelength ~ 500 nm), similar to the wavelength of the yellow-green (515 nm) microspheres used to perfuse the rabbit heart in this study. Though Steyer's animal model was mouse and ours is rabbit, a big difference is not expected between the heart tissue properties of the two small mammals. Also, the attenuation parameters μ_{ex} = 0.032 ± 0.005 μm^{-1} and μ_{em} = 0.031 ± 0.005 μm^{-1} (mean ± standard deviation) measured from microspheres in this study's pig heart fall quite close to the range of values in the literature: μ_t = 0.037 ± 0.007 μm^{-1} (Flock et al. 1987) for pig tissue estimated at a wavelength of 633 nm, similar to the wavelength of the carmine-red microspheres used to perfuse the pig heart in this study (620 nm).

The effect of incorporating the difference in the attenuation coefficients between excitation and emission is not significant for vessel radii measurement in the context of blood flow simulations (refer to chapter 4 section 4.3.5.3 for analysis of radius sensitivity to difference in optical attenuation between excitation and emission and refer to chapter 5 section 5.3.7 for analysis of blood flow sensitivity to uncertainty in vessel radius estimation due to incorporating versus not incorporating difference in excitation and emission attenuation coefficients).

3.3.5 Optical Parameter Spatial Variation Map

To obtain a 3D optical parameter spatial variation map of the ventricular myocardium, first a generic ventricular myocardial geometry deformable template (cubic hermite mesh geometry)

was registered to a segmented pig ventricular myocardium containing microspheres (Fig. 3.9). Then we mapped an interpolated field of the spatial variation of the total optical tissue excitation attenuation coefficient, which was estimated from the microspheres embedded in the pig myocardial tissue, onto the registered cubic hermite mesh geometry of the heart.

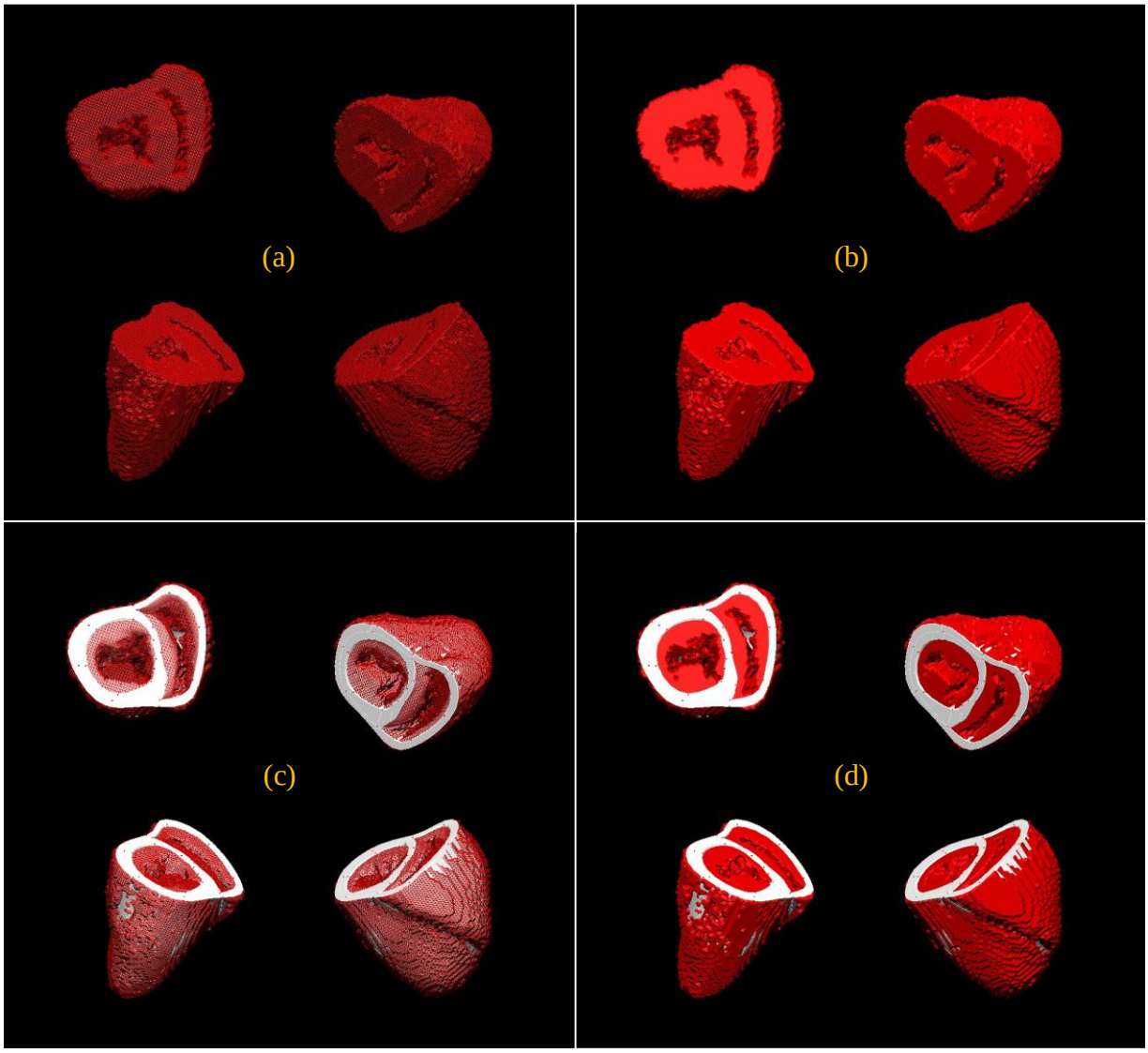


Figure 3.9: A generic ventricular myocardial geometry mesh template (white) is registered to a segmented pig ventricular myocardium (red). First shown is the segmented pig ventricular myocardium (red) rendered as a wireframe (a) and rendered as a shaded surface (b). Then shown is the mesh template (white) registered to the segmented ventricular myocardium (red), rendered as a wireframe (c) and shaded surface (d). The Sheffield Image Registration Toolkit (ShIRT) was used in this work to perform the registration (Barber et al. 2007) to fit a generic cubic hermite mesh of the ventricular heart geometry (Lamata et al. 2010) to the segmented binary image volume of the ventricular myocardium with a warping field.

Values of μ_{ex} and μ_{em} at each microsphere located in 3D Cartesian space were spatially interpolated to obtain continuous maps of the variation of optical attenuation properties across the myocardial tissue, discretised in space with a Delaunay triangulation using the Quickhull algorithm (Barber et al. 1996). Linear interpolation was performed between the scattered data points.

This facilitated visualizing the "hot spots," i.e. regions of the myocardium where the optical tissue attenuation parameter is high. Figs. 3.10-12 show the attenuation parameter field mapped onto the ventricular myocardial geometry and a visualization of the spatial variation of myocardial optical properties in 3D. The colour coding spectrum is shown in the colour bars in each figure and the value of the attenuation coefficient parameter is in the units of [1/micrometers].

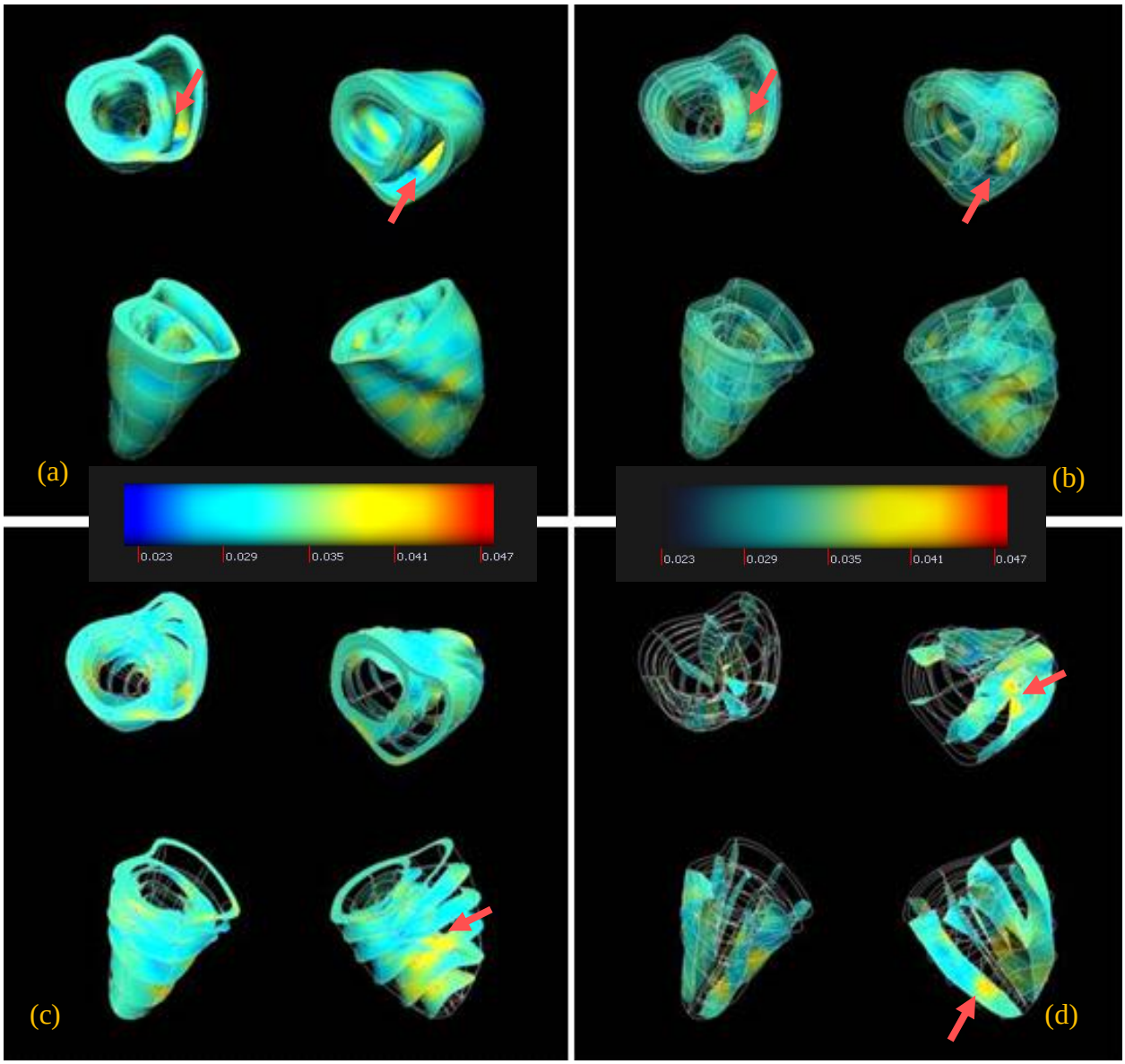


Figure 3.10: Pig ventricular myocardial geometry mesh color-mapped to the excitation attenuation coefficient (μ_{ex}) parameter field (a), where the spectrum is defined in the left color bar (units of μm^{-1}). The same field shown with semi-transparent surfaces obtained with an alpha channel (b) defined in the color bar on the right, to enhance view of "hot spots" where optical parameter was measured to be at its highest. Transverse cross-sectional slices (c) and radial slices (d) of the same field. The semi-transparent view, transverse and radial slices show that the largest hot spot or region of high optical tissue attenuation is not located on the epicardial surface but rather deeper in the tissue towards the endocardium (as pointed to by the red arrows).

Figs. 3.10-11 show in differing views, the pig ventricular myocardial geometry mesh color-mapped to the excitation attenuation coefficient parameter field. This field is shown in Fig. 3.10 (b) with semi-transparent surfaces (obtained by introducing an alpha channel defined in the colour bar on the right), to enhance view of "hot spots" where the optical tissue attenuation parameter was measured to be at its highest. The main hot spot occurs nearer the endocardium.

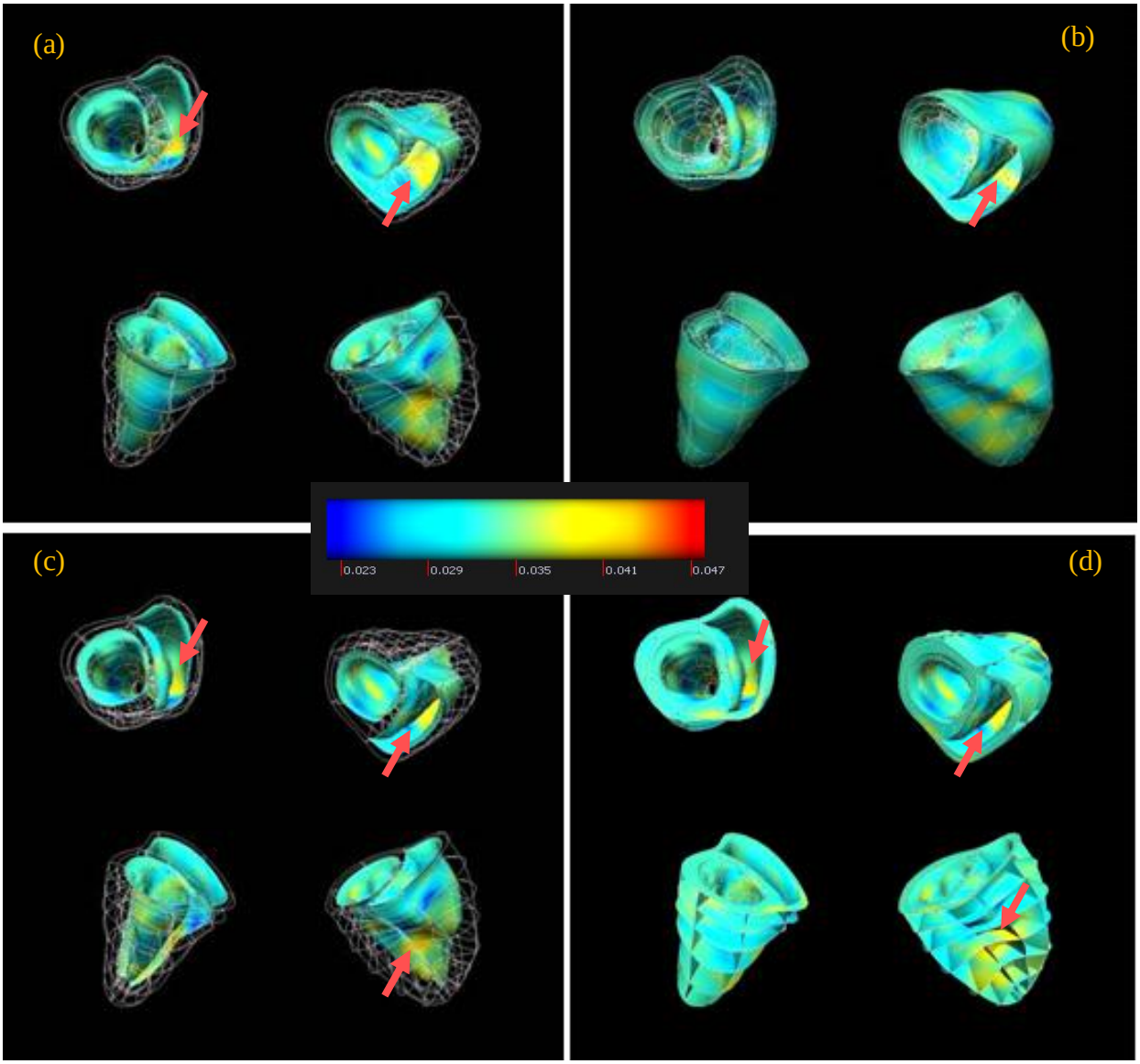


Figure 3.11: Endocardial layers (a), epicardial layers (b), ventricular cavities (c), and cross-radial slices into the ventricular endocardium (d) of the pig ventricular myocardial geometry mesh color-mapped to the excitation attenuation coefficient (μ_{ex}) parameter field (units of μm^{-1}), where the spectrum is defined in the color bar. The main largest "hot spot" or region with high attenuation parameter (as pointed to by red arrows) is located nearer the apex as opposed to the base of the heart.

In Fig. 3.11, endocardial layers, epicardial layers, ventricles, and cross-radial slices into the ventricular endocardium of the pig heart geometry mesh are color-mapped to the optical tissue excitation attenuation coefficient parameter field. The main hot spot is nearer to the heart apex.

Fig. 3.12 maps the same field onto transverse cross sectional slices across the pig ventricular myocardium showing the spatial variation in total optical tissue attenuation coefficient for incident excitation light. The slices shown are separated by 2mm. The white

arrows in Fig. 3.12 point to regions where the optical attenuation parameter was measured to be consistently higher than the average value ("hot spots"). These regions seem to anatomically correspond to the papillary muscles located in the ventricles (refer to Fig. 3.13) and the interventricular septal region (see Fig. 3.14).

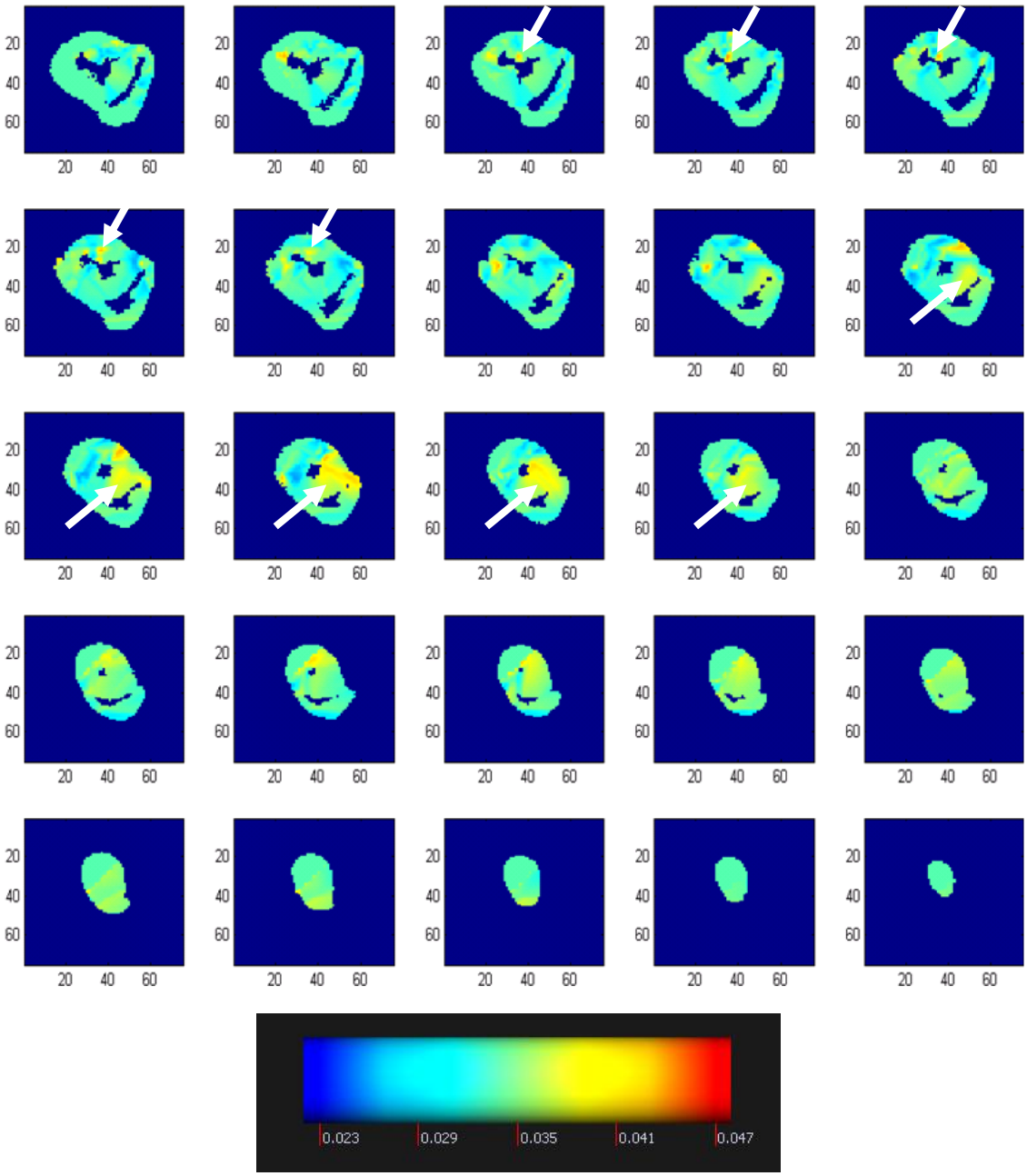


Figure 3.12: Transverse short-axis views across pig ventricular myocardium showing the spatial variation in total optical tissue attenuation coefficient for incident excitation light. Spectrum color bar represents the attenuation coefficient range (units of μm^{-1}). Each cross-sectional slice is 2 mm deeper in the long axis than the previous. Image dimensions: 8x8 cm^2. White arrows point to the papillary muscle and interventricular septal regions with consistently high optical tissue attenuation parameter.

Trabeculae carneae, anterior and posterior papillary muscles (Estes et al. 1966, Burch et al. 1968) and the septal papillary muscles (Restivo et al. 1989, Jezyk et al. 2010) facilitate ventricular ejection by systolic contraction. Papillary muscles are comprised of uniformly longitudinal fibres (Greenbaum et al. 1981, Streeter et al. 1966), as opposed to the fibres of the myocardial wall, which has a variation in fibre helix angle from endocardium to epicardium of approximately ± 60 degrees from the circumferential direction (Streeter et al. 1969). Higher optical attenuation parameter (as shown in Fig. 3.12) found in papillary muscles (circled in Fig. 3.13) with their vertical fibres as opposed to closer to in-plane myocardial fibres, suggests that fibre orientation may have a role to play in the observed variation in cardiac tissue's optical properties.

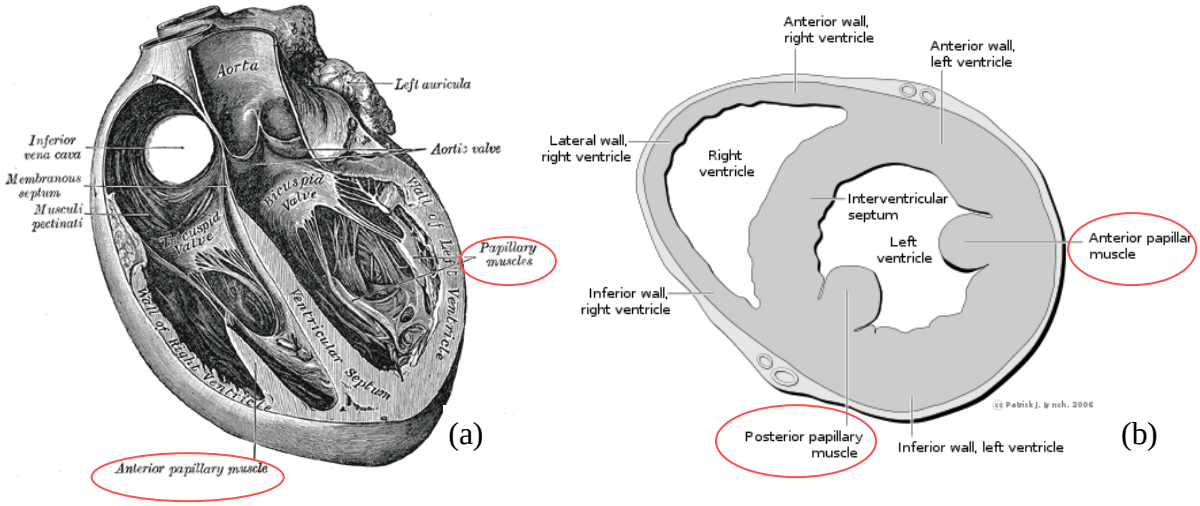


Figure 3.13: Coronal (a) and transverse (b) cross sections of the heart showing the ventricular papillary muscles (circled in red), common to mammalian hearts. [Sources: Gray (1918). Patrick J. Lynch, C. Carl Jaffe, MD, Yale University Center for Advanced Instructional Media Medical Illustrations, (1987-2000).]

Fig. 3.14 shows isosurface renderings of the optical excitation attenuation parameter, which suggest that the septum has higher optical attenuation (top row has isosurface at μ_{ex} = 0.038 μm^{-1}) than the myocardial free wall (bottom row has isosurface at μ_{ex} = 0.032 μm^{-1}). The slope of the transmural course of the fibre helix angle is steeper in the septal region as compared to other regions in the myocardium (Geerts et al. 2002), which means that the septum has a more

abrupt change in fibre orientation. Research suggests the interventricular septum to be a morphologically and functionally bi-layered structure with an abrupt change in fiber orientation through its middle (Boettler et al. 2005), which may thus be influencing the high degree of optical attenuation estimated in its tissue as opposed to the rest of the myocardium. Both the papillary muscles and septum have vertically oriented fibres (Geerts et al. 2002), and both have higher optical attenuation coefficients.

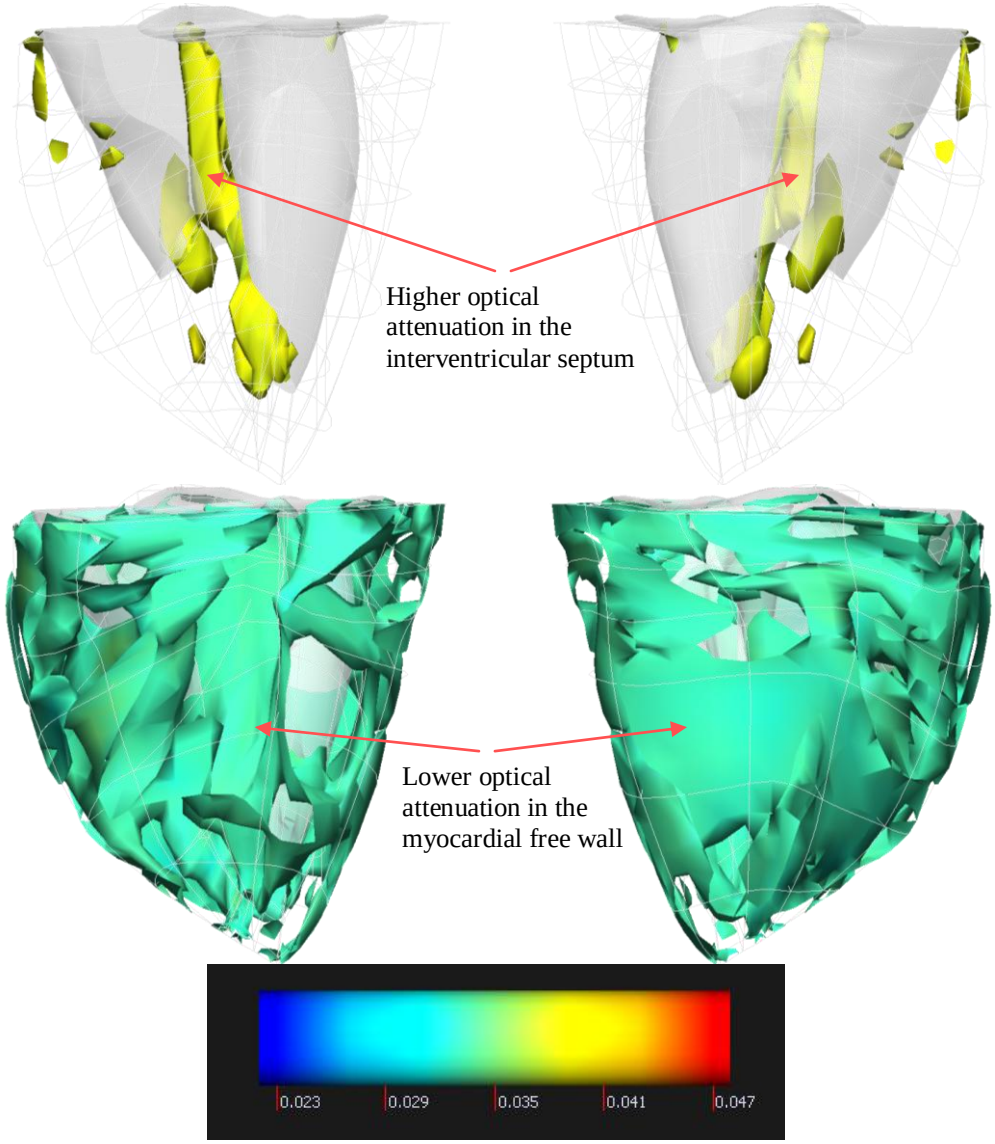


Figure 3.14: Isosurface renderings of the optical attenuation parameter suggest that the muscular interventricular septum that separates the left and right ventricles (shown in gray) has higher optical attenuation property (top row has isosurface at μ_{ex} = 0.038 μm^{-1}) than the myocardial free wall (bottom row has isosurface at μ_{ex} = 0.032 μm^{-1}).

3.4 Discussion

We implemented the method of measuring the total optical tissue attenuation coefficient from fluorescence microsphere images for observing the spatial variation in optical tissue properties across a whole organ. The method assumes that the fluorescent microspheres act as approximate point sources embedded in tissue. Measurements are possible across whole organs because the fluorescent microspheres can be perfused throughout the entire organ via the vasculature.

Optical tissue attenuation coefficient was different in a rat versus pig heart, and the measurements of this study closely agreed with previously published values. The results of this study indicate that optical tissue attenuation properties are not homogeneous within the myocardium (e.g. for porcine cardiac tissue at 633 nm wavelength: $\mu_{ex} = 0.032 \pm 0.005$ μm^{-1}). The effect of the difference in optical attenuation between excitation and emission and the variation in optical tissue attenuation parameters on the measurement of vessels embedded in tissue is discussed in chapter 4. The uncertainty in vessel radii caused by the variance in optical tissue properties and its effect on blood flow simulations is discussed in chapter 5.

The spatial heterogeneity of optical properties in cardiac tissue has implications for cryomicrotome vascular extraction and perhaps other imaging modalities as well, e.g. it may have potential implications for optical mapping recordings of cardiac arrhythmias. As observed in Figs. 3.10-12, there is variation in intramural optical attenuation properties across the myocardium. Our study suggests that papillary muscles and the interventricular septum have a higher optical attenuation than the myocardial free wall (Fig. 3.14). In Fig. 3.7, there are two outstanding peaks in the optical tissue attenuation coefficient at excitation in the pig heart. The first peak at $\mu_{ex} = 0.032$ μm^{-1} corresponds to the optical excitation attenuation parameter measured in the majority of the myocardial free wall, and the second peak at $\mu_{ex} = 0.038$ μm^{-1} corresponds to the optical excitation attenuation parameter measured in the

papillary muscles and majority of the interventricular septum, as can be observed with the isosurface renderings in Fig. 3.14. We suspect the higher optical attenuation in papillary muscles is due to their vertically oriented fibres as opposed to the more generally in-plane myocardial fibres (which have ± 60 degrees change). As for the interventricular septum, its functionally bilayered structure with abrupt change in fibre orientation may be the cause of its high optical attenuation property. More measurements from other imaged heart datasets are required to confirm our hypothesis that papillary muscle and interventricular septal tissue have higher optical attenuation properties than the myocardial free wall. Whether a consistent pattern of this observed variation in optical tissue properties exists within hearts of an animal species or across higher mammalian species such as pigs, dogs, and humans is the subject of future research. Further optical attenuation variation studies across more hearts of the same and differing species are required before a conclusion about the optical attenuation properties' spatial variation pattern, consistency, and correlation to myocardial fibre orientation can be confirmed.

Since the illumination light is not monochromatic, but is passed through a bandpass filter, the light has an excitation spectra and corresponding emission spectra, both of Gaussian profile. The range or bandwidth of frequencies of light entering the tissue also in part affects the variation range in the values of μ_{ex} and μ_{em}, which are sensitive to light frequency. The μ_{ex} and μ_{em} recorded for a microsphere depend heavily on the frequencies of photons exciting and emitted by that microsphere.

In some areas of the variation map in Figs. 3.10-12, the measurement confidence is lower due to the low number of data points (microspheres) found in the region. However, this is likely to have negligible influence on our objective, which is to use the microsphere parameter measurements for estimating vessel diameters, for which we need a spatially variant PSF model, parameters of which were estimated from microspheres (data points) abundantly

close to the vessels where perfusion of microspheres is high.

Chapter 4

Vessel Radius Estimation

According to Poiseuille's law, blood flow in a vessel is proportional to the fourth power of its radius. Thus even a small decrease in radius results in a large increase in vascular resistance and consequently a significant decrease in blood flow (Ishizaki et al. 1993). For this reason errors in vessel radii measurement can result in very large errors in both blood flow measurement and simulation. It is thus essential that vessel radii detection be highly accurate for blood flow simulations. This chapter describes the work done in estimating vascular radii from cryomicrotome images in which the vessels are blurred due to light scattering in tissue and the voxels in the centre of vessels are saturated due to the limited bit-depth of the camera. Section 4.1 introduces the current state-of-the art methods for estimating radius of vessels from biomedical images and explores vessel cross-sectional image restoration via deconvolution and vessel boundary delineation with deformable models. From this work we conclude that the deconvolution is unsuccessful in restoring the images, and the deformable contour's evolution is unreliable due to being highly sensitive to filter parameters. The limitation of this study's imaging modality due to the nonlinear effect of pixel saturation, CCD sensor blooming, and overflow to neighbour pixels, as discussed earlier in the introduction, is the reason that the deconvolution approach is invalid for cryomicrotome vessel measurement. Thus section 4.2 proposes the novel model-based template-matching vessel radius estimation that simulates pixel saturation and obviates deconvolution by accounting for blurring in its model of the vessel images and incorporating the vessel's tubular geometry and orientation in the radius estimation. This new radius estimation method is validated with phantoms (reduces error from 42.9% to 0.6% over previous FWHM method), compared with previous state-of-the art methods, and tested on pig heart and kidney vascular images in section 4.3.

4.1 Introduction

4.1.1 Vessel Radius Estimation

The full-width half maximum (FWHM) method has been used extensively for measurement of vessel size in medical images (Zhou et al. 1994, Hoogeveen et al. 1998, Botnar et al. 1999, Pedersen et al. 2000, Marxen et al. 2004, Rolf et al. 2008). In the FWHM radius estimation method, a Gaussian intensity distribution is assumed for the vessel cross-section and the FWHM is measured as the length across the half of the maximum intensity of the vessel cross-section profile. In this study, FWHM was measured along 1D line profiles across the vessel cross-sections as explained below. The implementations of the FWHM method used in this study are as follows:

- FWHM on Original Cross-section: In the original raw image, the FWHM is calculated along 1D line profiles across the vessel cross-section, crossing through the vessel centrepoint. The line across which the FWHM is calculated is each time rotated clockwise 1 degree around the cross-sectional centrepoint 360 times. In the raw original image, the vessel crosses the imaging plane at an oblique angle, due to which its cross-section is elliptical. Since the diameter of the cylinder will be the minimum distance between opposite boundary points across the elliptical cross-sectional centrepoint, the minimum of all the 360 FWHM measurements is used.
- FWHM on Resampled Slice: A resampled image is interpolated by reslicing a plane orthogonal to the vessel long axis. In this resampled image, the FWHM is calculated along 360 1D line profiles (as in the first implementation) across the vessel cross-section through the centrepoint. In the resampled image the vessel cross-section is circular due to the vessel crossing the resliced plane at a right angle, and thus the mean of all the FWHM measurements is used.

The above two implementations of the FWHM measured on the original cross-sectional slice and resampled perpendicular slice can both be performed on the raw and deconvolved vessel image volumes, which makes the four implementations of the FWHM method tested in this study as follows:

- FWHMrawOrig is FWHM measured on the raw (non-deconvolved) original cross-sectional (unchanged non-respampled slice) image.
- FWHMrawPerp is FWHM measured on the raw (non-deconvolved) perpendicular (resampled) image slice.
- FWHMdecOrig is FWHM measured on the deconvolved original cross-sectional (unchanged non-resampled slice) image.
- FWHMdecPerp is FWHM measured on the deconvolved perpendicular (resampled) image slice.

The deconvolution methods tested for image restoration of the cryomicrotome vessel images are discussed next.

4.1.2 Vessel Image Restoration

In this section, commonly-used and well-established 3D image restoration approaches in literature (McNally et al. 1999) were used as a benchmark for image restoration of vessel data. Minimum mean square error or Wiener least squares filtering (Gonzalez et al. 2002), regularized constrained least squares filtering (Jain 1989), and statistical maximum likelihood Richardson-Lucy deconvolution (Biggs 1997) were tested.

Computer-generated and artificial cylinder phantoms were used to evaluate image restoration of vessel images after deconvolution. These 3D computer-generated vessel phantoms were convolved with a PSF (defined in equation 2.6) with attenuation coefficients

defined as $\mu_{ex} = 0.032$ and $\mu_{em} = 0.031$. Using the same PSF, deconvolution techniques were applied to de-blur the blurred phantom, i.e. restore the original vessel from the degraded image. Oblique vessel angle and pixel saturation were also simulated in the vessel phantom to observe their effect on the deconvolution. The results of the deconvolution tests run on the vessel phantoms illustrated in Appendix C show the original, blurred, and deconvolved images of the embedded fluorescent cylinders and phantom data. The results demonstrate that saturated voxels in the vessel images cannot be restored with deconvolution, and the results deteriorate further for obliquely oriented vessels. This motivates a model-based method for vessel measurement instead of image restoration via deconvolution. Since the 8-bit intensity is clipped resulting in saturated voxels in the vessel images, model-based radius estimation is proposed in this study as a more suitable approach to vessel measurement because this new proposed method models the entire image acquisition process including pixel saturation.

4.2 Methods

Initially, as described in the first section of this chapter, we tried deconvolution to remove the haloes obscuring the vessel cross-sectional boundaries and other transparency artefacts, but the deconvolution is ineffective in restoring the vessel image data. Thus, a novel model-based method is proposed herein that renders image restoration unnecessary. This model-based template-matching method for radius detection incorporates the optical blurring in the vessel images due to tissue transparency (modelled by the PSF) and the vessel's geometry and orientation. Extracting vessel information requires building a description of the skeleton of the vessel tree, for which vessel segmentation is necessary, as elaborated next.

4.2.1 Image Processing Pipeline

The process of filtering the data for enhancing the vessels, segmenting and skeletonizing the vascular data, and pruning the extracted tree, followed by radius measurement, is summarized in the following steps (shown as a flowchart in Fig. 4.1 and with intermediate outcomes in Fig. 4.2):

- ***Enhancement:*** The vessels in the original image (see Fig. 4.2a) were enhanced with a multi-scale vesselness filter in two sets – large (see Fig. 4.2b) and small vessels (see Fig. 4.2f) separately.
- ***Binarization:*** The large vessels were binarized with a global Otsu (Otsu 1979) threshold (see Fig. 4.2c), and the small vessels were binarized with Sauvola (Sauvola et al. 2000) local adaptive thresholding (see Fig. 4.2g).
- ***Segmentation:*** Connected component analysis was used to remove blobs caused by fluorescent cast leakage in the tissue (see Fig. 4.2d) for obtaining the large vessels (see Fig. 4.2e) and was also applied to the combined outputs of the small and large vesselness filter (see Fig. 4.2h) for separating non-vessel structures (see Fig. 4.2i) and extracting the fully connected vasculature tree (see Fig. 4.2j).
- ***Skeletonization:*** Thinning was used to define the centrelines of all the vessel segments in the segmented vasculature (see Fig. 4.2k). Automatic correction algorithm pruned the reconstructed vasculature (see Fig. 4.2l) to remove spurious branches and loops (see Fig. 4.2m). Spline-fitting across all vessel segments smoothed out irregularities and jagged edges (see Fig. 4.2n).
- ***Reconstruction:*** The vascular tree was reconstructed as a 3D computational model of spline-fitted centrelines and associated radii. A novel model-based method was used to

measure the vessel segments, which were sized and coloured by their radii (see Fig. 4.2o).

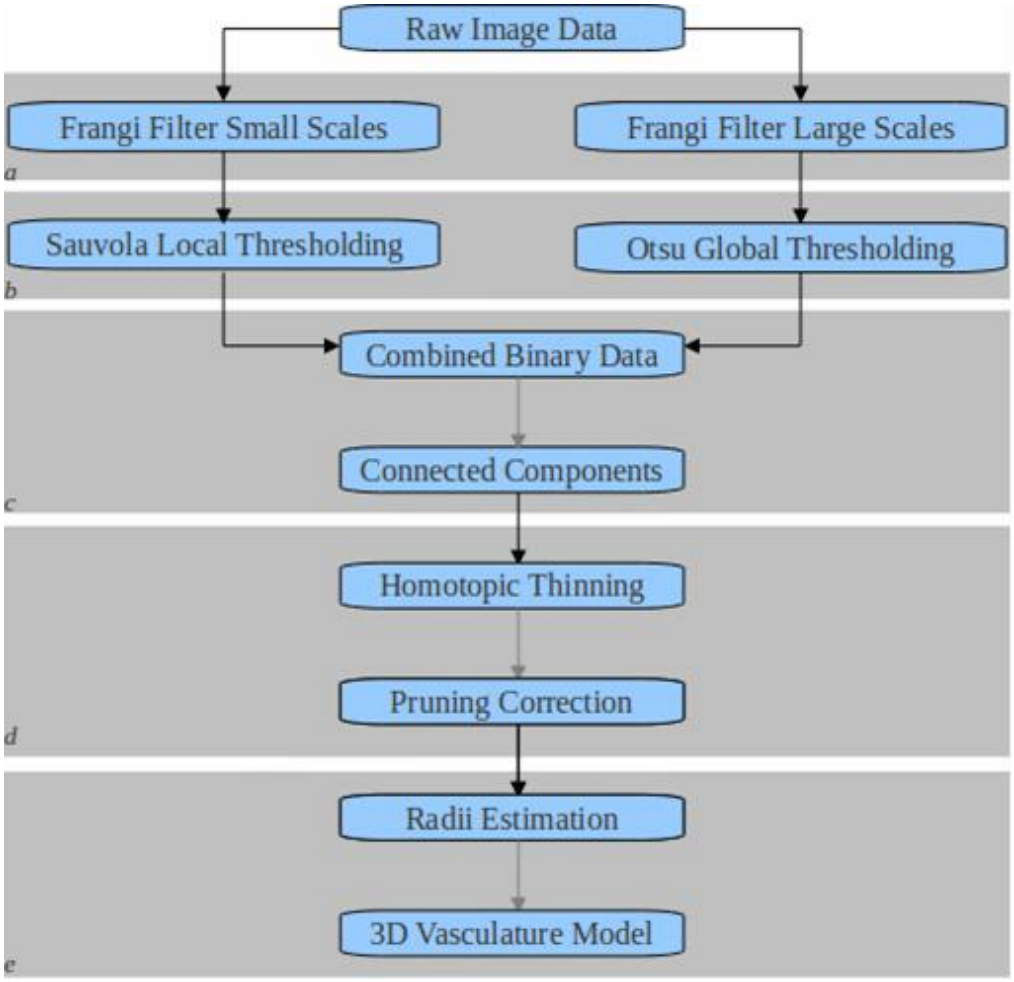


Figure 4.1: Flowchart diagram depicting the image processing algorithms used in the enhancement (a), binarization (b), segmentation (c), skeletonization (d), and reconstruction (e) of the vascular data.

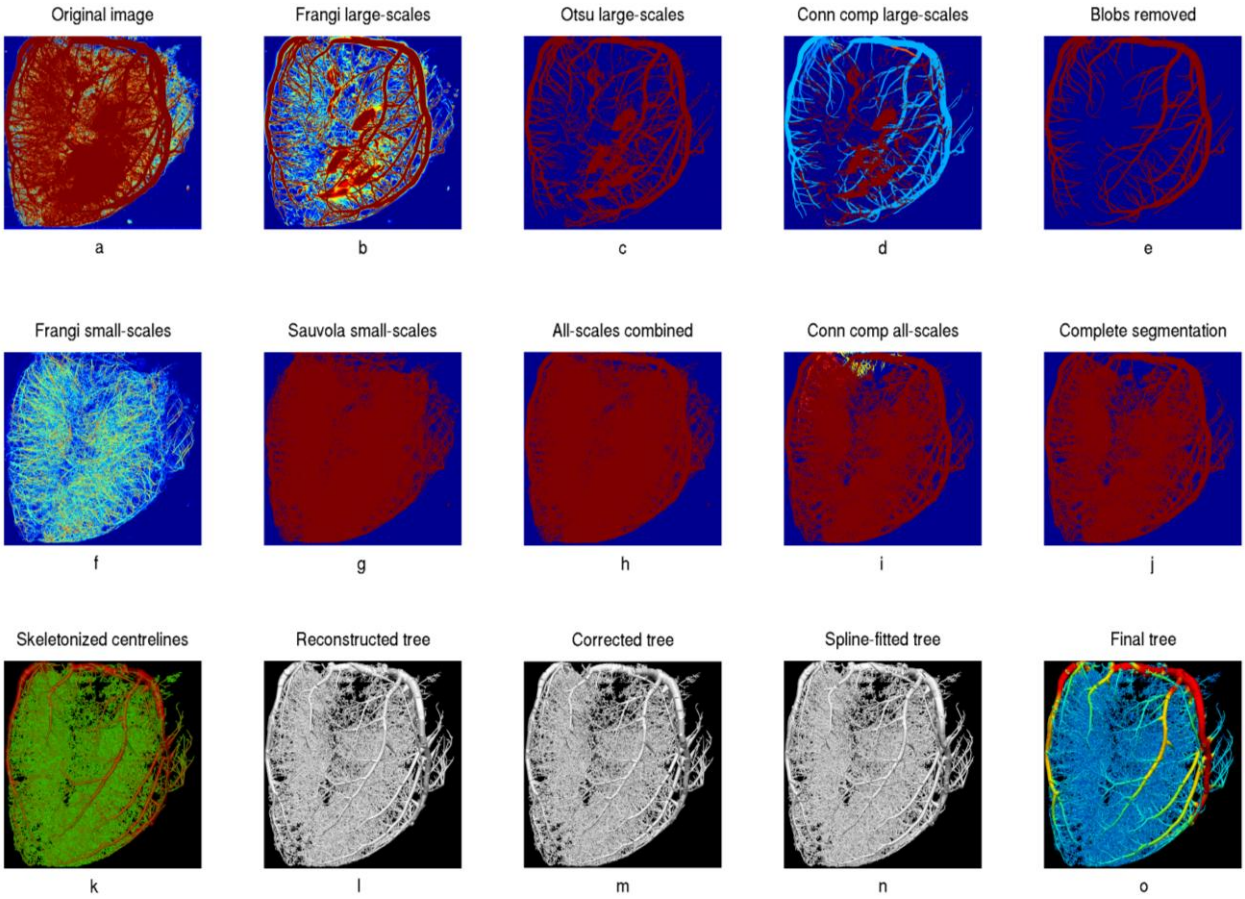


Figure 4.2: In the original image, shown as a MIP projection in the *x*-dimension of the original 8-bit grayscale image with a rainbow colormap (0-255) (a), large vessels were detected with multi-scale vesselness filtering (b) and Otsu global thresholding on the large-scales output (c). Connected component analysis (d) removed the blobs created by leakage of the fluorescent cast into the tissue to obtain just the large vessels (e). Small vessels were detected with multi-scale vesselness filtering. Note the blobs do not appear in the small-scale vesselness output because the small-scales only detect small vessel structures (f). Binarization was performed with local adaptive thresholding on the small-scales output (g). Then voxels in the combined binary image volume of all vessel scales (h) were categorized into connected components (i). The noise structures (i.e. small components unconnected to large tree) were removed leaving only the fully-connected vasculature (j). Skeletonization on the binary segmented vasculature, coloured in red, defined the vessel centrelines, coloured in green (k). The vascular tree (l) was processed with an automatic algorithm that eliminated spurious branches, removed redundant arterial loops, and reassigned connections at junction nodes with extra conjoining segments in the tracked centrelines. The corrected vessels (m) were fitted with splines to smooth out irregularities and jagged high curvature points (n), to finally reconstruct a 3D model of the vascular network coloured by the vessel radii (o). Image volume dimensions: 1463x1353x1280 voxels, where the voxel size is $(50\ \mu m)^3$.

4.2.2 Vessel Enhancement and Binarization

4.2.2.1 Filtering

As depicted in Fig. 4.2, for extracting vessels of all sizes from the original image (Fig. 4.2a), multi-scale detection was applied on the original image volume with a filter which calculates the eigenvalues of the Hessian at each voxel to compute the likeliness of the voxel being part of a tube-like structure (Frangi et al. 1998). The images were processed twice across two sets (small and large) of scales. The small scales (Fig. 4.2f) ranged from 0.005 – 0.1 mm with a step size of 0.005 mm and the large scales (Fig. 4.2b) ranged from 0.1 – 2 mm with a step size of 0.05 mm (scales set to the sizes of the vessels to be extracted). In the Frangi vesselness filtering scale ranges, the smallest scale was based on the smallest vessel radius that can be detected from the cryomicrotome imaging modality due to its resolution limit and the largest scale was based on the generic radius of the largest artery in the coronary vasculature in porcine hearts. An alternative computationally efficient technique would have been to specify a variable geometric step size where the next scale is equal to a factor multiplied by the previous scale. At larger sizes due to the large value of the 3D Gaussian filter scale, the vessels respond to a range of scales, not just to a single value of the Gaussian filter's sigma. Another approach that has the potential to be an efficient method is to apply progressively coarser step sizes at progressively larger scales. However, previous published methods of vessel detection (e.g. Krissian et al. 2000) which use a variable step size have the potential to miss small vessels and vessel junctions that can result in broken and disconnected vessels (exact step-size, scales, and results detailed in the "Comparison with Previous Radius Estimation Method" subsection 4.3.1 of the "Results" section 4.3). Thus to ensure vessels are not missed due to not being detected at a particular scale, we employed a fine step size, to in particular account for small vessels (refer to Appendix D.1 for a detailed comparison of the constant versus variable step size vesselness filtering).

Frangi vesselness was applied on small and large scales separately for two reasons: First, the fluorescent dye injected into the coronary arterial network can leak into the tissue from damaged arterial junctions and create blobs in the image data. These blob-like or noise structures that may appear tube-like at some scales were able to be filtered out at other scales. Second, the small and large scale outputs of the Frangi filter were required to be binarized separately as they needed distinct threshold levels.

4.2.2.2 Thresholding

The small-scale vesselness output was binarized (Fig. 4.2g) with Sauvola local adaptive thresholding. By trial and error, for local adaptive thresholding on small-scale vesselness data, the optimal block size was found to be n = (0.5 mm)^3; the weight parameter of the standard deviation was set to k = 1 from a range of [0 1], and the dynamic range of standard deviation was defined as R = 128 for 8-bit images (Sauvola et al. 2000). For block b with a voxel intensity mean $m(b)$ and standard deviation $s(b)$, the Sauvola local adaptive threshold $T(b)$ was calculated as $T(b) = m(b) \cdot \left[1 + k \cdot \left(\frac{s(b)}{R} - 1\right)\right]$. In this Sauvola threshold equation, the R parameter is a normalization factor and the k is the weighting parameter, both for the standard deviation of the block. Sauvola calculates an adaptive threshold for each block using the regional mean locally adjusted by each block's standard deviation, normalized (by R) and weighted (by k). The principle behind Sauvola's local binarization is to calculate the local threshold for each block of the image based on the local mean and local standard deviation of the block. If a block has high contrast in the intensities of its voxels (i.e. high variance between the intensities of the vessels and background), the local mean suffices as a threshold because it divides the vessels from the background; whereas if the block has low contrast in the intensities of its voxels (i.e. low variance between intensities of the vessels and background),

the threshold should be below the mean, by an amount proportional to the normalized local standard deviation in order to not miss the small vessels at lower intensities comparable to the background levels. Since the thresholding was not sensitive to the weight parameter *k*, it was set to $k = 1$ for the cryomicrotome vessel extraction, and hence the Sauvola threshold equation was reduced to $T(b) = \frac{m(b) \cdot s(b)}{R}$.

The large scale vesselness output was binarized with a single global threshold (Fig. 4.2c) selected to optimally divide the gray level into two classes (Otsu 1979). The small-scale output required local adaptive binarization because the vesselness was not consistent for all vessel sizes. The large scale output needed only a single global threshold value (and did not require local thresholding) because the high vesselness level of the large vessels was clearly distinguished from the background. However, for small-scale vessels, the Sauvola local adaptive thresholding works more effectively than Otsu local thresholding because it adapts the threshold according to the standard deviation of the distribution of the vesselness values, whereas the Otsu local method fails for thresholding smaller-scale vesselness response because there is no clear contrast but rather a wide distribution of vesselness values with a high variance (refer to Appendix D.2 for a detailed comparison of the local Otsu and Sauvola methods). Section 4.2.2.3 discusses blob removal, which is the reason why the small-scale and large-scale vesselness outputs were filtered separately with Sauvola and Otsu thresholding, respectively.

4.2.2.3 Blob Removal

After binarizing the large-scale output, the cast leakage blobs were removed with connected component analysis (Fig. 4.2d). Since thin vessels do not appear in the large scale output, the major tree structure and leakage blobs are not connected on the binary volume of the large

scale output, and thus connected component analysis on the binary volume of the large scale output allows filtering out the blobs caused by leaking from the thin vessels. Hence the separate processing for large and small vesselness scales. For obtaining the complete segmentation, the large-scales vesselness output thresholded with Otsu's method and subsequent to blob removal (Fig. 4.2e) was combined to the small-scales vesselness output thresholded with Sauvola local adaptive binarization. This operation applied a logical OR on each voxel, resulting in all vessel scales in the same image volume (Fig. 4.2h). An advantage of both Otsu and Sauvola thresholding was that the threshold level was automatically calculated from the images, and no manual interaction was required from the user. Additionally, further tuning of the parameter values for Sauvola's local adaptive thresholding was not required as the parameter values reported above worked for all the datasets processed in this study.

4.2.3 Segmentation and Skeletonization

Once the Frangi vesselness outputs were thresholded and combined, the resultant binary image of the vasculature was further corrected by removing noise using a 3D connected component labelling analysis (as shown in Fig. 4.2i). The largest connected component found in the 3D image volume was the vascular tree. After non-vessel structures disconnected from the vascular tree were removed (Fig. 4.2j), holes in the vessels were filled with a flood-fill morphological reconstruction operation on the binary images, which changed fully-surrounded connected background pixels to foreground pixels, stopping upon reaching the inner vessel boundaries (Soille 1999). Then a non-contrast medial-axis thinning technique (Lee et al. 1994) was employed to skeletonise the vasculature in the binary images. The thinning defined the vessel centrelines from the binary segmented vascular image volume (centrelines superimposed upon the vasculature in Fig. 4.2k). In the reconstructed vascular network (Fig.

4.2l), irregularities of the segmented vascular boundaries resulted in spurious branches, which were automatically removed as follows: Any vessel segment which terminated just after branching off of a main artery was deleted. Multiple connections to a single node from a common main branch were detected as redundant arterial loops and reduced to a single connection path. This was performed by tracing all the paths to each node in the arterial tree from the root node and keeping only the path of least resistance or highest flow. Following the automatic correction procedures, the processed tree (Fig. 4.2m) was fitted with cubic hermite splines to smooth out irregularities and high curvature points to reconstruct a 3D model of the vascular network (illustrated in Fig. 4.2n).

4.2.4 Model-based Template-matching Radius Measurement

Once a skeleton defining the vessel centerlines was extracted from the images, radius estimation for each vessel segment was performed. For this purpose, a novel method based on characterization of the point spread function and estimation of optimal radius was developed, using a model of the image acquisition process. The following steps detail how vessel radius was estimated with the model-based template-matching method (reconstruction model is colour-coded to measured radius in Fig. 4.2o):

4.2.4.1 Vessel Model Generation

- **Initialization**: Since the model-based method uses an iterative minimization scheme, to obtain a starting point close to the minimum of the objective function, the initial radius of each vessel branch was estimated as half the FWHM measured on a deconvolved version of the resampled perpendicular image slice of the vessel image volume (FWHMdecPerp as defined earlier in section 4.1.1).

- **Vessel Extraction**: For each vessel segment branch, the slices of the original image volume (Fig. 4.2a) and slices of the final binary segmentation (Fig. 4.2j) containing the branch were extracted. A 3D binary mask was created by automatic seeded region growing performed on the slices of the final binary segmentation containing the branch. The seed starting point was the vessel branch's centreline midpoint defined from the vessel centrelines traced on the skeletonised vasculature (Fig. 4.2k). The 3D binary mask was applied to the slices of the original image volume containing the branch to extract just the small local image block containing only the vessel branch of interest.
- **Deconvolution**: The microsphere image volume lying nearest to the extracted vessel branch was also extracted (fluorescent microsphere beads perfused in the vasculature appear as bright clusters of voxels in bottom two panels of Fig. 1.4). The nearest lying microsphere image volume was extracted by 3D seeded region-growing with heuristic thresholding (refer to chapter 3 and van Horssen et al. 2010). The initial seed point in the region growing for extracting the microsphere image volume was the central voxel of the microsphere obtained by finding the local maxima in the microsphere images. The extracted microsphere image volume was fitted to the PSF model (Rolf et al. 2008) to estimate the PSF parameters for deconvolution of the extracted vessel branch image volume. Richardson-Lucy (Biggs 1997) method and the microsphere-estimated PSF were used for deconvolution of the extracted image volume of the vessel branch.
- **Radius Measurement**: In the deconvolved image volume of the branch, FWHM was measured across the vessel cross-section in a plane orthogonal to the vessel long axis (FWHMdecPerp as defined earlier in section 4.1.1). The initial radius

estimate of the vessel branch was calculated as half of the FWHMdecPerp diameter measure.

- **Vessel Template:** a template $V_t(r)$ with initial radius r of a vessel segment was simulated as a cylinder between the two vessel branch endpoints with coordinates $p(x_c,y_c,z_c)$ and $p(x_n,y_n,z_n)$ in 3D space (see Fig. 4.3). The radius is iteratively updated.
- **Point Spread Function:** the point spread function $PSF(\mu_{ex}, \mu_{em})$ function (Rolf et al. 2008) defined in equation (4.1) was modelled to simulate light transport in the tissue, and excitation and emission of light from the tissue surface:

$$PSF\left(\mu_{ex},\mu_{em}\right) = I_0 \frac{e^{-\mu_{ex}z} e^{-\mu_{em}d}}{4\pi\left(r^2\right)} * e^{\frac{-\left(x^2+y^2\right)}{2\sigma^2}} \quad (4.1)$$

where the asterisk symbol represents 2D convolution in the plane of the imaged tissue surface, I_0 is the original intensity of the point source (normalized to 1), x, y, and z are the coordinates, where z is the depth of the point source in tissue and d is the radial distance from the point source, $\sqrt{x^2+y^2+z^2}$. The parameters μ_{ex} and μ_{em} are the total optical tissue attenuation coefficient for excitation and emission, respectively. The lens blur scale is represented by σ, which was measured to be 68 μm for the camera in the cryomicrotome setup (Rolf et al. 2008).

- **Parameter Estimation:** the optical tissue attenuation parameters were measured locally for each vessel branch from the fluorescent microsphere lying nearest the vessel. A simulated microsphere phantom of 15μm diameter, convolved with the PSF model, was fitted to the extracted 3D volume image stack of the nearest microsphere for obtaining the parameter estimates.
- **Vessel Phantom:** a vessel phantom V_p was generated as a 3D volume image by convolving the vessel template with the PSF, as written in equation (4.2):

$$V_p = V_t(r) * PSF(\mu_{ex}, \mu_{em}) \quad (4.2)$$

- **Simulated Image:** a simulated vessel image $I_s(x,y)$ was obtained by reslicing the vessel phantom V_p in an x-y cross-sectional plane (demonstrated in Fig. 4.3).
- **Pixel Saturation:** since the real vessel image (8-bit depth) is distorted by CCD pixel saturation, this is also simulated in the simulated vessel image as the blooming effect. After the vessel model is convolved with the PSF, the blooming is simulated on each of the simulated vessel images by identifying all the amplified (from the gain caused by the convolution of the vessel model with the PSF) pixels with intensities greater than the maximum intensity. Starting from the centre of the convolved vessel image, if the pixel intensity exceeds the saturation level 255 (the maximum intensity for the 8-bit CCD sensor), the overflow (pixel intensity – 255) is equally divided and added to the neighbouring pixels. This is recursively repeated for all the pixels with intensities higher than 255 until there are no pixels over this saturation threshold. This blooming effect simulation is based on the technique used by Ientilucci (2000).

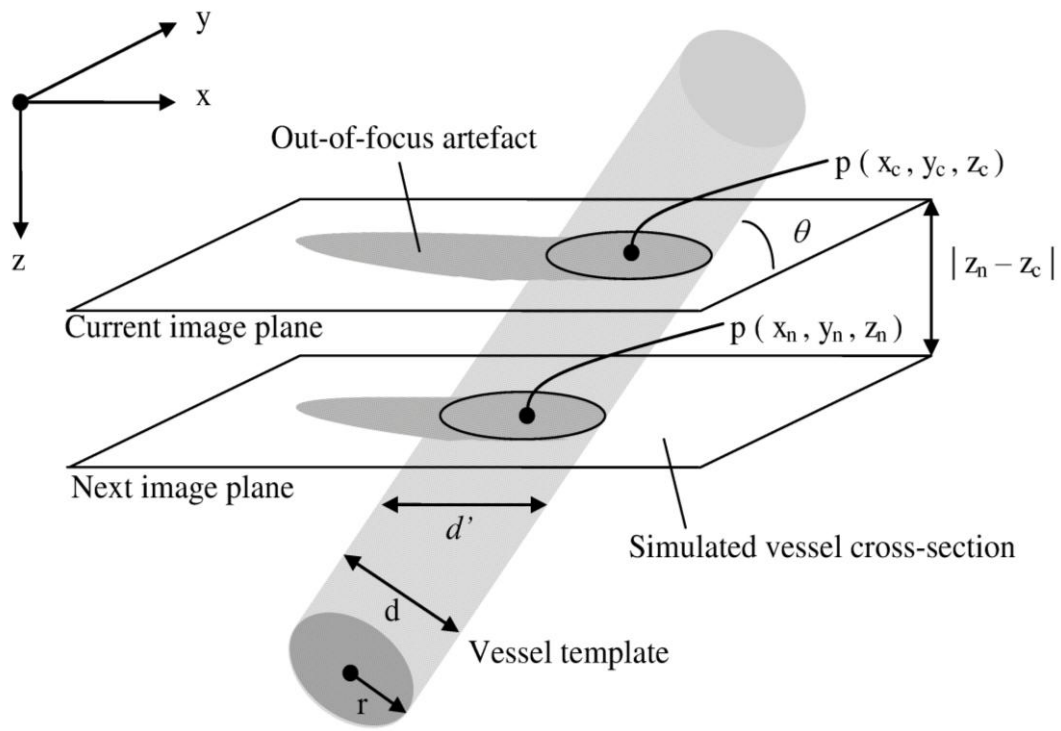


Figure 4.3: The diagram illustrates geometry of the vessel relative to the imaging plane where r is the actual vessel radius, d is the diameter, d' is the observed diameter in the imaging plane, z_c is the depth or z-coordinate of the current slice, z_n is the z-coordinate of the next slice, θ is the angle of the vessel to the imaging plane, (x_c,y_c) and (x_n,y_n) are the x-y coordinates of the current and next vessel centerpoints, respectively. The simulated vessel cross-sectional image is produced by the convolution of the PSF with a cylindrical model of the vessel segment for optimal vessel radius estimation.

4.2.4.2 Similarity Metric

- **Spread Measure:** measures of the simulated $I_s(x,y)$ and real $I_r(x,y)$ vessel images were obtained as the full-width at half-maximum (FWHM) of the cross sections, represented as M_s and M_r respectively in equation (4.3):

$$\begin{aligned} M_s &= FWHM\left[I_s(x,y)\right] \\ M_r &= FWHM\left[I_r(x,y)\right] \end{aligned} \tag{4.3}$$

The FWHM was measured as the distance between points at which the intensity was half of the maximum in a line profile across the vessel cross-section. When vessels were oriented oblique to the imaging plane, the vessel orientation was taken into account as the FWHM was measured in a resampled plane orthogonal to the vessel segment's long axis (FWHMrawPerp as defined earlier in section 4.1.1). In this

method, the FWHM was used not as a measure of vessel radius, but rather as a measure of the vessel cross-sectional spread in matching the simulated image to the real vessel image for parameter fitting.

4.2.4.3 Optimization Method

- **Objective Function:** an objective cost function C as a function of the vessel radius r was defined as the squared error between spread measures M_s and M_r, according to equation (4.4):

$$C(r) = (M_s - M_r)^2 \quad (4.4)$$

The absolute error difference between the spread measures of the simulated and real cross-sections was used as the objective function to be minimized for fitting the simulated vessel model to the real vessel image.

- **Minimization Algorithm:** nonlinear optimization was performed with the quasi-Newton line search method (Waltz et al. 2006) to minimize the difference between the real and simulated images.
- The above steps were repeated to obtain vessel radius estimates for all branches over the entire vasculature. Note: if microspheres are not available, then this method can employ a user-defined constant PSF.

4.3 Results

In this section, the proposed vessel extraction and radius measurement methods are compared against the previously published Krissian et al. (2000) method (section 4.3.1) and the FWHM radius estimation method (sections 4.3.6). All four implementations of the FWHM method listed in section 4.1.1 are tested. The methods proposed in this study are validated using computer generated phantoms (section 4.3.2), ground-truth artificial vessels (section 4.3.3),

manual segmentation of original raw vessel image data (section 4.3.1), and Murray's law as the criterion (section 4.3.7). The preciseness and robustness (section 4.3.4) and sensitivity (section 4.3.5) of the proposed model-based radius estimation to partial volume effect, optimization constraints and bounds, PSF parameter settings, and optical parameter variation is also presented. Finally, this study's proposed vessel detection methods are used to reconstruct 3D computational representations of whole-organ vasculatures extracted from training (section 4.3.8) and test (section 4.3.9) cryomicrotome image datasets. As an extension, the vessel detection of this study is also applied to CT data (section 4.3.10).

4.3.1 Validation Against Previous Vessel Detection Method

To provide a comparison of the performance of the vasculature extraction method presented in this study, we compared our results with those extracted from the model-based method developed by Krissian et. al. (2000). This approach enhances the vessels with multi-scale filtering similar to the Frangi vesselness filtering used in this study. Both Krissian's and our vessel extraction methods were tested on the same block of the porcine coronary vasculature data with 14 scales of the 3D Gaussian kernel used to filter vessels of size 0.1-5 voxels (scales chosen to correspond to radii of vessels to be extracted from the block). For the porcine coronary vasculature data tested using Krissian's method, multi-scale Gaussian filtering was applied at the following scales: 0.0707107, 0.0955377, 0.129082, 0.174403, 0.235638, 0.318372, 0.430155, 0.581186, 0.785245, 1.06095, 1.43346, 1.93676, 2.61677, and 3.53553 voxels. In comparison, the method presented in this study specified a step size of 0.1 voxel for the small scales [0.1-0.9] voxels and a step size of 1 voxel for the large scales [1-5] voxels. The main difference in the results lies in the detection of the vessel centrelines, wherein Krissian's method preprocesses the image data prior to thinning with ridge extraction by finding the local maxima in the multi-scale response, assuming that the local maxima will be

located at the central points of the vessels. The method presented in this study instead applies medial axis thinning on the binary segmentation obtained after connected component analysis. Additionally, Krissian's method binarizes the local extrema image with hysteresis thresholding, whereas the method in this study performs local adaptive thresholding to ensure small thin vessels are not missed because of intensity variation in the vessels.

The comparison results are presented in Fig. 4.4. A manual segmentation of the porcine coronary arterial sub-tree was used as the gold standard in the comparison. Fig. 4.4 shows the maximum intensity projections of the original image (first column), filtered output (second column), centrelines (third column), skeleton (fourth column), and 3-D reconstructed vasculature model (fifth column) created by the manual segmentation (top row), automatic method proposed in this thesis (middle row), and Krissian's method (bottom row). For vessel extraction from cryomicrotome images, the method proposed in this thesis performs better than Krissian's method in terms of detecting true vessels and eliminating false vessels, as discussed next and shown by the results in Table 4.1.

Table 4.1 lists the true / false and positive / negative voxels along with accuracy, specificity, sensitivity, and negative / positive predictive values of each method. These results show that in comparison, Krissian's method does not robustly accommodate a large variation in the intensity of the vessels. It fails in two ways on the cryomicrotome images: 1) the method misses many true vessels and junctions because it is not robust to the vessels' intensity variation especially in the small thin vessels (this results in broken and missed vessels), and 2) the method detects many false vessels because it does not differentiate the disjointed noise structures from the main vasculature network.

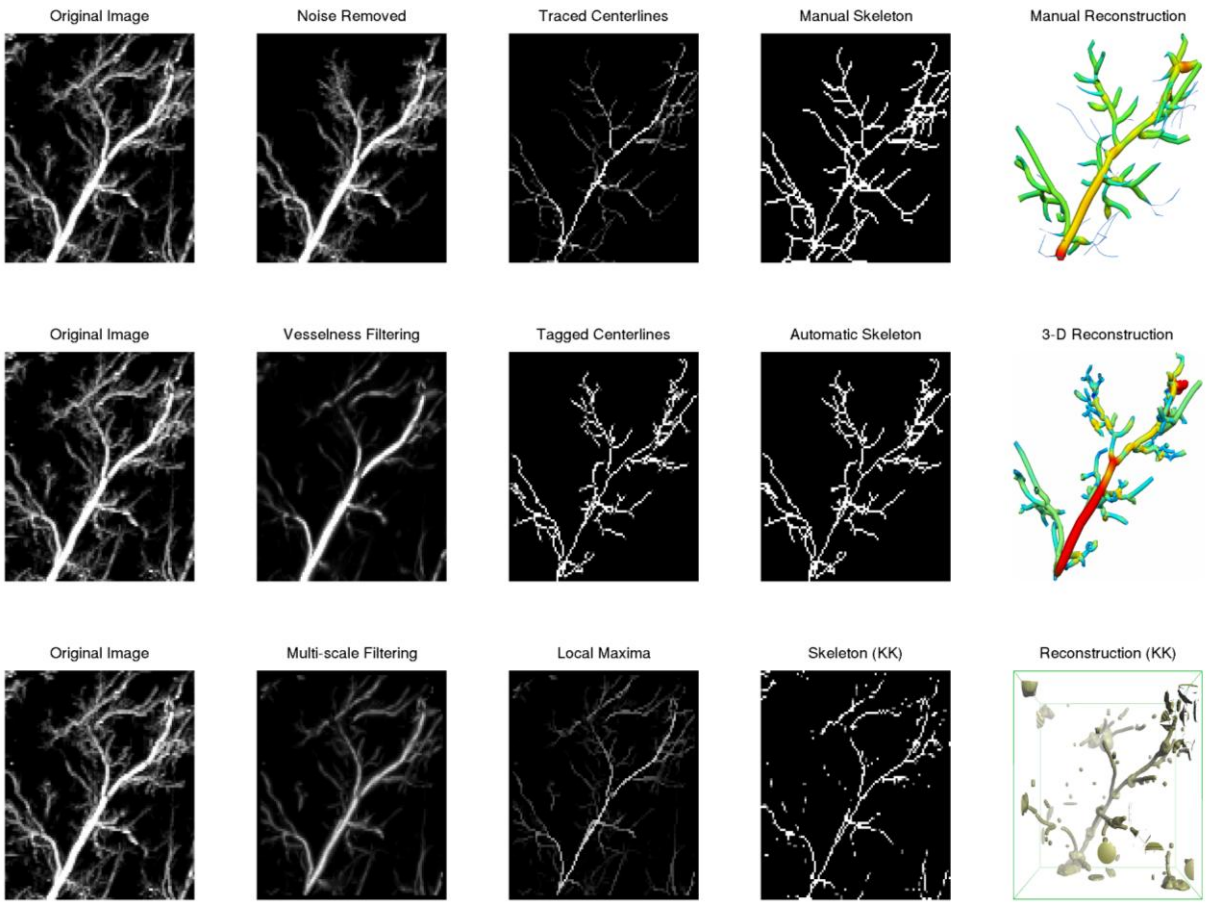


Figure 4.4: Comparison of the vessel detection of Krissian's (KK) method (bottom row) with the method presented in this study (middle row) using manual segmentation as the gold standard (top row).

	Krissian's method	Method presented in this study
Number of positives	772	944
Number of negatives	599228	599056
Number of false positives	552	279
Number of false negatives	1067	622
Number of true positives	220	665
Number of true negatives	598161	598434
Accuracy	0.9973	0.9985
Specificity	0.9991	0.9995
Negative predictive value	0.9982	0.9989
Sensitivity	0.1709	0.5167
Positive predictive value	0.2849	0.7044

Table 4.1: Results of the voxels classified in the vessel detection by the previous (Krissian et al. 2000) and presented methods. Only voxels in the vasculature skeleton (fourth column of Fig. 4.4) have been used to calculate the values in this table. The proposed method in this thesis has higher positive predictive value, negative predictive value, sensitivity, specificity, and accuracy than Krissian's method for vascular extraction from cryomicrotome images.

4.3.2 Simulated Phantom Validation of Radius estimation

Earlier on in chapter 3 of this thesis, the FWHM measure was tested on vessels oriented perpendicular to the imaging plane (FWHMrawPerp as defined earlier in section 4.1.1), however, this section demonstrates results of radius estimation tests on vessels oriented obliquely to the imaging plane at several angles from the cutting surface.

To compare the performance of the proposed novel model-based template-matching method with previous methods of vessel radius estimation, vessels of ten different radii (r = 5 to 50 voxels with step-size of 5 voxels) were each simulated at 15 different angles (θ = 15° to 85° with step-size of 5°) from the x-y or imaging plane (refer to Fig. 4.3). Fig. 4.5 shows the middle-size (r = 25 voxels) vessel at the largest (θ = 85°) and smallest (θ = 15°) angles, corresponding respectively to the closest to perpendicular and closest to parallel with respect to the x-y, imaging, or cutting plane. A green circle is shown superimposed on the vessel cross-sections as an approximate circle whose radius is the average distance from the vessel centerpoint to the boundary points to visually demonstrate the non-circularity of vessel cross-sections at increasingly smaller angles.

As illustrated in the graph of Fig. 4.6, the smaller the angle, the more inaccurate the vessel measurement is with FWHM (all four implementations of FWHM defined in section 4.1.1 are tested in Fig. 4.6) and other radii-estimation methods in the original cross-sectional image and image interpolated from the 3D vessel volume to be a cross-sectional slice perpendicular to the vessel cylinder's long axis. Fig. 4.6 illustrates the comparison of the model-based template-matching radius estimation with three previous methods (explained later on in this section) for the vessel of radius r = 25 voxels performed on the raw simulated vessel cross-sectional image generated by convolving the vessel cylinder template with the tissue PSF (termed as

"Convolved" in Fig. 4.6 legend) and performed also on the deconvolved vessel cross-sectional image (termed as "Deconvolved" in Fig. 4.6 legend). Deconvolution was performed with iterative Richardson-Lucy restoration using the synthetically generated PSF.

The radius estimation is performed on both the original observed vessel cross-sectional image (termed as "Cross-section" in the legend of Fig. 4.6) and on the vessel cross-section interpolated from the 3D vessel volume image to be perpendicular to the vessel cylindrical long axis (termed as "Perpendicular Slice" in Fig. 4.6 legend). In comparison to the proposed model-based method, the three other radius estimation methods tested on the computer-generated simulated phantoms are detailed here below:

1. FWHM Method – All four implementations described earlier in section 4.1.1 are tested on both the raw and deconvolved versions of both the original cross-section and resampled perpendicular slice.
2. Boundary Distance – The vessel radius is approximated as the average distance of the vessel boundary (shown as dashed yellow line in Fig. 4.5) points from the vessel centerpoint (calculated as centre of mass of boundary points).
3. Theta Method – the vessel diameter *d* is calculated according to equation 4.5 shown below:

$$\theta = \arctan\left(\frac{|z_n - z_c|}{\sqrt{(y_n - y_c)^2 + (x_n - x_c)^2}}\right)$$
$$d = d'(\sin\theta) \qquad (4.5)$$

Where, *d'* is the diameter observed in the raw vessel cross-sectional image in Fig. 4.3. The angle θ is the angle of the vessel axis from the imaging plane, and it can be estimated from the vessel segment's start and end node coordinate points (as illustrated in Fig. 4.3). The boundary-distance radius x 2 is used as the observed diameter *d'*.

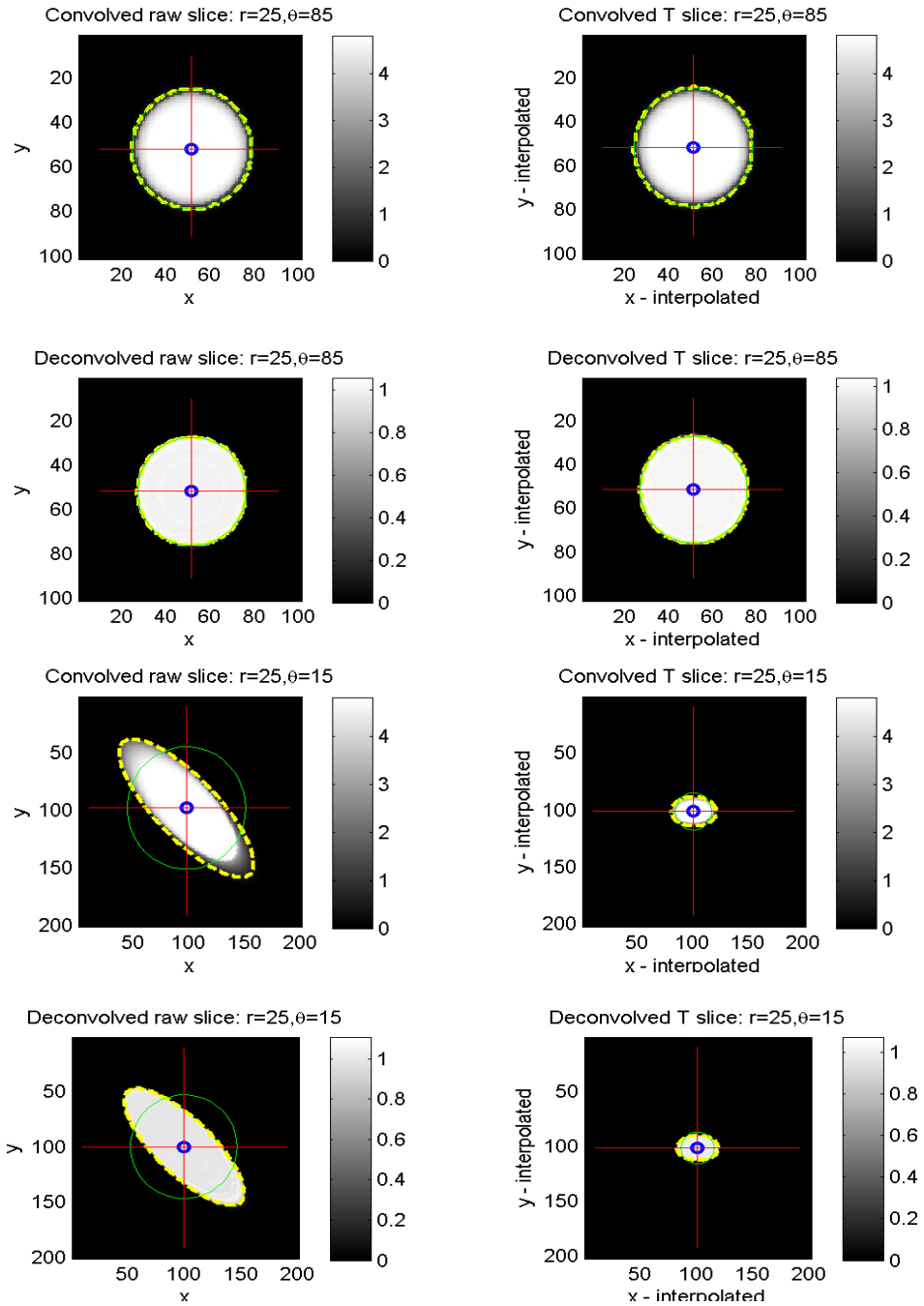


Figure 4.5: The cross-sectional images of a simulated vessel cylinder model of radius = 25 voxels for two different angles (measured from the image or *x*-*y* plane as shown in Fig. 4.3). The vessel cross-sectional image slice (denoted as "Convolved raw slice") is shown along with the perpendicular cross-sectional image slice, which is interpolated from the 3D vessel volume to be perpendicular to the cylinder's long axis (denoted as "Convolved T slice"). Deconvolution of the original cross-sectional image slice (denoted as "Deconvolved raw slice") and of the interpolated perpendicular cross-sectional image slice (denoted as "Deconvolved T slice") are shown also. "Convolved" means pre-deconvolution and "Deconvolved" means post-deconvolution; "Raw" means "original cross-section"; "T" means "resampled perpendicular slice". FWHM measured on the "Convolved raw slice" is equivalent to FWHMrawOrig; FWHM measured on the "Convolved T slice" is equivalent to FWHMrawPerp; FWHM measured on the "Deconvolved raw slice" is equivalent to FWHMdecOrig; and FWHM measured on the "Deconvolved T slice" is equivalent to FWHMdecPerp (defined in section 4.1.1). Vessel centerpoint (blue circle), intensity line profiles across which FWHM was measured (red lines), boundary of the vessel cross-section (yellow line), and the average radius of the vessel boundary (green circle) are shown also.

The radius estimation is performed four times with each of the first two methods (FWHM and boundary distance): on the original raw vessel cross-section (FWHMrawOrig), on the interpolated perpendicular vessel cross-section (FWHMrawPerp), on the deconvolved raw vessel cross-section (FWHMdecOrig), and on the deconvolved interpolated perpendicular vessel cross-section (FWHMdecPerp) – implementations defined earlier in section 4.1.1. The theta method works only on the raw vessel cross-section and does not work on an interpolated slice perpendicular to the vessel axis. The theta method is thus performed only two times: on the original raw vessel cross-section and on the deconvolved raw vessel cross-section.

From Fig. 4.6, we observe that deconvolution hardly changes the results in the radius estimation for the FWHM method (i.e. FWHMrawOrig ~= FWHMdecOrig and FWHMrawPerp ~= FWHMdecPerp). Additionally, measuring radii on the interpolated slice perpendicular to the vessel axis results in more accurate radii estimates (i.e. FWHMrawPerp and FWHMdecPerp are more accurate than FWHMrawOrig and FWHMdecOrig), as expected. However, the FWHM radius measure (FWHMdecPerp) performed on the interpolated cross-section perpendicular to the vessel long axis is still far from the actual radius even after vessel deconvolution with Richardson-Lucy restoration. Except for the novel model-based template-matching, all previous methods fail to accurately estimate the vessel radius and their error increases as the angle of the vessel from the cutting or imaging plane decreases. This is expected because the closer to parallel a vessel is to the imaging plane, the more out-of-focus light from the vessel below the surface will obscure the image captured. This simulation demonstrates that the model-based template-matching method consistently offers a more accurate estimation of vessel radii regardless of the size or orientation of the vessel.

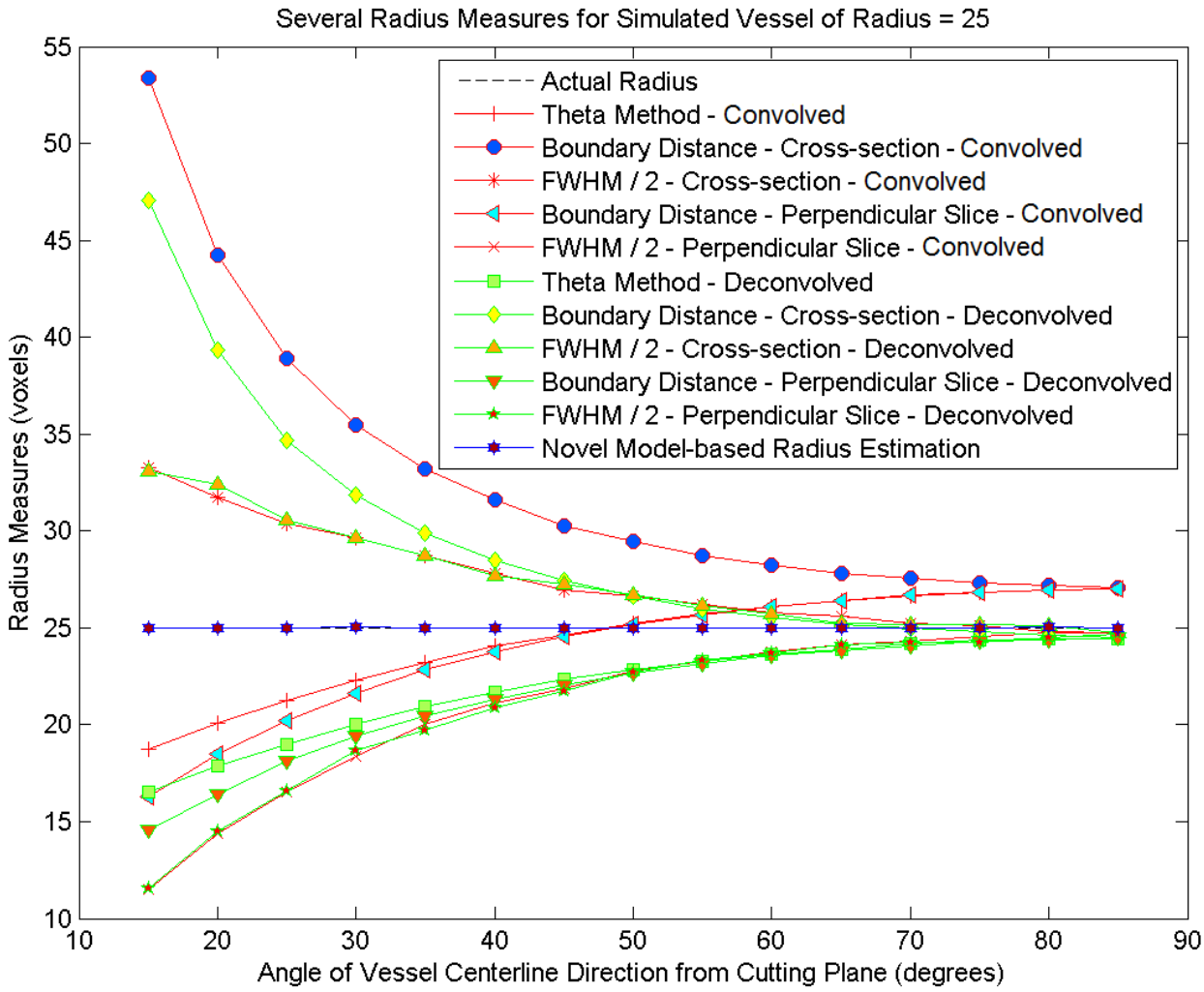


Figure 4.6: Radius estimation methods performed on the "Convolved" (original simulated vessel image produced by convolving a vessel cylindrical template with the tissue PSF model) and the "Deconvolved" (simulated convolved vessel image deconvolved with Richardson Lucy restoration using the same tissue PSF) for both the "Cross-section" (original image vessel-cross sectional slice) and the "Perpendicular Slice" (vessel cross-sectional image interpolated from the 3D vessel volume to be perpendicular to the vessel cylinder's long axis). "FWHM / 2 – Cross-section – Convolved" is equivalent to FWHMrawOrig / 2; "FWHM / 2 – Perpendicular Slice – Convolved" is equivalent to FWHMrawPerp / 2; "FWHM / 2 – Cross-section – Deconvolved" is equivalent to FWHMdecOrig / 2; and "FWHM / 2 – Perpendicular Slice – Deconvolved" is equivalent to FWHMdecPerp / 2 (defined in section 4.1.1). The FWHM provides a diameter measure, and so FWHM / 2 gives the vessel radius.

4.3.3 Ground Truth Validation of Radius estimation

To provide a comparison and metric of performance for vessel radius measurement, the proposed model-based method was validated on artificial vessel phantoms embedded in gel and imaged with the cryomicrotome against the FWHM radius estimation method (all implementations defined in section 4.1.1 tested herein), a standard technique for vascular measurement. The artificial vessel phantoms were used to evaluate the validity of vessel radius

measurement using implementations of the current state-of-the-art FWHM method prior to and after image deconvolution and the proposed model-based method. The measurements with FWHM on the raw and deconvolved vessel images and with the model-based method are presented in section 4.3.3.3.

4.3.3.1 Validation Methods – FWHM Vessel Estimation

The implementations of the FWHM method tested in this vessel radius estimation validation study are outlined earlier in section 4.1.1. The four implementations of the FWHM method tested were as follows – FWHMrawOrig on the raw original cross-sectional image, FWHMrawPerp on the raw resampled perpendicular slice, FWHMdecOrig on the deconvolved version of the original cross-sectional image, FWHMdecPerp on the deconvolved version of the resampled perpendicular slice.

4.3.3.2 Validation Data – Artificial Vessel Phantoms

In the validation study, artificial vessel phantoms were used since the shape of the structures was known and microscope measurements were available as the gold standard. For validating radius estimation on the cryomicrotome imaging modality there is no better alternative to inserting artificial vessel-like tubular cylinders of fluorescent cast hardened and measured with a microscope prior to being embedded in the gel and frozen and imaged. However, given the similarity of this preparation we believe the phantom data we have used are both sufficient and relevant for radius estimation validation in that they are of comparable size to the vessels and are composed of the same hardened fluorescent cast just as the coronary arteries visualized in the images.

Cryomicrotome images of three embedded fluorescent cylinders (Rolf et al. (2008)) of known diameter (measured using a microscope) were used as the artificial vessel phantoms to evaluate the validity of vessel radius measurement. Three artificial vessels of diameters 510

± 10 μm (5.1 ± 0.1 voxels), 300 ± 40 μm (3.0 ± 0.4 voxels), and 170 ± 10 μm (1.7 ± 0.1 voxels) were embedded in a tissue-mimicking gel and sliced and imaged with the cryomicrotome at 50-μm^3 voxel size (cross-sectional images of the vessels shown in Fig. C.3 in Appendix C).

4.3.3.3 Validation Results – Vessel Radius Measurement

The radii measurements of the three artificial embedded vessels are shown as box plots in Fig. 4.7. The deconvolution was performed with the PSF fitted to microspheres embedded in the same gel as the artificial vessels with attenuation coefficient $\mu_{ex} = \mu_{em} = 0.0022\ \mu m^{-1}$, as obtained by Rolf et al. (2008). The deconvolution method was Richardson-Lucy and the PSF model was the one presented in equation (2.6).

The results show that for saturated vessels (e.g. the large vessel) the Richardson-Lucy deconvolution causes the vessel radius to be underestimated with the FWHM measurement (FWHMdecOrig and FWHMdecPerp). This matches the vessel phantom prediction in Appendix C, in which Fig. C.2 illustrates the deconvolution of the saturated image of an oblique vessel phantom. The obliqueness coupled with the saturation results in an inaccurately shortened vessel cross-sectional profile after deconvolution, and hence FWHM (FWHMdecOrig and FWHMdecPerp) underestimates the vessel size. FWHM works better for the small non-saturated vessels, particularly when measured in the resampled plane perpendicular to the vessel axis after deconvolution (FWHMdecPerp). However, for large vessels, over exposure causes pixel saturation and loss of data, and the deconvolution can result in *hole-effects* (see Figs. C.1-2 in Appendix C) and inaccurate vessel measurement. The model-based method produces the best results irrespective of the size of the vessel, with the simulation of all aspects of the image acquisition process.

As observed in Fig. 4.7, the reliability of the FWHM method (all implementations) is affected by the size of the vessel and voxel intensity saturation, which can result in under- or over-estimation of the vessel radii. Even after deblurring the images, the FWHM method (FWHMdecOrig and FWHMdecPerp) fails to accurately estimate vessel radii for all three sizes in Fig 4.7. On the other hand, the novel model-based template-matching method does not require deconvolution as it accounts for the blurring in its vessel model and it results in the least error in radius for all three vessel sizes. In conclusion, the model-based method consistently gives accurate radii estimates robust to the vessel size and voxel intensity saturation.

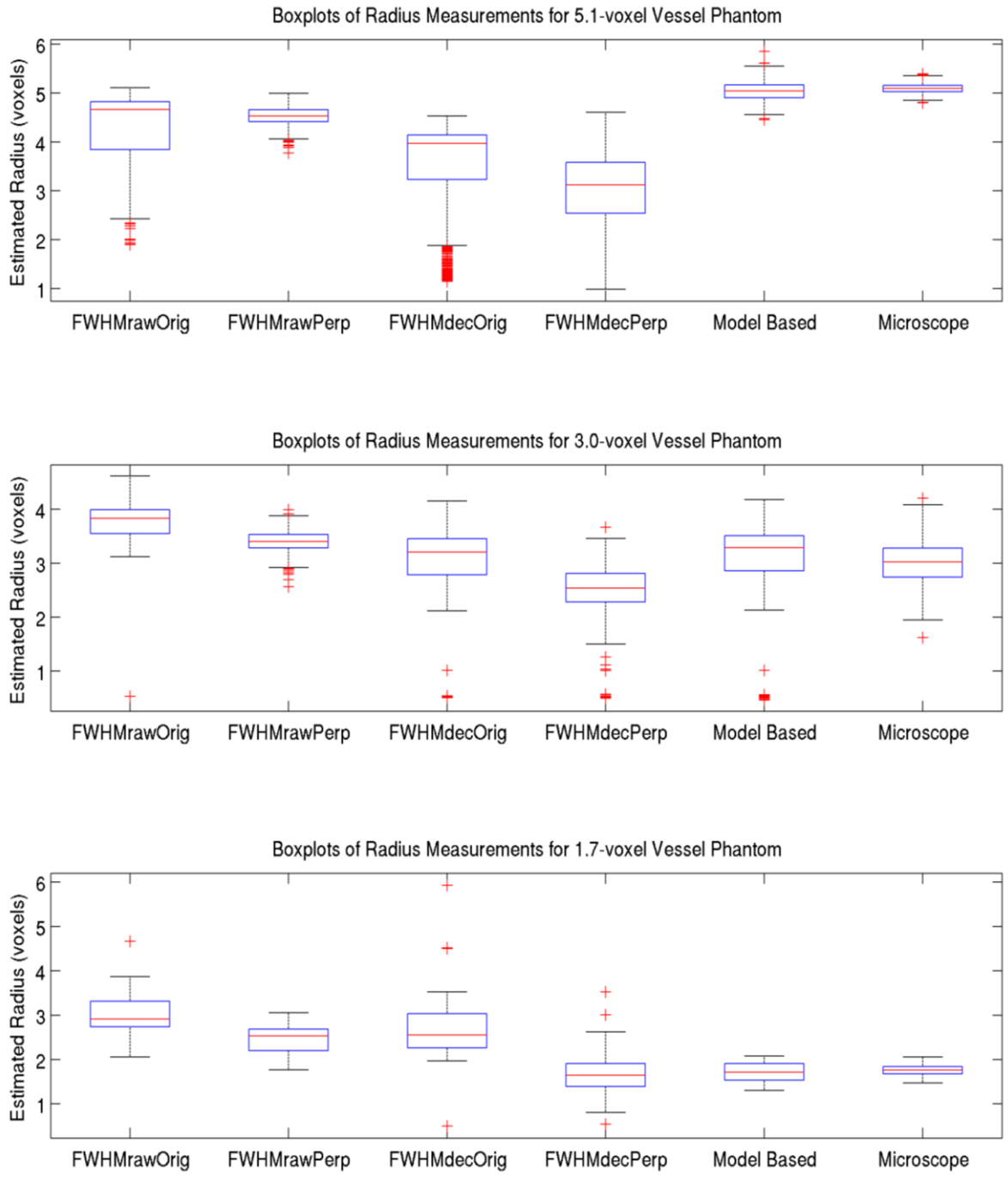


Figure 4.7: Boxplots of the diameter measurements of three vessel sizes (5.1 voxel vessel in top figure, 3.0 voxel vessel in middle figure, and 1.7 voxel vessel in bottom figure). The vessel size estimation methods compared are the model-based template-matching method presented in the study and FWHM (four implementations of the FWHM method as follows – FWHMrawOrig on the raw original cross-sectional image, FWHMrawPerp on the raw resampled perpendicular slice, FWHMdecOrig on the deconvolved version of the original cross-sectional image, FWHMdecPerp on the deconvolved version of the resampled perpendicular slice). The microscope measurements are used as the gold standard for measurement validation of the other methods. Due to errors in the manufacturing process, the 3.0 voxel artificial vessel actually had much rougher edges and consequently a much larger variation (four times larger standard deviation) in its radius (300 ± 40 μm) as measured by the microscope as opposed to the 1.7 voxel (170 ± 10 μm) and 5.1 voxel (510 ± 10 μm) vessels.

4.3.4 Preciseness of Radius estimation

For microvessels of size 2 voxels or less, subvoxel measurement inaccuracy can produce significantly incorrect radius estimation results. To gauge the preciseness of the radius estimation, and its robustness to partial volume effect and to assess the limitations of vessel radius measurement of microvessels, this section compares the radius estimation of vessels from a low resolution image volume (0.83 mm voxel resolution) and a high resolution image volume (0.23 mm voxel resolution) of the porcine heart cryomicrotome dataset. The vessel node points of the low resolution dataset were scaled to match the high resolution dataset node points, and no registration was required since the two datasets are naturally aligned. The maximum intensity projections of the two image volumes are shown in Fig. 4.8.

From Fig. 4.9, we can observe that the radius estimation is robust to the change in resolution; also, we see that vessels smaller than 1 mm have larger error difference between low and high resolution as compared to vessels larger than 1 mm. This is expected because the lower resolution image volume's voxel resolution is 0.83 mm / voxel, which means that in the lower resolution image volume data vessels smaller than 0.83 mm will be highly affected by partial volume effect, which affects both the radii estimate calculated by the FWHM (FWHMrawPerp) and the radii estimate optimized by the model-based template matching method. However, vessels that are larger than the voxel resolution limit of 0.83 mm / voxel, are quite well matched in their estimated radii from both low and high resolution image volume datasets. Fig. 4.10 shows the histograms of the difference $|r_{hi} - r_{lo}| / r_{hi}$ in radii measured from the low resolution and high resolution images with the model-based method. We see that there are a larger number of smaller vessels (< 1 mm) with a larger difference in radii between low and high resolution data than bigger vessels (> 1 mm). Finally, Fig. 4.11 plots the histograms of the vessel radii measured from both low and high resolution datasets,

from which we see that the difference is larger for smaller vessels and the lower resolution dataset overestimates smaller vessels in comparison to the higher resolution dataset. This overestimation is due to the poorer voxel resolution in the lower resolution dataset, due to which a vessel of subvoxel size will appear as a full voxel or more in the image.

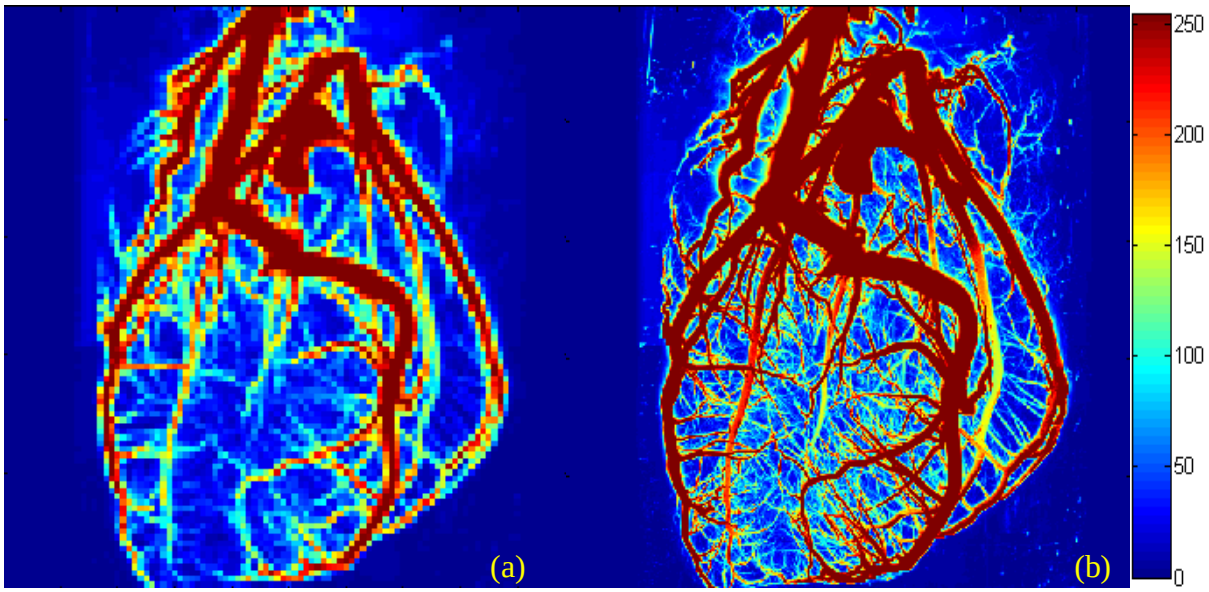


Figure 4.8: Two different maximum intensity projections of the (a) low resolution (0.83 mm voxel resolution) and (b) high resolution (0.23 mm voxel resolution) cryomicrotome image volume of the porcine heart (8-bit intensity).

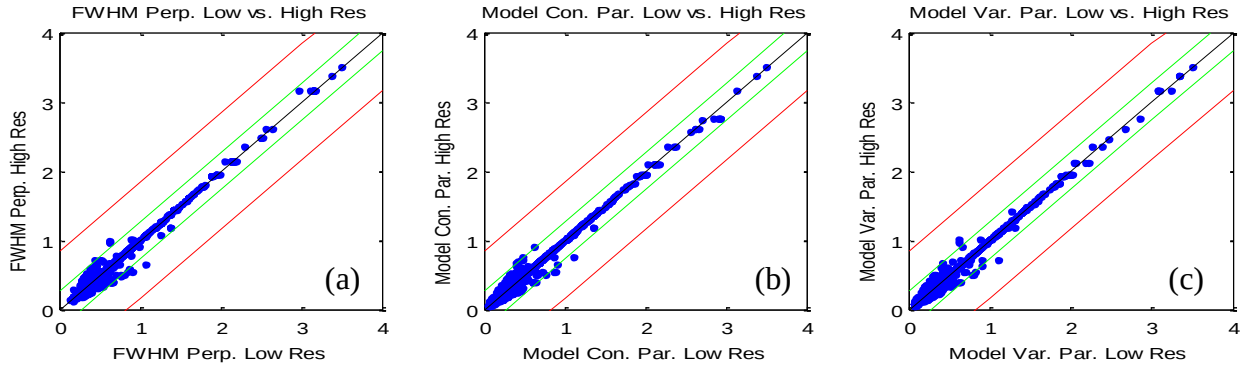


Figure 4.9: Matched vessel radii (mm) measured with FWHM (FWHMrawPerp) in perpendicular slice (a) and model-based with constant (b) versus varying (c) optical parameters, measured from both the high and low resolution image volumes. The central black line represents a perfect match. The inner green lines enclose a difference of one high resolution voxel and the outer red lines enclose a difference of one low resolution voxel.

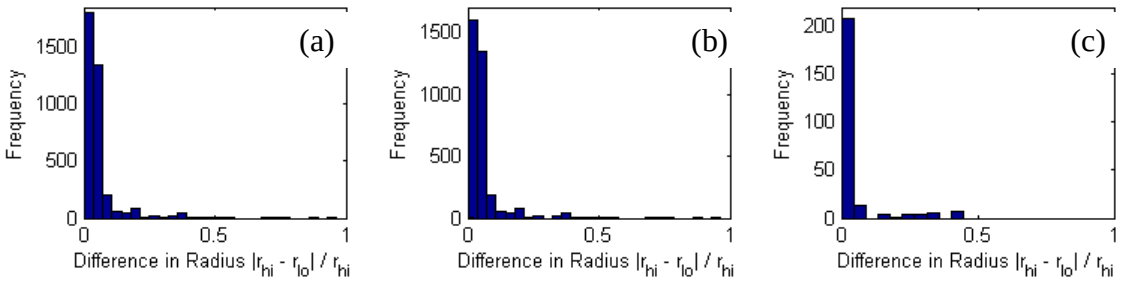


Figure 4.10: Histograms of the difference in radii measured from the low resolution and high resolution images, shown for all the vessels (a), for vessels smaller than 1 mm in radius (b), and for vessels larger than 1 mm in radius (c). The method for radius estimation is model-based template-matching (constant optical parameters) for this figure.

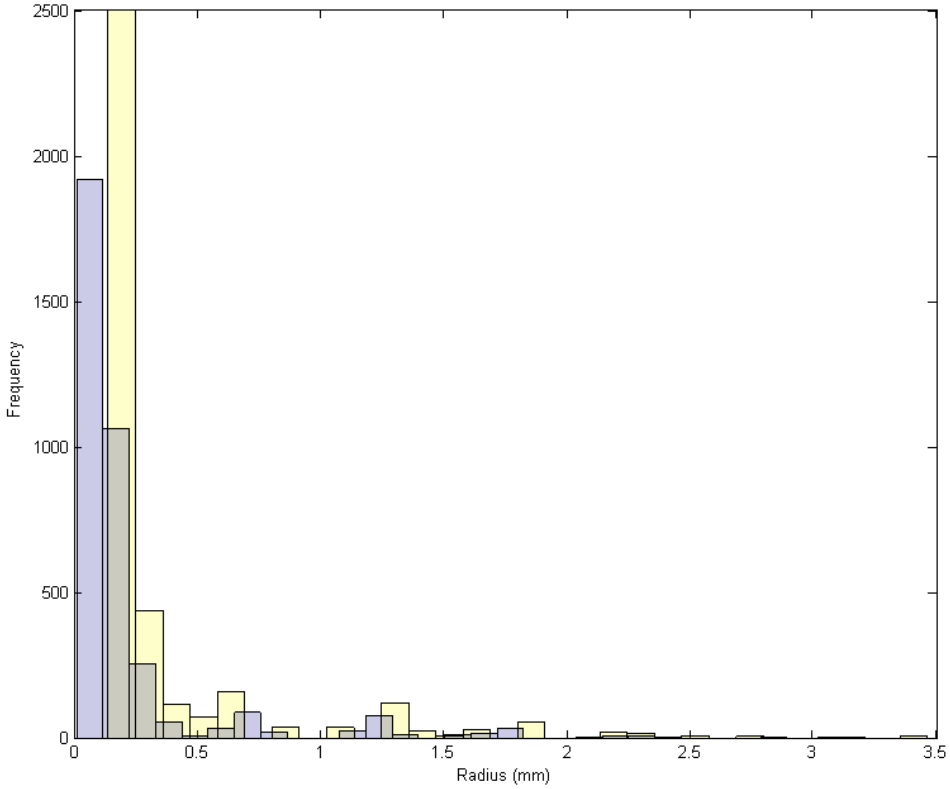


Figure 4.11: The histogram plot shows superimposed histograms of the matched corresponding vessel radii measured from both the low resolution (yellow histogram bars) and high resolution (blue histogram bars) image volumes. The method for radius estimation is model-based template-matching (constant optical parameters) for this figure.

4.3.5 Sensitivity Analysis of Radius estimation

This section assesses the effect of incorporating the optical tissue properties and their intramural spatial variation in the measurement of tissue-embedded vessels in the cryomicrotome images. The model-based radius estimation was performed in two cases – 1)

with constant optical parameters (mean values of the attenuation coefficient distributions plotted in Chapter 3) and 2) varying optical parameters (measured from microspheres embedded throughout the tissue). The model-based radii estimates with constant and varying parameters are compared directly in a scatter plot in Fig. 4.12 (a). Smaller vessels were more sensitive to spatially varying optical tissue parameters showing larger differences in estimated radius. This suggests the need to measure spatial variation in optical tissue parameters for accurate radius estimation of small vessels (< 10 voxels in radius). The difference between the constant versus spatially varying optical tissue parameter cases of the model-based radii was at the sub-voxel level for 90.29% of the measurements. For smaller vessels the sub-voxel error becomes much more significant than for larger vessels.

4.3.5.1 Sensitivity Map of Radius Estimation to Regional PSF Parameterization

The sensitivity of radii estimates to the model-based method's regional parameterization of the PSF using microsphere images is hereby visually illustrated on the reconstructed vasculature. To quantitatively visualize the effect of regional variation in optical parameters, the coronary vasculature was coloured in Fig. 4.13 according to the percentage difference in between model-based radius estimates for the constant versus varying optical parameters, calculated as $100 * |r_{Con} - r_{Var}| / r_{Var}$. This percentage difference is plotted against vessel radius in Fig. 4.12(b). The percentage difference increases as vessel size decreases.

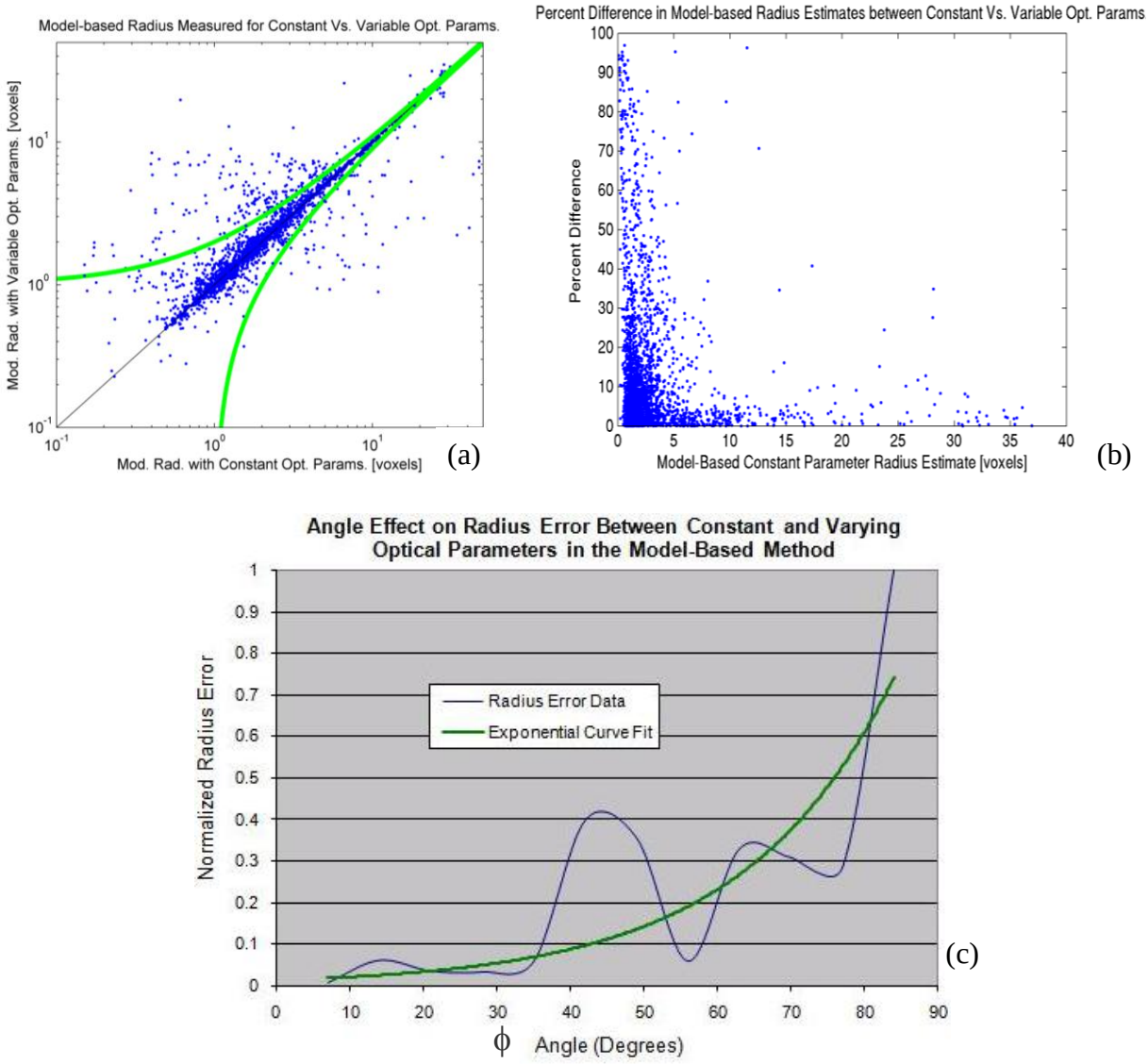


Figure 4.12: (a) Comparison of the model-based radius estimation with varying versus constant optical parameters. The radii are plotted in voxels and the green lines represent a difference of one voxel. (b) Percent difference in model based radii estimates between constant and variable optical parameters plotted against the model based radius estimate for the vessel using constant parameters. Note: only differences between methods are shown, not which is more accurate. These radius estimates are for constrained bounded optimization. For unconstrained unbounded radius estimation results, see Appendix E. (c) Effect of the vessel branch's angle (measured from the *z*-axis) on the error difference between the constant and varying optical parameter cases in the model-based radii estimates shown in the graph of the normalized radius error between the two cases plotted against the angle of the vessel branch from the *z*-axis. The angle plotted on the x-axis of graph (c) in this figure is $\phi = 90° - \theta$. The angle θ discussed earlier in the main text is the vessel branch's angle from the imaging plane as shown in Fig. 4.3 and the angle plotted on the x-axis of graph (c) in this figure is ϕ, which is measured from the z-axis, and is thus equal to $90° - \theta$.

The graph in Fig. 4.12 (c) shows that the angle of the vessel branch has a definite effect on the error difference in between the radius estimates calculated with the constant versus varying optical parameters in the model-based method. For vessels oriented at a small angle from the *z*-axis, the vessel is almost perpendicular to the imaging plane and thus there is less out-of-focus light from below the surface and consequently a smaller error difference between the constant and varying optical parameter cases of the model-based method. For vessels oriented at a large angle from the *z*-axis, the vessels become more in-plane or parallel with respect to the image plane and thus there is more out-of-focus light from below the surface and consequently a larger error difference between the constant and varying optical parameter cases of the model-based method. At an angle of 0° from the *z*-axis, the vessel would be perfectly perpendicular to the imaging plane and the out-of-focus light on the imaging plane from the fluorescent cast in the vessel below the surface would be very low, resulting in lower radius error. Conversely, at an angle of 90° from the *z*-axis, the vessel would be running completely in-plane or parallel with the imaging plane, and the out-of-focus light on the imaging plane from the fluorescent cast in the vessel would be much higher, resulting in higher radius error. So as the angle of the vessel branch from the z-axis increases, the radius error increases. Vessel branches were binned into 12 intervals of angles and the maximum absolute error difference in between the radii estimates of the constant and varying cases in each interval was used in order to measure the worst-case possible radius error for each interval of the angles.

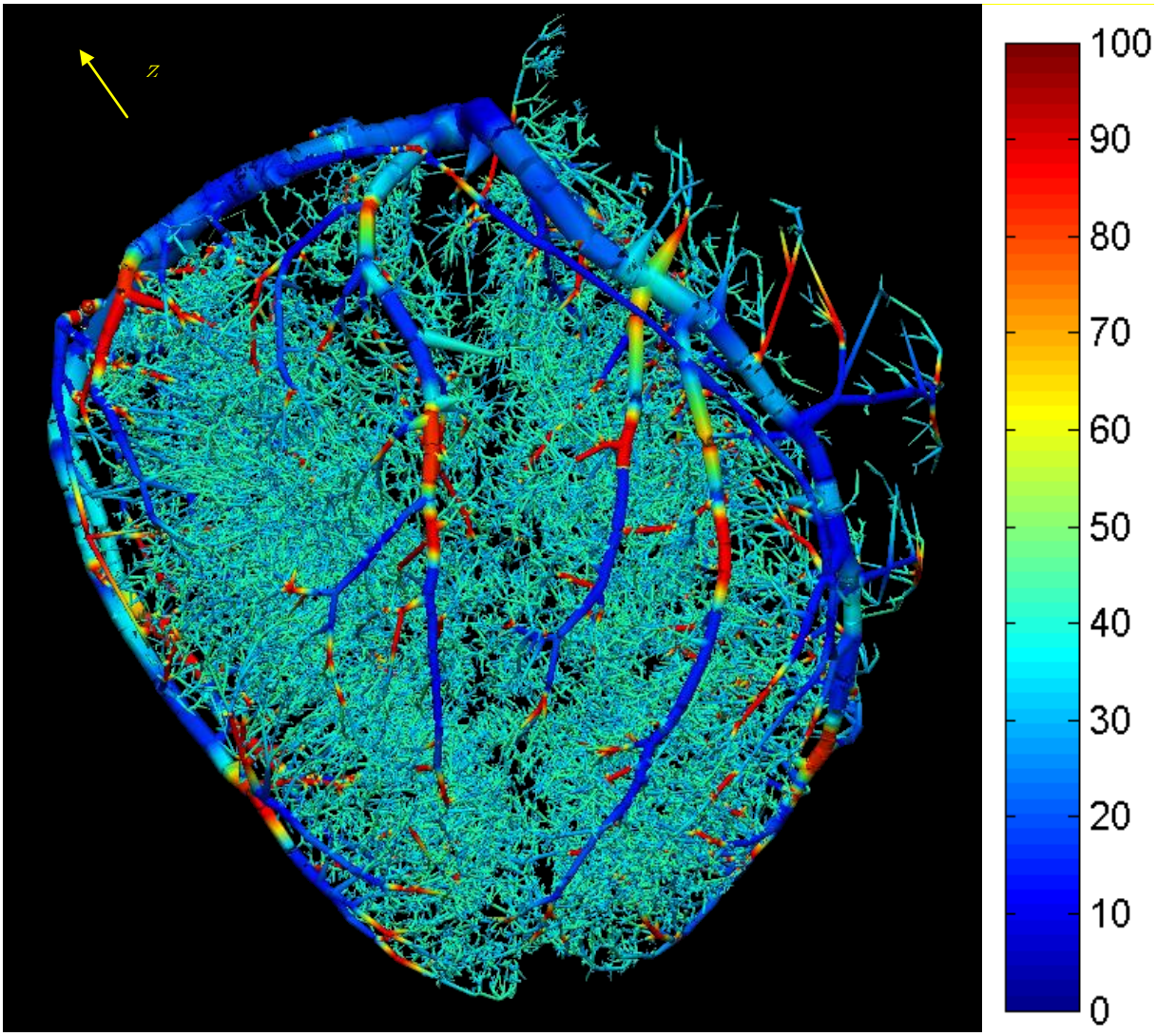


Figure 4.13: 3D reconstruction of the porcine coronary vasculature coloured by percentage difference between model-based radii estimates for constant versus varying optical parameters. Absolute percentage difference colour mapping defined in spectral colour bar. Difference error value range is from 0-100%. The effect of the vessel branch's angle on the error difference in between the radii estimates obtained with the constant versus varying optical parameters in the model-based method is shown in Fig. 4.12 (c).

4.3.5.2 Optical Parameter Variation over Distance in Tissue

As observed in Fig. 4.12, at the subvoxel level, the radius measure was sensitive to variation in optical parameters estimated from microspheres embedded in the pig heart. To visualize the variation in optical parameters over distance in the tissue, the difference in the parameter values measured from distinct microspheres plotted against the distance between the microspheres is shown in Fig. 4.14. Microspheres located nearer to each other had more similarity in the measured parameter, suggesting local regional variation in intramural optical properties. The effect this variation has on the radius estimation is discussed next.

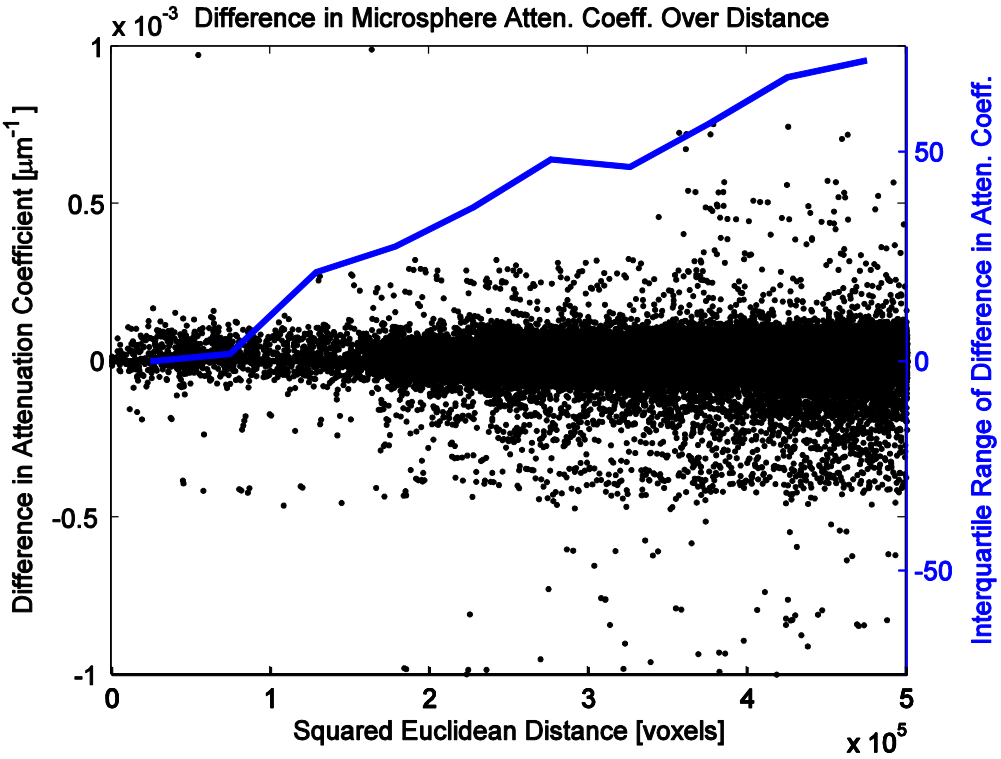


Figure 4.14: Variation over distance in excitation attenuation coefficient measured from microspheres embedded in the porcine myocardium. Each data point depicts the difference in the parameter value measured from two distinct microspheres plotted against the distance between the two microspheres. Also shown is the interquartile range of the difference in the parameter plotted over distance.

4.3.5.3 Sensitivity of Radius Estimation to PSF Parameters

In Fig. 4.15, the radii estimates obtained with the model-based method with different parameter settings in the PSF model — constant versus variable attenuation coefficients, single ($\mu_t = \mu_{ex} = \mu_{em}$) versus separate attenuation coefficients for excitation (μ_{ex}) and emission (μ_{em}), constrained versus unconstrained estimation — are compared directly with each other. The error between FWHM (FWHMrawPerp) and model-based radii estimates is larger than the error in model-based radii due to uncertainty in the parameters. The sensitivity of a blood flow simulation to errors in the vessel radii estimates originating from uncertainty in the optical PSF parameters is discussed in chapter 5 in the section entitled "Radius Measure Accuracy".

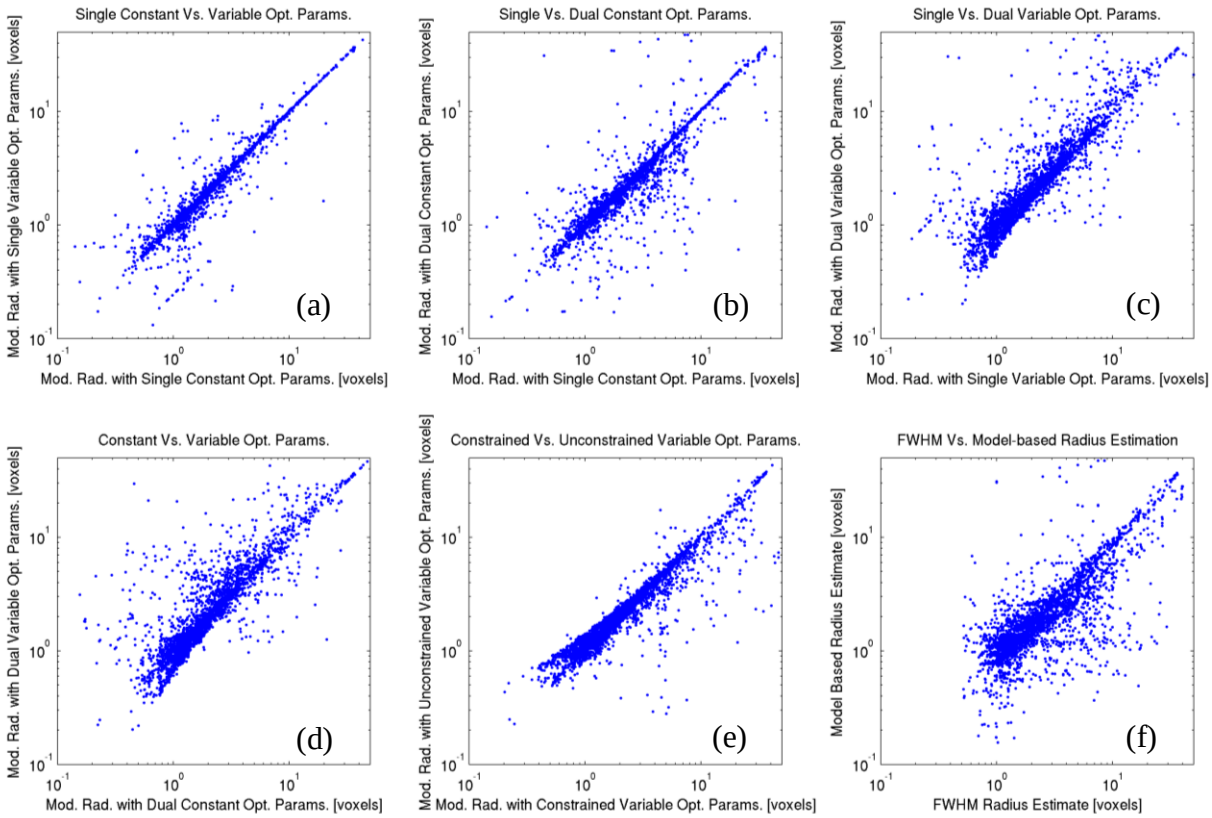


Figure 4.15: (a) Direct comparison of vessel radii estimated with a single ($\mu_t = \mu_{ex} = \mu_{em}$) constant versus variable optical parameter, (b) single (μ_t) versus dual (μ_{ex} and μ_{em}) constant optical parameters in the PSF model, (c) single versus dual variable optical parameters, (d) constant versus variable optical parameters, (e) constrained versus unconstrained parameters, (f) direct comparison of the FWHM (FWHMrawPerp) method radii estimates with the model-based radii estimates.

4.3.5.4 Partial Volume Effect on Radius Sensitivity to Optical Parameter Variation

To test the sensitivity of radius estimation to optical parameter variation in the presence of partial volume effect, the model-based radius estimation was performed on downsampled datasets, as shown in Fig. 4.16. The standard deviation of the difference in model-based radii-estimates for constant versus spatially varying optical properties was 0.1691 voxel for lower resolution (voxel size of 0.83 mm) image data and 0.0058 voxel (voxel size of 0.23 mm) for higher resolution image data. The estimated radius differs much more between the constant and varying parameter cases for lower resolution and in particular for smaller vessels. Smaller vessels (in both the high and low resolution data, but more so in lower resolution image data) are more sensitive to spatially varying optical tissue parameters. The partial volume effect increases the sensitivity of radius estimation to the variation of the optical parameters. This suggests the need to measure spatial variation in optical tissue parameters for accurate radius estimation of small vessels (< 1 mm in radius). The difference between the constant versus spatially varying optical tissue parameter cases of the model-based template-matching radius estimation methods is at the sub-voxel level (this is significant for small vessels). For the measured vessel radii, in the low resolution plot the difference is less than one low resolution voxel (0.83 mm) for all points apart from five outliers, and in the high resolution plot the difference is less than one high resolution voxel (0.23 mm) for all points apart from two outliers.

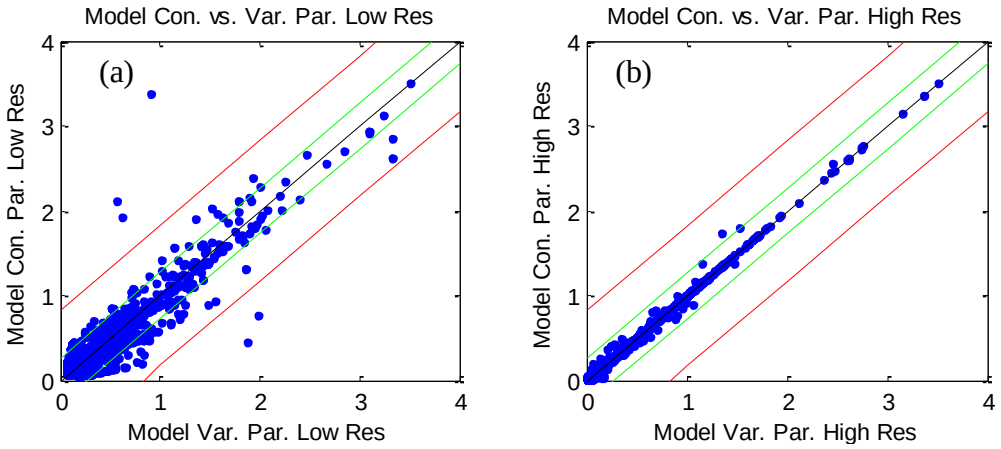


Figure 4.16: The two plots ((a) is low resolution and (b) is high resolution) compare the model-based radius estimation with varying versus constant optical parameters. The radii are plotted in millimetres and the green and red lines enclose a difference of one high-resolution (0.23 mm) and one low-resolution (0.83 mm) voxel, respectively. Note: only differences between methods are shown, not which is more accurate.

4.3.6 Comparison of Radius estimation Methods

This section calculates the difference between radii estimates from separate methods and characterizes the error difference in between the methods according to vessel sizes and angles.

4.3.6.1 FWHM on Raw Original versus Interpolated Perpendicular Slice

Fig. 4.17 shows that FWHM results in radically different radii estimates when performed on the raw original cross-sectional slice (FWHMrawOrig) versus the interpolated perpendicular slice (FWHMrawPerp), and thus the method's ambiguity can result in disparate estimates. FWHM is not reliable because on the original raw cross-sectional slice (FWHMrawOrig) it is obscured by halo and on the interpolated perpendicular slice (FWHMrawPerp), it is still obscured by halo and also further introduces interpolation errors.

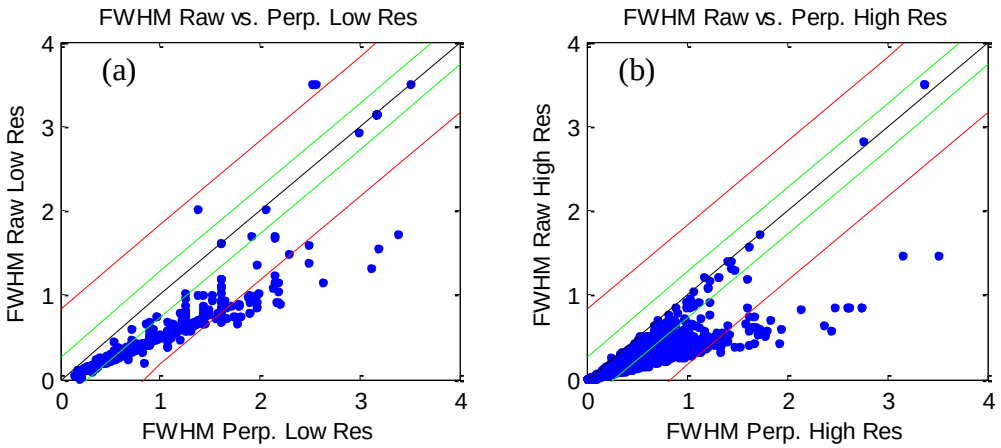


Figure 4.17: The two plots ((a) is low resolution and (b) is high resolution) compare the radius estimated with FWHM on a raw original vessel cross-section (FWHMrawOrig) versus on an interpolated vessel cross-section perpendicular to the vessel axis (FWHMrawPerp). The radii are plotted in millimetres and the green and red lines enclose a difference of one high-resolution (0.23 mm) and one low-resolution (0.83 mm) voxel, respectively.

4.3.6.2 FWHM versus Model-based Radii Estimates

Fig. 4.18 compares vessel radii estimated by the FWHM method (FWHMrawOrig and FWHMrawPerp) versus the model-based template-matching method for both a constant and spatially variant optical attenuation field. As expected, the FWHM calculated on the raw original cross-sectional image slice (FWHMrawOrig) has much larger variance from the model-based method than the FWHM calculated on the interpolated slice that is perpendicular to the vessel axis (FWHMrawPerp). This is expected because in the raw original cross-sectional slice, FWHM radii (FWHMrawOrig) measure is influenced by how much the vessel cross-section is obscured by the halo, which is directly affected by the angle and tilt of the vessel. FWHM calculated on the interpolated slice perpendicular to the vessel axis (FWHMrawPerp) naturally produces better radii estimates because the perpendicular slice has a circular cross-section that is visibly less influenced by the halo artefact (see Fig. 4.5 in section 4.3.2). However, FWHM radii estimates are still not completely accurate even on the perpendicular slice (FWHMrawPerp) because haze from below the surface will obscure the vessel cross-section even if it is visualized in a plane perpendicular to its vessel axis, since the

perpendicular slice itself is interpolated from the original raw image that is distorted with the out-of-focus light.

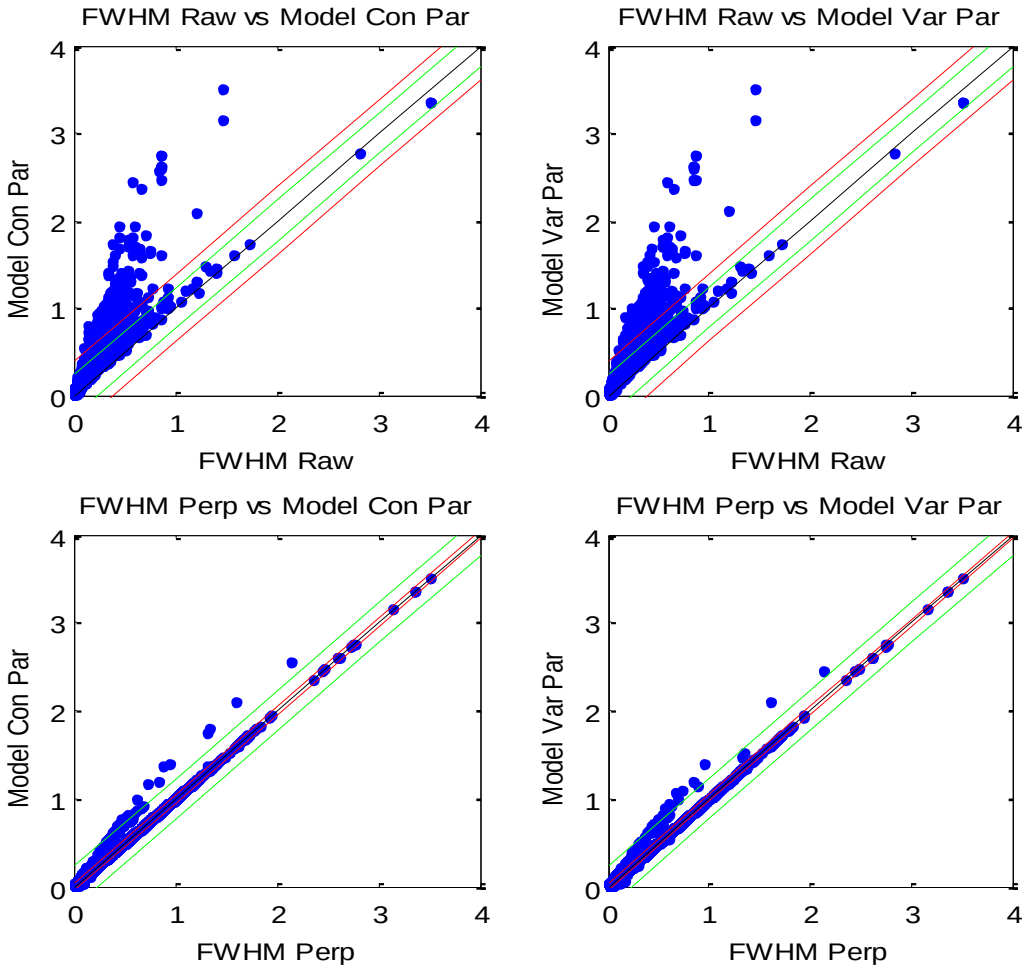


Figure 4.18: Comparison of the radius estimated by FWHM on a raw original vessel cross-sectional image slice (FWHM Raw = FWHMrawOrig) or on an interpolated image slice perpendicular to the vessel axis (FWHM Perp = FWHMrawPerp) with the radius estimated by model-based template-matching method with constant (Model Con Par) or varying (Model Var Par) optical tissue parameters. Radii measurements are plotted in units of millimetres. Red lines enclose a difference of 4σ (where σ is the standard deviation of the difference between the two methods), green lines enclose a difference of one voxel (0.23 mm), and the black line represents a perfect match between the two methods.

To visualize the disparity in radii estimates between the FWHM (FWHMrawPerp) and model-based methods, the difference was mapped onto the reconstructed vasculature. Using the radii estimates of vessels in the coronary vasculature model extracted and reconstructed from the porcine coronary vascular image dataset shown earlier in Fig. 4.2, the coronary vasculature

was coloured according to percentage difference between the FWHM radius estimate measured on the perpendicular resampled image (FWHMrawPerp) and model-based radius estimate (constant optical parameter case), as shown in Fig. 4.19. The percentage difference was calculated as $100 * |r_{FWHM} - r_{Model}| / r_{FWHM}$. This percentage difference is plotted against vessel radius in right panel of Fig. 4.20. The smaller vessels in general had a larger percentage difference between the FWHM (FWHMrawPerp) and model-based method in radii measure. Also, it can be observed that the vessels with a larger bias between the FWHM (FWHMrawPerp) and model-based radii estimates have a more oblique angle, tilted ($\theta < 45°$) as opposed to perpendicular ($\theta > 45°$), from the imaging plane (the plane perpendicular to the z-axis, the direction of which is shown as yellow arrow in Fig. 4.19). The least error in between the model-based and FWHM (FWHMrawPerp) radii estimates is when a vessel is perpendicular to the cutting plane ($\theta = 90°$) and the worst error is when a vessel is parallel to the cutting plane ($\theta = 0°$). This is because the FWHM (FWHMrawPerp) will give a more biased radii measurement for vessels at a highly oblique angle from the imaging plane because it does not account for the out-of-focus light from below (when the vessel is tilted or oblique) that distorts the vessel size by skewing the vessel cross-section. The model-based method incorporates the vessel's orientation into the radius estimation, and is thus not affected by the angle like the FWHM (FWHMrawPerp) method.

In order to directly compare the radii estimates measured with the FWHM (FWHMrawPerp) and model-based methods, all the vessel radii measurements are plotted as data points in a scatter graph in Fig. 4.20(a). As expected, the error increases as vessel size decreases.

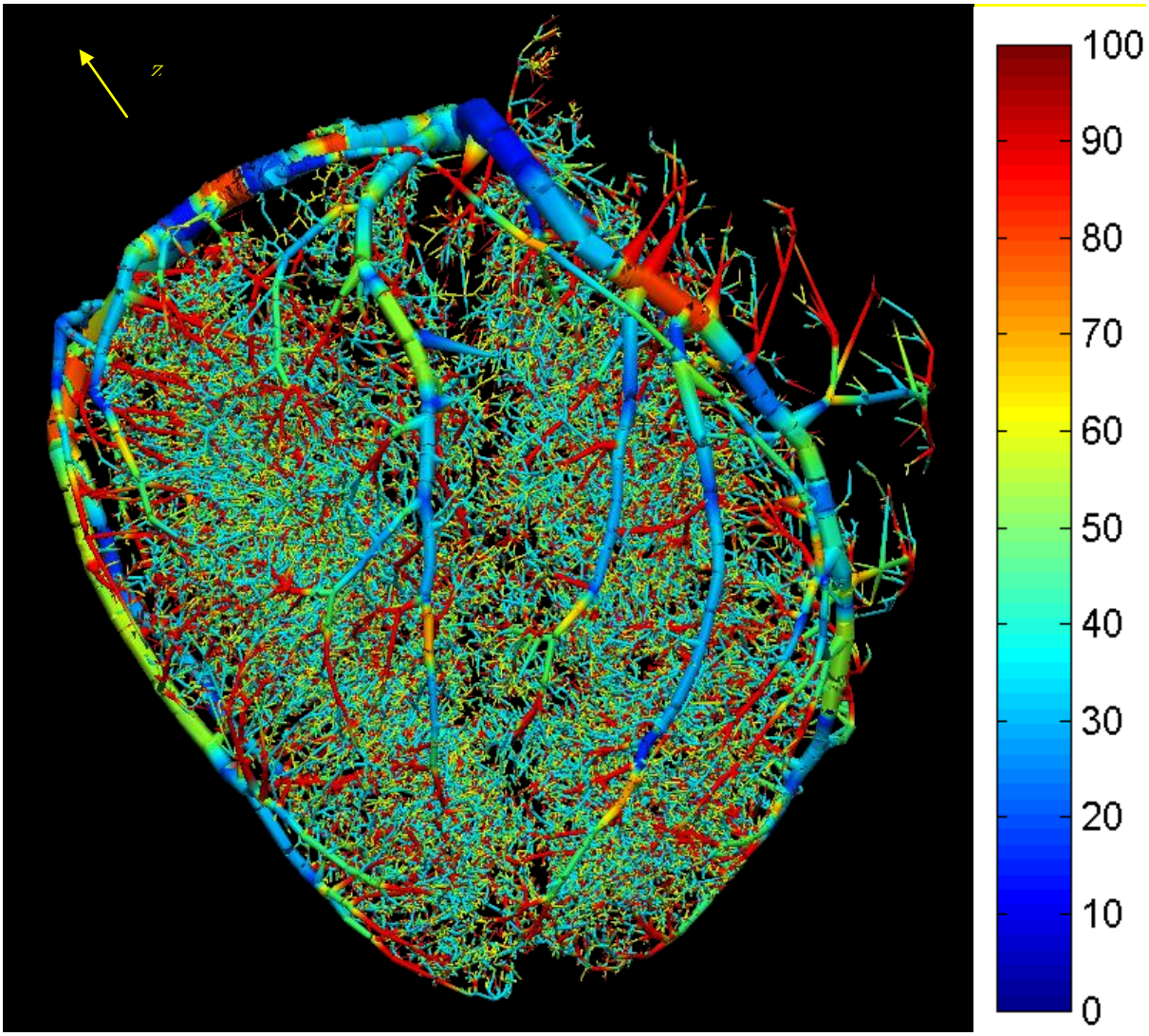


Figure 4.19: 3D reconstruction of the porcine coronary vasculature coloured by percentage difference between FWHM on vessel cross section in plane perpendicular to the vessel axis (FWHMrawPerp) and model-based (constant optical parameters for the PSF) method. Absolute percentage difference colour mapping defined in spectral colour bar. Difference error value range is from 0-100%. The constant values used in the optical parameters were the mean of the distribution of estimated attenuation coefficients (see Chapter 3). The effect of the vessel branch's angle on the error difference in between the radii estimates obtained with the FWHM (FWHMrawPerp) and model-based methods is shown in Fig. 4.20 (c).

The graph in Fig. 4.20 (c) shows that the angle of the vessel branch has a definite effect on the error difference in between the radius estimates calculated with the FWHM (FWHMrawPerp) and model-based methods.

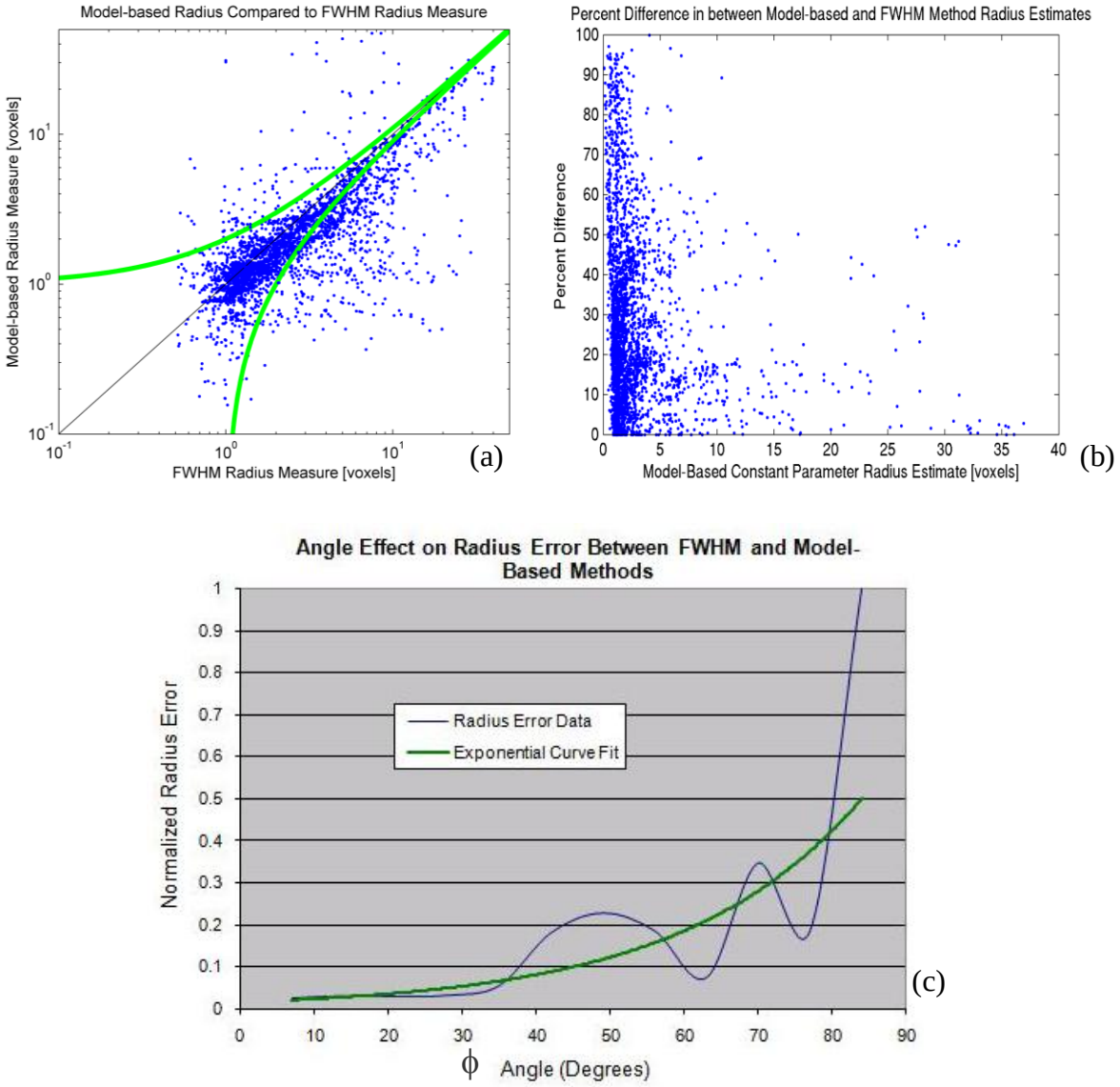


Figure 4.20: (a) Comparison of the model-based radius estimation (constant optical parameter case) with the FWHM radius estimate measured in the raw original cross-sectional image in the resampled plane perpendicular to vessel long axis (FWHMrawPerp). The radii are plotted in voxels and the green lines represent a difference of one voxel. (b) Percent difference between the model based and FWHM (FWHMrawPerp) radii estimates plotted against the model based radius estimate using constant parameters. (c) Effect of the vessel branch's angle (measured from the *z*-axis) on the error difference between FWHM (FWHMrawPerp) and model-based radii estimates shown in the graph of the normalized radius error between the two methods plotted against the angle of the vessel branch from the *z*-axis. The angle plotted on the x-axis of graph (c) in this figure is $\phi = 90° - \theta$. The angle θ discussed earlier in the main text is the vessel branch's angle from the imaging plane as shown in Fig. 4.3 and the angle plotted on the x-axis of graph (c) in this figure is ϕ, which is measured from the z-axis, and is thus equal to $90° - \theta$.

For vessels oriented at a small angle from the *z*-axis, the vessel is almost perpendicular to the imaging plane and thus there is less out-of-focus light from below the surface and consequently a smaller error difference between the FWHM (FWHMrawPerp) and model-based methods. For vessels oriented at a large angle from the *z*-axis, the vessels become more in-plane or parallel with respect to the image plane and thus there is more out-of-focus light from below the surface and consequently a larger error difference between the FWHM (FWHMrawPerp) and model-based methods. At an angle of 0° from the *z*-axis, the vessel would be perfectly perpendicular to the imaging plane and the out-of-focus light on the imaging plane from the fluorescent cast in the vessel below the surface would be very low, resulting in lower radius error. Conversely, at an angle of 90° from the *z*-axis, the vessel would be running completely in-plane or parallel with the imaging plane, and the out-of-focus light on the imaging plane from the fluorescent cast in the vessel would be much higher, resulting in higher radius error. So as the angle of the vessel branch from the z-axis increases, the radius error increases. Vessel branches were binned into 12 intervals of angles and the maximum absolute error difference in between the radii estimates of the two methods in each interval was used in order to measure the worst-case possible radius error for each interval of the angles.

4.3.7 Agreement with Murray's Law for Vasculature

Kassab et al. (1995) showed that the relationship between parent and daughter radii at vessel junctions in vasculature closely matched Murray's law. Although Murray's law is not a validity test but rather a mathematical/physiological hypothesis relating parent and daughter blood vessel radii, it can serve as a standard for comparison between radius estimation methods. Our underlying assumption in this analysis is that whichever radius estimation method follows Murray's law more closely is more accurate according to the results presented

in Kassab et al. (1995). Since it is difficult to find any other gold standard measure of accuracy in radius estimation of perfused vasculature optical images, we use herein Murray's law as a criterion to compare the FWHM (FWHMrawOrig and FWHMrawPerp) method with the model-based template-matching method.

Cecil Murray, a physiologist of the early 1900s, analyzed the branching of vessels in the vascular system. He derived a relationship between the radii of parent and daughter vessels at branching nodes. In order to determine the vessel radius that requires minimum expenditure of energy for blood flow in vasculature, he minimized the objective function that is the sum of the rate at which work is done on the blood and the metabolic rate of the vessel. The rate of work is the product of blood flow rate and pressure drop. The metabolic rate is assumed to be proportional to the volume of the blood. By optimizing the objective function, Murray obtained an equation that relates the cube of the radius of a parent vessel to be the sum of the cubes of the radii of the daughter branches. This relation is known as Murray's law (Murray 1926):

$$r_p^3 = r_{d1}^3 + r_{d2}^3 \tag{4.6}$$

Kassab et al. (1995) presented an analysis of how the uniform shear stress hypothesis results in the same relationship as Murray's law. Assuming blood as an incompressible Newtonian viscous fluid, the boundary condition as no-slip on the vessel wall, the vessels as cylindrical tubes with laminar and uniaxial flow without change in the axial direction, the wall shear stress is proportional to flow over radius cube:

$$Q = \pi \frac{r^3}{4\mu} \tau_w \tag{4.7}$$

In the above equation, Q is the rate of blood flow, r is the radius of the vessel, μ is the coefficient of viscosity of blood, and τ_w is the shear stress at the vessel wall. Applying the above relationship for the daughter and parent vessel branches along with conservation of mass, we obtain the following equation for a bifurcation node – the rate of flow in the parent vessel branch Q_p is equal to the sum of the flow rates in the daughter branches:

$$Q_p = Q_{d1} + Q_{d2} \quad \Rightarrow \quad \frac{r_p^{\,3}}{\mu_p}\tau_{wp} = \frac{r_{d1}^{\,3}}{\mu_{d1}}\tau_{wd1} + \frac{r_{d2}^{\,3}}{\mu_{d2}}\tau_{wd2} \tag{4.8}$$

Assuming that the shear strain rate or the coefficients of viscosity and the wall shear stresses are the same in all three vessels (uniform shear stress hypothesis), equation 4.8 is reduced to the Murray's law presented in equation 4.6.

As seen in Figs. 4.21-22, for both a pig kidney and heart image dataset, we tested Murray's law for the vasculature vessel radii measured in our study and found that the agreement between Murray's law and the relationship between vessel radii measurements of parents and daughter branches is stronger for the new model-based template-matching radius estimation method than the old FWHM (FWHMrawOrig and FWHMrawPerp) approach in both the pig heart and kidney. Figs. 4.21-22 plot the histograms of the ratio of sum of the cubes of daughter branch radii to that of the cube of the parent branch radii, calculated using FWHM method on the original raw cross-sectional image slice (FWHMrawOrig) and on an interpolated vessel cross-section image slice perpendicular to the vessel axis (FWHMrawPerp) and the model-based template-matching method with constant and spatially varying PSF parameters. The ratio of sum of the cubes of daughter branch radii to that of the cube of the parent branch radii $\left(r_{d1}^3 + r_{d2}^3\right)/\, r_p^3$ should ideally be 1 according to Murray's law, i.e. the sum of the cubes of daughter vessel radii should be equal to the cube of the parent vessel radius.

The model-based method has stronger agreement with Murray's law since the ratio is closer to 1 for more junctions in the novel method than the FWHM method (FWHMrawOrig and FWHMrawPerp). As shown in plot titles of Figs. 4.21-22, the mean is closer to 1 and the standard deviation of the distribution is smaller for the model-based method compared to the FWHM method (FWHMrawOrig and FWHMrawPerp). Also, it is observed that incorporating spatial variation in the optical tissue properties makes the agreement between model-based radius estimation and Murray's law even stronger. This indicates that incorporating optical tissue properties and the variance thereof in the tissue increases the agreement of the radius estimation with Murray's law as a test for radius measure.

As a final observation, the relationship between parent and daughter vessel radii in coronary vasculature seems to have a much more clearly distinct agreement with Murray's law than in the renal vasculature. We suspect this may be due to the anatomic differences between the coronary and renal arteries. The renal circulation has a complex system of specialized arteries that purify blood through a filtration system. Blood enters the renal arteries from the abdominal aorta and perfuses the adrenal gland through the inferior suprarenal artery branch. The renal artery divides into a posterior (segmental) branch and an anterior branch, which subdivides into the superior, anterosuperior, anteroinferior, and inferior segmental arteries. Lobar arteries emanating from the segmental arteries branch out into interlobar arteries for perfusing the renal lobes. The blood flows from the interlobar arteries into the arcuate arteries, which arc around the renal lobes. Interlobular arteries shoot straight off the side of the arcuate arteries and branch laterally into the afferent vessels that perfuse the nephrons (waste elimination units) through the glomerulus networks, which are clusters of elongated vessels (different than the interweaved structure of a coronary capillary bed). Unlike the capillary beds of the coronary circulation, blood from the glomerulus flows into an efferent arteriole, not a venule. The resistance of the efferent arteriole is the anatomically key difference in between

renal and coronary circulation that creates high pressure within the glomerulus, allowing ultrafiltration of fluids and soluble molecules out of the blood into the Bowman's capsule, which collects the filtrate into urine. Finally, blood from the efferent arterioles drains into renal veins after going through the peritubular capillaries, which encircle tubules of the nephron and reabsorb or excrete ions and minerals as needed between blood in the capillaries and urine in the nephron tubules through chemical gradients, osmosis, and sodium pumps. In some nephrons (juxtamedullary), the blood also is transferred from the efferent vessels into the vasa recta renis which intertwine with the loop of Henle and maintain a concentration gradient through countercurrent exchange in order to concentrate the urine (Gray 1918).

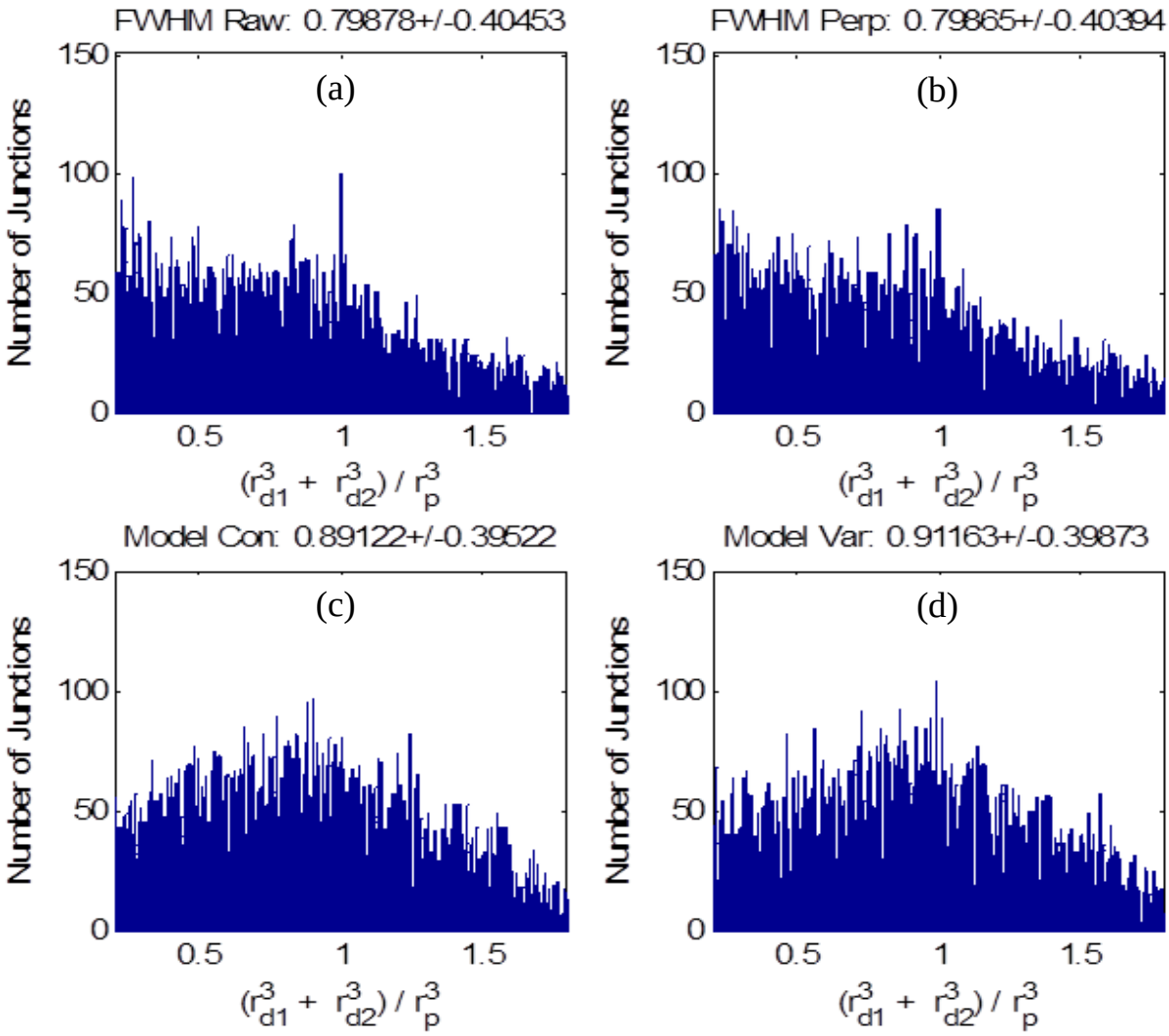


Figure 4.21: For pig kidney, histograms of the ratio of sum of the cubes of daughter branch radii to that of the parent branch radii calculated using the FWHM method in a raw original cross-sectional (FWHM Raw = FWHMrawOrig) slice (a) and in an interpolated slice perpendicular (FWHM Perp = FWHMrawPerp) to vessel axis (b) and model-based template-matching method with constant PSF parameters (c) and spatially variant PSF parameters (d), showing junctions (bifurcations and trifurcations) following Murray's law. Title contains the mean ± standard deviation of each histogram.

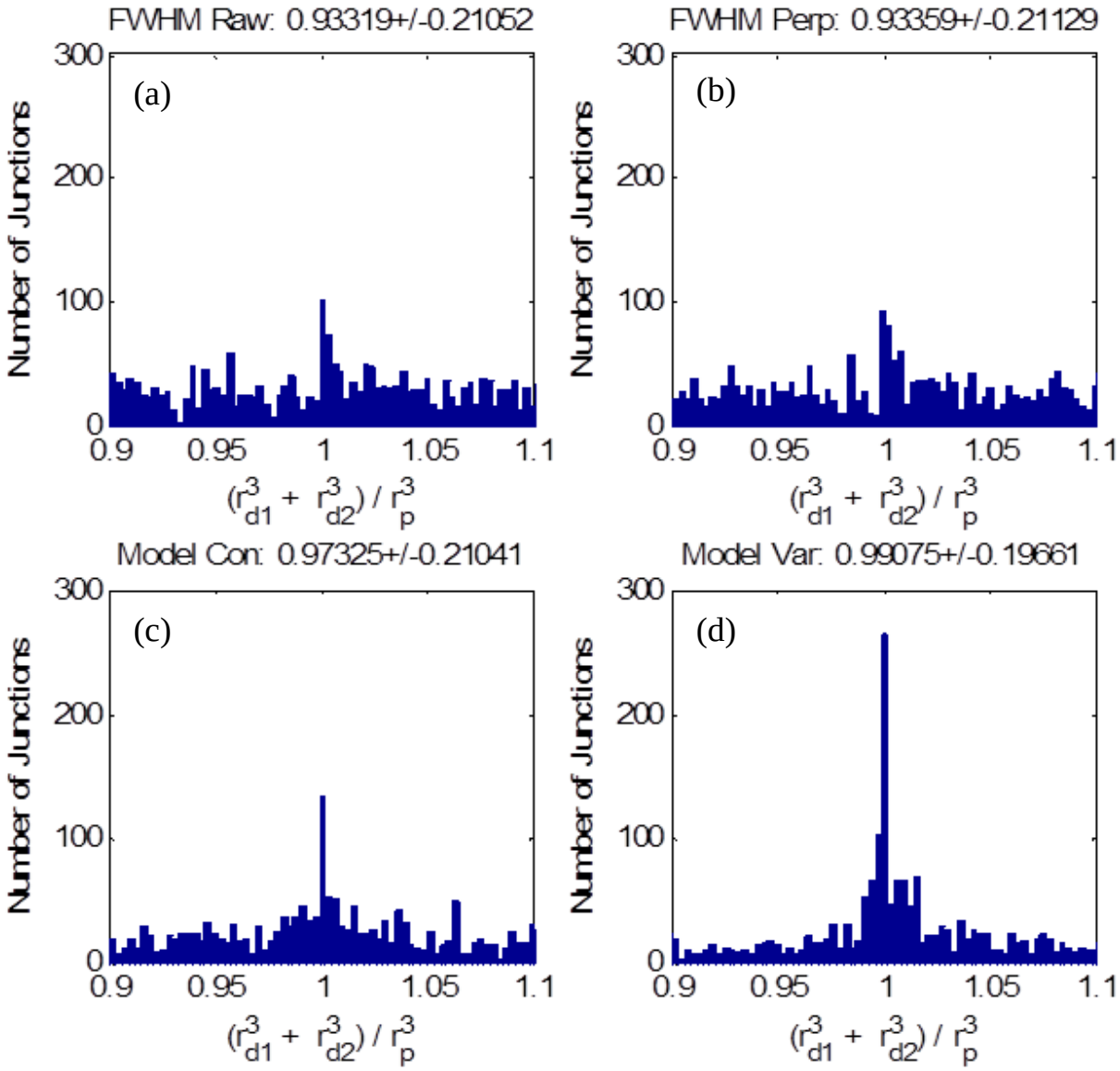


Figure 4.22: For pig heart, histograms of the ratio of sum of the cubes of daughter branch radii to that of the parent branch radii calculated using the FWHM method in a raw original cross-sectional (FWHM Raw = FWHMrawOrig) slice (a) and in an interpolated slice perpendicular (FWHM Perp = FWHMrawPerp) to vessel axis (b) and model-based template-matching method with constant PSF parameters (c) and spatially variant PSF parameters (d), showing junctions (bifurcations and trifurcations) following Murray's law. Title contains the mean ± standard deviation of each histogram.

4.3.8 Training Data - Reconstructed Vasculature Models

This section presents the results on cryomicrotome vascular training datasets, which the segmentation and skeletonization algorithm pipeline was developed on. The parameters determined on the basis of these development sets are given in Table 4.2.

Algorithm	Parameter	Value
Sauvola local adaptive thresholding	Block size	$(0.5\ \text{mm})^3$
	Standard deviation weight parameter	1 from range [0-1]
	Standard deviation dynamic range	128 (8-bit data)
Frangi multi-scale vesselness filtering	Small scales lower limit	0.005 mm
	Small scales step size	0.005 mm
	Small scales upper limit	0.1 mm
	Large scales lower limit	0.1 mm
	Large scales step size	0.05 mm
	Large scales upper limit	2 mm

Table 4.2: Parameters determined for 8-bit grayscale 50-μm voxel cryomicrotome porcine vascular data.

The complete 3D reconstructions of the coronary vasculatures of two image volume sets of porcine hearts and a 3D reconstruction of the renal vasculature of one image volume dataset of a porcine kidney lobe are visualized in this section. The first image volume set has two sub-trees (Fig. 4.23), each of which was perfused with a separate colour of dye. The differing optical parameters of the two distinct colours of dye in the two separate sub-trees were incorporated separately into the model-based template-matching radius estimation depending on which dye the vessel was perfused with.

Fig. 4.24 visualizes the 3D reconstruction of the second pig heart coronary vasculature, the two sub-trees of which were perfused with the same colour of dye. Fig. 4.25 shows the coronary vasculature reconstruction with and without smaller vessels and Fig. 4.26 shows it in sagittal and transverse cross-sections, which also show the vessels in the myocardium surrounding the ventricular cavities.

Radii of the detected vessels ranges from 0.12 to 3.5 mm, which is colour mapped onto the vessels from blue (smaller vessels) to red (larger vessels) in Figs. 4.23-26. The renal vasculature of a kidney lobe is visualized in Fig. 4.27. This kidney vascular reconstruction demonstrates that the model-based template-matching radius estimation algorithm can be performed on optical vascular images of other organs.

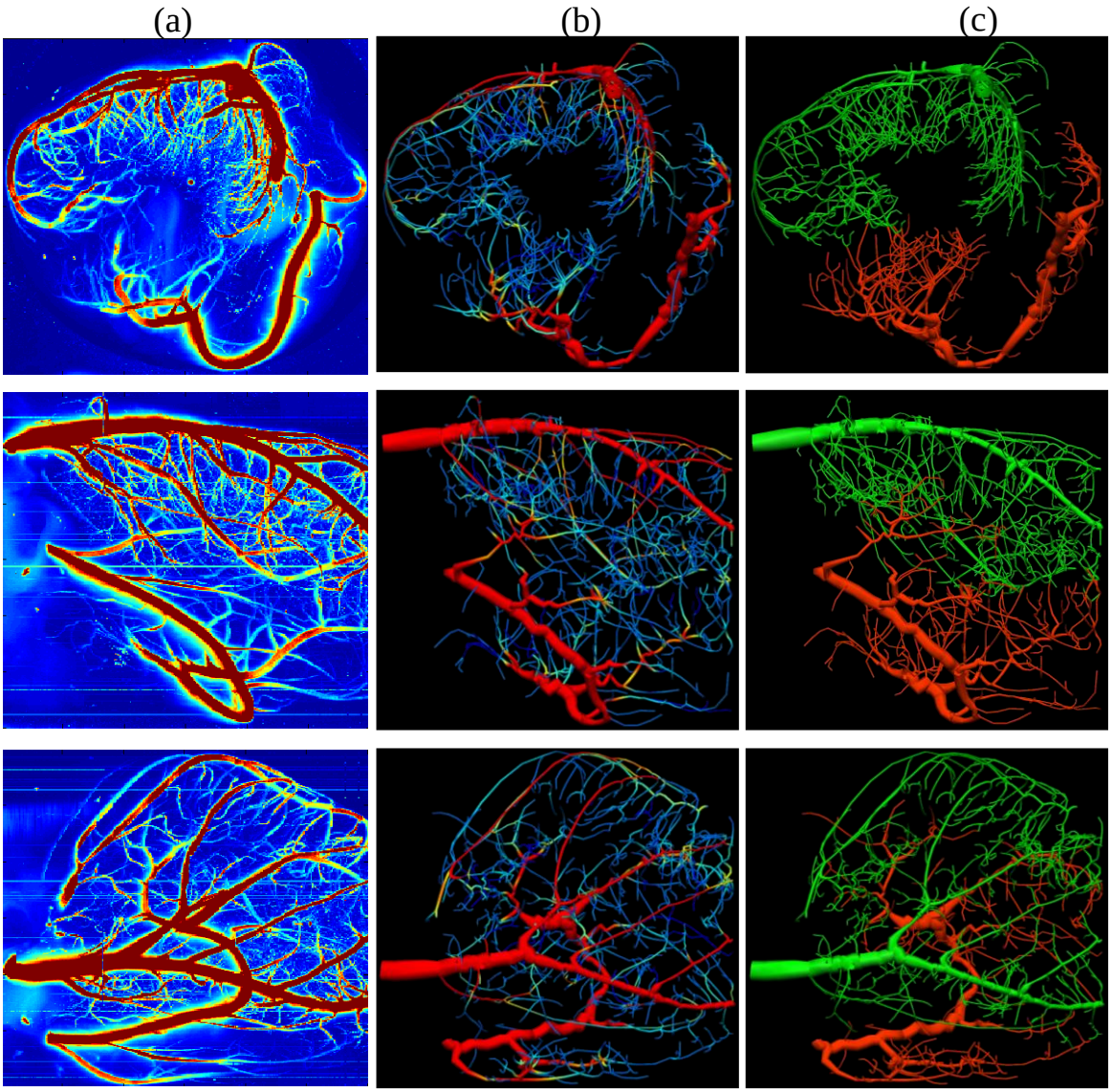


Figure 4.23: Maximum intensity projections (a) of a pig heart image dataset. Complete 3D reconstruction of the coronary vasculature coloured according to vessel radius (b). Radii of the detected vessels ranges from 0.12 to 3.5 mm, which is colour mapped onto the vessels from blue (smaller vessels) to red (larger vessels). Also the vasculature was coloured to show the two distinct subtrees (c). The two subtrees of this heart were perfused with two different colors of fluorescent cast dye – green and red, and different optical parameters for the vessels filled with the red fluorescent dye cast material (620 nm emission wavelength at which optical tissue attenuation coefficient is ~0.04/µm) versus green fluorescent dye cast material (530 nm emission wavelength at which optical tissue attenuation coefficient is ~0.03/µm). Image dimensions: 70x70 mm^2.

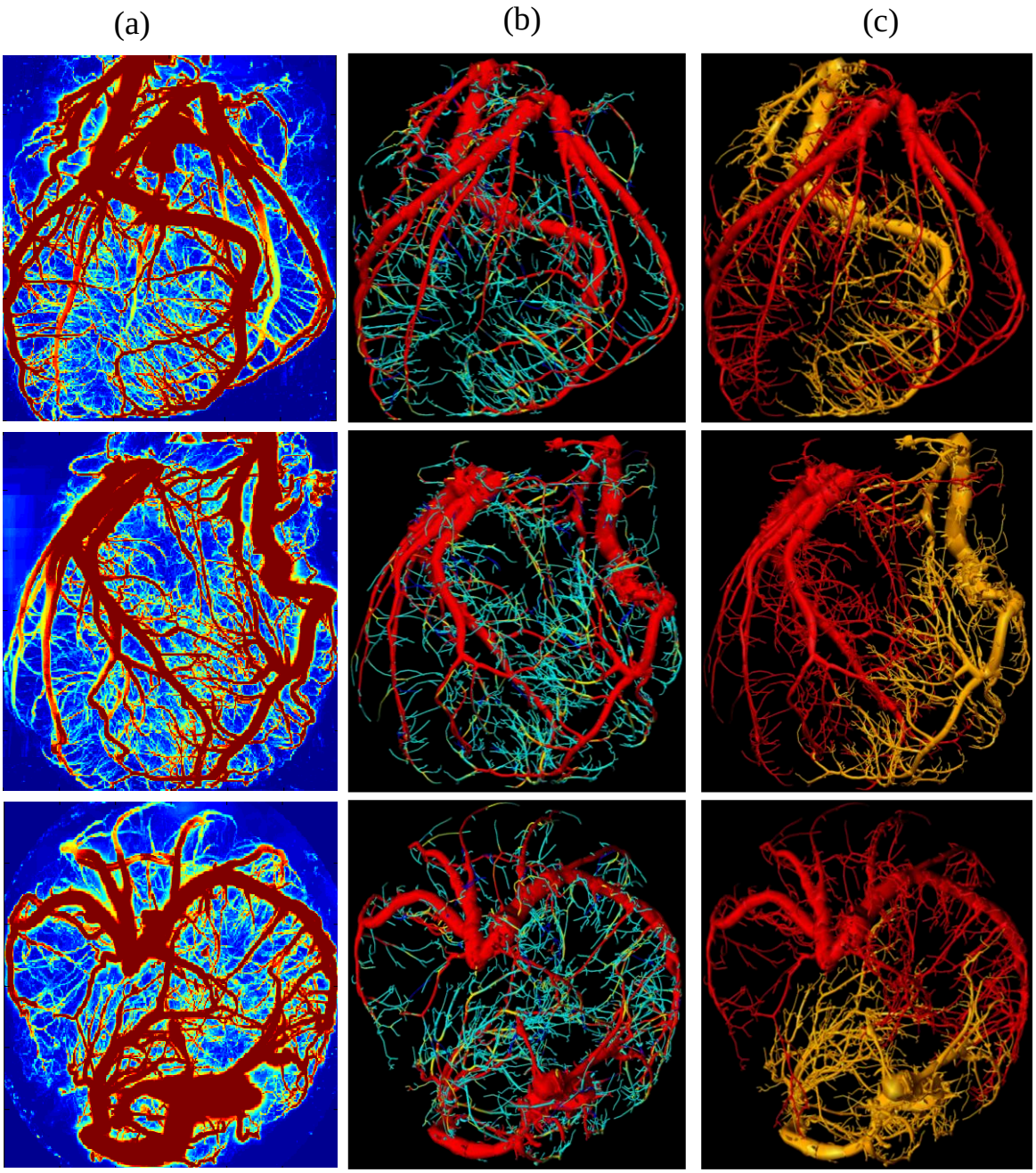


Figure 4.24: Maximum intensity projections (a) of a pig heart image dataset. Complete 3D reconstruction of the coronary vasculature of the porcine heart coloured according to vessel radius (b), and according to subtree (c). Optical attenuation parameter is 0.037/μm for the red dye cast. Radii of the detected vessels ranges from 0.12 to 3.5 mm, which is colour mapped onto the vessels from blue (smaller vessels) to red (larger vessels). Image dimensions: 70x70 mm^2.

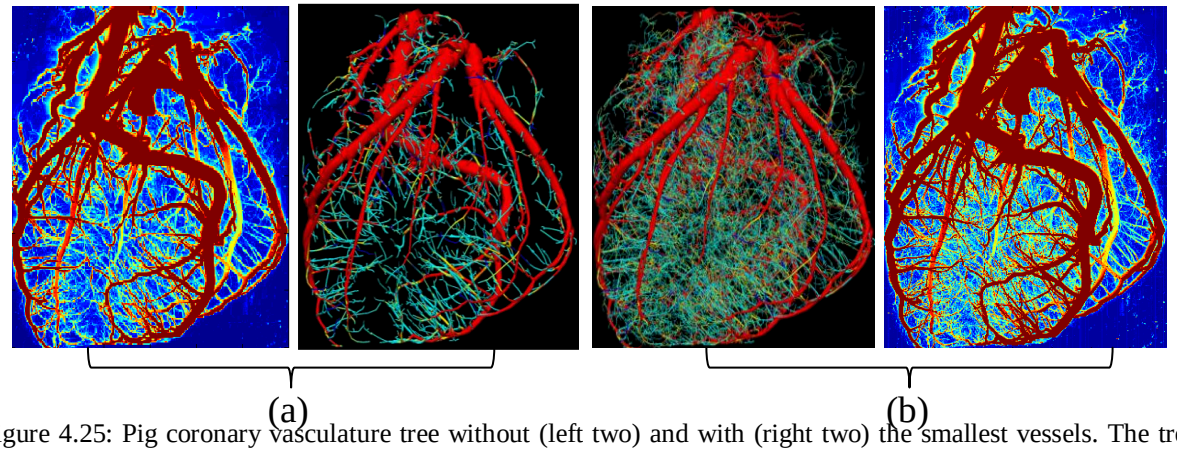


Figure 4.25: Pig coronary vasculature tree without (left two) and with (right two) the smallest vessels. The tree without the smallest vessels allows us to see the branching structure of the large vessels without them being obscured / hidden behind the small vessels. The tree with the small vessels is the complete coronary vasculature that was extracted and reconstructed. Image dimensions: 70x70 mm^2.

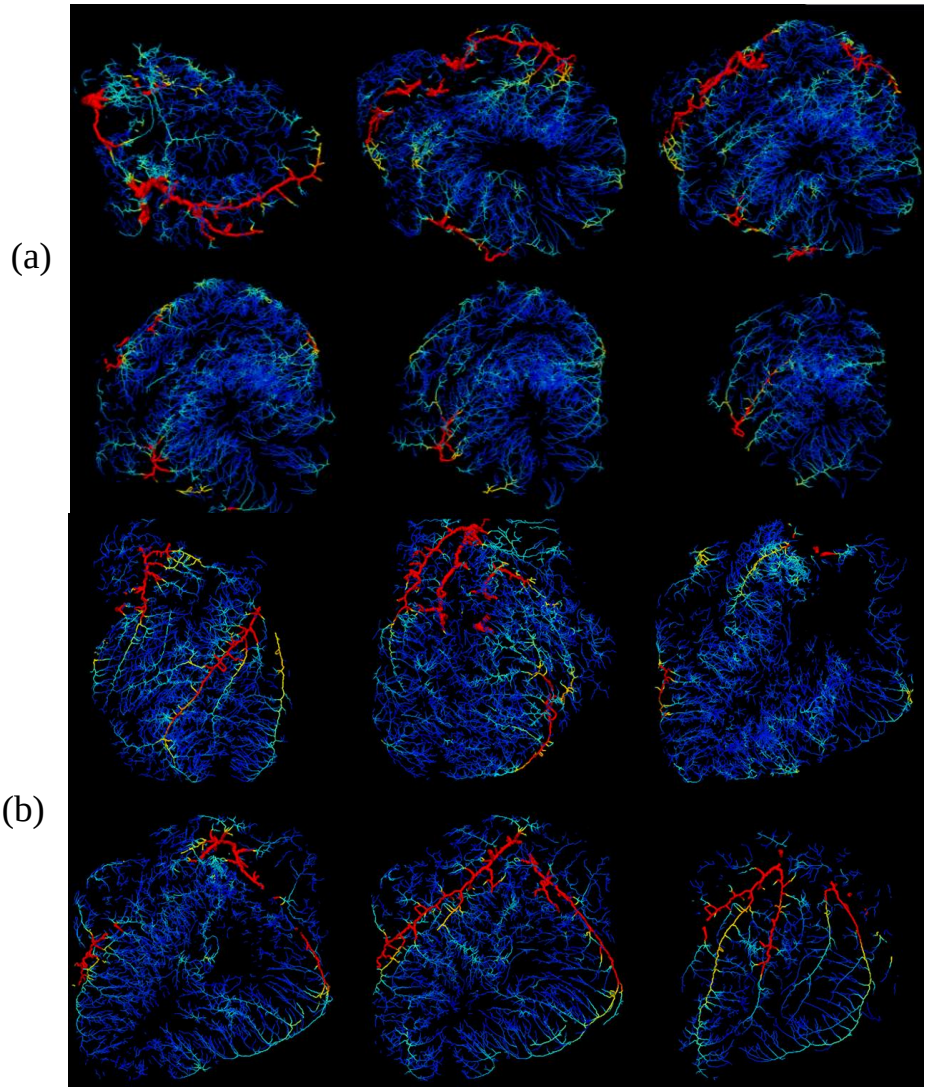
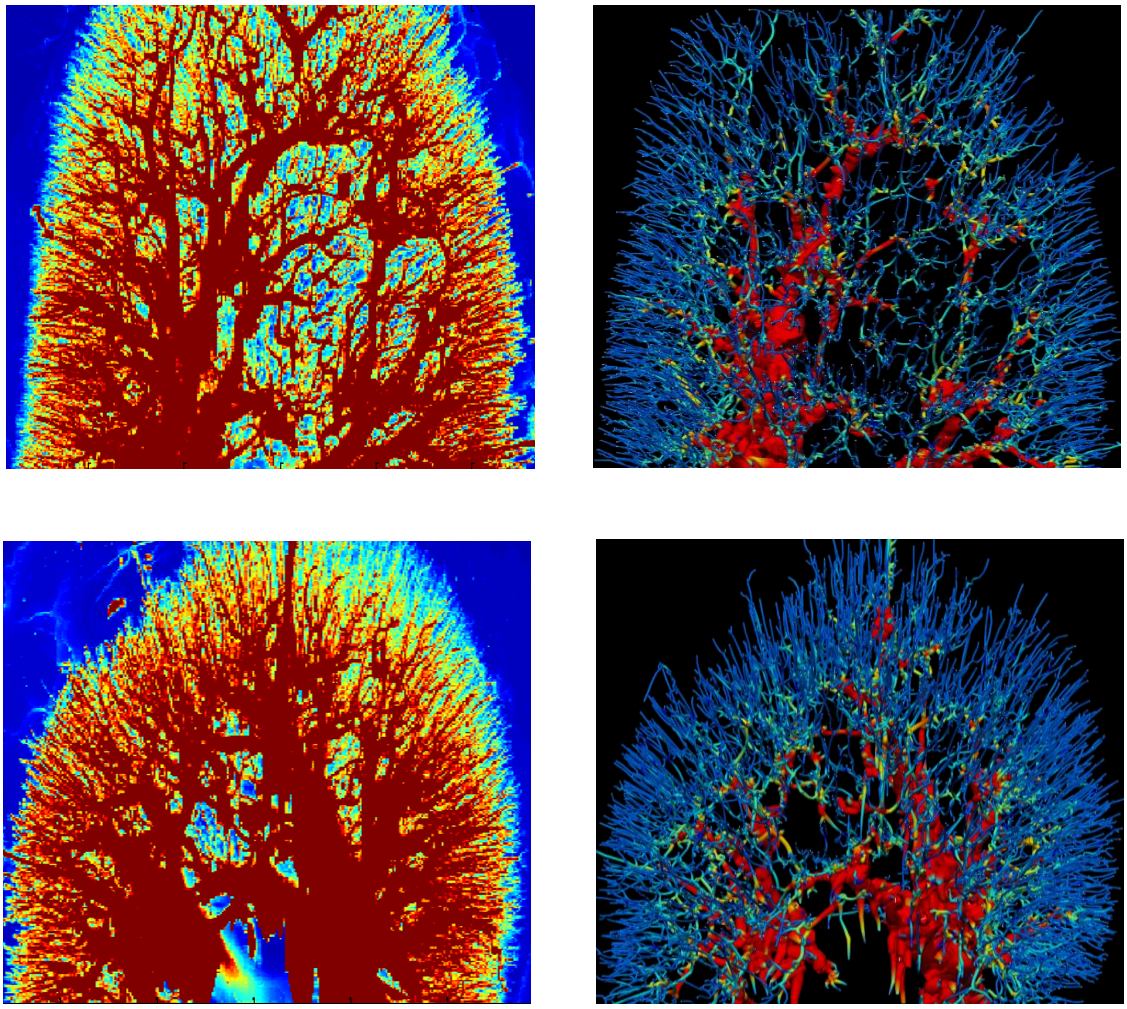


Fig. 4.26: Complete 3D reconstruction of the coronary vasculature of the porcine heart visualized in transverse (a) and sagittal (b) cross-sections. The left and right ventricles that are visible as cavities in the transverse cross-sections collapsed during the perfusion of the fluorescent dye in the coronary vasculature. Image dimensions: 70x70 mm^2.



(a) (b)

Figure 4.27: (a) Maximum intensity projections of a porcine kidney lobe cryomicrotome image dataset. (b) 3D reconstruction of the renal vasculature of the porcine kidney lobe coloured according to vessel radius. Radii of the detected vessels range from 0.1 to 3.2 mm, which is colour mapped onto the vessels from blue (smaller vessels) to red (larger vessels). Image dimensions: 50x50 mm^2.

4.3.9 Test Data - Reconstructed Vasculature Models

To demonstrate the developed vasculature detection methods, this section presents the results of tests made on test datasets with the parameters (listed in Table 4.2) determined from the training datasets unchanged. 3D computational representations of whole-organ porcine coronary vasculatures reconstructed with the vessel extraction method proposed in this thesis are shown (Fig. 4.28-9). The 3D models reconstructed from the cryomicrotome datasets demonstrate that the vasculature extraction method presented in this work is applicable for

extracting vessels from different organs and is also robust to varying dimensions, fluorescent cast, and other variations in the imaging setup.

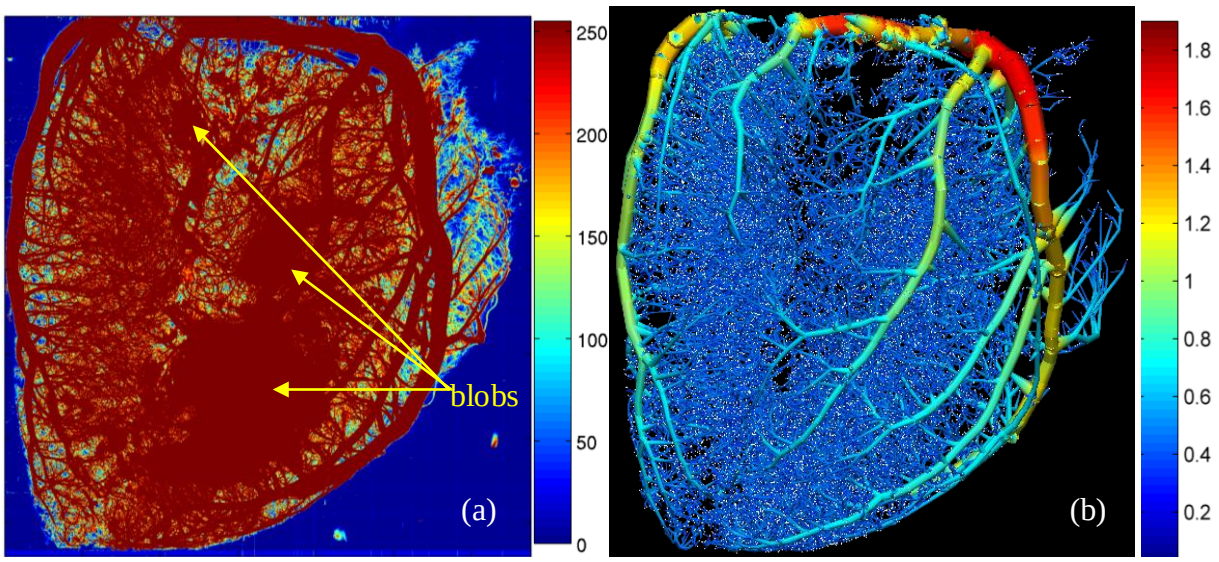


Figure 4.28: (a) Maximum intensity projection of a porcine coronary vascular cryomicrotome image volume (1463x1353x1280 voxels) with voxel intensity ranging from 0-255 in the 8-bit data with voxel resolution of $(50\mu m)^3$. (b) Complete 3D reconstruction of the coronary vasculature of the porcine heart coloured according to vessel radius. Radii of the detected vessels ranges from 0.03 – 1.9 mm, which is colour mapped onto the vessels according to the colourbar. A total of 92272 vessel segments were extracted.

As shown in Figs. 4.28-9, the vascular extraction automatically is able to successfully remove blobs caused by leakage of the fluorescent cast into tissue in these test cryomicrotome images.

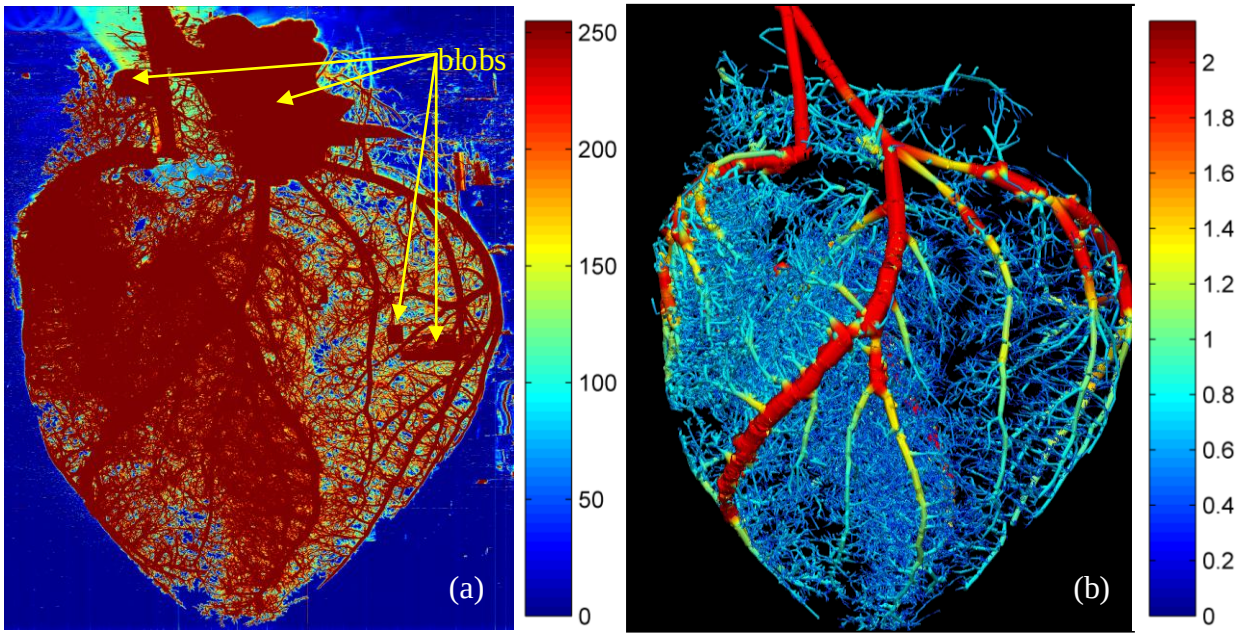


Figure 4.29: (a) Maximum intensity projection of a porcine coronary vascular cryomicrotome image volume (1440x1255x1970 voxels) with voxel intensity ranging from 0-255 in the 8-bit data with voxel resolution of $(50\mu m)^3$. (b) Complete 3D reconstruction of the coronary vasculature of the porcine heart coloured according to vessel radius. Radii of the detected vessels ranges from 0.025 – 2.15 mm, which is colour mapped onto the vessels according to the colourbar. A total of 97712 vessel segments were extracted.

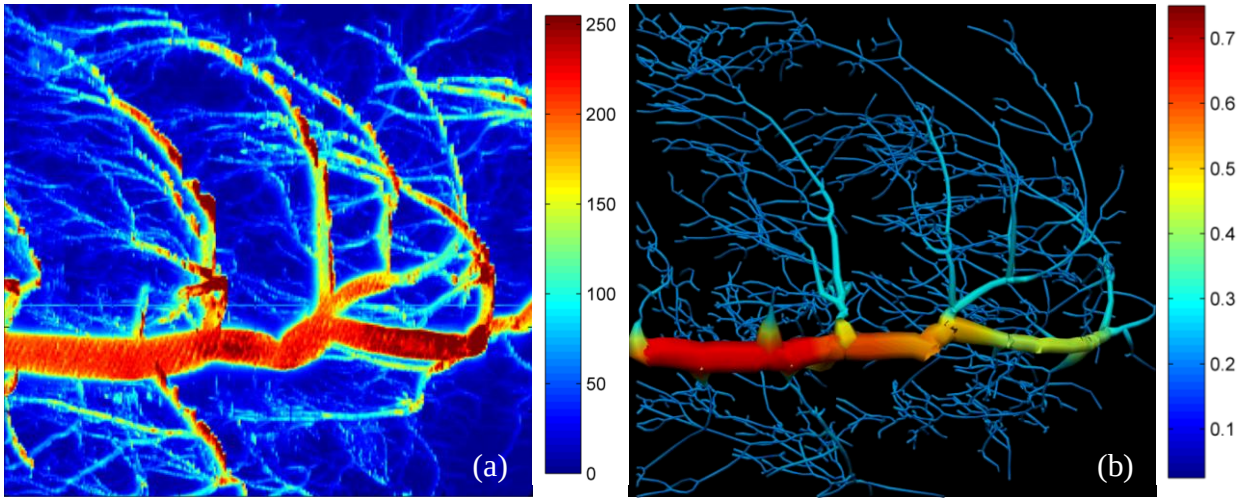


Figure 4.30: Maximum intensity projection (a) of a block of porcine heart cryomicrotome image dataset and its 3D reconstruction (b). Radii of the detected vessels ranges from 0.025 – 0.75 mm, which is colour mapped onto the vessels from blue (smaller vessels) to red (larger vessels). A total of 1292 vessel segments were measured. Image volume dimensions: 300x300x300 $voxel^3$ = 15x15x15 mm^3 (voxel size was 50 μm^3 cube) with a total of 27 million voxels.

Figure 4.30 shows that details of the microvasculature that can be missed with a manual visual segmentation due to intensity variation are also extracted by the vascular extraction method presented in this work.

4.3.10 Extension Data - Reconstructed Vasculature from CT Images

To demonstrate the applicability of our work to other modalities, the vessel detection methods presented in this study (detailed in sections 4.2.2-3) is also tested on rat coronary (Lee et al. 2007) and human pulmonary vasculature imaged with CT. The processing on these hearts is shown in Fig. 4.31-2. The application of the vessel detection methods presented in this thesis on CT datasets suggests that it can be extended to other imaging modalities.

Both CT and cryomicrotome image volumes are acquired through photon detection, albeit the photon energy is much lower for optical modalities than for x-ray modalities. This is why optical modalities are reflection geometries wherein the incident light on the imaged object is scattered back towards the source and detected by sensors on the same side. CT on the other hand is a transmission geometry wherein the x-rays pass through the imaged object and are detected by sensors on the other side. X-rays are highly directional with much less diffraction and scatter than visible light. Both modalities, however, generate 3-D image volumes (the difference of course is that the cryomicrotome sections the block physically and captures slices each time whereas CT reconstructs slices from projections).

The automatic vasculature extraction in this thesis is based on the pixel intensities or brightness values in the 3-D digital image volumes. For vessel extraction, the automatic image processing pipeline applied to cryomicrotome data was also effective for CT images because the underlying method of 3-D hessian-based multi-scale line filtering utilized in this thesis extracts tubular structures at multiple scales, and these objects of interest (vessels at multiple scales) are the same (bright tubular structures) in both cryomicrotome and CT.

The same parameters (listed in Table 4.2) applied on the cryomicrotome images also worked well on the CT images. In the automatic image processing pipeline presented in this work, the

parameters are of two kinds: 1) local adaptive thresholding parameters related to the block size and weight and normalization of the standard deviation of the voxel intensities in the block; 2) vesselness filtering parameters related to the scales / sizes of the vessels to be extracted.

Regarding the thresholding parameters, the thresholding of vessels was not sensitive to the weighting parameter (which was effectively eliminated by setting k = 1). For memory efficiency, the vesselness filtered output is always converted to 8-bit data in the automatic vascular extraction software program developed in this thesis project and hence R = 128 (parameter setting for 8-bit data) works well for local adaptive thresholding of both cryomicrotome and CT data subsequent to the vesselness filtering. The block size of 0.5 mm (isometric in all directions) originally set for the cryomicrotome worked for the CT data also because this block size applies specifically to the local thresholding of only the small scale output of the vesselness filtering, which for small-scales is set to filter the images at scales ranging from 0.005 mm – 0.1 mm (this range remained unchanged whether processing cryomicrotome or CT data). Essentially this isometric block size of 0.5 mm in each dimension works for thresholding any vesselness data filtered for the scale range 0.005 mm – 0.1 mm.

Regarding the vesselness filtering parameters, the thresholding pipeline in this work makes the vascular extraction robust to the vesselness scale selection. In other words, even if certain scales of vessels are not specified and consequently the vessels of certain sizes are outputted with lower vesselness than vessels of other sizes in the filtered images, the local adaptive thresholding still extracts them because it is robust to voxel intensity variation in vessels.

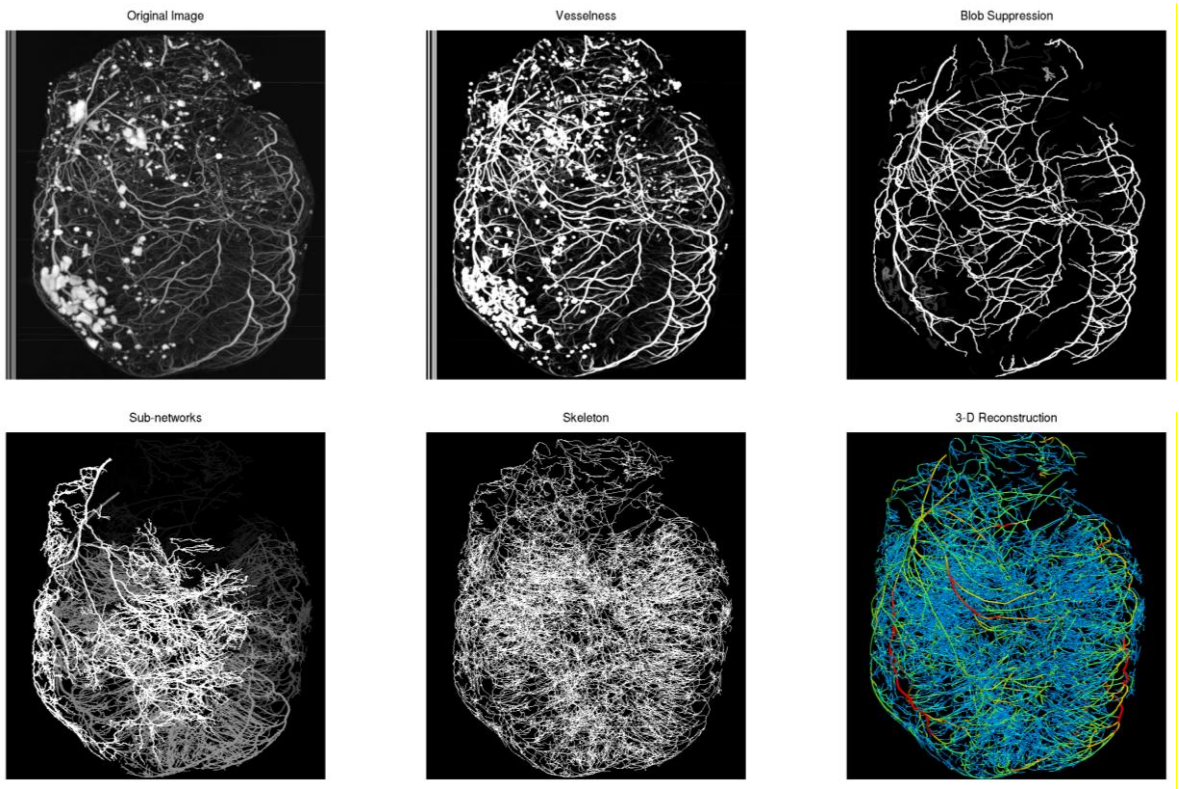


Figure 4.31: Vascular extraction method application on rat coronary arterial network, which is 16-bit grayscale bitdepth with a volume of 550x570x755 voxels where the isotropic voxel size was 20.9 µm. The vesselness and connected component analysis facilitate removing the blobs from the image, following which the sub networks in the rat coronary can be identified and skeletonized to obtain a 3D reconstruction. These maximum intensity projections are visualized along the y-dimension.

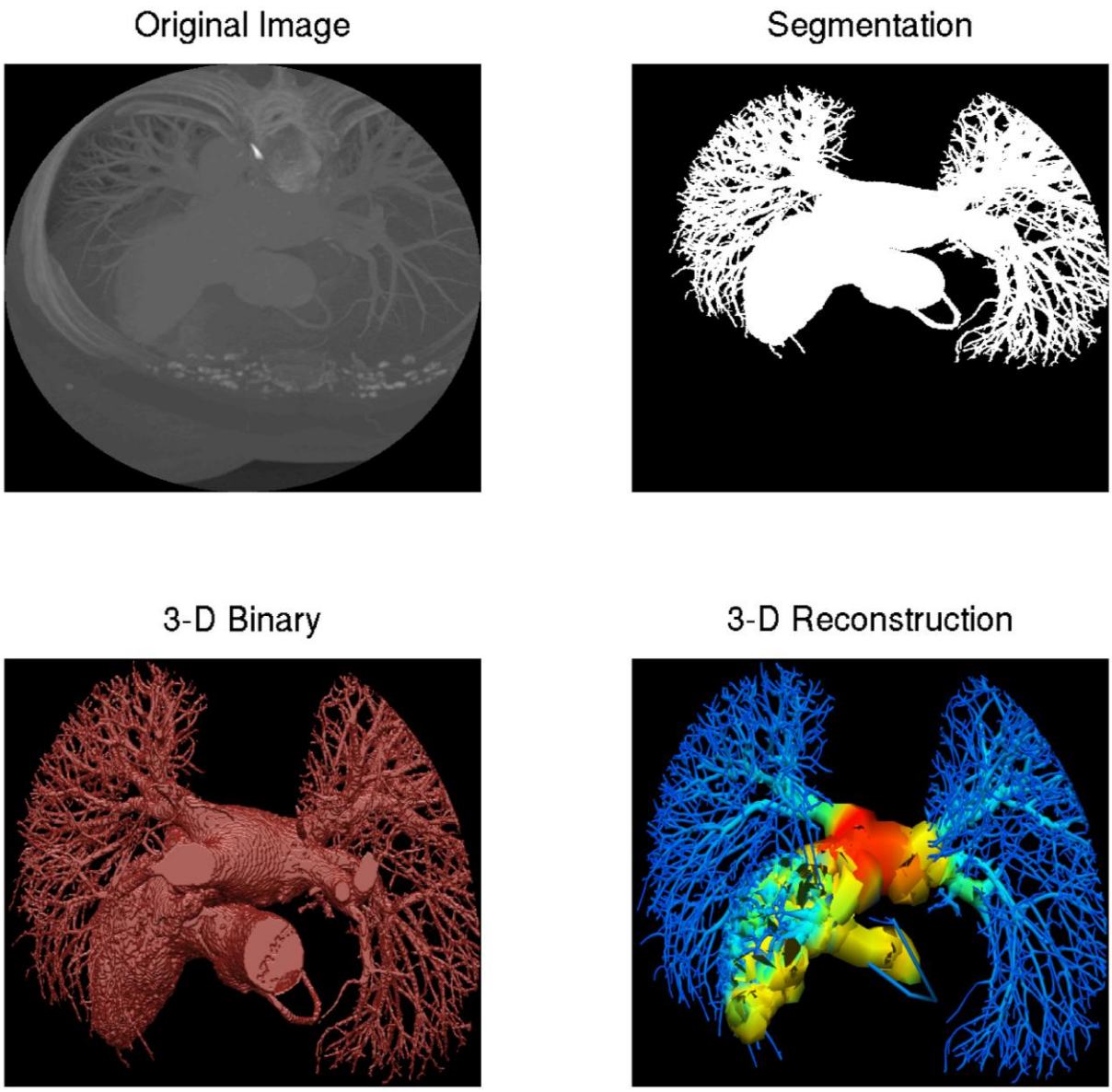


Figure 4.32: Vascular extraction method application on a human patient pulmonary arterial CT data, which is 16-bit grayscale bitdepth with a volume of 512x512x120 voxels where the voxel spacing was 0.429 mm x 0.429mm x 1 mm. These maximum intensity projections are visualized along the y-dimension.

Figure 4.32 demonstrates that the vascular extraction method in this study is extendable to tomographic imaging modalities in clinical applications and can be used to reconstruct patient vascular networks of any organ such as heart or lung imaged with CT. A fully automated and customizable vascular extraction tool, VasEx, has been developed as part of this work, which automatically detects vessel scales, extracts the vasculature from any tomographic vessel data, and visualizes the reconstructed network in 3D with any specific options specified by the user.

4.4 Discussion

In this study, we have developed a model-based method that automatically extracts and reconstructs vascular networks with accurate morphological measurements from 3D optical fluorescence cryomicrotome images. An automatic pre-processing pipeline has been implemented combining several techniques for enhancing, binarizing, segmenting, and skeletonizing the vascular data. This vessel detection method has been shown to compare favourably with previously published model-based method of vessel detection (Krissian et al. 2000) when a manual segmentation of original raw vessel image data was used as the gold standard. The vessel detection proposed in this study is also applicable to extract vasculature from other imaging modalities such as CT.

Pursuant to vessel detection, highly accurate morphometry of the vasculature is obtained with the model-based template-matching vessel radius estimation, which optimizes vessel radius by fitting a simulated vessel image to the real vessel data. The method extracts images of markers of known shape and size embedded in the same tissue as the vasculature to model the image acquisition process, which is then used to measure the vessels. This inherently accounts for the tissue transparency and out-of-focus light that results in optical blurring of the vessel image data.

Correction of the out-of-focus light or image restoration was tested with the Richardson-Lucy deconvolution method. This deconvolution suppressed the halo and transparency artifacts effectively to sharpen the vessel boundaries in the smaller vessels, but was ineffective for larger vessels. As a side effect, it darkened the image and created holes in large vessels. This issue originated from the limited bit-depth of the camera pixels in the image acquisition. It was observed that over-exposure of the CCD sensors from the fluorescence emitted off the large

vessels led to saturation in the original images, which caused *hole-effects* in the Richardson-Lucy method. This deconvolution technique does not account for the saturation in the centre of the vessel because a Gaussian vessel intensity profile is assumed in the PSF, while saturation causes the cross-section to be non-Gaussian in profile. In order to account for the optical blurring and saturation effects, the model-based method was presented to accurately estimate vessel radii in the cryomicrotome vasculature image data. The model-based method obviates image restoration with deconvolution since it incorporates pixel saturation, the vessel geometry, orientation, and the optical properties of the tissue in the radius estimation.

The model-based method also incorporates regional variation in the optical tissue parameters, measured from the microspheres embedded in the tissue. To analyse the effect of intramural distance on variation in optical tissue properties, the difference between the measured optical parameter values from distinct microspheres was plotted against the distance between the microspheres. The smaller the distance was between the microspheres, on average the less the difference was in their measured parameter value. In other words, the difference in optical parameter value measured from microspheres was found to be correlated with the distance between the microspheres, which indicates intramural regional variation in the optical tissue properties. This variation is accounted for in the model-based vessel measurement by estimating the PSF parameters locally from the nearest embedded microsphere for radius estimation of each vessel. Radii estimates from the model-based method with the constant and varying parameters were compared directly with each other. The estimated radius differed much more between the constant and varying parameter cases for smaller vessels, which are more sensitive to the spatial variation. This sensitivity of radii estimates to optical parameter variation increases in the presence of partial volume effects in lower resolution image datasets. This suggests the need to measure local spatial variation in optical tissue parameters for

accurate radius estimation of smaller vessels (< 10 voxels in radius) in particular because for these smaller vessels, the difference is more significant percentage-wise. Additionally, the difference in the model-based radii estimate between the constant versus spatially varying optical parameters is much less than the difference between the model-based and FWHM (FWHMrawPerp) radii estimates. So the results show that incorporating the PSF in the radius estimation is more important than incorporating the spatial variation in the PSF parameters.

Nevertheless, the model-based radius measure is sensitive to optical parameter variation, difference in excitation and emission attenuation coefficients, and optimization constraints and bounds. However, the uncertainty in blood flow simulations due to uncertainty in the radius estimation arising from the optical parameter variation, difference in excitation and emission attenuation coefficients, and optimization constraints and bounds, is much less than the uncertainty in blood flow simulations arising from uncertainty in boundary conditions (refer to chapter 5 section entitled “Radius Measure Accuracy”).

The proposed method’s motivation is that due to saturated voxels and vessel cross-sections blurred with the imaging modality's response, it is not possible to measure vessel radius in cryomicrotome images accurately with just the intensity information without incorporating a model of the imaging modality's PSF or imaging response, which we measure with microsphere fluorescent beads. Furthermore, the PSF parameters were found to spatially vary intramurally; thus it is not possible to correct the radius with a constant ratio based on the optical parameters. Since no analytical expression is available to relate the vessel radius to the PSF parameters and as the effect of pixel saturation cannot be related to the vessel radius analytically, the model-based method instead optimizes the vessel branch radius by matching a simulated image directly to the real image.

The accuracy of the proposed model-based method was validated using computer-generated simulations and ground truth phantoms containing vessel-like tubes imaged with the cryomicrotome. Both the new model-based and prior FWHM methods (all four implementations mentioned in section 4.1.1) were tested on the phantom data. For obliquely oriented vessels, FWHM on a raw original cross-section (FWHMrawOrig) can result in very different radii than the FWHM on an interpolated cross-sectional image slice that is perpendicular to the vessel axis (FWHMrawPerp). FWHM is not reliable because on the raw original cross-sectional slice (FWHMrawOrig) it is obscured by halo and on the interpolated perpendicular slice (FWHMrawPerp), it is still obscured by halo and also further introduces interpolation errors. The FWHM method resulted in erroneous radii estimates of the oblique vessels in the raw original images (FWHMrawOrig and FWHMrawPerp) whereas the proposed method consistently gave more accurate estimates regardless of the vessel size or orientation. The model-based template-matching resulted in the most accurate radii estimates for all diameters studied. On the other hand, deconvolution (Richardson-Lucy method) improved the FWHM (FWHMdecOrig and FWHMdecPerp) radius estimates of the small vessels whose image data was not saturated, but deconvolution of saturated image data of the large vessel resulted in underestimation of the radius with the FWHM method (FWHMdecOrig and FWHMdecPerp). The FWHM method (FWHMdecOrig and FWHMdecPerp) was thus susceptible to error for measuring saturated image data. Conversely, the proposed model-based method was more robust to these issues because it accounted for out-of-focus light, optical blurring, and saturation. The difference between the FWHM (FWHMrawPerp) radius estimate and the model-based radius estimate was larger for obliquely oriented and smaller size vessels. Oblique (θ < 45° w.r.t. imaging plane) and smaller (< 10

voxels in radius) vessels are more susceptible to erroneous radius estimation when the optical blurring effect is not incorporated.

As another test on the radius estimates, the Murray's law of the relationship of the vessel radii of parent vessels branching into daughter vessels and uniform shear hypothesis have been shown to agree more strongly for the model-based radius estimation method than for the FWHM method (FWHMrawOrig and FWHMrawPerp). Kassab et al. (1995) also found that the vessel radii in coronary vasculature agree closely with Murray's law. As compared to using a single constant optical tissue parameter, incorporating varying spatial optical tissue parameters increased the agreement between Murray's law and the radii estimated by the model-based method. So this indicates that the model-based template-matching radius estimation and incorporation of optical tissue properties and their intramural spatial variation increases the agreement (to Murray's law) of radii estimates in comparison to the FWHM (FWHMrawOrig and FWHMrawPerp) method's radii estimates, when using Kassab's research on Murray's law as the criterion.

Finally, the proposed vascular extraction was run on pig heart and kidney training and test cryomicrotome image datasets, which were segmented, skeletonised, and measured to reconstruct whole-organ vasculature. To facilitate collaboration and sharing, the 3D multi-scale whole-organ computational model representations reconstructed from vasculature imaged with the cryomicrotome datasets in this study have been made available on a web-based (http://amdb.isd.kcl.ac.uk:8080/AMDBWebInt/) anatomical model database management system-Anatomical Models Database, to support the reuse of geometrical and functional models of the heart (Gianni et al. 2010).

Chapter 5

Myocardial Perfusion Flow Modelling

The purpose of this study was to compare quantitative microsphere perfusion in the myocardium with coronary arterial flow calculated with a 1D blood flow simulation on the porcine coronary vasculature reconstructed in chapter 4. Blood flow simulation was performed with the Hagen-Poiseuille model in the reconstructed arterial network to obtain pressure, conductance, and blood flow rate at each branch in the tree across the whole coronary vasculature. At each branch in the tree, flow rate was calculated using the conductance and pressure drop across the branch. The Poiseuille blood flow simulation was compared to regional microsphere perfusion distribution. The same pig coronary vasculature which was imaged for blood flow modelling had been previously perfused with microspheres (micrometer size fluorescent beads). At each branch in the arterial tree, the number of microspheres that passed through it in the vasculature was counted. Shortest path tracing also allowed defining the source (LCX or LAD) for every branch in the LCA arterial tree and obtaining the myocardial perfusion regions of these main branches of the LCA (the reconstructed vasculature used in this study only had the LCA tree). The regional microsphere distribution (number of microspheres counted going through a branch, normalized by the total number of microspheres counted in the entire LCA perfused region of myocardium) was compared to the regional flow (flow rate in a branch normalized by the total flow rate in the root artery, i.e. LCA). As vessels became smaller, an increasing discrepancy was observed in the microsphere perfusion and flow model. To analyze this discrepancy, we studied the distribution of microspheres at bifurcations. In bifurcating vessels that had a much smaller cross-sectional area than their parent branch and in bifurcating vessels that came out at a large oblique branching angle from the parent branch's direction, the fraction of microspheres (microspheres

in daughter branch divided by the microspheres in parent vessel) that were counted in those branches deviated from the fraction of flow (flow in daughter branch divided by flow in parent vessel). A model of this error parameterised by the branching angle and daughter-to-parent ratio of the vessel cross-sectional area is shown to accurately predict the biased distribution of the microspheres. For instance, at bifurcating segments with the largest branch angles, ranging from 100˚ - 120˚, there was 24% error in between the fraction of flow predicted by the 1-D Poiseuille model and the fraction of microspheres. This error was reduced to 7.4% error by incorporating the disproportionate microsphere distribution model.

5.1 Introduction

Microspheres are micrometer size beads that when infused into an organ, become embedded in the microvasculature at the capillary bed, interstitial tissue, or venules, depending on their size (Maxwell et al. 1985, Prinzen et al. 2000, Tian et al. 2003). Using this technique, blood perfusion distribution in the myocardium and other organs has been quantified with radioactive and fluorescent microspheres in past research (Glenny et al. 1993, Prinzen et al. 1994, Chien et al. 1995, Van Oosterhout et al. 1998, Raab et al. 1999). The regional perfusion of different areas in an organ can then be measured by the density or fraction of microspheres detected and counted in particular regions, relative to mass or total number of microspheres, respectively. In the past, the fluorescence, radioactivity, or count / density of the microspheres was measured in histological sections or tissue samples obtained from a region of interest to estimate regional perfusion (Luchtel et al. 1998, De Visscher et al. 2003, De Visscher et al. 2006). This method was limited to only one or at most a few regions of interest, being time-consuming and inefficient for whole organ perfusion analysis especially in large animals (Eucker et al. 2010). More recently, the cryomicrotome modality allows the whole organ to be sectioned into micrometer-thin slices and imaged after the microspheres are injected and the

organ is frozen (Glenny et al. 2000, Decking et al. 2004, Lamm et al. 2005). As discussed in Chapter 3,the location of each and every microsphere can be estimated from the high-resolution whole-organ image volume stack (Bernard et al. 2000, Vincent et al. 2001, Van Horssen et al. 2008, Van Horssen et al. 2010).

Though microspheres are considered the de facto gold standard of perfusion measurements as employed in the above-mentioned studies (assuming microspheres distribute in direct proportion to flow), there have also been reports in the literature (Bassingthwaighte et al. 1990 and Prinzen et al. 2000) which mention discrepancy between regional flow and microsphere perfusion measurements (disproportionate distribution of microspheres). Therefore, in this study our objective is to quantify and assess regional coronary perfusion with microspheres compared to a flow simulation model. Being particles like red blood cells, microspheres are affected by bifurcation flow effects. Flow partitioning at bifurcations in arteries is most directly affected by the daughter-to-parent cross-sectional area ratios (Feuerstein et al. 1976, Lee et al. 2008) and branching angles (Karino et al. 1985, Tadjfar et al. 2004). Several studies have reported the area ratio and branch angle as the most important parameters in flow distribution modelling (Lou et al. 1992, Pedersen et al. 1992, Friedman et al. 1998). Hence, the area ratio and branch angle are used to fit a two-parameter model to the error between microsphere perfusion and regional flow in this study. The microsphere perfusion data is measured as regional counts of the beads in the tissue and the regional flow estimation is obtained from a blood flow simulation performed on the reconstructed vascular network (from chapter 4).

Blood flow simulation studies have been the subject of past research in modelling hemodynamics in the arterial network (Pries et al. 1990, Pries et al. 1994, Olufsen et al. 2000, Myers et al. 2001). In this study we model blood flow as a steady laminar flow of Newtonian fluid with constant viscosity through a cylindrical rigid tube model of a vessel segment. For

such a model, the Navier–Stokes equations are simplified to the linear static 1-D Hagen-Poiseuille flow model (Wilson 1991, Thompson et al. 1997, Galdi et al. 2005, Zhonghai et al. 2010), which according to the literature gives acceptable results in biological circulatory systems (Pries et al. 1996, Gabrys et al. 2006) and has been employed in past research for blood flow simulations in arteries (Zijlstra et al. 1988, Bruinsma et al. 1988, Spaan 1991, Sigalotti et al. 2003, Geven et al. 2004, Doddi et al. 2008, Traupe et al. 2010).

Blood flow simulations require setting the outlet boundary conditions at the terminals of the arterial network. As discussed by Vignon-Clementel et al. 2006, many three-dimensional models of blood flow in the literature use zero traction or constant pressure outlet boundary conditions. However, this can result in inaccurate blood pressure computation (Perktold et al. 1995, Taylor et al. 1998, Stroud et al. 2002, Oshima et al. 2001, Cebral et al. 2003, Stuhne et al. 2004). For simulations of blood flow in arteries, the outlet boundary conditions represent the downstream vascular resistance, which is dependent on the smaller arteries, arterioles, and capillaries that are downstream to the terminal artery in the flow model. The ideal flow model would include the full three-dimensional computational representation of the entire circuit. However, modelling the vast extent and complexity of the arterial tree is difficult due to limited image data and resolution. In this study the boundary conditions are computed based on the fed volume of each terminal, and the constant-pressure boundary conditions are applied on the same vasculature only as a proof-of-concept to show the large errors that can result in flow predictions by ignoring the effect of the downstream circulation. Additional to the outlet boundary conditions prerequisite, for performing the flow simulation, a computational model of the arteries is required, which in this study was the reconstructed vasculature, extracted from cryomicrotome image data.

Cryomicrotome imaging has not only the advantage of resolution, but also of allowing estimation of regional microsphere perfusion at regions of user-defined size and volume in the whole organ. Furthermore in addition to the embedded microspheres, the vasculature of the whole organ down to micro-vessels can also be imaged after fluorescent cast material is perfused in the organ (Spaan et al. 2005, Ter Wee et al. 2006, Lagerveld et al. 2007, Spaan et al. 2008, Van Den Wijngaard et al. 2008, Van Den Wijngaard et al. 2009, Van Horssen et al. 2009, Lagerveld et al. 2010, Van Den Wijngaard et al. 2010, Van Den Wijngaard et al. 2011, Lagerveld et al. 2011). The detailed rich cryomicrotome image volumes, which allow three-dimensional localization of microspheres and vessel morphometry, provide feasible data to investigate errors in models of regional myocardial perfusion by comparing microsphere regional perfusion data with a linear steady-state 1-D blood flow simulation in the vasculature.

Three cryomicrotome image datasets were acquired of a pig heart – vasculature, microspheres, and myocardium. A 1-D blood flow simulation was performed on the extracted and reconstructed vasculature using the Hagen-Poiseuille model. Microspheres were detected and assigned to their nearest terminal branch in the vasculature to count the number of microspheres that passed through each branch in the vasculature. In order to obtain boundary conditions for the terminals of the reconstructed vasculature, binary segmentation of the ventricles was obtained from the cryomicrotome images of the myocardium (see Fig. 5.2 b) to map the fed volume of each terminal onto the vasculature. The methods section describes the image acquisition, vasculature extraction and measurement, microsphere detection and assignment to vasculature, myocardial ventricular segmentation, and the blood flow simulation. The fitting of the daughter-to-parent ratio of the vessel cross-sectional area and the branching angle data to the error between the flow prediction and microsphere perfusion data to obtain a model of disproportionate microsphere distribution is then outlined. The results section graphically illustrates and quantitatively demonstrates the comparison between the

regional microsphere perfusion and regional blood flow distribution throughout the vasculature and myocardium. It also plots the surface fitted to the area ratio and branch angle parameterised model of the error between microsphere and flow distribution. Using these results, a correction of the 1-D flow with the disproportionate microsphere distribution model is proposed, which increases the agreement of the predicted regional flow with the experimental regional microsphere perfusion.

5.2 Methods

The first step was image acquisition, which was subsequently followed by microsphere detection, myocardial ventricular segmentation, and vasculature extraction and measurement (see Fig. 5.1). The porcine cryomicrotome image data used in this study is shown in Fig 5.2. After the image processing steps were completed, a 1-D blood flow simulation was performed on the reconstructed arterial network. Microspheres were assigned to their source terminal node in the vasculature and the shortest path weighted by maximal flow was calculated from the root node to each terminal in order to count the number of microspheres that passed through each of the branches along the paths to the terminals. This also allowed defining the main source or parent artery (LCX, LAD) of each branch, terminal, and microsphere. Fed volumes (voxels) along with the microspheres were assigned to each terminal and summed up the tree to obtain the regional perfusion data. A Hagen-Poiseuille model of blood flow was simulated on the reconstructed coronary vasculature (image data shown in Fig. 5.2) with the fed volume at the terminals as the boundary conditions. Finally, for computationally modelling the disagreement between the microsphere perfusion and 1-D flow simulation, the branching angles and daughter-to-parent cross-sectional area ratios of all bifurcating branches in the network were calculated and fitted to the microsphere perfusion data. Each of these steps is elaborated in the sections below.

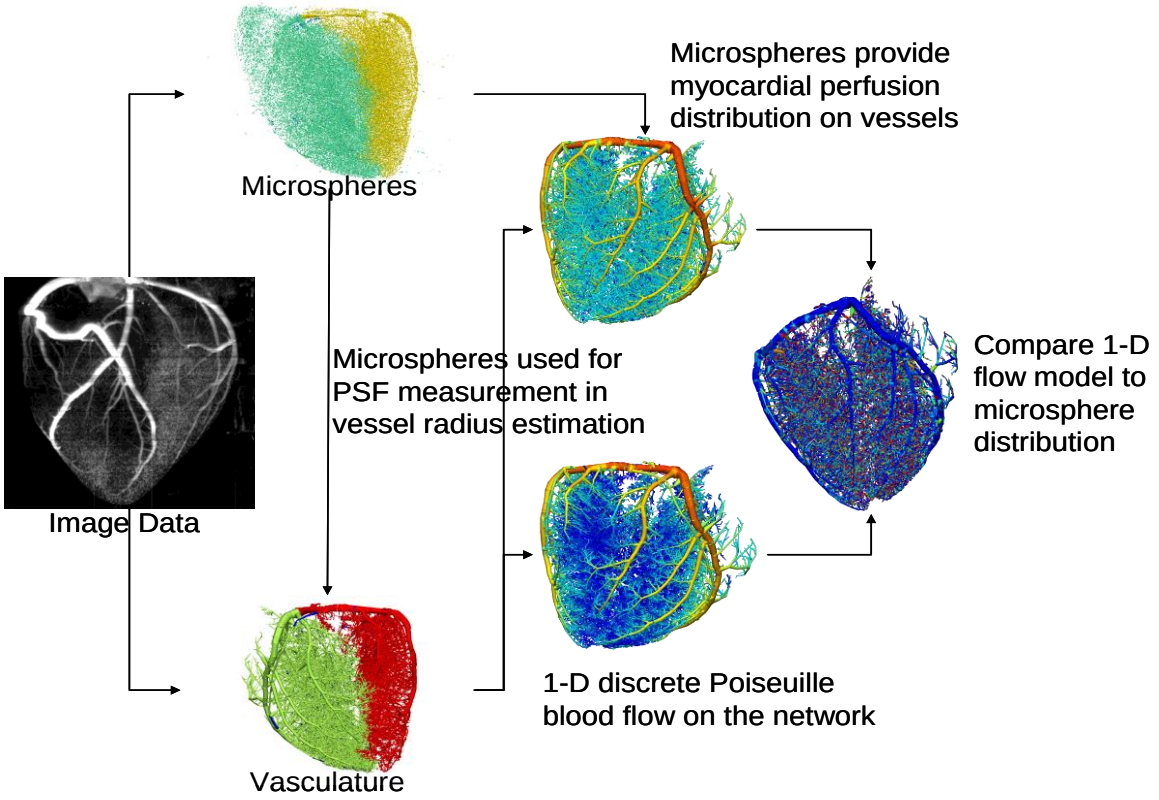


Figure 5.1: Schematic illustration of microsphere (chapter 3) and vasculature (chapter 4) extraction and regional coronary perfusion measurement.

5.2.1 Image Acquisition

The imaging cryomicrotome at the Department of Biomedical Engineering, Academic Medical Centre, University of Amsterdam (Spaan et al. 2005) was used to image a pig heart that was perfused with microspheres and fluorescent cast material in the vasculature (see Fig. 5.2). Three image datasets were obtained based on separate filter settings – the myocardial outline images, microsphere images, and vasculature images. The image acquisition from the cryomicrotome modality was performed according to the procedures explained in Van Horssen et al. 2009.

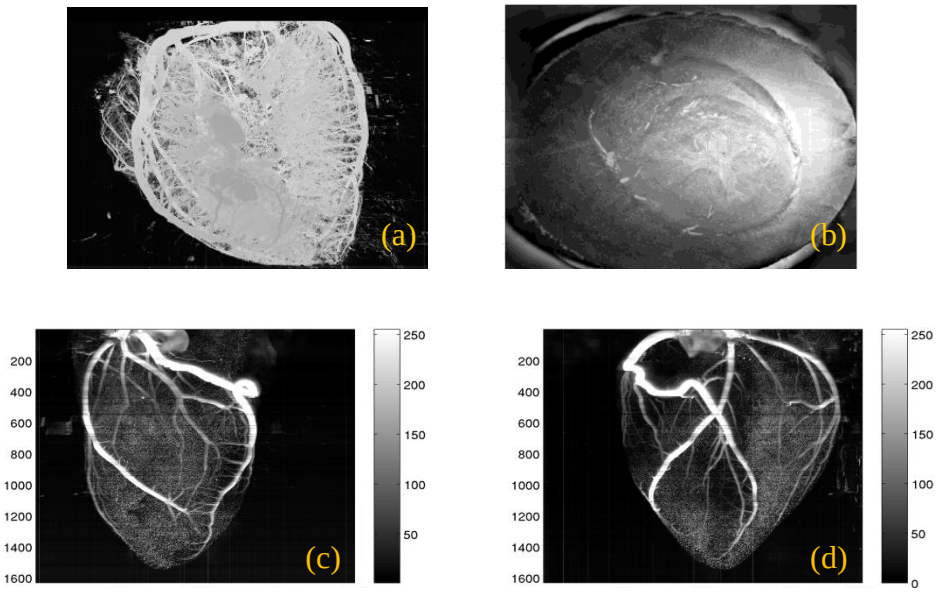


Figure 5.2: Maximum intensity projection of the coronary vasculature (a), myocardial outline image (b) and microsphere images (bottom (c) and (d)). Voxel resolution is 50 micrometers cubed.

5.2.2 Microsphere Detection

The individual fluorescent microsphere beads (15 micrometer diameter) were captured in the cryomicrotome image volume stack as clusters of bright connected pixels (as shown in Fig. 5.2c-d), and the three-dimensional location of each microsphere in the pig heart was determined according to the heuristical region-growing described in chapter 3 section 3.2.3.

5.2.3 Myocardial Segmentation

An outline image volume of the myocardium captured by the digital camera in the cryomicrotome was segmented to produce a binary image stack of the left ventricular myocardium. This segmented binary image volume of the myocardium was used in calculating the fed volume boundary conditions of each individual terminal (refer to section 5.2.6).

5.2.4 Vasculature Reconstruction

The 3-D vasculature image dataset of the pig heart was extracted and measured according to the methods described in chapter 4 section 4.2. The pig heart whose vasculature was extracted

for this study (see Fig. 5.2 a) only contained the left coronary arterial (LCA) tree since no fluorescent cast material was inserted in the right coronary artery during the experimental procedure (the pig heart used in this chapter is dataset # 6 in Table 1.1) .

5.2.5 1-D Blood Flow Simulation

An arterial network flow simulation can give flow rates in each branch of the vascular tree, based on the conductance of each branch, which can be calculated from the length and radius of that segment. The input and output boundary conditions have to be defined either by the flow rate or the pressure at the input and terminal nodes. The flow in each segment and pressure at every node can be computed given the conductance of the segment, and the viscosity of blood is known. The segment conductance is $G = Q / \delta_p$, where Q is the volumetric flow rate [cubic millimeter / second] and δp is the pressure drop [pascals]. At any node, the sum of the inflows must equal the sum of the outflows. In the case of a bifurcation, this can be expressed as:

$$\begin{aligned} Q_p &= Q_{d1} + Q_{d2} \\ G_p(P_i - P_n) &= G_{d1}(P_n - P_{o1}) + G_{d2}(P_n - P_{o2}) \end{aligned} \tag{5.1}$$

In equation (1), Q_p is the flow in the parent branch and Q_{d1} and Q_{d2} are the flows in the two daughter branches. G_p is the conductance of the parent branch and G_{d1} and G_{d2} are the conductances of the two daughter branches. The pressure drop across the parent branch is the difference between the input pressure P_i and the pressure at the junction node P_n. The pressure drops across the daughter branches are the differences between the pressure at the junction node and the output pressures P_{o1} and P_{o2}, respectively. This is visually illustrated in Fig. 5.3 below:

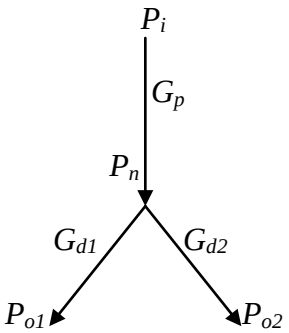


Figure 5.3: Sample bifurcation network with input and output pressures and known conductances for the parent and daughter branches.

The conductance G for each segment was calculated with the segment branch radius r, length L, and assuming viscosity of blood μ = 0.0035 Pascal-second:

$$G = \frac{\pi r^4}{8\mu L} \tag{5.2}$$

Flow equations applied at every node in the network resulted in a system of linear equations in which the unknown nodal pressures were solved for.

5.2.6 Boundary Conditions

Three sets of boundary conditions (one homogeneous and two heterogeneous) were applied to the reconstructed vasculature model in the blood flow simulation. In the first set (homogeneous boundary conditions), the input pressure was set to 100 mm-Hg and the output pressures at the terminal nodes were set to 60 mm-Hg. These values were based on Chilean et al. 1991, who found that for a coronary perfusion pressure of 100 mm-Hg, the subendocardial arteriolar pressures were 60±4 mm-Hg for vessels ranging from 80-120 μm in diameter. The terminal vessels in the pig heart extracted from the cryomicrotome vasculature dataset were in a similar size range of 50-200 μm. Note - the constant pressure boundary conditions flow model is performed in this work only as proof of concept to show the large errors that can

result in flow predictions if the effect of the downstream vascular resistance on the arterial pressure is ignored.

In the second set (heterogeneous boundary conditions), the fed volume (number of voxels) perfused by each terminal was used to calculate the fraction of the total flow as the boundary condition at that terminal. The number of voxels perfused by or belonging to each terminal was determined as described in section 5.2.7 below. In the third set (heterogeneous boundary conditions), the number of microspheres perfused by and assigned to each terminal was used to calculate the fraction of the total flow as the boundary condition at that terminal. The number of microspheres perfused by each terminal was determined as described in section 5.2.8 below. Note – the microsphere perfusion boundary conditions flow model is performed in this work only as a proof of concept to compare the errors in flow simulations performed with the fed volume versus the microsphere perfusion measurements as the boundary conditions. In the modelling of disproportionate microsphere distribution at bifurcations and in the comparison of the flow-predictions and real experimental microsphere perfusion measurements of regional myocardial blood distribution, the microsphere perfusion based boundary conditions flow model was not used; rather only the fed volume based boundary conditions flow model was used.

The coronary volumetric flow rate is Q = 200 millilitres per minute and the volumetric flow rate per unit mass of tissue for the heart is given as q_m = 70 millilitres per minute for 100 grams of tissue (Guyton and Hall 2000). The mass density of myocardial tissue is given as ρ = 1.05 grams per millilitre (Gopal et al. 1994). In the network used in this work, only the LCA subtree was imaged and extracted. After the segmentation of the myocardium, the LCA perfused tissue volume (calculated to be 72.8% of the total myocardium) was computed from the number of voxels (volumetric pixels) in the LCA perfused region (refer to section 5.2.7) to be V_{LCA} = 1.0990e+05 cubic millimetres = 109.9 millilitres. The volumetric

flow rate specified at the inlet boundary condition was calculated to be $Q_{LCA} = V_{LCA} \bullet \rho \bullet q_m =$ 1346.3 cubic millimetres per second. The outlet flow boundary condition of each terminal was calculated as a fraction of the inlet flow boundary condition, where the fraction was obtained as the proportionate fed volume of each terminal, i.e. the proportion of voxels perfused by the terminal (relative to the total number of voxels in the entire LCA perfused region). Perfusion homogeneity was assumed, i.e. the assumption that the flow is proportional to the fed volume. Voxel assignment to terminal nodes is described in the next section 5.2.7.

5.2.7 Nodal Voxel Count

Firstly, the outline images of the porcine heart were segmented to identify the voxels belonging to the myocardium (refer to Fig. 5.4), separated from the voxels classified as ventricular cavity or background. Since only the LCA arterial tree was perfused and imaged in this study, voxels whose distance to the nearest terminal was larger than the distance between the nearest terminal and its nearest neighbour terminal were labelled as region perfused by the RCA. Each voxel in the myocardial region perfused by the LCA was assigned to the nearest terminal node in the vasculature. The nearest terminal node for each LCA region voxel was identified as the one which was the shortest Euclidean distance from the voxel centre point. The distance was normalised by the terminal node radius to account for vessel size in the assignment to terminals.

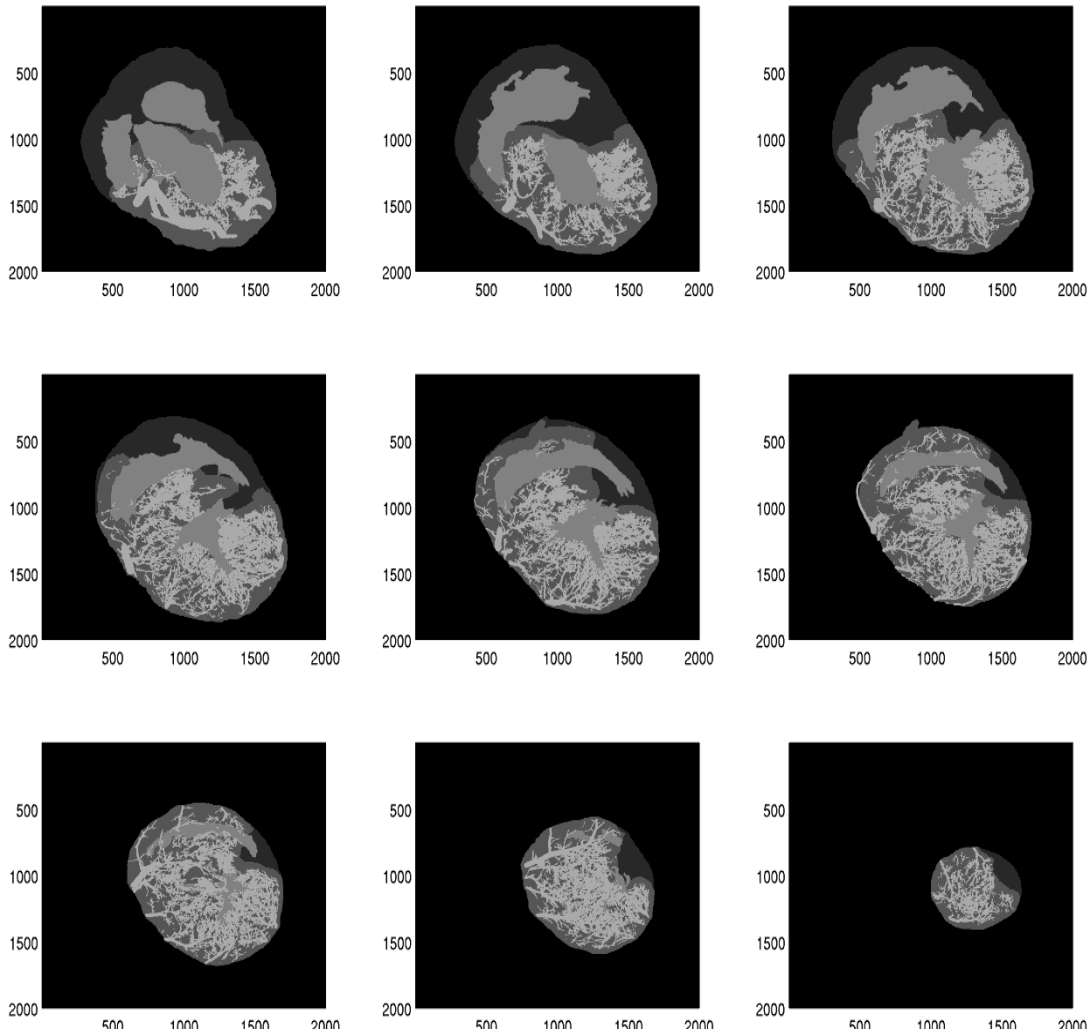


Figure 5.4: From darkest to brightest – background, RCA-perfused myocardium, LCA-perfused myocardium, ventricles, vessels, and microspheres.

5.2.8 Nodal Microsphere Count

In order to compare a 1-D blood flow simulation to the microsphere distribution, a count of the number of microspheres that passed through each node in the vasculature was obtained. This was done so that the regional distribution of microspheres (number of microspheres that passed through the branch relative to the total number inserted in the heart) that passed through each branch in the vasculature could be directly compared with the regional distribution of flow (flow in the branch relative to the total flow in the input artery) in that branch of the vasculature. Each microsphere was assigned to its nearest terminal node in the vasculature. Microspheres that were located inside vessels were assigned to their nearest node in the vasculature, and the microspheres that were located outside of vessels were assigned to their

nearest terminal of the vasculature. Microspheres located only within the LCA perfused region were assigned and counted. This resulted in a count of microspheres at every terminal node.

The entire arterial tree was subsequently represented as a graph in an adjacency matrix, wherein nodes in the vasculature were defined as vertices and segments connecting two nodes were defined as edges. The graph was weighted by the flow in each edge (segment), which was calculated from the 1-D blood flow simulation. The blood flow simulation results in pressure values at each node, and the conductance of each edge (segment) is already known from the segment length and radius. The flow in each edge (segment) was simply calculated as the pressure drop along it multiplied by its conductance.

The shortest path weighted by maximal flow was calculated from the root node (LCA) to each terminal node. To obtain a count of the number of microspheres that passed through each of the nodes along the paths to the terminals, the number of microspheres at each terminal was added to the count of microspheres at each of the nodes that fell in the shortest path from the root node to that particular terminal node. In this way, after iterating over all terminal nodes, the count of microspheres that passed through was obtained at every node in the entire vasculature. The shortest path tracing also defined the main source or parent artery (LCX, LAD) of each branch (segment), node, and microsphere. This information can be used for defining distinct perfusion regions and microsphere distributions for the LCX versus LAD.

5.2.9 Parameterised Model Fitting

The model fitted to microsphere distribution data at junctions is parameterised in this study with two variables, daughter-to-parent cross-sectional area ratio and branching angle. Using the nodal coordinate points of the vessels estimated with the vascular segmentation and skeletonization methods (refer to section 5.2.4), the bifurcation angle (θ) is calculated using

the dot product of the parent and daughter branch vectors (see Fig. 5.5) for all branching vessel segments as follows:

$$\begin{aligned}
\vec{p}_v &= \left[x_b - x_p, y_b - y_p, z_b - z_p\right] \\
\vec{d}_v &= \left[x_d - x_b, y_d - y_b, z_d - z_b\right] \\
\vec{d}_v \cdot \vec{p}_v &= \left\|\vec{d}_v\right\|\left\|\vec{p}_v\right\|\cos\theta \\
\theta &= \arccos\left(\frac{\vec{d}_v \cdot \vec{p}_v}{\left\|\vec{d}_v\right\|\left\|\vec{p}_v\right\|}\right) \\
\alpha &= 180 - \theta
\end{aligned} \tag{5.3}$$

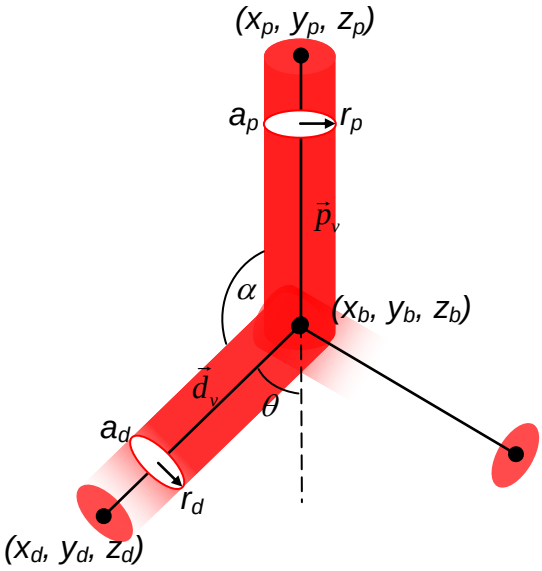


Figure 5.5: Schematic depicting the branching angle and cross-sectional areas of parent and daughter branches at a bifurcation.

Using the vessel branch radii measured with the vasculature extraction and morphometry methods described in section 2.4, the area ratio a_r is calculated for all bifurcating vessels as follows:

$$a_r = \frac{a_d}{a_p} = \frac{\pi r_d^2}{\pi r_p^2} \tag{5.4}$$

The fractional microsphere distribution (distribution in daughter branch divided by distribution in parent branch) in a bifurcating branch predicted by the 1-D Poiseuille flow model (assuming

microspheres distribute proportional to blood) is termed $m_{Q,}$ and the fractional microsphere distribution in the same bifurcating branch that was observed in the real experimental image data is termed m_R. The difference between the real microsphere and flow-predicted distributions is modelled by $f_{m,}$ which is the two-parameter (function of branching angle and area ratio) model that accounts for the disproportionate distribution of microspheres at bifurcations:

$$m_R - m_Q = f_m(\theta, a_r) \tag{5.5}$$

For surface fitting, the branching angle (θ) and area ratio (a_r) data were specified as the two independent variables, and the difference between the real and flow-predicted fractional microsphere distribution (m_R - m_Q) was specified as the dependent variable. Using linear polynomial regression, the function f_m was fitted as a quadratic polynomial surface of the form below:

$$f_m(\theta, a_r) = c_\theta \cdot \theta + c_{a_r} \cdot \frac{1}{a_r} + c_{\theta^2} \cdot \theta^2 + c_{\theta a_r} \cdot \frac{\theta}{a_r} + c_{a_r{}^2} \cdot \frac{1}{a_r{}^2} \tag{5.6}$$

As shown later in the results section, the error or discrepancy between the fractional microsphere and flow distributions increases as the branching angle increases (direct proportionality), but it increases when the area ratio decreases (inverse proportionality). A better estimate of the actual microsphere distribution can then be predicted (m_C) by correcting the microsphere distribution estimated from the 1-D flow simulation (m_Q). This correction is applied to the microsphere distribution estimated from the 1-D flow with the disproportionate microsphere distribution model f_m, which is a function of the branching angle (θ) and area ratio (a_r) are as follows:

$$m_C = m_Q + f_m(\theta, a_r) \tag{5.7}$$

The model was fitted, i.e. trained, to the data measured in the LAD subtree and it was tested on the data measured in the LCX subtree, as shown in the results section.

5.2.10 Poisson Process Modelling of Error in Microsphere Distribution

To effectively compare the blood flow simulation to the microsphere perfusion, the randomness of the microsphere distribution at the smallest vessels has to be accounted for. Typically, the number of microspheres detected in the coronary vasculature (74073 were detected in the LCA perfused region of the myocardium in the pig heart of this study) is comparable to the number of terminal vessels detected in the vascular images (42071 terminal nodes were detected in the LCA subtree). Thus the range of individual microsphere counts assigned at the smallest vessels is in the order of 0-2 microspheres (see Fig. 5.6 for the histogram of the microsphere counts at terminals). In order to model the individual microspheres as finite events in the smaller vessels, the fractional distribution of microspheres into a branching vessel is modelled as a Poisson process. The real experimental microsphere (m_R), flow-predicted (m_Q), and model-corrected m_C, fractional distribution data were binned into 15 intervals over 3 different parameters – area ratio, branching angle, and fractional flow distribution. The Poisson maximum likelihood estimate and 95% confidence intervals of the real experimental, flow-predicted, and model-corrected fractional distribution data were estimated for each bin using the following equations. For a sample of n measured values j_i, the maximum likelihood estimate $\hat{\lambda}_{MLE}$ of the parameter λ of the Poisson population from which the sample was drawn is given by:

$$\hat{\lambda}_{MLE} = \frac{1}{n}\sum_{i=1}^{n} j_i \tag{5.8}$$

The results demonstrate the increased prediction accuracy of the model-corrected fractional distribution over the flow-predicted distribution offered by the fitting.

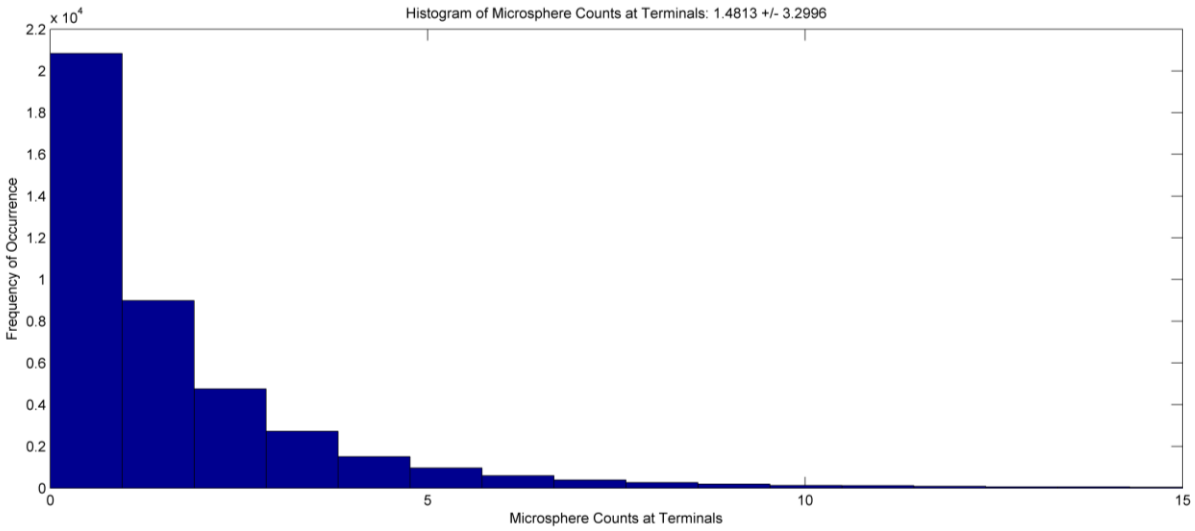


Figure 5.6: Histogram of the microspheres counted at the terminals. Mean ± standard deviation of the distribution is given in the title.

5.3 Results

5.3.1 Perfusion Territories

As discussed earlier, the disproportionate microsphere distribution model was trained on the LAD and tested on the LCX. The sources (LAD / LCX) of each node and branch in the vasculature was determined from the source path tracing performed for summing up the microsphere and voxel (fed volume) counts up the tree. In Fig. 5.7, the microspheres and vasculature are distinctly coloured according to the perfusion region of their source artery, left circumflex (LCX) or left anterior descending (LAD). Visually Fig. 5.7 demonstrates the much

larger perfusion region of the LAD compared to the LCX and also the clear separation between the perfusion territories of the two main arteries.

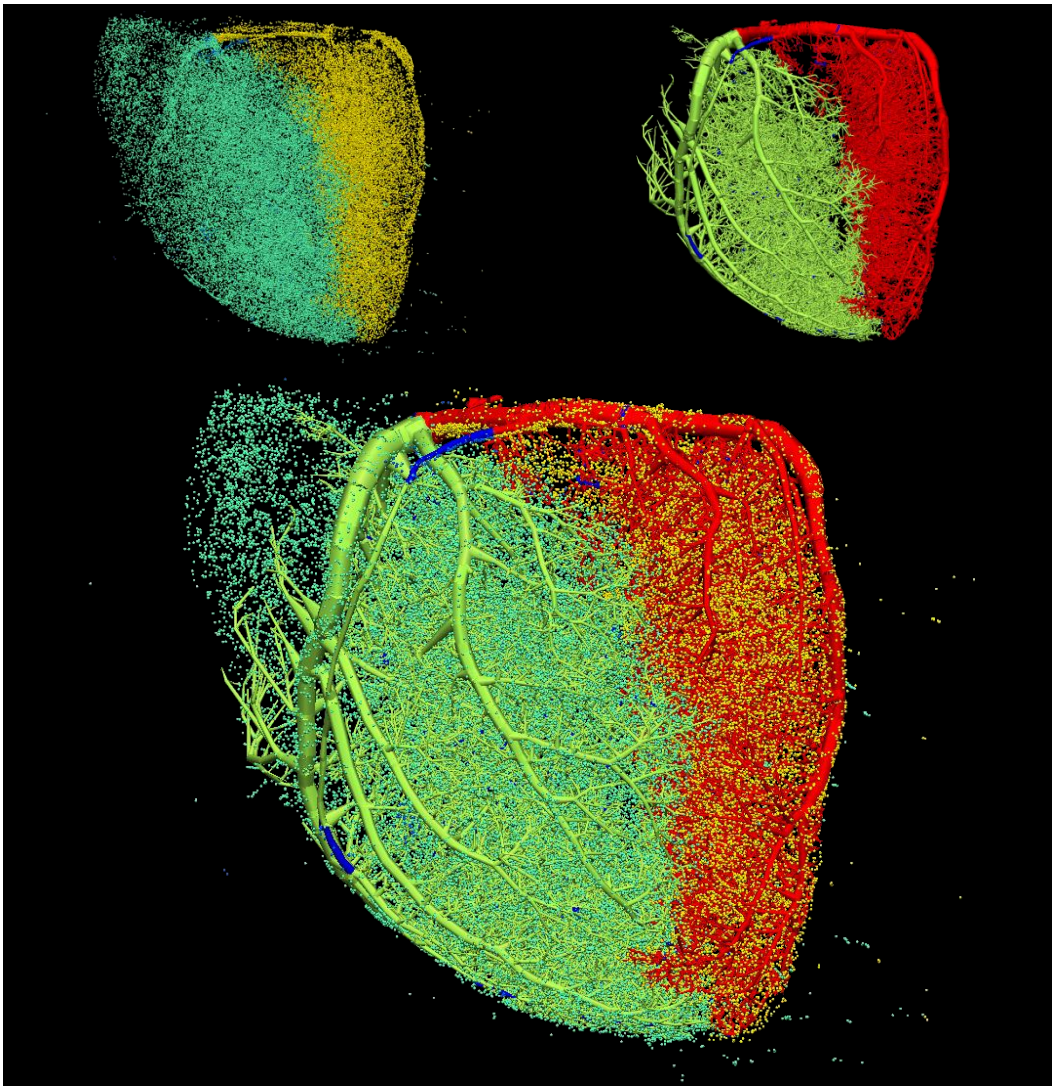


Figure 5.7: The microspheres and vasculature are coloured by the perfusion regions of the LCX (yellow-red) and LAD (blue-green). The perfusion regions are clearly distinct, and it is visually demonstrated that the LAD has a larger perfusion region. The far-lying noise, detected as microspheres, is ignored based on a distance heuristic.

5.3.2 Pressure and Flow Measurements

The 1-D flow simulation performed on the reconstructed coronary vasculature resulted in flow and pressure values at each branch across the entire arterial tree. The arterial pressure calculated with the 1-D linear static Hagen-Poiseuille blood flow model was mapped onto the vasculature as shown in Fig. 5.8.

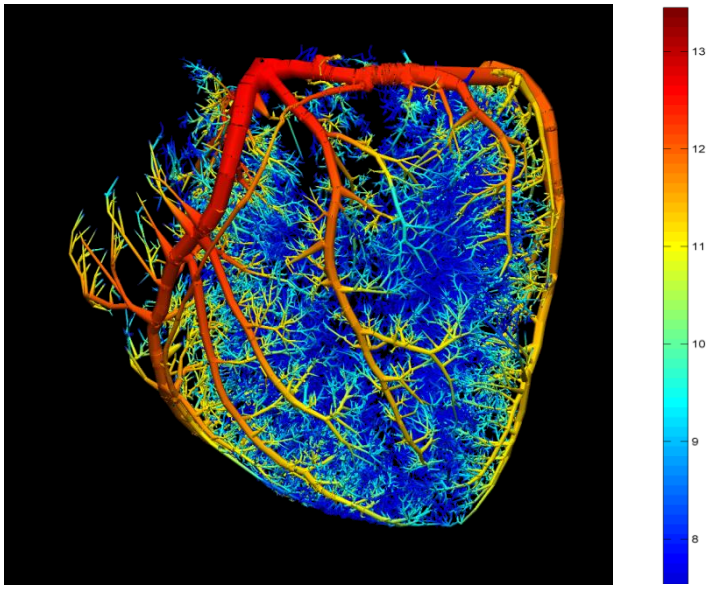


Figure 5.8: Arterial pressure calculated using the 1-D Hagen-Poiseuille blood flow simulation mapped onto the vasculature. The colorbar shows the colormapping of the range 7.9 – 13.3 kilopascals.

5.3.3 Comparison of 1-D Blood Flow and Microsphere Distribution

In order to visually compare the 1-D linear static blood flow simulation with the microsphere perfusion, the flow through every branch in the vasculature was normalized by the total flow in the root artery (LCA). Similarly, the microsphere count or number of microspheres that passed through each branch was normalized by the total number of microspheres detected. Fig. 5.9 maps the regional flow and microsphere perfusion onto the vasculature and shows the vasculature coloured by the percent difference between the microsphere and flow distributions.

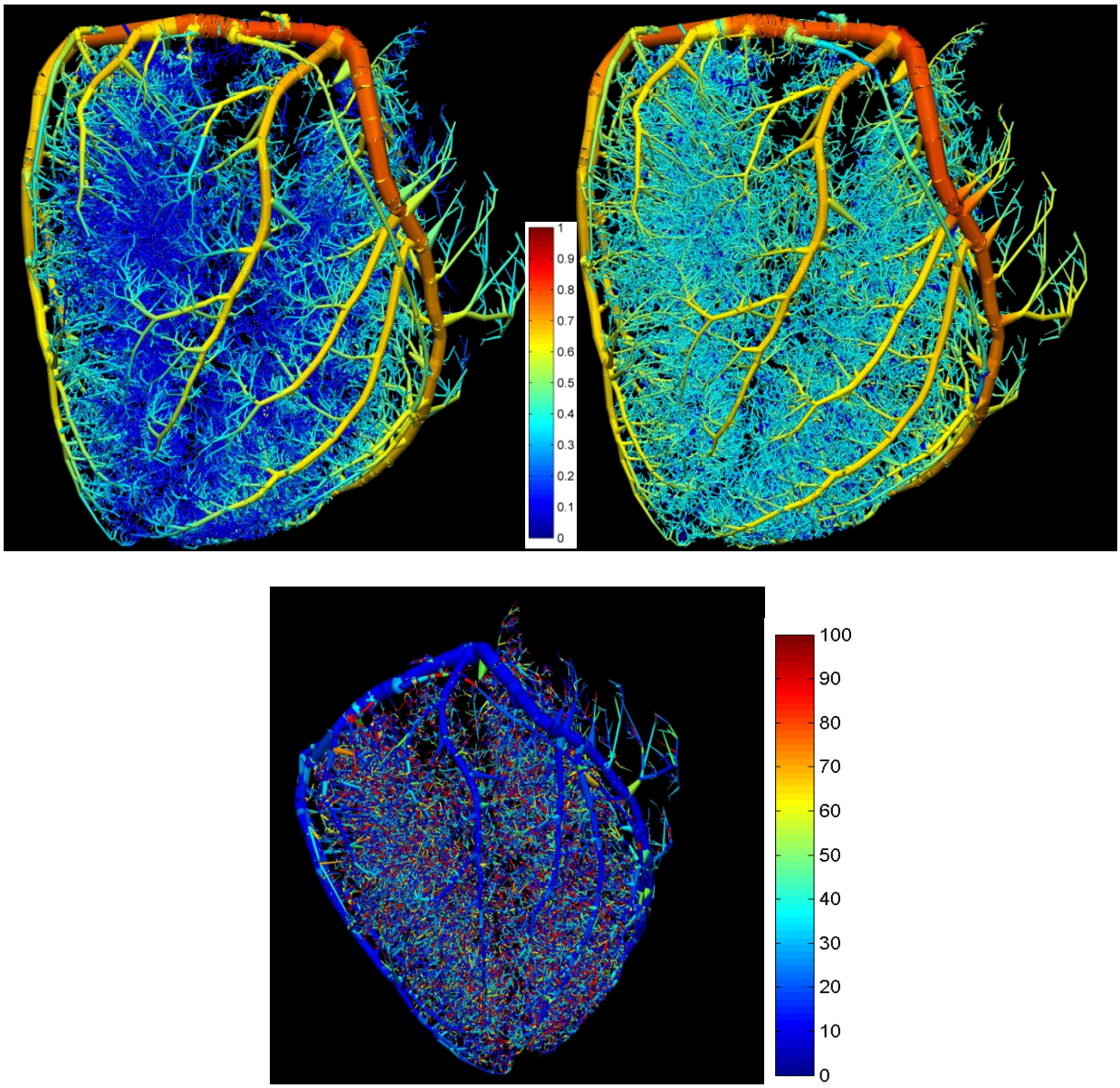


Figure 5.9: The vasculature is colored by simulated regional flow (a) and regional microsphere distribution (b). These are both ratios (distribution in the branch relative to total distribution). Both are normalized to range from 0-1 (shown in colorbar) by dividing the regional flow or count by the total flow or total microsphere count, respectively, in the LCA region of the heart. The vasculature is colored by the percent difference (c) between the 1-D flow simulation and the microsphere measurements of regional coronary perfusion. The percentage difference (0-100%) color-mapping is defined in the color bar.

Regarding direct comparison of the microsphere perfusion to the flow model, Fig. 5.10 below compares the 1-D flow simulation with the microsphere perfusion in the LCX and LAD. In this study, in the 1-D flow simulation, the variable outlet flow boundary conditions are based on the fractional fed volume of each terminal.

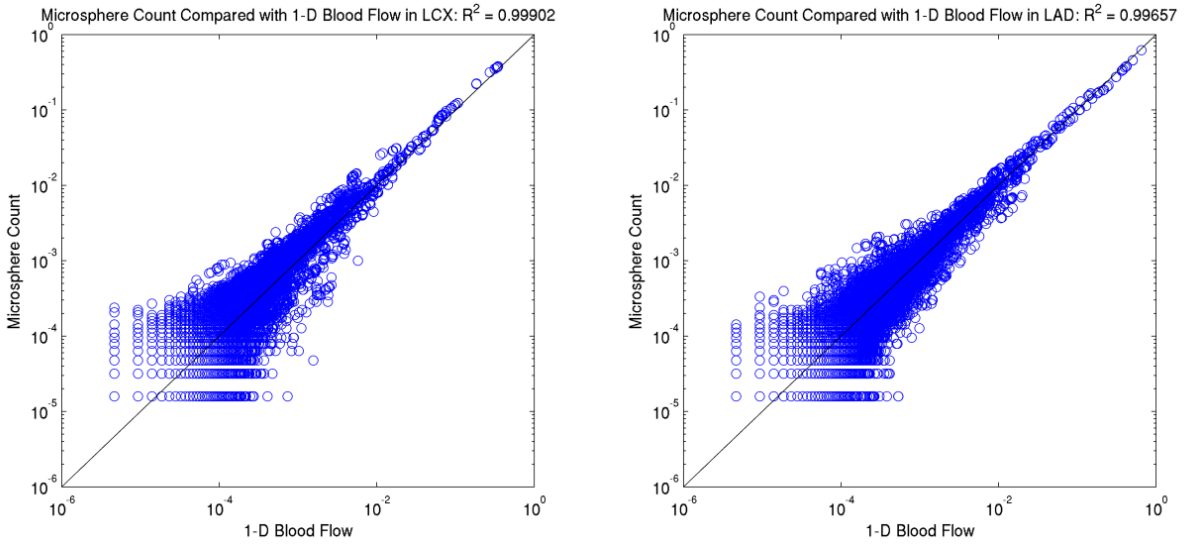


Figure 5.10: 1-D flow simulation compared against microsphere perfusion in the LCX and LAD arteries. These are both dimensionless unit-less ratios (distribution in the branch relative to total distribution). Both are normalized to range from 0-1 by dividing the regional flow or count by the total flow or total microsphere count, respectively, in the LCA region of the heart. Of the 93227 microspheres detected in the entire myocardium, 62321 were detected in the LCA perfused region. In the 1-D blood flow simulation, the total flow rate at the inlet (LCA root node) was 1346.3 cubic millimetres per second and the variable outlet flow boundary conditions were fractions of this inlet flow based on the fractional fed volume of each terminal.

The modelling of the discrepancy observed at points of lower fractional flow distribution in Fig. 5.10 between the 1-D blood flow and the microsphere perfusion due to the disproportional distribution of microspheres is discussed in section 5.3.5.

5.3.4 The Effect of Boundary Conditions on Flow Simulations

In comparing the 1-D flow simulation results to the microsphere perfusion studies, the sensitivity of 1-D flow simulations to the boundary conditions prescribed at the terminals is discussed herein. Fig. 5.11 shows the comparisons of the flow simulation performed with constant pressure boundary conditions, varying flow boundary conditions based on the number of microspheres perfused through the terminal and the fed volume (number of voxels) assigned to each terminal. Constant pressure boundary conditions are much less realistic since the pressure at all the terminals will not be homogeneous (Vignon-Clementel et al. 2006) and they are performed here only to demonstrate the large error in perfusion measurements that can occur if they are assumed. Variable flow boundary conditions based on the fractional fed

volumes at the terminals result in a better agreement of the 1-D flow model with the regional microsphere perfusion data. Additionally, the fed volume summed up the LCA subtree at each point in the vasculature is compared with the regional microsphere perfusion. Both the fed volume and the microsphere perfusion data were also used to determine the terminal boundary conditions in the 1-D flow model. The microsphere perfusion based flow boundary conditions were simulated only to compare with the flow simulations performed with the other boundary conditions.

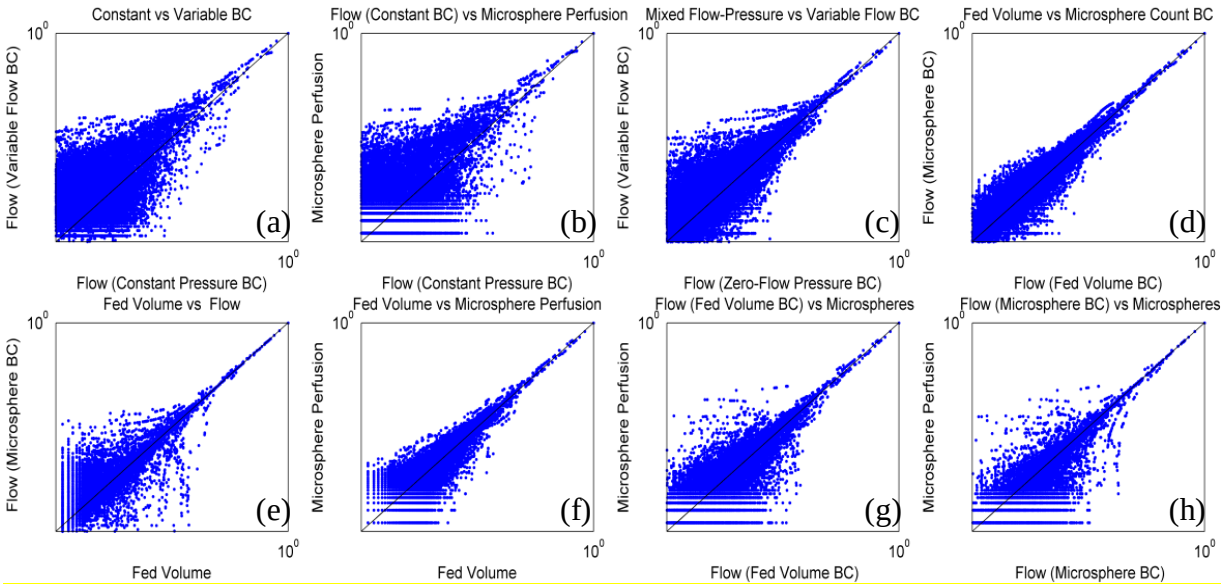


Figure 5.11: This figure demonstrates the discrepancy (especially at smaller vessels) between the microsphere distributions, terminal fed volumes, and 1-D flow simulations in explaining the regional perfusion of the myocardium. Direct comparisons of the flow simulations performed with constant versus varying boundary conditions, pressure versus flow boundary conditions, and mixed pressure-flow (pressure prescribed at zero-flow terminals) boundary conditions. Direct comparisons of the fed volume and microsphere counts at each nodal point summed up the tree and also direct comparisons of the 1-D flow simulation performed with the varying flow boundary conditions calculated based on the fed volume versus the count of perfused microspheres of each terminal. The flow simulations in turn are compared to the regional microsphere perfusion. These are all dimensionless unit-less ratios (distribution in the branch relative to total distribution). All are normalized to range from 0-1 by dividing the regional flow or count by the total flow or total microsphere or voxel count, respectively, in the LCA region of the heart.

Subpanels in Fig. 5.11 are described below (section 5.2.6 provides details of how the constant pressure and variable flow boundary conditions were set):

- Fig. 5.11 (a) is a scatter plot comparing a 1-D flow simulation performed with constant pressure boundary conditions to a 1-D flow simulation performed with

variable flow boundary conditions. This comparison shows the large error that can occur in a flow simulation that assumes constant pressure boundary conditions, which are not an accurate assumption for terminals of varying size.

- Fig. 5.11 (b) is a scatter plot comparing microsphere perfusion with a 1-D flow simulation performed with constant pressure boundary conditions. There is large disagreement between microsphere distribution and the flow simulation because the constant pressure boundary conditions are an invalid assumption.
- Fig. 5.11 (c) is a scatter plot comparing a 1-D flow simulation performed with mixed flow-pressure boundary conditions (constant pressure prescribed at zero flow terminals) to a 1-D flow simulation performed with variable flow boundary conditions. In the mixed flow-pressure boundary conditions flow simulation, the terminals where the fed volume (based on the number of voxels assigned to each terminal) was zero were assigned a constant pressure boundary condition, and terminals where the fed volume was nonzero were assigned a proportional flow boundary condition. The zero flow terminals are limitations caused because of the discreteness of the microspheres and fed volume units (voxels are discrete elements). Since the microsphere and voxel assignment is affected by terminal size, a nearby lying large terminal may be assigned all microspheres or voxels close to a smaller terminal, thus leaving the smaller terminal with zero microspheres or voxels assigned, and hence zero flow boundary condition. A small microsphere-to-terminal ratio or small voxel-to-terminal ratio caused by the lack of sufficient microspheres embedded in the myocardium or lack of sufficient voxels in the myocardial segmentation obtained from the myocardial outline images can cause this issue due in part to the limited voxel resolution of the myocardial outline images resulting in a coarser myocardial segmentation.

- Fig. 5.11 (d) is a scatter plot comparing a 1-D flow simulation performed with variable flow boundary conditions calculated based on the microspheres assigned to each terminal to a 1-D flow simulation performed with variable flow boundary conditions calculated based on the fed volume (number of voxels) assigned to each terminal. This shows that a 1-D flow simulation is highly sensitive to boundary conditions, and microsphere boundary conditions result in a different flow solution than fed volume boundary conditions.
- Fig. 5.11 (e) is a scatter plot comparing fed volume summed up across the full vasculature to a 1-D flow simulation with variable flow boundary conditions calculated based on microspheres assigned to each terminal. This plot shows that there is substantial difference between a myocardial perfusion model based on the fed volume and a myocardial perfusion model based on a microsphere boundary condition flow simulation.
- Fig. 5.11 (f) is a scatter plot comparing microsphere perfusion with fed volume across the full vasculature. At smaller vessels, the microsphere distribution starts diverging from the fed volume distribution.
- Fig. 5.11 (g) is a scatter plot comparing the regional microsphere perfusion to a 1-D flow simulation with variable flow boundary conditions calculated based on fed volume at each terminal. Again, there is discrepancy between a myocardial perfusion model based on the microsphere perfusion data and a myocardial perfusion model based on a fed volume boundary condition flow simulation.
- Fig. 5.11 (h) is a scatter plot comparing the regional microsphere perfusion across the myocardium to a 1-D flow simulation with variable flow boundary conditions calculated based on microspheres assigned to each terminal. The flow simulation

still deviates from the microsphere perfusion distribution even though its boundary conditions are based on microsphere counts themselves.

The results in Fig. 5.11 illustrate the high sensitivity of the flow simulation to the boundary conditions. This is an important aspect of flow modelling requiring accurate terminal boundary conditions to account for the downstream vascular resistance, which if ignored can result in inaccurate flow simulations.

5.3.5 Model Correction of Predicted Microsphere Distributions

The discrepancy between the 1-D flow simulation (i.e. the predicted microsphere distribution) and the real experimental microsphere perfusion was modelled with a two parameter model fitted to the error difference in between the microsphere and 1-D flow measurements. The coefficients of the polynomial quadratic fitted in the disproportionate microsphere distribution model in equation (5.6) are as follows: c_{a_r} = 11.3, c_{θ} = -0.022, $c_{a_r^2}$ = -33.95, $c_{\theta a_r}$ = -0.175, c_{θ^2} = 0.0009. The area ratio coefficients indicate a strong primarily nonlinear quadratic dependency of the error on the area ratio. The branch angle coefficients indicate a primarily linear and negligible quadratic dependency of the error on the branch angle. Thus the coefficients in particular highlight that disproportionate distribution of microspheres is sensitive to both branching angle and cross-sectional area ratio. These two parameters were found to have high correlation with the error between the fractional microsphere and fractional flow distribution at bifurcations. For the branching angle, R^2_{θ} = 0.69, where the positive correlation indicates a direct proportionality between the error and branch angle, i.e. the error increases as the branch angle increases (see Fig. 5.12). For the area ratio, R^2_{ar} = -0.67, where the negative correlation indicates an inverse proportionality between the error and area ratio, i.e. the error increases as the area ratio decreases (see Fig. 5.12). The vessel diameter on the other hand has much less correlation to the error with a correlation coefficient value of R^2_d = -

0.015. This indicates the error in between microspheres and regional flow distribution is not significantly sensitive to the vessel size or errors in vessel measurement but is more directly influenced by the branch angle and area ratio parameters. Additionally, the branching angle and area ratio are not correlated to vessel size (R^2 = -0.002) or errors in radii.

With regards to the relationship of these parameters to the fractional microsphere distribution at bifurcations, as the branching angle decreases, the fractional microsphere distribution increases (as shown in Fig. 5.12). As expected and discussed earlier, this is because microspheres are more likely to enter vessels that branch off at a smaller angle from their parent branch. As the area ratio increases, the fractional microsphere distribution also increases (Fig. 5.12) because the microspheres are more likely to flow down vessel branches with larger flow (i.e. larger cross-sectional area).

The statistical modelling above demonstrates that microsphere or flow partitioning into a daughter branch is directly correlated or proportional to the daughter-to-parent area ratio squared, which is $a_r^2 = a_d^2 / a_p^2 = (\pi \cdot r_d^2)^2 / (\pi \cdot r_p^2)^2$. Thus the distribution of flow or microspheres is related to the radius to the fourth power. This is intuitively reasonable, since in the Poiseuille equation, conductance and flow are also related to the radius to the fourth power. So in essence, the statistical modelling resulted in the same conclusion as a computational modelling approach based on Poiseuille flow would yield.

Another important point of discussion here in modelling the microsphere and flow distribution is whether a linear regression to the cosine of the branching angle, cos(θ), would result in a better fit than a linear regression of just the branching angle (θ). The cosine of the branching angle has a direct relationship with and influence on flow partitioning, and hence could be used to fit a more advanced model of microsphere distribution prediction. A linear regression to cos(θ) resulted in a higher magnitude of the regression slope (0.4323) compared

to a linear regression to θ (0.004832). However, the coefficient of determination in the goodness-of-fit statistics was not improved: 0.32 for linear regression to the branching angle directly and 0.31 for linear regression to the cosine of the branching angle. So the quality of the fit was practically the same for both. Additionally, the limitation with the cosine model is that all data of daughter vessels that branch out at an angle greater than 90° have to be eliminated because cos(θ) is only valid in relation to flow partitioning for branch angles in the range $0° \leq \theta \leq 90°$. Due to this limitation we chose to fit a model with the branching angle parameter itself to avoid losing the data of daughter vessels branching off at angles larger than 90°.

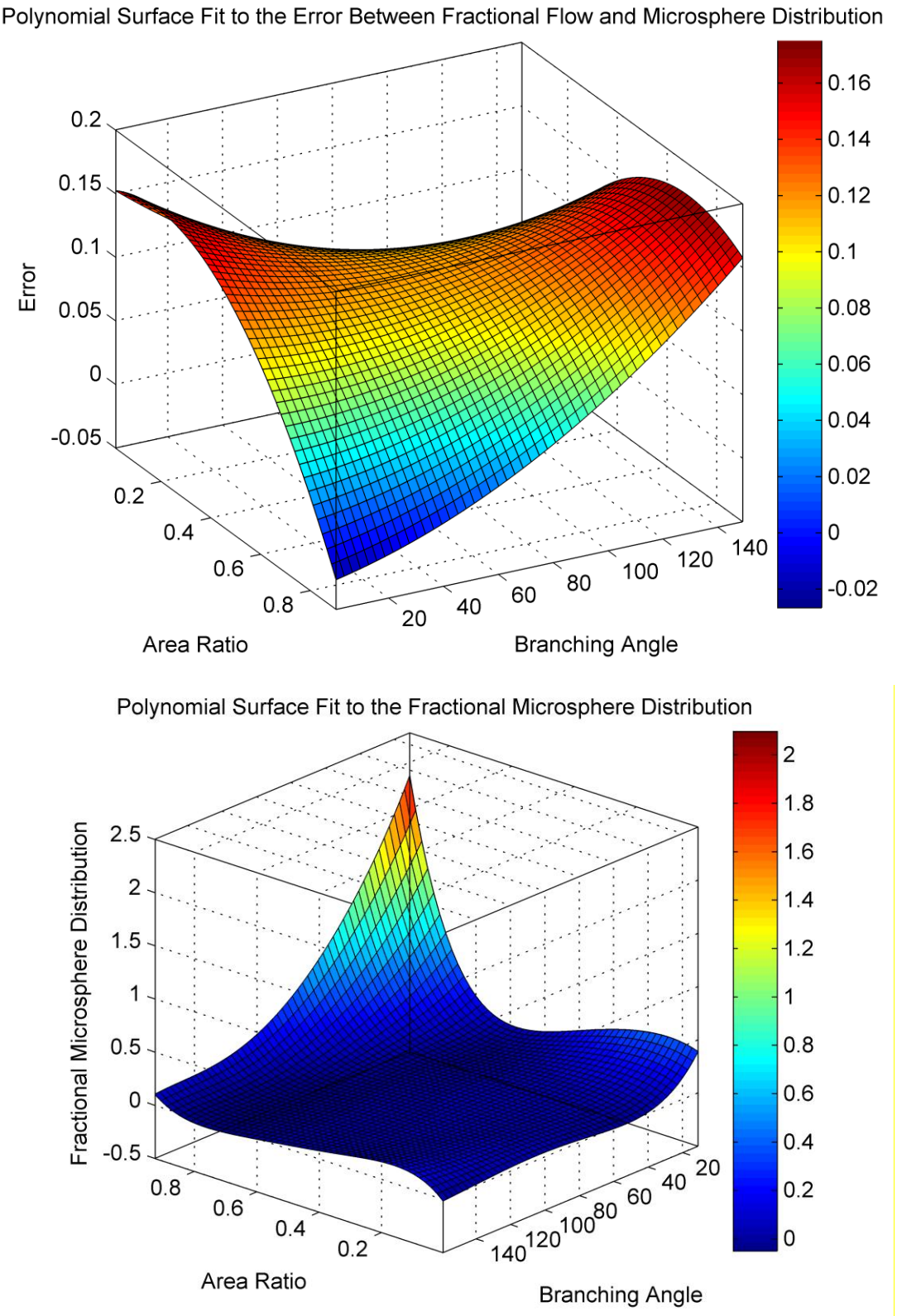


Figure 5.12: Polynomial surface fitted to the fractional microsphere distribution itself and fitted to the error between the fractional flow and fractional microsphere distribution parameterized by the branching angle (θ) and area ratio (a_r). The fractional microsphere distribution colormapping is defined in colorbar.

5.3.6 Poisson Fits to Binned Microsphere Distributions

For both the LAD on which the model was trained and the LCX on which the model was tested, Poisson distributions were fitted to the binned fractional microsphere distributions, which were separated into intervals over the area ratio, branching angle, and fractional flow distribution ranges. The Poisson fits returned the maximum likelihood estimates and 95% confidence intervals of the real experimental, model-corrected, and flow-predicted microsphere distributions in each bin. As observed in Fig. 5.13-15, the disproportionate microsphere distribution model more accurately predicts the microsphere distributions by correcting the flow-predicted microsphere distributions as it incorporates the effects of the branching angle and area ratio.

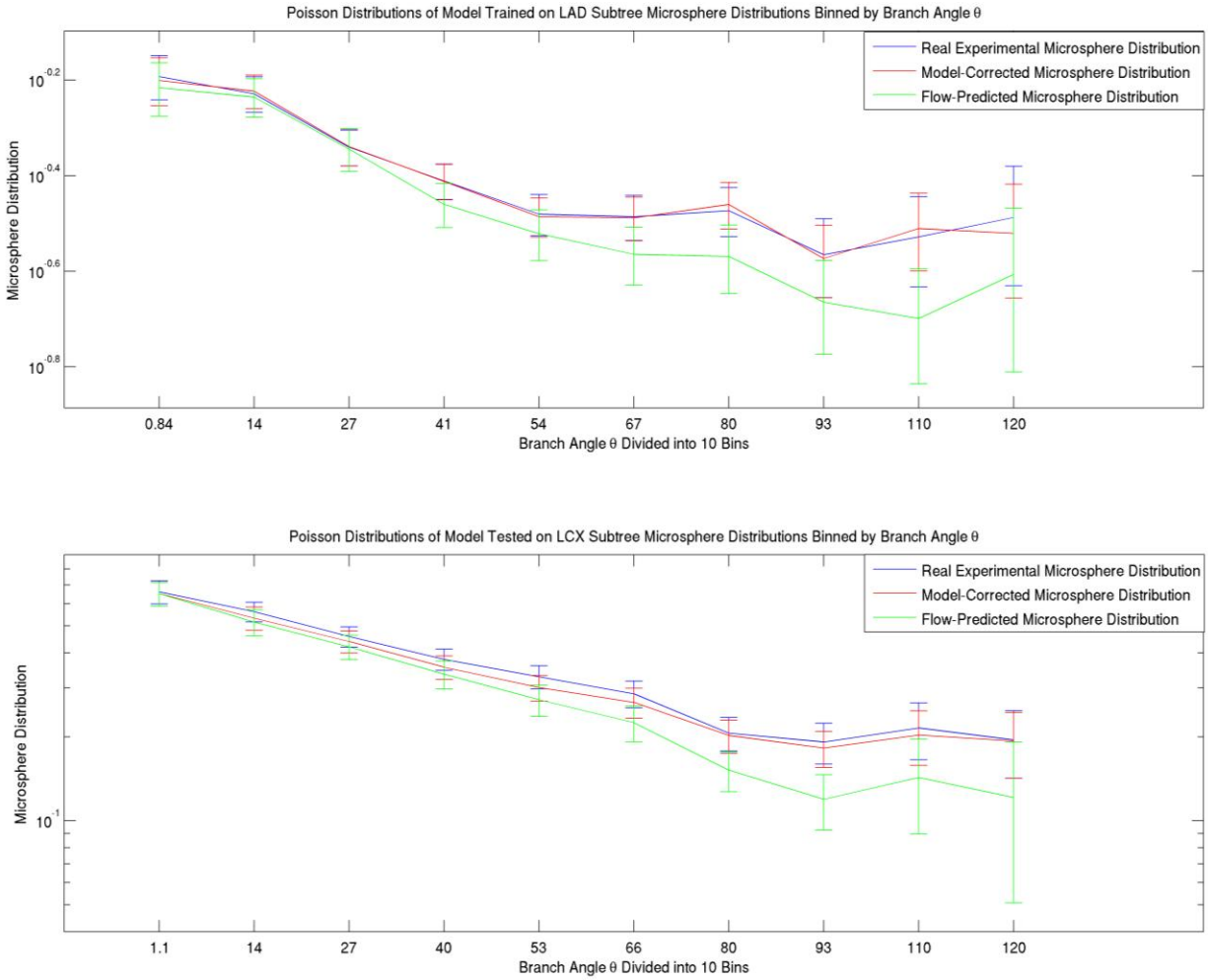


Figure 5.13: To account for the randomness in the distributions, Poisson fits to the microsphere distributions binned by branching angle for the model fitted on the LAD tree data and tested on the LCX tree data. The Poisson maximum likelihood estimates and 95% confidence intervals of each bin are shown with the errorbars. The disproportionate microsphere distribution model, incorporating the effects of the branching angle and area ratio, increases the agreement between predicted and real experimental microsphere perfusion data by correcting the 1-D flow model. The flow simulation was performed with fractional fed volume boundary conditions. The numbers labeled on the tick marks on the x-axis are not individual numbers but rather they are representative of ranges, i.e. 1-14, 14-27, 27-41,…etc.

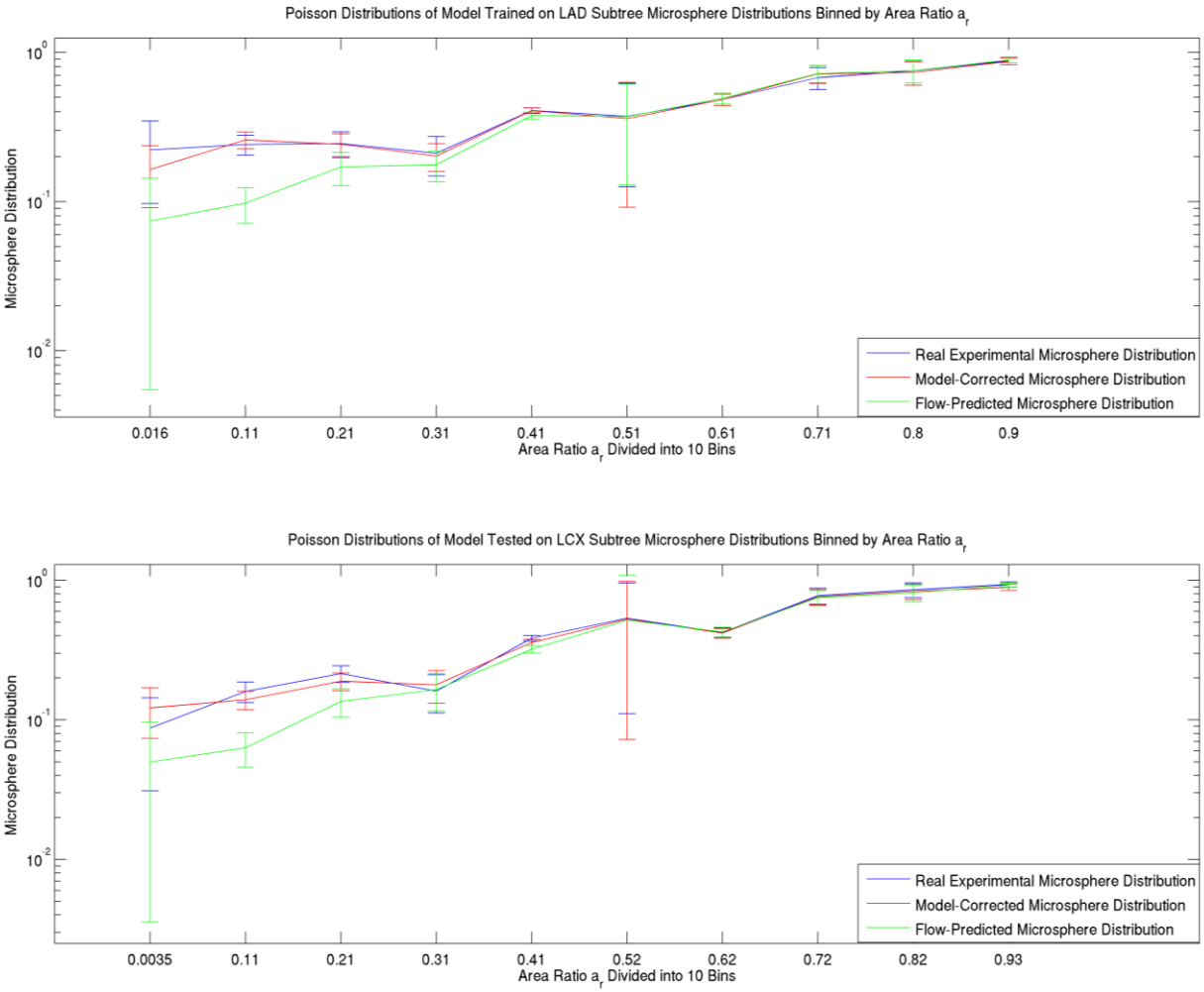


Figure 5.14: To account for the randomness in the distributions, Poisson fits to the microsphere distributions binned by area ratio for the model fitted on the LAD tree data and tested on the LCX tree data. The Poisson maximum likelihood estimates and 95% confidence intervals of each bin are shown with the errorbars. The disproportionate microsphere distribution model, incorporating the effects of the branching angle and area ratio, increases the agreement between predicted and real experimental microsphere perfusion data by correcting the 1-D flow model. The flow simulation was performed with fractional fed volume boundary conditions. The numbers labeled on the tick marks on the x-axis are not individual numbers but rather they are representative of ranges, i.e. 0.01-0.11,0.11-0.21, …, etc.

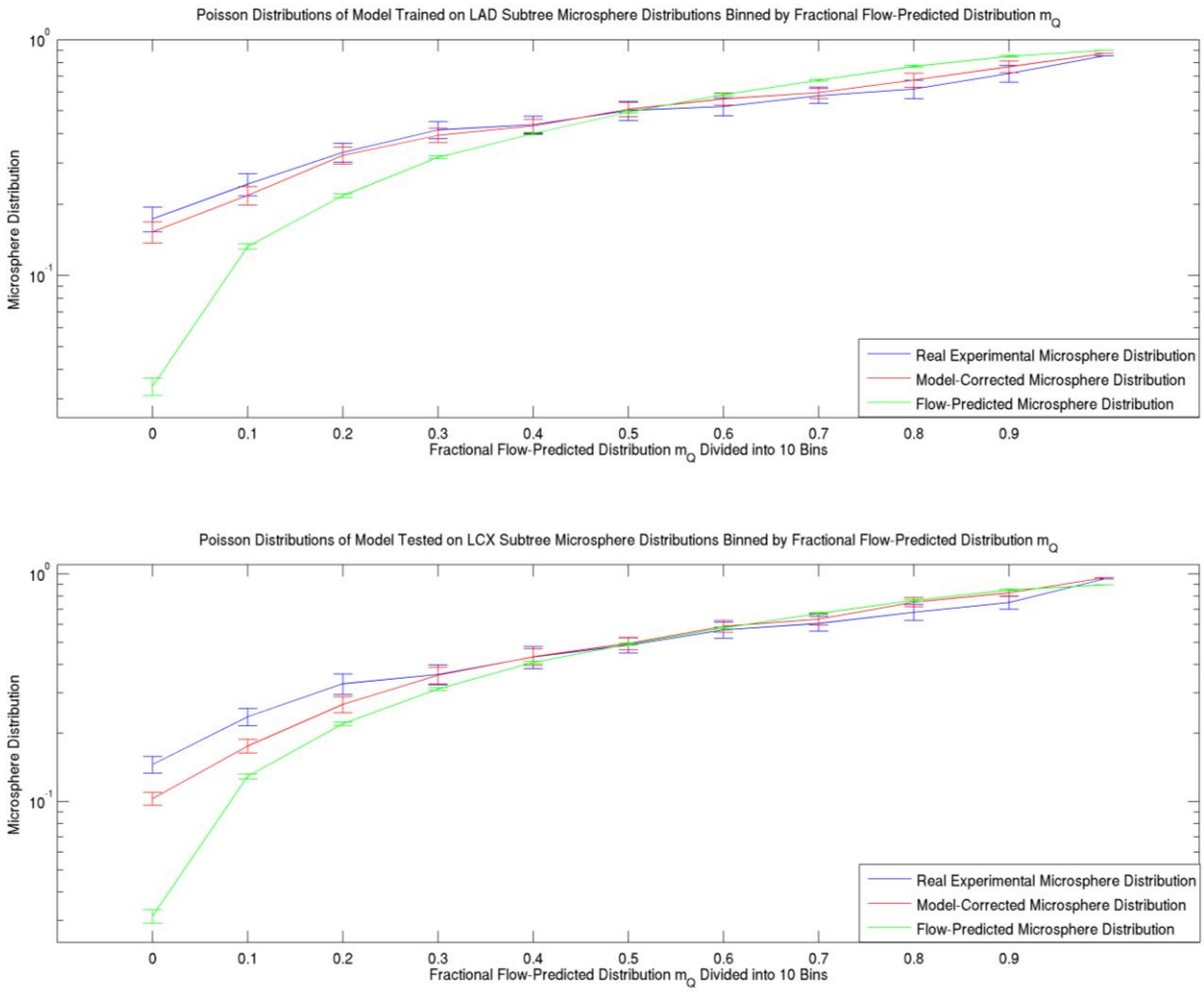


Figure 5.15: To account for the randomness in the distributions, Poisson fits to the microsphere distributions binned by fractional flow for the model fitted on the LAD tree data and tested on the LCX tree data. The Poisson maximum likelihood estimates and 95% confidence intervals of each bin are shown with the errorbars. The disproportionate microsphere distribution model, incorporating the effects of the branching angle and area ratio, increases the agreement between predicted and real experimental microsphere perfusion data by correcting the 1-D flow model. The flow simulation was performed with fractional fed volume boundary conditions. The numbers labeled on the tick marks on the x-axis are not individual numbers but rather they are representative of ranges, i.e. 0-0.1,0.1-0.2,0.2-0.3, …, etc.

5.3.7 Radius Measure Accuracy

In this section we discuss the accuracy of the vessel radius measurements and the implications of this on the accuracy of the blood flow simulations and whether the vessel radius estimates are sufficiently accurate for blood flow simulations. The uncertainty in vessel radius due to the constant versus varying cases of optical parameters was subvoxel (< 1 voxel) in 90.29% of the branches. From the artificial vessel phantom (isotropic 50µm voxel size) validation study, we found that the FWHM method of radius estimation, when performed on the raw data without correcting for the optical blurring, resulted in 11.4%, 13.3%, and 42.9% error on average for the 510µm diameter (5.1 voxels in radius), 300µm diameter (3.0 voxels in radius), and 170µm diameter (1.7 voxels in radius) vessel phantoms, respectively. In comparison, the model-based method resulted in 1.2%, 1.0%, and 0.6% error on average for the same phantoms, respectively. The average error 1.2% for the large 5.1 voxel vessel is an error of 0.06 voxels (subvoxel error << 1 voxel) in radius estimation. This extremely low error is expected as the conditions are simplified: the vessel phantom is a cylinder embedded in a homogeneous medium.

In the final part of the study, the vessel radius estimation was applied in simulating 1D steady-state Poiseuille blood flow on the reconstructed vasculature. The 1D flow model was compared to the regional distribution of fluorescent microspheres perfused in the same heart whose vasculature was reconstructed. This is because microsphere perfusion measurements are the current established gold standard for coronary flow / perfusion distribution measurements (Glenny et al. 1993, Robertson et al. 2007). The radius estimation in this study was sufficiently accurate so that the error in the flow from errors in radius measurement was much less than the error between the 1D flow-model on the vasculature and the microsphere perfusion.

Fig. 5.16 (a) plots the difference in between 1D flow simulations calculated using vessel radii measured with FWHM versus model-based method. It demonstrates the large error in 1D flow simulation that can occur when using FWHM instead of the model-based method for the vessel radius estimation. Herein the FWHM diameter estimates were measured as FWHMdecPerp (defined earlier in section 4.1.1) and resulted in an error of 1.4 (mean) ± 3.2 (standard deviation) voxels in vessel radii estimates as compared to the model-based method. Fig. 5.16 (b) plots the difference in between 1D flow simulations calculated using vessel radii measured with single (same value for excitation and emission) versus double (separate values for excitation and emission) optical parameters. The single optical parameter case meant that the PSF model (see equation 2.5) only had one single optical tissue attenuation coefficient ($\mu_t = \mu_{ex} = \mu_{em}$); and, the double optical parameter case meant that the PSF model (see equation 2.6) had two different optical tissue attenuation coefficients for excitation (μ_{ex}) and emission (μ_{em}). Fig. 5.16 (c) plots the difference in between 1D flow simulations calculated using vessel radii measured with constant versus variable optical parameters. In the constant optical parameter case, the mean values of the measured excitation and emission optical tissue attenuation coefficients were used in the PSF model for radii measurement of all vessel branches; and, in the variable optical parameter case, individual unique values of the excitation and emission optical tissue attenuation coefficients measured from the local fluorescent biomarker were used in the PSF model for radii measurement of each vessel branch. Fig. 5.16 (d) plots the difference in between 1D flow simulations calculated using vessel radii measured with PSF optical parameters estimated using constrained versus unconstrained minimization. In the constrained minimization, the optical tissue parameters (excitation and emission attenuation coefficients) were constrained by the condition $\mu_{ex} > \mu_{em}$ and bounded such that $0.001\ \mu m^{-1} \leq \mu_{ex} \leq 0.050\ \mu m^{-1}$ and $0.001\ \mu m^{-1} \leq \mu_{em} \leq 0.050\ \mu m^{-1}$ in the parameter estimation, whereas in the unconstrained minimization, the optical tissue parameters were optimized

without any constraints or bounds. Fig. 5.16 (e) plots the difference in between 1D flow simulations with no error versus with added error in the vessel radii estimates. It demonstrates the error in flow due to a simulated radii error added to the vessels in the reconstructed vasculature (of dataset # 6 in Table 1.1) of 0 ± 0.25 voxels, the standard deviation of uncertainty in model-based radii estimates due to variation in optical parameters. This shows that radii error of 0.25 voxel results in a negligible uncertainty in the blood flow simulation, particularly when compared to the large uncertainty in the blood flow simulation originating from changes to the boundary conditions, as shown in boxplot (f) in Fig. 5.16. Fig. 5.16 (f) plots the difference in between 1D flow simulations performed with boundary conditions set according to the fed volume versus the perfused microsphere count of each terminal. The fed volume boundary conditions were based on the number of voxels assigned to each terminal and the microsphere boundary conditions were based on the number of microspheres assigned to each terminal. This boxplot illustrates the high sensitivity of the flow simulation to changes in boundary conditions. Finally, Fig. 5.16 (g) plots the difference in between the regional flow distributions based on the 1D flow model versus the microsphere perfusion data. There is disagreement between these two experimental (microsphere distribution measurements) and mathematical (1-D flow simulation) myocardial perfusion models.

Though there is difficulty in quantifying error due to lack of a gold standard in cryomicrotome vessel measurement, we have shown that the error in flow due to the uncertainty in model-based radius measurement is far less significant than the error between the 1D flow simulations with fed-volume versus perfused-microsphere based boundary conditions. The 1D flow simulation is much more sensitive to change in boundary conditions than to the error in vessel radii measured with the model-based method.

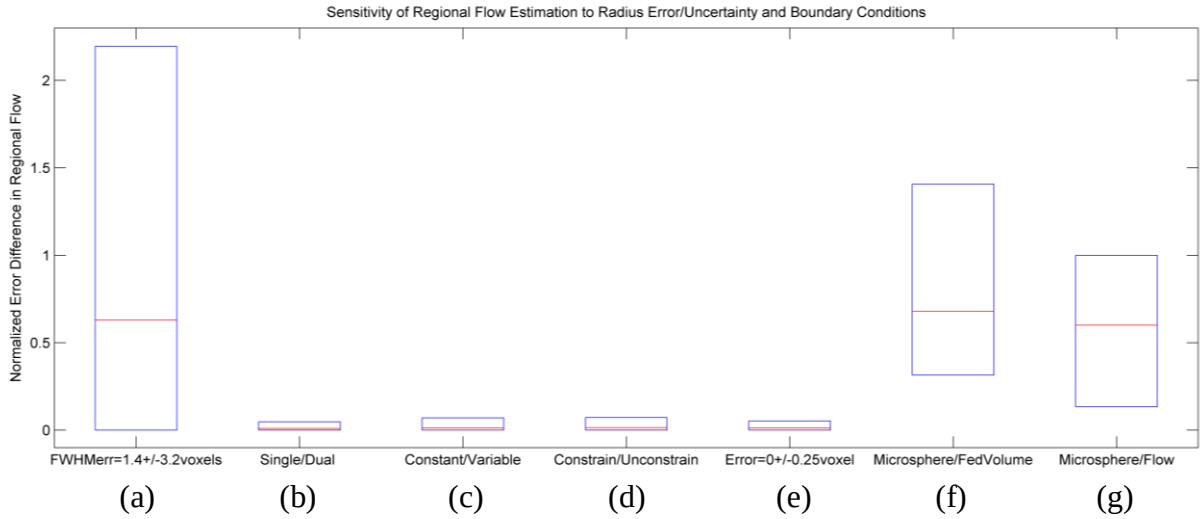


Figure 5.16: The first boxplot shows the normalized absolute error difference between regional flow distributions calculated using vessel radii measured with the FWHM versus model-based method. Error in the FWHM radii estimate is – FWHMerr = 1.4 ± 3.2 voxels (a). The next four boxplots show the normalized absolute error difference between regional flow distributions calculated using vessel radii estimated with single (μ_t) versus dual (μ_{ex} and μ_{em}) optical parameters in the PSF model – Single/Dual (b), constant versus variable optical parameters – Constant/Variable (c), constrained versus unconstrained optimization – Constrained/Unconstrained (d), and a simulated added error of mean = 0 and standard deviation = 0.25 voxels – Err = 0 ± 0.25 voxels (e). The second to last boxplot shows the normalized absolute error difference between regional flow distributions calculated using a 1D steady-state Poiseuille blood flow model simulation on reconstructed porcine vasculature with the boundary conditions based on microspheres perfused from each terminal versus fed volume of each terminal – Microsphere/FedVolume (f). The final boxplot shows the normalized absolute error difference between the regional flow distributions measured from microsphere perfusion data in the porcine coronary cryomicrotome images and estimated using a 1D steady-state Poiseuille blood flow model simulation on the vasculature reconstructed from the same pig heart – Microsphere/Flow (g).

In summary, our results indicate that the radius measures have subvoxel accuracy and the uncertainty in flow due to the uncertainty in model-based radius estimates is much less than the uncertainty in flow due to a change in boundary conditions. The difference in flow due to different radius measures (due to different parameter settings of the PSF) is much less than the difference between the flow model and microsphere perfusion data. Comparing the large error in flow due to the prior FWHM method versus the relatively small error due to the model-based method, the work in this study has improved vessel radius estimation such that radius error is no longer the limiting factor for accurate blood flow simulations. The vessel radius estimation in this work from cryomicrotome images is accurate for 1D regional flow distribution simulations in consideration of the fact that the error in radius estimation causes

much less error in flow than the boundary conditions, and the uncertainty in flow from radius error is far less than the error between the regional flow distributions calculated with the 1D flow model and measured with the microsphere distribution. The flow is more sensitive to changes in boundary conditions than to the vessel radius optimization settings of a single versus double optical parameters, constant versus varying optical parameters, or constrained versus unconstrained minimization.

5.4 Discussion

This study compared quantitative microsphere perfusion in the myocardium with coronary arterial flow calculated with a linear static 1-D blood flow model. The results indicated discrepancy between the regional flow predicted by the 1-D Poiseuille model and regional flow measured from microspheres. This error is due to the disproportionate distribution of microspheres dividing at bifurcations. The error between microspheres and flow was found to be sensitive to branching angle and area ratio. Using these two parameters, a model was fitted to the fractional microsphere data in this study and used to correct the 1-D flow-predicted microsphere distribution. This disproportionate distribution model more accurately estimated the real experimental microsphere distribution by correcting the 1-D flow predicted distribution of coronary perfusion.

In this coronary perfusion analysis study, among several, three factors are the most important to account for in modelling blood flow. The first is the terminal boundary conditions, to which the final flow solution is highly sensitive. The choices of constant versus variable boundary conditions or pressure versus flow boundary conditions or fed volume based versus microsphere count based boundary conditions all influence the flow simulation. As demonstrated in the results in comparison against the microsphere perfusion, an implementation assuming constant output boundary pressures at all the terminals, regardless of

their size can result in grossly inaccurate coronary perfusion estimation. Pressures across all the terminals are not homogeneous but rather dependent upon the flows through them. In a more realistic simulation, varying flow boundary conditions is a much more optimal choice, wherein the terminal flows can be set such that their sum equals the input flow. The flow boundary conditions can be calculated according to the number of perfused microspheres or fed volume of each terminal, as done in this study. The fed volume in this study was calculated as the number of voxels in a binary image of the segmented myocardium (specifically the LCA perfused region) assigned to each terminal node based on a distance heuristic normalized by the size of the terminal vessel. The fed volume boundary condition based flow simulation inherently assumes spatial homogeneity of myocardial perfusion. However, the spatial heterogeneity of myocardial perfusion and its influence on the calculation of terminal flows is subject of further research as this may well be one of the underlying causes of why microspheres do not always distribute proportional to the 1-D flow.

The second factor to be accounted for modelling blood flow in a reconstructed vascular model is the errors in vessel radius estimation. As discussed in section 5.3.7, the work in this study has improved the error margin of the radius estimation such that it is no longer the limiting factor for accurate blood flow simulations on vasculature models reconstructed from cryomicrotome images. By incorporating a model of the image acquisition in the radius estimation, the model-based method reduces the error in the radius estimation and consequently flow estimation to be far less than the error in flow estimation due to uncertainty in outlet boundary conditions. Regarding whether the errors in flow due to errors in radius causes the discrepancy between the microsphere perfusion measurements and flow simulation using fed volume boundary conditions, the two parameters that the error between microspheres and the flow model was most sensitive to were branching angle and area ratio, not vessel radii. The magnitude of the coefficients in the disproportionate microsphere distribution model listed

in the results indicate that the error in between the flow and microspheres was highly influenced by and quadratically related to area ratio and linearly related to branching angle. The error was not well correlated to the vessel size, and thus the error in between the microspheres and flow model is not primarily caused by errors in radius estimation but is rather caused by the disproportionate distribution of microspheres due to flow partitioning at bifurcations, which is most directly affected by branching angle and area ratio.

The third factor that is important to account in modelling blood flow with microspheres is the discreteness of bead counts as they reach the microvasculature. At larger vessels, the microspheres will likely distribute proportional to the flow, but at smaller vessels, randomness plays a more important role in their distribution. According to past literature, less than 400 microspheres in a region will give statistically inaccurate perfusion measurements (Prinzen & Bassingthwaighte 2000). Hence, modelling their distribution as finite discrete Poisson processes is necessary to account for the randomness at terminal boundary nodes, as done in this study.

Chapter 6

Conclusions

The work in this study has developed a new improved method of vasculature reconstruction and blood flow simulation on a coronary arterial network extracted using optical fluorescence microtomographic images of both vessels and microspheres in combination. The method applies the cryomicrotome images of microspheres in two ways: first, in the classical method of measuring *unknown-objects* (vessels) using *known-objects* (microspheres), which serve as fiducial biomarkers with which a model of light transport in tissue is computed to simulate and optimize the radii of the vessels; second, in coronary perfusion measurement wherein the regional distributions of the microspheres, embedded throughout localized regions of the vasculature, are measured. Using this approach, whole-organ vasculatures of several hearts and other organs have been reconstructed in 3D computational representations with micro-vessels down to the range of 0.03 mm radius. The vessel detection methods proposed in this thesis also worked well in extracting vasculature from CT (computed tomography) images as well, demonstrating their applicability to 3D image volume datasets obtained with tomographic modalities.

These vessel detection and radius estimation methods have been validated with manual segmentation and comparison with previously published methods, ground truth microscope measurements of embedded vessels, and simulated phantoms of computer-generated vessels. The radii estimated with the model-based method also conform well to the uniform shear stress hypothesis and Murray's law at vessel junctions. The new radius estimation method significantly improves accuracy of vessel radius estimation and consequently blood flow measure, as compared to other radius estimation methods such as FWHM.

In comparing the new proposed method to previous state-of-the art vessel radius estimation methods, the study also revealed that incorporating models of light transport in tissue increases the accuracy of the vessel radius estimation for the vasculature imaged by the cryomicrotome. Additionally, small vessel radius estimation with the model-based method was sensitive to variation in optical tissue parameters and thus was significantly enhanced via the inclusion of a spatially variant PSF model for more accurate radius estimation.

6.1 Summary

This thesis develops, implements, and evaluates a novel method for accurately extracting radii of blood vessels in cryomicrotome image data that incorporates the vessel geometry, orientation, and optical tissue properties into the vessel radius estimation. The influence of incorporation of optical tissue properties and their intramural spatial variation was evaluated and accurate models of coronary and renal vasculatures from cryomicrotome images were reconstructed. To obtain this goal, several substeps were completed:

1. PSF Model: A theoretical model of the PSF (improved version of Rolf et al. 2008) was fitted to real experimental images of microspheres embedded in tissue to estimate optical tissue attenuation coefficient parameters to be incorporated in the vessel radius estimation.
2. Segmentation and skeletonization: A binary mask of the segmented vasculature was obtained after removing non-vessel noise structures. 3D skeletonization was performed on the vasculature mask to obtain vessel centrelines.
3. Radius estimation: A cylindrical model of the vessel segment was convolved with the PSF model to simulate the image formation. The cross-sectional image produced at the image plane of the convolved vessel segment model was fitted to the real observed

cross-sectional image at the current image plane to estimate the best fit of the vessel radius for the particular vessel segment.

4. Vasculature reconstruction: The radius estimation was performed for all the segments in the vessel network, thus allowing the rendering of a whole-organ vasculature reconstruction for pig heart and kidney lobe.
5. Coronary perfusion measurement: A 1D Hagen-Poiseuille steady-state blood flow simulation was performed on the coronary arterial network of a porcine vascular reconstruction. Microsphere perfusion data in the same heart was compared to the flow simulation. The discrepancy between the perfusion data and flow model was modelled with branching angle and area ratio as the parameters to predict the disproportionate distribution of microspheres. The model increased the accuracy of the prediction of microsphere distribution with the 1D flow model.

6.2 Methods

After reviewing the relevant literature and experimenting with different methods, the following important decisions were made regarding which algorithms to use for PSF model validation, optical parameter estimation, segmentation, skeletonization, and vessel radius estimation:

6.2.1 Optical parameter estimation

- An analytical PSF model, based on the excitation and emission optical tissue attenuation coefficients was validated with numerical Monte Carlo simulation of photons.
- As an application of fluorescent microspheres embedded in tissue for PSF parameter estimation, individual microspheres were extracted and used as fiducial

markers for fitting the theoretical PSF model to obtain optimal values of optical parameters. This technique assumes the subvoxel-size microspheres as point sources embedded in tissue (as proposed by McNally et al. 1999 and Rolf et al. 2008). This is a plausible method of measuring attenuation coefficient at different regions in the heart because the microspheres can be perfused into the tissue through the vasculature. This allows for a novel implementation of the classic approach of measuring unknown objects (perfused vessels) with information gathered (optical parameters) from known objects (embedded microspheres).

6.2.2 Vascular extraction

- The vasculature was segmented from the background and non-vessel noise structures by multi-scale vessel detection with Frangi's vesselness filter followed by connected component labelling. Thinning was used to obtain the vessel centrelines, and an automatic cleaning algorithm was coded to delete spurious branches and eliminate loops. Finally, cubic hermite splines were fitted to each vessel segment to smooth out irregularities and jagged high curvature points.
- Since the vessel cross-sections are degraded by out-of-focus light, measuring the vessel radii from the blurred vessel boundaries is unreliable. We tested image restoration to remove the out-of-focus light in the vascular image data but found that deconvolution turned out to be ineffective because of ringing and intensity saturation causing the voxels inside the vessel to decrease in intensity. When tested in validation, the commonly-used FWHM radii-estimation method resulted in inaccurate vessel radii estimates, being affected by the halo caused by vessels' oblique orientation and optical blurring. Therefore, a new model based template-

matching radius estimation incorporating the vessel geometry, orientation, optical blurring, and pixel saturation was developed and implemented.

6.2.3 Coronary Perfusion Flow Estimation

- The regional distributions of microspheres perfused throughout the myocardium of a porcine heart were measured and mapped onto the reconstructed coronary vasculature of the same porcine dataset.
- A 1-D Hagen-Poiseuille model of blood flow was simulated on the reconstructed coronary vasculature for comparison to the regional microsphere perfusion data.

6.3 Contributions

The most significant contributions of this thesis to scientific research are as follows:

6.3.1 Methodological

- A novel combined approach is presented for vascular reconstruction and coronary perfusion estimation which simultaneously uses microspheres and vessel data obtained from the cryomicrotome. The microspheres are used for both estimating the image formation model employed in the vascular extraction and for regional perfusion measurements mapped to the extracted coronary arterial tree.
- An automatic vasculature extraction program, entitled VasEx, has been written. It implements the image processing pipeline presented in this work to enhance vessels with multi-scale vesselness filtering, remove noise with connected component analysis, trace vessel centerlines with thinning, prune out loops and spurious branches with an automatic cleaning algorithm, measure vessel radii with a model-based method, and fit splines to the vessel centerlines to reconstruct a 3D computer model of the vasculature.

- A novel algorithm incorporating the vessel geometry and orientation and the imaging modality's PSF has been developed to extract accurate vessel radii from cryomicrotome images. The new model-based template-matching radius estimation method has been validated with both computer generated vessel phantoms and ground truth microscope measurements of embedded vessels.
- A method for measuring optical tissue properties has been implemented with fluorescent microspheres that act as approximate point sources when embedded in tissue, and allow analyzing the intramural spatial variation of optical tissue properties. The optical parameters measured with this method matched previously published literature values.
- Our tests revealed that incorporating models of light transport in tissue greatly increases the accuracy of the vessel radius estimation for the vasculature imaged by the cryomicrotome over the prior FWHM method. We found that a constant optical attenuation parameter PSF model is sufficient for the model-based radius estimation of large vessels; however, small vessels are more sensitive to intramural variation of optical tissue properties and would thus require a spatially variant PSF model for more accurate radius estimation.

6.3.2 Anatomical

- Our study of optical parameter measurement in porcine cardiac tissue suggests that fibre orientation may have a role to play in intramural variation of cardiac tissue optical properties. Papillary muscles with their vertical fibres and the interventricular septum with its functionally bilayered structure with an abrupt change in fibre orientation through its middle seem to have higher optical attenuation than the closer to in-plane fibres in the myocardial free wall.

- An analysis of the radii of parent vessels branching out into daughter branches at bifurcations and trifurcations revealed that the relationship between the radii of the parent and daughter branches estimated in this study quite reasonably agrees with Murray's law.
- Whole-organ vasculatures of several hearts and other organs (datasets listed in Table 1.1) have been reconstructed, with micro-vessels measured down to the range of 0.03 mm.

6.4 Limitations and Future Research

Limitations and future experimental and methodological improvements to this study are discussed herewith.

6.4.1 Data Dependency Requirements

The relevance of optical parameter estimation for vessel radius estimation is that a coronary vasculature reconstruction model coupled with a heart mesh geometry model mapped with the optical parameter field can be used for mapping the attenuation coefficient parameter value local to a region of the myocardial tissue directly to individual vessels in that local region for the model-based template-matching vessel radius estimation (refer to chapter 4). In model-based vessel radius estimation (refer to chapter 4), the optical tissue attenuation coefficient is parameterized in the PSF, which is convolved with a simulated cylindrical vessel model for creating a simulated vessel cross-sectional image. The simulated vessel image is utilized in minimizing the difference between the simulated and real vessel cross-sectional images for optimizing the radii of each of the blood vessels. So ideally known objects (microspheres) embedded in tissue can be used to measure tissue properties, which in turn would be used to measure unknown objects (vessels) embedded in the same tissue. Specifically, optical

parameter information estimated from fiducial markers (microspheres embedded in tissue) in a region of the tissue will allow extracting radii information of vessels embedded in the same region of tissue by simulating models of the vessel cross sectional images convolved with a PSF that is parameterized by the local attenuation parameters. The limitation for using optical parameters measured from fluorescent microsphere images in vessel radius estimation is that it can only be performed for images containing both microspheres and vessels.

6.4.2 Data Acquisition Experimental Improvements

Experimental improvements to the cryomicrotome imaging modality are underway to improve the imaging of the vasculature: 1) higher resolution lens able to capture subvoxel microvessels and a higher resolution camera lens implanted inside the cryomicrotome next to the tissue block to provide even higher resolution images that would be used for validation purposes; 2) higher bit-depth photo-detectors to record a larger range of intensities for avoiding pixel saturation in the middle of large vessels; 3) black ink tissue staining to decrease the effects of tissue transparency, which causes out-of-focus light and haloes surrounding vessel cross-sections; and finally, 4) an experimental inset that could allow dynamically estimating the optical parameters of the tissue being currently imaged with an optical coherence tomography system, which would allow recording of the optical parameters for later use in the simulation of vessel images for the model-based template-matching vessel radius estimation. These experimental improvements are being evaluated at the Biomedical Engineering and Medical Physics Department, Academic Medical Center, University of Amsterdam. In any case, the above-mentioned improvements would not obviate the novel model-based radius estimation presented in this study. The model-based vessel estimation algorithm would still be required for the vascular data imaged in tissue stained with black ink, since the black ink can only increase absorption in the tissue, but cannot completely stop photons originating from sources

at depth from reaching the tissue surface and causing out-of-focus artefacts. Similarly, increasing the bit-depth would help resolve pixel saturation, but even the unsaturated images would require the model-based method for radius estimation because the vessel cross-sections would still be obscured at the boundaries by out-of-focus fluorescence.

6.4.3 Future Research in Optical Parameter Estimation

Although this study seems to indicate differences in attenuation between the free wall and septal region and papillary muscle, more research with measurements from multiple heart image datasets is required before a pattern of spatial variation of optical properties in intramural tissue can be observed, verified, and correlated to myocardial tissue structure. In the future, it would be useful to couple the heart models of the coronary vasculature, myocardial fibre sheets, and ventricular geometry with optical parameter spatial variation field mapped onto them. This would allow further observing correlation among the optical tissue properties and ventricular geometry, myocardial fibre orientation, and vasculature, such as a pattern of change in optical parameters correlated to the myocardial fibre orientation change in direction from endocardial to epicardial layers.

In the current parameter estimation scheme, a gradient descent optimization method was used to minimize the error between simulated and real microsphere images to find optimal parameter values in 3D parameter space. To further extend the parameter estimation, in the future we recommend fitting a 3D continuous smooth approximation function to the optical attenuation parameter field over the myocardium. This would reduce the potential effect of outliers, which will be compensated for by the values measured in neighbouring microspheres. Future research is recommended to extend the work in this study by measuring optical tissue properties from several hearts (of the same and differing species) all perfused with roughly equal number and same color of microspheres to see if an actual consistent pattern of variation

is observable in or across species. If it is, further analysis should be undertaken to study whether this variation of tissue optical properties is correlated to fibre orientation in the myocardium.

The Monte Carlo simulation was run only on a single vessel (see Appendix A.2), but in the future it could be useful to do a full simulation of microspheres and vessels embedded in tissue along with a full simulation of the cryomicrotome setup of incoming filtered light entering tissue, emission light emitted by the fluorescent objects being blurred by the camera lens and recorded by the CCD sensors. This would allow for understanding more accurately the light distribution of fluorescent tubular and spherical objects embedded in tissue in the cryomicrotome setup. A distributed multi-threaded implementation of parallelized photon migrations in the Monte Carlo method would allow computationally efficient numerical simulations for modeling light transport and optical parameter estimation in biological tissue. Although computationally intensive, this simulation is recommended for future research to analyze the errors in every aspect of the image acquisition modelling in this work. In the limited time and scope of this present work, the Monte Carlo simulation on a single vessel of varying size and angle suggested that the error in radius estimation using a linear PSF model was negligible in the context of blood flow simulation.

At present, the microsphere parameter estimation has been done only on a subsample of all the microspheres lodged in the vasculature. This was because of limitations in computation time. However, in the future we plan to perform the parameter estimation in an iterative approach, where we would initialize the parameter estimation of surrounding microspheres with the values of a few “seed” microspheres whose parameters were estimated in the first round and continue until all the microspheres were covered. Finally a 3D spatially continuous field would be fit to this scattered data to obtain a high resolution map of the spatial variation of optical

parameters in the heart. We also plan to run a parallel implementation to speed up the parameter estimation from the thousands of microspheres in each heart.

Although spatial variation of optical parameters was not very large for the hearts studied in this example, the spatial variation could be wider for other hearts, such as infarcted hearts. In this study, infarcted heart data was not available, but in the case of the future availability and measurement of optical attenuation coefficients from such images, we suspect that the infarcted region containing dead tissue will have different optical properties. In such cases, the model-based template-matching algorithm proposed in this study will be able to incorporate the variation in the optical properties for accurate vessel extraction in normal, infarcted, or otherwise pathologically affected heart regions.

6.4.4 Future Research in Vessel Radius Estimation

Currently in the novel model-based template-matching radius estimation method, the vessel model used in simulating vessel cross-sectional images is a cylinder. In actuality the vessels are curved tubes, so it would be more accurate to simulate the vessel as a curved tube that would be convolved with a PSF model of the tissue light distribution effect to obtain a simulated image of the vessel cross-section to be fitted to the real vessel cross-sectional image for vessel radii optimization. However, the assumption of a linear cylinder as a model of a vessel is valid because the work in this study performs model-based radius estimation for small local segments of each vessel. Though worth testing in future extensions of this work, we expect that employing curved models of vessels for model-based radius measurement will not make any substantial difference over the local linear cylindrical models used in this work.

The current implementation of the model-based template-matching method uses the vessel orientation from the skeletonization and vessel centrelines. The angle of each vessel segment

is calculated from its start and end node coordinates, but errors in vessel angle estimation could affect the radius estimation. In the future, the model-based method can be further improved by estimating the vessel angle along with the vessel radius. Both the vessel segment's angle and radius could be fine-tuned from their initial estimates. The angle calculated from the endpoints and half of the FWHM estimated on the deconvolved cross-sectional image orthogonal to the vessel long axis would be the initial starting estimates, which could then be optimized in an expectation maximization approach to match, i.e. minimize the difference between, the FWHM of the simulated vessel cylindrical model and the FWHM of the real vessel image.

6.4.5 Future Research in Myocardial Perfusion Measurements

In this work, one of the main original contributions is the use of microspheres as both fiducial markers to estimate the vasculature and as particles to estimate regional coronary perfusion. This allows the microspheres to be used as known markers for measurement of the imaging modality's response function and simultaneously for their classical use in perfusion measurements. From visualizing the microspheres and vasculature together, it is visually demonstrated that many microspheres were located inside of large arteries. Characterizing this behaviour and finding possible reasons is a further area of research in microsphere deposition and distribution. Further research is thus needed to determine the percentage of microspheres that never make it to the microvasculature. Whether this behaviour is an experimental artefact caused by microsphere clustering or an issue to do with the size of the microspheres is still to be confirmed. In this study, the microspheres that were located inside vessels were assigned to their nearest node in the vasculature, and the microspheres that were located outside of vessels were assigned to their nearest terminal of the vasculature.

Regarding the methodology of this work, in this study, the microspheres were assigned to terminal nodes based on their Euclidean distance. However, an improved computational strategy for assigning microspheres to terminals would be to employ simultaneous region growing at all the terminals to grow out perfusion regions for all the terminals weighted by their flows and assign microspheres based on which terminal's perfusion region they fall in. However, this would be computationally very expensive and require a very fine binarization of the myocardial mesh.

This study used microspheres of 15 micrometer diameter. An experiment employing different sizes of microspheres all perfused in the same heart would be highly useful to determine if the size of the microspheres plays a role in their discrepancy in flow estimation. The smaller microspheres would be closer to representing blood cells, and it would be interesting to observe microsphere perfusion distribution with these smaller microspheres if the viscosity of the microsphere solution and input flow rate were matched to the viscosity of blood and coronary perfusion rate, respectively. In essence, the microspheres could be used as phantom blood cells.

In the experiment performed to perfuse the pig heart in this study, the RCA was occluded during the perfusion and thus cast was not injected into the right coronary arterial network. Due to this experimental issue, the RCA arterial network was unavailable for extraction and reconstruction. However, though the RCA was occluded, many microspheres were located in the right ventricular myocardium. It is possible that the microspheres may have been perfused through the RCA. It is also a possibility that the RCA was completely occluded, and the microspheres were only inserted through the LCA. If this is the case, then this could mean that a significant percentage of blood perfusing the right ventricular myocardium originates from the LCA. In order to investigate this, in the future it would be useful to run the methods

described in this study on a heart with both the RCA and LCA perfused. Then it could be determined how much of the right ventricular myocardium is perfused by the LCA, and whether microspheres found in the right ventricle could only have reached there via the RCA or if they could have reached there via the LCA alone. It would also be useful to insert distinct colors of microspheres in the RCA, LAD, and LCX and compare their distributions to the distributions obtained of single-color microspheres injected throughout the heart. The distinct color of microspheres could provide validation for the single-color microsphere study in terms of assessing defined perfusion regions of the arteries and validating calculated percentage of blood flow and regional perfusion. The comparison of fractional microsphere count and fractional flow could be performed on the multi-color and single-color microsphere studies for further corroboration.

Another experimental issue with the vasculature is the viscosity of the fluorescent dye, which can prevent the cast from entering and perfusing smaller vessels in some areas, thus resulting in an incomplete vasculature extraction. It would be a useful study to investigate how much the viscosity could be decreased to increase the microvasculature extracted even down to capillaries and venules before the cast starts leaking into tissue, in order to further understand the trade-off between leakage into tissue and extraction down to the micro-vessels.

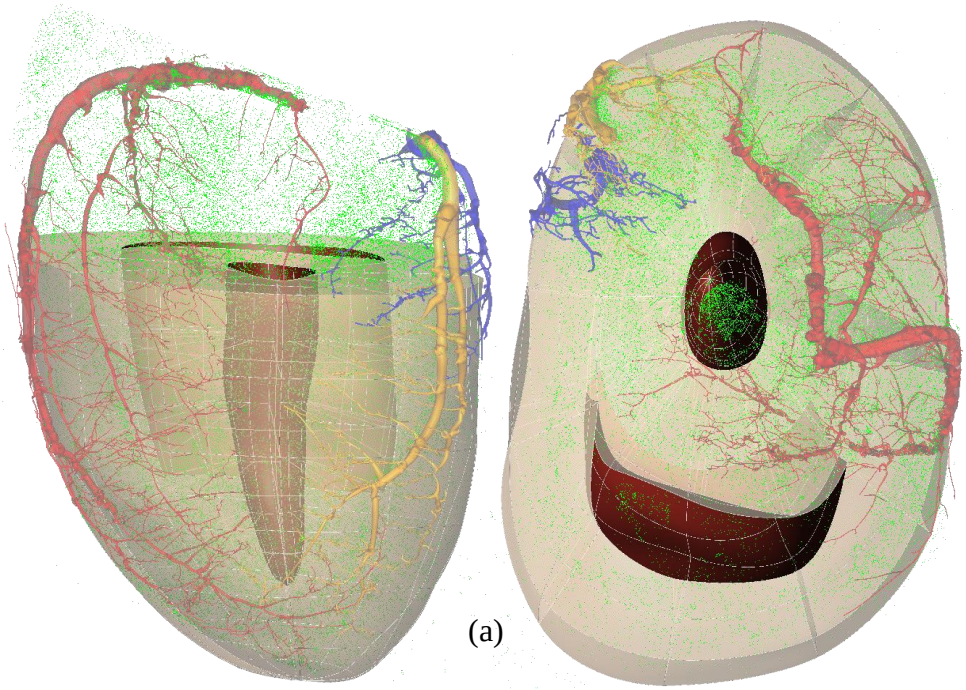
Regarding the mathematical model of blood flow employed in this research, a future recommendation is to solve the 1-D time-dependent form of the Navier-Stokes equations on a full arterial network and compare that to the Hagen-Poiseuille simulation and microsphere distribution. Finally, to aid clinical corroboration with other imaging modalities, in the analysis of a 1-D blood flow simulation and microsphere distribution, it would be useful to compare the two in individual circumferential volume regions in the left ventricle. From the blood flow simulations, the total volumetric flow rate to a specific region could be calculated as the sum

total of all the flows in all the terminal nodes in the region. This total volumetric flow rate could then be divided by the total mass of that volume region to obtain a volume flow per unit mass. From the microsphere distribution, the volume flow per unit mass in a volume region can be calculated as the total flow rate in the entire heart multiplied by the density of microspheres in a region normalized by the total number of microspheres in the entire heart. The values of volume flow per unit mass obtained from the blood flow simulation and microspheres could thus be compared in each of the circumferential volume regions.

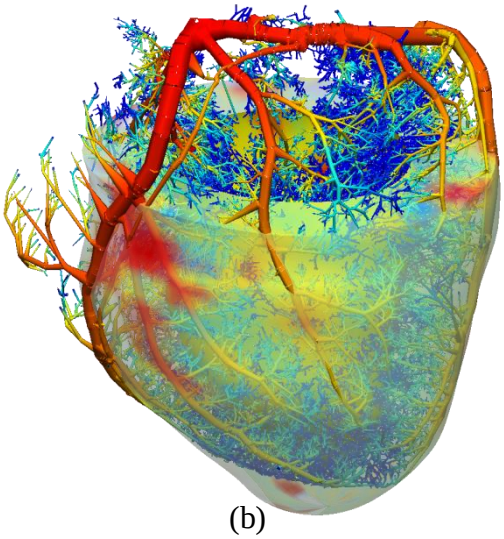
6.4.6 Future Research in Coupled Vascular-Ventricular Modelling

A highly useful future extension to this research would be the coupling of the reconstructed vasculature models extracted in this study with poromechanical ventricular models. This could be accomplished by coupling the terminals at varying sizes of the arteries to a computational ventricular myocardial mesh in order to model blood flow and pressure in the myocardium. For example, as shown in Fig. 6.1, the pressure field estimated from the blood flow simulation in the vasculature can be mapped onto the myocardium represented as a computational mesh model of the ventricles, which was obtained by fitting a generic ventricular mesh template to the binary segmentation of the ventricles.

In Fig. 6.1, the cubic Hermite mesh model of the left ventricle was generated by customising a predefined ventricular template (Lamata et al. 2010) with a deformable image registration procedure (Barber et al. 2005, Barber et al. 2007) and cubic Hermite mesh variational warping. The image registration produced a mapping field between the template mesh and the pig ventricle binary image, and the variational warping method fitted the cubic Hermite mesh template to the pig ventricle binary image by deforming it according to the mapping field (Lamata et al. 2011).



(a)



(b)

Figure 6.1: Coronary vasculature superimposed with the myocardial ventricular mesh (a). Arterial pressure calculated using the 1-D blood flow simulation mapped onto the vasculature and cubic hermite mesh of the left ventricle of the same heart (b). As expected, the pressure is higher at the epicardium from where the epicardial arteries branch out into the myocardium; and the pressure decreases nearer the endocardium.

The pressure mapped onto the myocardium shows "hot spots," i.e. where pressure is high at the epicardium especially at the points where the epicardial arteries couple / interact with the ventricular myocardium. The pressure decreases nearer the endocardium as expected.

References

[1] R. S. Acharya and R. Gaborski, “Robust snake model,” in *Proceedings IEEE Conference on Computer Vision and Pattern Recognition. CVPR 2000 (Cat. No.PR00662)*, 2000, vol. 1, pp. 452–457.

[2] D. A. Agard, “Optical sectioning microscopy: cellular architecture in three dimensions.,” *Annual Review of Biophysics and Bioengineering*, vol. 13, pp. 191–219, Jan. 1984.

[3] G. J. Agin and T. O. Binford, “Computer description of curved objects,” *IEEE Transactions on Computers*, vol. C-25, no. 4, pp. 439–449, Apr. 1976.

[4] A. Agrawal, T. J. Pfefer, N. Gilani, and R. Drezek, “Three-dimensional characterization of optical coherence tomography point spread functions with a nanoparticle-embedded phantom,” *Optics Letters*, vol. 35, no. 13, p. 2269, Jun. 2010.

[5] A. C. Akcay, J. P. Rolland, and J. M. Eichenholz, “Spectral shaping to improve the point spread function in optical coherence tomography,” *Optics Letters*, vol. 28, no. 20, p. 1921, Oct. 2003.

[6] J. Aldrich, “R. A. Fisher and the Making of Maximum Likelihood 1912-1922,” *Statistical Science*, vol. 12, no. 3, pp. 162 – 176, 1997.

[7] S. Allender, P. Scarborough, V. Peto, and M. Rayner, “Eurpean Cardiovascular Disease Statistics, British Heart Foundation, Health Promotion Research Group and Health Economics Research Center,” University of Oxford, 2008.

[8] B. G. Anderson and W. D. Anderson, “Scanning electron microscopy of microcorrosion casts; Intracranial and abdominal microvasculature in domestic animals,” *The American Journal of Anatomy*, vol. 153, no. 4, pp. 523–36, Dec. 1978.

[9] B. G. Anderson, W. D. Anderson, and R. J. Seguin, “Renal microvasculature of the black bear (Ursus americanus).,” *Acta Anatomica*, vol. 132, no. 2, pp. 124–31, Jan. 1988.

[10] J. Annese, D. M. Sforza, M. Dubach, D. Bowden, and A. W. Toga, “Postmortem high-resolution 3-dimensional imaging of the primate brain: blockface imaging of perfusion stained tissue,” *NeuroImage*, vol. 30, no. 1, pp. 61–9, Mar. 2006.

[11] I. Arganda-Carreras, R. Fernández-González, A. Muñoz-Barrutia, and C. Ortiz-De-Solorzano, “3D reconstruction of histological sections: Application to mammary gland tissue,” *Microscopy Research and Technique*, vol. 73, no. 11, pp. 1019–29, Oct. 2010.

[12] N. Armande, P. Montesinos, O. Monga, and G. Vaysseix, “Thin Nets Extraction Using a Multi-scale Approach,” *Computer Vision and Image Understanding*, vol. 73, no. 2, pp. 248–257, Feb. 1999.

[13] S. M. Arribas, C. J. Daly, M. C. González, and J. C. McGrath, “Imaging the vascular wall using confocal microscopy.,” *The Journal of physiology*, vol. 584, no. Pt 1, pp. 5–9, Oct. 2007.

[14] S. R. Arridge and J. C. Hebden, “Optical imaging in medicine: II. Modelling and reconstruction,” *Physics in Medicine and Biology*, vol. 42, no. 5, pp. 841–53, May 1997.

[15] S. R. Aylward and E. Bullitt, “Initialization, noise, singularities, and scale in height ridge traversal for tubular object centerline extraction,” *Medical Imaging, IEEE Transactions on Medical Imaging*, vol. 21, no. 2, pp. 61–75, 2002.

[16] S. Aylward and E. Bullitt, “Intensity ridge and widths for tubular object segmentation and description,” in *Proceedings of the Workshop on Mathematical Methods in Biomedical Image Analysis (MMBIA)*, 1996, p. 131.

[17] O. Azucena, J. Crest, J. Cao, W. Sullivan, P. Kner, D. Gavel, D. Dillon, S. Olivier, and J. Kubby, “Wavefront aberration measurements and corrections through thick tissue using fluorescent microsphere reference beacons,” *Optics Express*, vol. 18, no. 16, pp. 17521–32, Aug. 2010.

[18] C. T. Badea, M. Drangova, D. W. Holdsworth, and G. A. Johnson, “In vivo small-animal imaging using micro-CT and digital subtraction angiography,” *Physics in Medicine and Biology*, vol. 53, no. 19, pp. R319–50, Oct. 2008.

[19] B. Barber, D. Dobkin, and H. Huhdanpaa, “The Quickhull Algorithm for Convex Hulls,” *ACM Transactions on Mathematical Software*, vol. 22, no. 4, pp. 469 – 483, 1996.

[20] D. C. Barber, E. Oubel, A. F. Frangi, and D. R. Hose, “Efficient computational fluid dynamics mesh generation by image registration,” *Medical Image Analysis*, vol. 11, pp. 648–662, 2007.

[21] D. C. Barber and D. R. Hose, “Automatic segmentation of medical images using image registration: diagnostic and simulation applications,” *Journal of Medical Engineering & Technology*, vol. 29, pp. 53–63, 2005.

[22] J. B. Bassingthwaighte, M. A. Malone, and T. C. Moffett, “Molecular and particulate depositions for regional myocardial flows in sheep,” *Circulation Research*, vol. 66, pp. 1328–1344, 1990.

[23] J. B. Bassingthwaighte, T. Yipintsoi, and R. B. Harvey, “Microvasculature of the dog Left ventricular myocardium.,” *Microvascular Research*, vol. 7, no. 2, pp. 229–49, Mar. 1974.

[24] D. A. Beard, “Computational framework for generating transport models from databases of microvascular anatomy,” *Annals of Biomedical Engineering*, vol. 29, no. 10, pp. 837–43, Oct. 2001.

[25] D. A. Beard and J. B. Bassingthwaighte, “The fractal nature of myocardial blood flow emerges from a whole-organ model of arterial network,” *Journal of Vascular Research*, vol. 37, no. 4, pp. 282–96, Jan. 2000.

[26] P. E. Beighley, P. J. Thomas, S. M. Jorgensen, and E. L. Ritman, “3D architecture of myocardial microcirculation in intact rat heart: a study with micro-CT,” *Advances in Experimental Medicine and Biology*, vol. 430, pp. 165–75, Jan. 1997.

[27] E. Bennink, “Analysis of coronary microvascular structures on the enhancement and detection of microvessels in 3D imaging cryomicrotome data, MS Thesis,” Eindhoven University of Technology, 2007.

[28] M. D. Bentley, M. C. Ortiz, E. L. Ritman, and J. C. Romero, “The use of microcomputed tomography to study microvasculature in small rodents.,” *American journal of physiology. Regulatory, integrative and comparative physiology*, vol. 282, no. 5, pp. R1267–79, May 2002.

[29] S. L. Bernard, J. R. Ewen, C. H. Barlow, J. J. Kelly, S. McKinney, D. A. Frazer, and R. W. Glenny, “High spatial resolution measurements of organ blood flow in small laboratory animals,” *American Journal of Physiology. Heart and Circulatory Physiology*, vol. 279, no. 5, pp. H2043–2052, Nov. 2000.

[30] D. P. Bertsekas, *Constrained optimization and Lagrange multiplier methods*. Boston: , 1982.

[31] J. L. Beverage, R. V. Shack, and M. R. Descour, “Measurement of the three-dimensional microscope point spread function using a Shack-Hartmann wavefront sensor,” *Journal of Microscopy*, vol. 205, no. 1, pp. 61–75, Jan. 2002.

[32] J. Biemond, R. L. Lagendijk, and R. M. Mersereau, “Iterative methods for image deblurring,” *Proceedings of the IEEE*, vol. 78, no. 5, pp. 856–883, May 1990.

[33] D. S. Biggs and M. Andrews, “Acceleration of iterative image restoration algorithms,” *Applied optics*, vol. 36, no. 8, pp. 1766–75, Mar. 1997.

[34] M. Bilgen, “Constrained least-squares filtering for noisy images blurred by random point spread function,” *Optical Engineering*, vol. 33, no. 6, p. 2020, Jun. 1994.

[35] M. J. Bishop, G. Bub, A. Garny, D. J. Gavaghan, and B. Rodriguez, “An investigation into the role of the optical detection set-up in the recording of cardiac optical mapping signals: A Monte Carlo simulation study,” *Physica D: Nonlinear Phenomena*, vol. 238, no. 11–12, pp. 1008–1018, Jun. 2009.

[36] M. Björkman and K. Holmström, “Global optimization of costly nonconvex functions using radial basis functions,” *Optimization and Engineering*, vol. 1, no. 4, pp. 373–397, 2000.

[37] P. Boettler, P. Claus, L. Herbots, M. McLaughlin, J. D’hooge, B. Bijnens, S. Y. Ho, D. Kececioglu, and G. R. Sutherland, “New aspects of the ventricular septum and its function: an echocardiographic study.,” *Heart (British Cardiac Society)*, vol. 91, no. 10, pp. 1343–8, Oct. 2005.

[38] N. Bonnot, “Simulation of the saturation effect of CCD sensor used in machine vision system,” in *International Conference on Image and Signal Processing (ICISP), Agadir, Morocco*, 2003, pp. 25–27.

[39] R. M. Botnar, M. Stuber, P. G. Danias, K. V. Kissinger, and W. J. Manning, “Improved Coronary Artery Definition With T2-Weighted, Free-Breathing, Three-Dimensional Coronary MRA,” *Circulation Research*, vol. 99, no. 24, pp. 3139–3148, Jun. 1999.

[40] E. Boutsianis, H. Dave, T. Frauenfelder, D. Poulikakos, S. Wildermuth, M. Turina, Y. Ventikos, and G. Zund, “Computational simulation of intracoronary flow based on real coronary geometry.,” *European Journal of Cardio-Thoracic Surgery*, vol. 26, no. 2, pp. 248–56, Aug. 2004.

[41] R. E. Brown, “The pattern of the microcirculatory bed in the ventricular myocardium of domestic mammals,” *The American Journal of Anatomy*, vol. 116, pp. 355–74, Mar. 1965.

[42] P. Bruinsma, T. Arts, J. Dankelman, and J. A. Spaan, “Model of the coronary circulation based on pressure dependence of coronary resistance and compliance.,” *Basic research in cardiology*, vol. 83, no. 5, pp. 510–24.

[43] T. J. Brukilacchio, Q. Zhang, T. Gaudett, and L. Wang, “Characterization of the point spread function for diffuse optical tomographic imaging and the effect of noise on resolution,” *Proceedings of SPIE*, vol. 4250, pp. 489–507, 2001.

[44] A. Brun, H. Knutsson, H.-J. Park, M. E. Shenton, and C.-F. Westin, “Clustering Fiber Traces Using Normalized Cuts.,” *Medical image computing and computer-assisted intervention : MICCAI ... International Conference on Medical Image Computing and Computer-Assisted Intervention*, vol. 3216/2004, no. 3216, pp. 368–375, Sep. 2004.

[45] G. E. Burch, N. P. DePasquale, and J. H. Phillips, “The syndrome of papillary muscle dysfunction,” *American Heart Journal*, vol. 75, no. 3, pp. 399–415, Mar. 1968.

[46] R. A. B. Burton, G. Plank, J. E. Schneider, V. Grau, H. Ahammer, S. L. Keeling, J. Lee, N. P. Smith, D. Gavaghan, N. Trayanova, and P. Kohl, “Three-dimensional models of individual cardiac histoanatomy: tools and challenges,” *Annals of the New York Academy of Sciences*, vol. 1080, pp. 301–19, Oct. 2006.

[47] K. R. Castleman, *Digital image processing*. Englewood Cliffs, NJ: Prentice Hall International, 1979.

[48] J. R. Cebral, M. Castro, O. Soto, R. Loehner, P. J. Yim, and N. Alperin, "<title>Finite element modeling of the Circle of Willis from magnetic resonance data</title>," in *Medical Imaging 2003*, 2003, pp. 11–21.

[49] V. E. Centonze and J. G. White, "Multiphoton excitation provides optical sections from deeper within scattering specimens than confocal imaging," *Biophysical Journal*, vol. 75, no. 4, pp. 2015–24, Oct. 1998.

[50] B. Chalmond, "Image restoration using an estimated Markov model," *Signal Processing*, vol. 15, no. 2, pp. 115–129, Sep. 1988.

[51] R. C. Chan, W. C. Karl, and R. S. Lees, "A new model-based technique for enhanced small-vessel measurements in X-ray ciné-angiograms.," *IEEE Transactions on Medical Imaging*, vol. 19, no. 3, pp. 243–55, Mar. 2000.

[52] Y. Chen, W. Li, M. Xia, and K. Yang, "Model-based restoration and reconstruction for underwater range-gated imaging," *Optical Engineering*, vol. 50, no. 11, p. 113203, Nov. 2011.

[53] Z. Chen and S. Molloi, "Automatic 3D vascular tree construction in CT angiography," *Computerized Medical Imaging and Graphics : The Official Journal of the Computerized Medical Imaging Society*, vol. 27, no. 6, pp. 469–79, 2003.

[54] W. F. Cheong, S. A. Prahl, and A. J. Welch, "A review of the optical properties of biological tissues," *IEEE Journal of Quantum Electronics*, vol. 26, no. 12, pp. 2166–2185, 1990.

[55] G. L. Chien, C. G. Anselone, R. F. Davis, and D. M. Van Winkle, "Fluorescent vs. radioactive microsphere measurement of regional myocardial blood flow," *Cardiovascular Research*, vol. 30, no. 3, pp. 405–412, Sep. 1995.

[56] W. M. Chilian, "Microvascular pressures and resistances in the left ventricular subepicardium and subendocardium," *Circulation Research*, vol. 69, no. 3, pp. 561–570, Sep. 1991.

[57] M. P. Chwialkowski, Y. M. Ibrahim, H. F. Li, and R. M. Peshock, "A method for fully automated quantitative analysis of arterial flow using flow-sensitized MR images," *Computerized Medical Imaging and Graphics : the Official Journal of the Computerized Medical Imaging Society*, vol. 20, no. 5, pp. 365–78, 1996.

[58] E. Coelho, "L'artériograpie des coronaires chez l'homme vivant (Coronary arteriography of living humans)," *Cardiologia, International Archives of Cardiology*, vol. 22, pp. 45–61, 1953.

[59] R. W. Cole, Ushare, and C. M. Brown, “Measuring and interpreting point spread functions to determine confocal microscope resolution and ensure quality control.,” *Nature Protocols*, vol. 6, no. 12, pp. 1929–41, Dec. 2011.

[60] J. E. Connolly, “The development of coronary artery surgery: personal recollections,” *Texas Heart Institute journal / from the Texas Heart Institute of St. Luke’s Episcopal Hospital, Texas Children's Hospital*, vol. 29, no. 1, pp. 10–4, Jan. 2002.

[61] A. J. Cornelissen, J. Dankelman, E. VanBavel, H. G. Stassen, and J. A. Spaan, “Myogenic reactivity and resistance distribution in the coronary arterial tree: a model study.,” *American journal of physiology. Heart and circulatory physiology*, vol. 278, no. 5, pp. H1490–9, May 2000.

[62] A. J. M. Cornelissen, J. Dankelman, E. VanBavel, and J. A. E. Spaan, “Balance between myogenic, flow-dependent, and metabolic flow control in coronary arterial tree: a model study.,” *American journal of physiology. Heart and circulatory physiology*, vol. 282, no. 6, pp. H2224–37, Jun. 2002.

[63] A. Cournand, “Cardiac catheterization; development of the technique, its contributions to experimental medicine, and its initial applications in man,” *Acta Medica Scandinavica. Supplementum*, vol. 579, pp. 3–32, Jan. 1975.

[64] M. J. Cowley, “Tribute to a legend in invasive/interventional cardiology Melvin P. Judkins, M.D. (1922-85),” *Catheterization and Cardiovascular Interventions : Official Journal of the Society for Cardiac Angiography & Interventions*, vol. 64, no. 2, pp. 259–61, Mar. 2005.

[65] S. J. Crick, M. N. Sheppard, S. Y. Ho, L. Gebstein, and R. H. Anderson, “Anatomy of the pig heart: comparisons with normal human cardiac structure,” *Journal of Anatomy*, vol. 193, no. 1, pp. 105–19, Jul. 1998.

[66] P. D’Ambra, M. Guarracino, and D. Talia, Eds., “Euro-Par 2010 - Parallel Processing,” in *Euro-Par’10 Proceedings of the 16th international Euro-Par conference on Parallel processing: Part II*, 2010, vol. 6272.

[67] G. De Visscher, M. Haseldonckx, and W. Flameng, “Fluorescent microsphere technique to measure cerebral blood flow in the rat,” *Nature Protocols*, vol. 1, no. 4, pp. 2162–70, Jan. 2006.

[68] G. De Visscher, M. Haseldonckx, W. Flameng, M. Borgers, R. S. Reneman, and K. van Rossem, “Development of a novel fluorescent microsphere technique to combine serial cerebral blood flow measurements with histology in the rat.,” *Journal of Neuroscience methods*, vol. 122, no. 2, pp. 149–56, Jan. 2003.

[69] U. K. M. Decking, V. M. Pai, E. Bennett, J. L. Taylor, C. D. Fingas, K. Zanger, H. Wen, and R. S. Balaban, “High-resolution imaging reveals a limit in spatial resolution of blood flow measurements by microspheres.,” *American Journal of*

Physiology. Heart and Circulatory Physiology, vol. 287, no. 3, pp. H1132–40, Sep. 2004.

[70] M. T. Dehkordi, S. Sadri, and A. Doosthoseini, "A review of coronary vessel segmentation algorithms.," *Journal of Medical Signals and Sensors*, vol. 1, no. 1, pp. 49–54, Jan. 2011.

[71] W. Denk and H. Horstmann, "Serial block-face scanning electron microscopy to reconstruct three-dimensional tissue nanostructure," *PLoS Biology*, vol. 2, no. 11, 2004.

[72] L. Ding, R. Splinter, and S. B. Knisley, "Quantifying spatial localization of optical mapping using Monte Carlo simulations.," *IEEE Transactions on Biomedical Engineering*, vol. 48, no. 10, pp. 1098–107, Oct. 2001.

[73] S. K. Doddi and P. Bagchi, "Lateral migration of a capsule in a plane Poiseuille flow in a channel," *International Journal of Multiphase Flow*, vol. 34, no. 10, pp. 966–986, Oct. 2008.

[74] C. Y. Dong, K. Koenig, and P. So, "Characterizing point spread functions of two-photon fluorescence microscopy in turbid medium," *Journal of Biomedical Optics*, vol. 8, no. 3, pp. 450–9, Jul. 2003.

[75] C. T. Dotter and L. H. Frische, "Visualization of the coronary circulation by occlusion aortography: a practical method," *Radiology*, vol. 71, no. 4, pp. 502–24, Oct. 1958.

[76] M. Duta, J. Thiyagalingam, A. Trefethen, A. Goyal, V. Grau, and N. Smith, "Parallel simulation for parameter estimation of optical tissue properties," in *Euro-Par'10 Proceedings of the 16th international Euro-Par conference on Parallel processing: Part II*, 2010, pp. 51–62.

[77] S. Eiho and Y. Qian, "Detection of coronary artery tree using morphological operator," in *Computers in Cardiology*, 1997, pp. 525–528.

[78] M. Elad and A. Feuer, "Restoration of a single superresolution image from several blurred, noisy, and undersampled measured images.," *IEEE Transactions on Image Processing : A Publication of the IEEE Signal Processing Society*, vol. 6, no. 12, pp. 1646–58, Jan. 1997.

[79] T. Endo, "Study of the tumor vessels in depressed-type early gastric cancers," *Dig. Endoscopy*, vol. 17, no. 3, pp. 210–217, 2005.

[80] A. Erhardt, G. Zinser, D. Komitowski, and J. Bille, "Reconstructing 3-D light-microscopic images by digital image processing," *Applied Optics*, vol. 24, no. 2, p. 194, Jan. 1985.

[81] E. H. Estes, F. M. Dalton, M. . L. Entman, H. B. Dixon, and D. B. Hackel, “The anatomy and blood supply of the papillary muscles of the left ventricle,” *American Heart Journal*, vol. 71, no. 3, pp. 356–62, Mar. 1966.

[82] S. A. Eucker, B. D. Hoffman, R. Natesh, J. Ralston, W. M. Armstead, and S. S. Margulies, “Development of a fluorescent microsphere technique for rapid histological determination of cerebral blood flow.,” *Brain Research*, vol. 1326, pp. 128–34, Apr. 2010.

[83] D. Faber, F. van der Meer, M. Aalders, and T. van Leeuwen, “Quantitative measurement of attenuation coefficients of weakly scattering media using optical coherence tomography.,” *Optics Express*, vol. 12, no. 19, pp. 4353–65, Sep. 2004.

[84] R. G. Favaloro, D. B. Effler, L. K. Groves, D. J. Fergusson, and J. S. Lozada, “Double internal mammary artery-myocardial implantation. Clinical evaluation of results in 150 patients,” *Circulation*, vol. 37, no. 4, pp. 549–55, Apr. 1968.

[85] C. Fetita, O. Lucidarme, F. Prêteux, and P. Grenier, “CT hepatic venography: 3D vascular segmentation for preoperative evaluation,” *International Conference on Medical Image Computing and Computer-Assisted Intervention*, vol. 8, no. Pt 2, pp. 830–7, Jan. 2005.

[86] I. A. Feuerstein, O. A. E. Masry, and G. Round, “Arterial bifurcation flows – effects of flow rate and area ratio,” *Canadian Journal of Physiology and Pharmacology*, vol. 54, no. 6, pp. 795–808, Dec. 1976.

[87] S. T. Flock, B. C. Wilson, and M. S. Patterson, “Total attenuation coefficients and scattering phase functions of tissues and phantom materials at 633 nm,” *Medical Physics*, vol. 14, no. 5, pp. 835–41, 1987.

[88] W. Forssmann, “Sondierung des rechten herzens (Exploration of the right heart),” *Klin Wochenschr*, vol. 8, no. 8, p. 2085, 1929.

[89] A. F. Frangi, W. J. Niessen, K. L. Vincken, and M. A. Viergever, “Multiscale vessel enhancement filtering,” *Medical Image Computing and Computer Assisted Intervention*, vol. 1496, pp. 130–137, 1998.

[90] A. Frangi, W. Niessen, K. Vincken, and M. Viergever, *Medical Image Computing and Computer-Assisted Intervention — MICCAI’98*, vol. 1496, no. 3. Berlin/Heidelberg: Springer-Verlag, 1998, pp. 130–137.

[91] M. H. Friedman and Z. Ding, “Relation between the structural asymmetry of coronary branch vessels and the angle at their origin,” *Journal of Biomechanics*, vol. 31, no. 3, pp. 273–278, Dec. 1997.

[92] J. G. Fujimoto, S. A. Boppart, G. J. Tearney, B. E. Bouma, C. Pitris, and M. E. Brezinski, “High resolution in vivo intra-arterial imaging with optical coherence tomography,” *Heart*, vol. 82, no. 2, pp. 128–133, Aug. 1999.

[93] E. Gabryś, M. Rybaczuk, and A. Kędzia, “Blood flow simulation through fractal models of circulatory system,” *Chaos, Solitons & Fractals*, vol. 27, no. 1, pp. 1–7, Jan. 2006.

[94] G. P. Galdi and A. M. Robertson, “The Relation Between Flow Rate and Axial Pressure Gradient for Time-Periodic Poiseuille Flow in a Pipe,” *Journal of Mathematical Fluid Mechanics*, vol. 7, no. S2, pp. S215–S223, May 2005.

[95] A. Garcia-Sanz, A. Rodriguez-Barbero, M. D. Bentley, E. L. Ritman, and J. C. Romero, “Three-dimensional microcomputed tomography of renal vasculature in rats.,” *Hypertension*, vol. 31, no. 1 Pt 2, pp. 440–4, Jan. 1998.

[96] A. Garny, J. Cooper, and P. J. Hunter, “Toward a VPH/physiome toolkit,” *Wiley Interdisciplinary Reviews*, vol. 2, no. 2, pp. 134–147, 2009.

[97] L. Geerts, P. Bovendeerd, K. Nicolay, and T. Arts, “Characterization of the normal cardiac myofiber field in goat measured with MR-diffusion tensor imaging.,” *American journal of physiology. Heart and circulatory physiology*, vol. 283, no. 1, pp. H139–45, Jul. 2002.

[98] S. Geman and D. Geman, “Stochastic Relaxation, Gibbs Distributions, and the Bayesian Restoration of Images,” *IEEE Transactions on Pattern Analysis and Machine Intelligence*, vol. PAMI-6, no. 6, pp. 721–741, Nov. 1984.

[99] D. A. Gerneke, G. B. Sands, R. Ganesalingam, P. Joshi, B. J. Caldwell, B. H. Smaill, and I. J. Legrice, “Surface imaging microscopy using an ultramiller for large volume 3D reconstruction of wax- and resin-embedded tissues.,” *Microscopy Research and Technique*, vol. 70, no. 10, pp. 886–94, Oct. 2007.

[100] M. C. F. Geven, V. N. Bohté, W. H. Aarnoudse, P. M. J. van den Berg, M. C. M. Rutten, N. H. J. Pijls, and F. N. van de Vosse, “A physiologically representative in vitro model of the coronary circulation,” *Physiological Measurement*, vol. 25, no. 4, pp. 891–904, Aug. 2004.

[101] D. Gianni, S. McKeever, T. Yu, R. Britten, H. Delingette, A. Frangi, P. Hunter, and N. Smith, “Sharing and reusing cardiovascular anatomical models over the Web: a step towards the implementation of the virtual physiological human project,” *Philosophical Transactions. Series A, Mathematical, Physical, and Engineering Sciences*, vol. 368, no. 1921, pp. 3039–56, Jun. 2010.

[102] R. W. Glenny, S. L. Bernard, and W. J. Lamm, “Hemodynamic effects of 15-microm-diameter microspheres on the rat pulmonary circulation.,” *Journal of Applied Physiology*, vol. 89, no. 2, pp. 499–504, Aug. 2000.

[103] R. W. Glenny, S. Bernard, and M. Brinkley, “Validation of fluorescent-labeled microspheres for measurement of regional organ perfusion,” *Journal of Applied Physiology*, vol. 74, no. 5, pp. 2585–2597, May 1993.

[104] R. W. Glenny, S. L. Bernard, and H. T. Robertson, “Pulmonary blood flow remains fractal down to the level of gas exchange,” *Journal of Applied Physiology*, vol. 89, no. 2, pp. 742–748, Aug. 2000.

[105] R. C. Gonzalez and R. E. Woods, *Digital image processing*. Prentice-Hall Press, 2002.

[106] A. S. Gopal, A. M. Keller, Z. Shen, P. M. Sapin, K. M. Schroeder, and D. L. King, “Three-dimensional echocardiography: In vitro and in vivo validation of left ventricular mass and comparison with conventional echocardiographic methods,” *Journal of the American College of Cardiology*, vol. 24, no. 2, pp. 504–513, Aug. 1994.

[107] R. Gorlin and W. J. Taylor, “Selective revascularization of the myocardium by internal-mammary-artery implant,” *The New England journal of medicine*, vol. 275, no. 6, pp. 283–90, Aug. 1966.

[108] A. Goyal, “Vasculature Reconstruction From 3D Cryomicrotome Images (DPhil Thesis),” Dept. of Computer Science, University of Oxford, 2012.

[109] A. Goyal, J. Lee, P. Lamata, J. van den Wijngaard, P. van Horssen, J. Spaan, M. Siebes, V. Grau, and N. Smith, “Model-based Vasculature Extraction from Optical Fluorescence Cryomicrotome Images, In review,” *IEEE Transactions on Medical Imaging*, 2012.

[110] A. Goyal, J. van den Wijngaard, P. van Horssen, V. Grau, J. Spaan, and N. Smith, “Intramural spatial variation of optical tissue properties measured with fluorescence microsphere images of porcine cardiac tissue,” in *Annual International Conference of the IEEE Engineering in Medicine and Biology Society. IEEE Engineering in Medicine and Biology Society*, 2009, vol. 2009, pp. 1408–11.

[111] H. Gray, *Anatomy of the Human Body*, 20th U.S. . Philadelphia: Lea & Febiger, 1918.

[112] J. Grayson, J. W. Davidson, A. Fitzgerald-Finch, and C. Scott, “The functional morphology of the coronary microcirculation in the dog.,” *Microvascular Research*, vol. 8, no. 1, pp. 20–43, Jul. 1974.

[113] R. A. Greenbaum, S. Y. Ho, D. G. Gibson, A. E. Becker, and R. H. Anderson, “Left ventricular fibre architecture in man,” *British heart journal*, vol. 45, no. 3, pp. 248–63, Mar. 1981.

[114] A. Grinvald, E. E. Lieke, R. D. Frostig, and R. Hildesheim, “Cortical point-spread function and long-range lateral interactions revealed by real-time optical imaging of macaque monkey primary visual cortex,” *J. Neuroscience*, vol. 14, no. 5, pp. 2545–2568, May 1994.

[115] G. G. Guilbault, *Practical fluorescence*, 2nd ed., vol. 2nd Editio. New York [etc.] : Dekker, 1990, p. 812.

[116] K. D. Hagspiel, J. R. Stone, and D. A. Leung, "Renal angioplasty and stent placement with distal protection: preliminary experience with the FilterWire EX.," *Journal of Vascular and Interventional Radiology : JVIR*, vol. 16, no. 1, pp. 125–31, Jan. 2005.

[117] J. E. Hall, *Guyton and Hall Textbook of Medical Physiology: With STUDENT CONSULT Online Access (Guyton Physiology)*. Saunders, 2010, p. 1120.

[118] J. E. Hall, *Guyton and Hall Textbook of Medical Physiology: Enhanced E-book (Google eBook)*. Elsevier Health Sciences, 2010, p. 1120.

[119] Q. S. Hanley, P. J. Verveer, M. J. Gemkow, D. Arndt-Jovin, and T. M. Jovin, "An optical sectioning programmable array microscope implemented with a digital micromirror device," *Journal of Microscopy*, vol. 196, no. Pt 3, pp. 317–31, Dec. 1999.

[120] R. M. Haralock and L. G. Shapiro, *Computer and robot vision, Vol I*. Boston, MA, USA: Addison-Wesley Longman Publishing Co., Inc., 1991, pp. 28–48.

[121] S. W. Hasinoff and K. N. Kutulakos, "A Layer-Based Restoration Framework for Variable-Aperture Photography," in *2007 IEEE 11th International Conference on Computer Vision*, 2007, pp. 1–8.

[122] T. Haver, E. C. Raber, and P. Urayama, "An application of spatial deconvolution to a capillary-based high-pressure chamber for fluorescence microscopy imaging," *Journal of Microscopy*, vol. 230, no. Pt 3, pp. 363–71, Jun. 2008.

[123] S. Heinzer, T. Krucker, M. Stampanoni, R. Abela, E. P. Meyer, A. Schuler, P. Schneider, and R. Müller, "Hierarchical microimaging for multiscale analysis of large vascular networks.," *NeuroImage*, vol. 32, no. 2, pp. 626–36, Aug. 2006.

[124] J. C. Hellinger, A. H. Pezeshkmehr, M. Razavi, and G. D. Rubin, "Designing renal artery protection devices: consideration of main renal artery anatomy," *Journal of Vascular and Interventional Radiology*, vol. 15, no. 2, p. S159, 2004.

[125] M. V. Herman, R. A. Heinle, M. D. Klein, and R. Gorlin, "Localized disorders in myocardial contraction: Asynergy and its role in congestive heart failure," *The New England Journal of Medicine*, vol. 277, no. 5, pp. 222–32, Aug. 1967.

[126] W. E. Higgins, W. J. T. Spyra, and E. L. Ritman, "Automatic extraction of the arterial tree from 3-D angiograms," in *Images of the Twenty-First Century. Proceedings of the Annual International Engineering in Medicine and Biology Society, Vol 2*, 1989, pp. 563–564.

[127] T. Hildebrand and P. Rüegsegger, “A new method for the model- • independent assessment of thickness in three- • dimensional images,” *Journal of Microscopy*, vol. 185, no. 1, pp. 67–75, 1997.

[128] Y. Hiraoka, J. W. Sedat, and D. A. Agard, “Determination of three-dimensional imaging properties of a light microscope system. Partial confocal behavior in epifluorescence microscopy,” *Biophysical Journal*, vol. 57, no. 2, pp. 325–33, Feb. 1990.

[129] D. W. Holdsworth and M. M. Thornton, “Micro-CT in small animal and specimen imaging,” *Trends in Biotechnology*, vol. 20, no. 8, pp. S34–S39, Aug. 2002.

[130] R. M. Hoogeveen, C. J. Bakker, and M. A. Viergever, “Limits to the accuracy of vessel diameter measurement in MR angiography.,” *Journal of Magnetic Resonance Imaging*, vol. 8, no. 6, pp. 1228–35, 1998.

[131] D. A. Hooks, K. A. Tomlinson, S. G. Marsden, I. J. LeGrice, B. H. Smaill, A. J. Pullan, and P. J. Hunter, “Cardiac microstructure: implications for electrical propagation and defibrillation in the heart.,” *Circulation research*, vol. 91, no. 4, pp. 331–8, Aug. 2002.

[132] A. Hoover, V. Kouznetsova, and M. Goldbaum, “Locating blood vessels in retinal images by piecewise threshold probing of a matched filter response,” *IEEE Transactions on Medical Imaging*, vol. 19, no. 3, pp. 203–210, 2000.

[133] Q. Huang and G. C. Stockman, “Generalized tube model: recognizing 3D elongated objects from 2D intensity images,” in *Proceedings of IEEE Conference on Computer Vision and Pattern Recognition*, 1993, pp. 104–109.

[134] B. R. Hunt, “The Application of Constrained Least Squares Estimation to Image Restoration by Digital Computer,” *IEEE Transactions on Computers*, vol. C-22, no. 9, pp. 805–812, Sep. 1973.

[135] P. J. Hunter and M. Viceconti, “The VPH-physiome project: standards and tools for multiscale modeling in clinical applications,” *IEEE Reviews in Biomedical Engineering*, vol. 2, pp. 40–53, 2009.

[136] P. Hunter, P. V. Coveney, B. de Bono, V. Diaz, J. Fenner, A. F. Frangi, P. Harris, R. Hose, P. Kohl, P. Lawford, K. McCormack, M. Mendes, S. Omholt, A. Quarteroni, J. Skår, J. Tegner, S. Randall Thomas, I. Tollis, I. Tsamardinos, J. H. G. M. van Beek, and M. Viceconti, “A vision and strategy for the virtual physiological human in 2010 and beyond.,” *Philosophical Transactions. Series A, Mathematical, Physical, and Engineering Sciences*, vol. 368, no. 1920, pp. 2595–614, Jun. 2010.

[137] Y. Huo, B. Kaimovitz, Y. Lanir, T. Wischgoll, J. I. . E. Hoffman, and G. S. Kassab, “Biophysical model of the spatial heterogeneity of myocardial flow,” *Biophysical Journal*, vol. 96, no. 10, pp. 4035–43, May 2009.

[138] Y. Huo, T. Wischgoll, and G. S. Kassab, “Flow patterns in three-dimensional porcine epicardial coronary arterial tree.,” *American Journal of Physiology. Heart and Circulatory Physiology*, vol. 293, no. 5, pp. H2959–70, Nov. 2007.

[139] G. M. Hutchins, M. M. Miner, and J. K. Boitnott, “Vessel caliber and branch-angle of human coronary artery branch-points,” *Circulation Research*, vol. 38, no. 6, pp. 572–576, Jun. 1976.

[140] E. J. Ientilucci, “Synthetic Simulation and Modeling of Image Intensified CCDs (IICCD), MS Thesis,” Rochester Institute of Technology, 2000.

[141] Ientilucci, Emmett J., Brown, Scott D., Schott, John R., and Raqueno, Rolando V., “Multispectral simulation environment for modeling low-light-level sensor systems,” *Proc. SPIE Vol. 3434*, vol. 3434, pp. 10–19, 1998.

[142] A. Ishimaru, *Wave propagation and scattering in random media*. New York: IEEE Press, 1997.

[143] Y. Ishizaki, Y. Bandai, K. Shimomura, and H. Abe, “Changes in splanchnic blood flow and cardiovascular effects following peritoneal insufflation of carbon dioxide,” *Surgical Endoscopy*, vol. 7, no. 5, pp. 420–423, 1993.

[144] J. A. Izatt, M. R. Hee, G. M. Owen, E. A. Swanson, and J. G. Fujimoto, “Optical coherence microscopy in scattering media,” *Optics Letters*, vol. 19, no. 8, p. 590, Apr. 1994.

[145] S. L. Jacques, “Light distributions from point, line and plane sources for photochemical reactions and fluorescence in turbid biological tissues,” *Photochemistry and Photobiology*, vol. 67, no. 1, pp. 23–32, Jan. 1998.

[146] A. K. Jain, *Fundamentals of Digital Image Processing*. Prentice-Hall, 1989.

[147] P. Jakubik, “Model-based restoration of vibrated images with geometry-free tomography: in-vessel viewing with the ITER European Home Team’s probe,” *Proceedings of SPIE*, vol. 3460, pp. 664–674, 1998.

[148] M. Jermyn, B. Pogue, H. R. Ghadyani, S. Davis, M. A. Mastanduno, and H. Dehghani, “A User-Enabling Visual Workflow for Near-Infrared Light Transport Modeling in Tissue - OSA Technical Digest,” in *Biomedical Optics*, 2012, p. BW1A.7.

[149] D. Jeżyk, B. Duda, J. Jerzemowski, and M. Grzybiak, “Positions of septal papillary muscles in human hearts,” *Folia Morphologica*, vol. 69, no. 2, pp. 101–100, May 2010.

[150] X. Jiang and D. Mojon, “Adaptive local thresholding by verification-based multithreshold probing with application to vessel detection in retinal images,” *IEEE Transactions on Pattern Analysis and Machine Intelligence*, vol. 25, no. 1, pp. 131–137, Jan. 2003.

[151] Z. L. Jiang, G. S. Kassab, and Y. C. Fung, “Diameter-defined Strahler system and connectivity matrix of the pulmonary arterial tree,” *Journal of Applied Physiology (Bethesda, Md. : 1985)*, vol. 76, no. 2, pp. 882–92, Mar. 1994.

[152] D. R. Jones, C. D. Perttunen, and B. E. Stuckman, “Lipschitzian optimization without the Lipschitz constant,” *Journal of Optimization Theory and Applications*, vol. 79, no. 1, pp. 157–181, 1993.

[153] D. Jones, M. Schonlau, and W. Welch, “Efficient Global Optimization of Expensive Black-Box Functions,” *Journal of Global Optimization*, vol. 13, no. 4, pp. 455 – 492, 1998.

[154] S. M. Jorgensen, O. Demirkaya, and E. L. Ritman, “Three-dimensional imaging of vasculature and parenchyma in intact rodent organs with X-ray micro-CT,” *American Journal of Physiology. Heart and Circulatory Physiology*, vol. 275, no. 3, pp. H1103–1114, Sep. 1998.

[155] B. Kaimovitz, G. S. Kassab, and Y. Lanir, “Morphology-based stochastic reconstruction of the pig coronaries in a 3D heart model,” *Journal of Biomechanics*, vol. 39, no. 1, p. S298, 2006.

[156] B. Kaimovitz, Y. Lanir, and G. S. Kassab, “Large-scale 3-D geometric reconstruction of the porcine coronary arterial vasculature based on detailed anatomical data,” *Annals of Biomedical Engineering*, vol. 33, no. 11, pp. 1517–1535, 2005.

[157] B. Kaimovitz, Y. Huo, Y. Lanir, and G. S. Kassab, “Diameter asymmetry of porcine coronary arterial trees: structural and functional implications.,” *American Journal of Physiology. Heart and Circulatory Physiology*, vol. 294, no. 2, pp. H714–23, Feb. 2008.

[158] B. Kaimovitz, Y. Lanir, and G. S. Kassab, “A full 3-D reconstruction of the entire porcine coronary vasculature,” *AAmerican Journal of Physiology. Heart and Circulatory Physiology*, vol. 299, no. 4, pp. H1064–76, Oct. 2010.

[159] S. Kansal, D. Roitman, and L. T. Sheffield, “Interventricular septal thickness and left ventricular hypertrophy. An echocardiographic study,” *Circulation*, vol. 60, no. 5, pp. 1058–65, Nov. 1979.

[160] R. Karch, F. Neumann, M. Neumann, and W. Schreiner, “Staged growth of optimized arterial model trees.,” *Annals of Biomedical Engineering*, vol. 28, no. 5, pp. 495–511, May 2000.

[161] T. Karino and H. L. Goldsmith, “Particle flow behavior in models of branching vessels. II. Effects of branching angle and diameter ratio on flow patterns.,” *Biorheology*, vol. 22, no. 2, pp. 87–104, Jan. 1985.

[162] M. Kass, A. Witkin, and D. Terzopoulos, “Snakes: Active contour models,” *International Journal of Computer Vision*, vol. 1, no. 4, p. 321—331, 1988.

[163] G. S. Kassab, J. Berkley, and Y. C. Fung, “Analysis of pig’s coronary arterial blood flow with detailed anatomical data,” *Annals of Biomedical Engineering*, vol. 25, no. 1, pp. 204–17, 1997.

[164] G. S. Kassab and Y. C. B. Fung, “The pattern of coronary arteriolar bifurcations and the uniform shear hypothesis,” *Annals of Biomedical Engineering*, vol. 23, no. 1, pp. 13–20, 1995.

[165] G. S. Kassab, D. H. Lin, and Y. C. Fung, “Morphometry of pig coronary venous system,” *The American Journal of Physiology*, vol. 267, no. 6 Pt 2, pp. H2100–13, Dec. 1994.

[166] G. S. Kassab, E. Pallencaoe, A. Schatz, and Y. C. Fung, “Longitudinal position matrix of the pig coronary vasculature and its hemodynamic implications,” *The American Journal of Physiology*, vol. 273, no. 6 Pt 2, pp. H2832–42, Dec. 1997.

[167] G. S. Kassab, C. A. Rider, N. J. Tang, and Y. C. Fung, “Morphometry of pig coronary arterial trees,” *The American Journal of Physiology*, vol. 265, no. 1 Pt 2, pp. H350–65, Jul. 1993.

[168] T. Katila, I. Magnin, P. Clarysse, J. Montagnat, and J. Nenonen, “Functional imaging and modeling of the heart,” *5th International Conference, FIMH 2009 Nice, France, June 3-5, 2009*, p. 537, 2009.

[169] A. K. Katsaggelos, J. Biemond, R. W. Schafer, and R. M. Mersereau, “A regularized iterative image restoration algorithm,” *IEEE Transactions on Signal Processing*, vol. 39, no. 4, pp. 914–929, Apr. 1991.

[170] A. K. Katsaggelos and K. T. Lay, “Maximum likelihood blur identification and image restoration using the EM algorithm,” *IEEE Transactions on Signal Processing*, vol. 39, no. 3, pp. 729–733, Mar. 1991.

[171] A. K. Katsaggelos, “Image identification and restoration based on the expectation-maximization algorithm,” *Optical Engineering*, vol. 29, no. 5, pp. 436–445, May 1990.

[172] H. U. Kauczor, “Contrast-enhanced magnetic resonance angiography of the pulmonary vasculature,” *Investigative Radiology*, vol. 33, no. 9, pp. 606–617, 1998.

[173] S. Kay, *Fundamentals of Statistical Signal Processing, Volume I: Estimation Theory (v. 1)*, 1st ed. Prentice Hall, 1993.

[174] J. J. Kelly, J. R. Ewen, S. L. Bernard, R. W. Glenny, and C. H. Barlow, “Regional blood flow measurements from fluorescent microsphere images using an Imaging CryoMicrotome,” *Review of Scientific Instruments*, vol. 71, no. 1, p. 228, Jan. 2000.

[175] A. I. Kholodnykh, I. Y. Petrova, K. V. Larin, M. Motamedi, and R. O. Esenaliev, "Precision of measurement of tissue optical properties with optical coherence tomography.," *Applied Optics*, vol. 42, no. 16, pp. 3027–37, Jun. 2003.

[176] A. D. Kim, "Transport theory for light propagation in biological tissue," *Journal of the Optical Society of America. A, Optics, Image Science, and Vision*, vol. 21, no. 5, pp. 820–7, May 2004.

[177] C. Kirbas and F. Quek, "A review of vessel extraction techniques and algorithms," *Association for Computing Machinery Computing Surveys*, vol. 36, no. 2, pp. 81–121, Jun. 2004.

[178] K. Krissian, G. Malandain, N. Ayache, R. Vaillant, and Y. Trousset, "Model-Based Detection of Tubular Structures in 3D Images," *Computer Vision and Image Understanding*, vol. 80, no. 2, pp. 130–171, Nov. 2000.

[179] D. Kundur and D. Hatzinakos, "Blind image deconvolution revisited," *IEEE Signal Processing Magazine*, vol. 13, no. 6, pp. 61–63, 1996.

[180] D. Kundur and D. Hatzinakos, "A novel blind deconvolution scheme for image restoration using recursive filtering," *IEEE Transactions on Signal Processing*, vol. 46, no. 2, pp. 375–390, 1998.

[181] R. L. Lagendijk, "Regularized iterative image restoration with ringing reduction," *IEEE Transactions on Acoustics, Speech, and Signal Processing*, vol. 36, no. 12, pp. 1874–1888, 1988.

[182] B. W. Lagerveld, R. D. ter Wee, J. J. . M. C. H. de la Rosette, J. A. E. Spaan, and H. Wijkstra, "Vascular fluorescence casting and imaging cryomicrotomy for computerized three-dimensional renal arterial reconstruction," *British Journal of Urology International*, vol. 100, no. 2, pp. 387–91, Aug. 2007.

[183] B. W. Lagerveld, P. van Horssen, M. P. Laguna, J. P. H. M. van den Wijngaard, M. Siebes, H. Wijkstra, J. J. M. C. H. de la Rosette, and J. A. E. Spaan, "Gradient changes in porcine renal arterial vascular anatomy and blood flow after cryoablation," *The Journal of Urology*, vol. 186, no. 2, pp. 681–6, Aug. 2011.

[184] B. W. Lagerveld, P. van Horssen, M. P. L. Pes, J. P. H. M. van den Wijngaard, G. J. Streekstra, J. J. M. C. H. de la Rosette, H. Wijkstra, and J. A. E. Spaan, "Immediate effect of kidney cryoablation on renal arterial structure in a porcine model studied by imaging cryomicrotome," *The Journal of Urology*, vol. 183, no. 3, pp. 1221–6, Mar. 2010.

[185] L. Lam, S. W. Lee, and C. Y. Suen, "Thinning methodologies-a comprehensive survey," *IEEE Transactions on Pattern Analysis and Machine Intelligence*, vol. 14, no. 9, pp. 869–885, 1992.

[186] P. Lamata, S. Niederer, D. Barber, D. Norsletten, J. Lee, R. Hose, and N. Smith, "Personalization of cubic Hermite meshes for efficient biomechanical simulations," in *Medical image computing and computer-assisted intervention : MICCAI ... International Conference on Medical Image Computing and Computer-Assisted Intervention*, 2010, vol. 13, no. Pt 2, pp. 380–7.

[187] P. Lamata, S. Niederer, D. Nordsletten, D. C. Barber, I. Roy, D. R. Hose, and N. Smith, "An accurate, fast and robust method to generate patient-specific cubic Hermite meshes.," *Medical Image Analysis*, vol. 15, no. 6, pp. 801–13, Dec. 2011.

[188] W. J. E. Lamm, S. L. Bernard, W. W. Wagner, and R. W. Glenny, "Intravital microscopic observations of 15-microm microspheres lodging in the pulmonary microcirculation.," *Journal of Applied Physiology*, vol. 98, no. 6, pp. 2242–8, Jun. 2005.

[189] S. Lang, *Calculus of several variables*. Reading, Mass: Addison-Wesley Pub. Co., 1973, p. 376.

[190] L. Lecornu, C. Roux, and J. J. Jacq, "Extraction of vessel contours in angiograms by simultaneous tracking of the two edges," in *16th Annual International Conference of the IEEE Engineering in Medicine and Biology Society6th Annual International Conference of the IEEE Engineering in Medicine and Biology Society*, 1994, pp. 678–679.

[191] J. Lee, "Computational Modelling of Coronary Structure and Flow Mechanics, DPhil Thesis," University of Oxford, 2009.

[192] J. Lee and N. Smith, "The Multi-Scale Modelling of Coronary Blood Flow," *Annals of Biomedical Engineering*, vol. 10, no. 1007, pp. 583–587, 2012.

[193] J. Lee and N. Smith, "Development and application of a one-dimensional blood flow model for microvascular networks.," *Proceedings of the Institution of Mechanical Engineers. Part H, Journal of engineering in medicine*, vol. 222, no. 4, pp. 487–511, May 2008.

[194] J. Lee and N. P. Smith, "Theoretical modeling in hemodynamics of microcirculation," *Microcirculation*, vol. 15, no. 8, pp. 699–714, 2008.

[195] J. Lee, P. Beighley, E. Ritman, and N. Smith, "Automatic segmentation of 3D micro-CT coronary vascular images," *Medical Image Analysis*, vol. 11, no. 6, pp. 630–47, Dec. 2007.

[196] J. Lee, S. Niederer, D. Nordsletten, I. Le Grice, B. Smaill, B. Smail, D. Kay, and N. Smith, "Coupling contraction, excitation, ventricular and coronary blood flow across scale and physics in the heart," *Philosophical Transactions. Series A, Mathematical, Physical, and Engineering Sciences*, vol. 367, no. 1896, pp. 2311–31, Jun. 2009.

[197] S. W. Lee, L. Antiga, J. D. Spence, and D. A. Steinman, “Geometry of the carotid bifurcation predicts its exposure to disturbed flow,” *Stroke: a Journal of Cerebral Circulation*, vol. 39, no. 8, pp. 2341–7, Aug. 2008.

[198] S. C. Lee, H. K. Kim, I. K. Chun, M. H. Cho, S. Y. Lee, and M. H. Cho, “A flat-panel detector based micro-CT system: performance evaluation for small-animal imaging,” *Physics in Medicine and Biology*, vol. 48, no. 24, pp. 4173–4185, Dec. 2003.

[199] T. C. Lee, R. L. Kashyap, and C. N. Chu, “Building Skeleton Models via 3-D Medial Surface Axis Thinning Algorithms,” *CVGIP: Graphical Models and Image Processing*, vol. 56, no. 6, pp. 462–478, Nov. 1994.

[200] I. LeGrice, G. Sands, D. Hooks, D. Gerneke, and B. Smaill, “Microscopic imaging of extended tissue volumes,” *Clinical and Experimental Pharmacology & Physiology*, vol. 31, no. 12, pp. 902–5, Dec. 2004.

[201] E. L. Lehmann and G. Casella, *Theory of Point Estimation (Google eBook)*. Springer, 1998, p. 590.

[202] M. Lemaitre, F. Meriaudeau, O. Laligant, and J. Blanc-Talon, “Restoration of Images with Atmospheric Perturbation Simulation,” in *Digital Image Computing: Techniques and Applications (DICTA’05)*, 2005, pp. 18–18.

[203] D. Lesage, E. D. Angelini, I. Bloch, and G. Funka-Lea, “A review of 3D vessel lumen segmentation techniques: models, features and extraction schemes.,” *Medical Image Analysis*, vol. 13, no. 6, pp. 819–45, Dec. 2009.

[204] C. Li, C. Xu, C. Gui, and M. D. Fox, “Level Set Evolution without Re-Initialization: A New Variational Formulation,” in *2005 IEEE Computer Society Conference on Computer Vision and Pattern Recognition (CVPR’05)*, 2005, vol. 1, pp. 430–436.

[205] D. Lloyd-Jones, R. J. Adams, T. M. Brown, M. Carnethon, S. Dai, G. De Simone, T. B. Ferguson, E. Ford, K. Furie, C. Gillespie, A. Go, K. Greenlund, N. Haase, S. Hailpern, P. M. Ho, V. Howard, B. Kissela, S. Kittner, D. Lackland, L. Lisabeth, A. Marelli, M. M. McDermott, J. Meigs, D. Mozaffarian, M. Mussolino, G. Nichol, V. L. Roger, W. Rosamond, R. Sacco, P. Sorlie, R. Stafford, T. Thom, S. Wasserthiel-Smoller, N. D. Wong, and J. Wylie-Rosett, “Heart disease and stroke statistics--2010 update: a report from the American Heart Association.,” *Circulation*, vol. 121, no. 7, pp. e46–e215, Feb. 2010.

[206] L. M. Lorigo, O. D. Faugeras, W. E. L. Grimson, R. Keriven, R. Kikinis, A. Nabavi, and C. F. Westin, “CURVES: Curve evolution for vessel segmentation,” *Medical Image Analysis*, vol. 5, no. 3, pp. 195–206, Sep. 2001.

[207] Z. Lou and W. J. Yang, “Biofluid dynamics at arterial bifurcations.,” *Critical reviews in biomedical engineering*, vol. 19, no. 6, pp. 455–93, Jan. 1992.

[208] S. Lu and S. Eiho, “Automatic detection of the coronary arterial contours with sub-branches from an x-ray angiogram,” in *IEEE Conference on Computers in Cardiology, Issue 5-8*, 1993, pp. 575–578.

[209] D. L. Luchtel, J. C. Boykin, S. L. Bernard, and R. W. Glenny, “Histological methods to determine blood flow distribution with fluorescent microspheres.,” *Biotechnic & Histochemistry : Official Publication of the Biological Stain Commission*, vol. 73, no. 6, pp. 291–309, Nov. 1998.

[210] G. Ludwig, “Capillary pattern of the myocardium methods,” *Achieve Experimental Pathology*, vol. 5, pp. 238–71, 1971.

[211] J. Markham and J. A. Conchello, “Fast maximum-likelihood image-restoration algorithms for three-dimensional fluorescence microscopy.,” *Journal of the Optical Society of America. A, Optics, image science, and vision*, vol. 18, no. 5, pp. 1062–71, May 2001.

[212] A. Marquina and S. Osher, “Explicit Algorithms For A New Time Dependent Model Based On Level Set Motion For Nonlinear Deblurring And Noise Removal,” *SIAM Journal on Scientific Computing*, vol. 22, pp. 387 – 405, 1999.

[213] D. M. Martinez, “Model-based motion estimation and its application to restoration and interpolation of motion pictures,” *NASA STI/Recon Technical Report N*, 1987.

[214] M. Marxen, M. M. Thornton, and C. B. Chiarot, “MicroCT scanner performance and considerations for vascular specimen imaging,” *Medical Physics*, vol. 31, no. 2, pp. 305–313, 2004.

[215] Y. Masutani, T. Schiemann, and K. H. Höhne, “Vascular shape segmentation and structure extraction using a shape-based region-growing model,” *MEDICAL IMAGE COMPUTING AND COMPUTER-ASSISTED INTERVENTATION — MICCAI’98 Lecture Notes in Computer Science*, vol. 1496, pp. 1242–1249, 1998.

[216] L. C. Maxwell, A. P. Shepherd, and C. A. McMahan, “Microsphere passage through intestinal circulation: via shunts or capillaries?,” *The American Journal of Physiology*, vol. 248, no. 2 Pt 2, pp. H217–24, Feb. 1985.

[217] J. G. McNally, T. Karpova, J. Cooper, and J. A. Conchello, “Three-dimensional imaging by deconvolution microscopy,” *Methods (San Diego, Calif.)*, vol. 19, no. 3, pp. 373–85, Nov. 1999.

[218] A. C. G. MD and J. E. H. PhD, *Textbook of Medical Physiology (Guyton Physiology)*. Saunders, 2000.

[219] R. W. Millard, “Induction of functional coronary collaterals in the swine heart,” *Basic Research in Cardiology*, vol. 76, no. 5, pp. 468–73, 1981.

[220] N. Mittal, Y. Zhou, C. Linares, S. Ung, B. Kaimovitz, S. Molloi, and G. S. Kassab, "Analysis of blood flow in the entire coronary arterial tree," *American Journal of Physiology. Heart and Circulatory Physiology*, vol. 289, no. 1, pp. H439–46, Jul. 2005.

[221] N. Mittal, Y. Zhou, S. Ung, C. Linares, S. Molloi, and G. S. Kassab, "A computer reconstruction of the entire coronary arterial tree based on detailed morphometric data.," *Annals of Biomedical Engineering*, vol. 33, no. 8, pp. 1015–26, Aug. 2005.

[222] S. Möhlenkamp, L. O. Lerman, Z. Bajzer, P. E. Lund, and E. L. Ritman, "Quantification of myocardial microcirculatory function with X-ray CT.," *Annals of the New York Academy of Sciences*, vol. 972, no. 1, pp. 307–16, Oct. 2002.

[223] J. R. Monck, A. F. Oberhauser, T. J. Keating, and J. M. Fernandez, "Thin-section ratiometric Ca2+ images obtained by optical sectioning of fura-2 loaded mast cells," *The Journal of Cell Biology*, vol. 116, no. 3, pp. 745–59, Feb. 1992.

[224] E. Moniz, *L'angiographie cérébrale, ses applications et résultats en anatomie, physiologie de clinique (Cerebral angiography, its applications and results in anatomy, physiology, and clinic*. Masson, Paris: , 1934.

[225] U. Morgner, W. Drexler, F. X. Kärtner, X. D. Li, C. Pitris, E. P. Ippen, and J. G. Fujimoto, "Spectroscopic optical coherence tomography," *Optics Letters*, vol. 25, no. 2, p. 111, Jan. 2000.

[226] R. L. Mueller and T. A. Sanborn, "The history of interventional cardiology: cardiac catheterization, angioplasty, and related interventions," *American Heart Journal*, vol. 129, no. 1, pp. 146–72, Jan. 1995.

[227] A. Murat Tekalp, H. Kaufman, and J. W. Woods, "Model-based segmentation and space-variant restoration of blurred images by decision-directed filtering," *Signal Processing*, vol. 15, no. 3, pp. 259–269, Oct. 1988.

[228] C. D. Murray, "The Physiological Principle of Minimum Work: I. The Vascular System and the Cost of Blood Volume," *Proceedings of the National Academy of Sciences of the United States of America*, vol. 12, no. 3, pp. 207–14, Mar. 1926.

[229] J. G. Myers, J. A. Moore, M. Ojha, K. W. .Johnston, and C. R. Ethier, "Factors influencing blood flow patterns in the human right coronary artery.," *Annals of Biomedical Engineering*, vol. 29, no. 2, pp. 109–20, Feb. 2001.

[230] D. Nain, A. Yezzi, and G. Turk, "Vessel Segmentation Using a Shape Driven Flow," in *MEDICAL IMAGE COMPUTING AND COMPUTER-ASSISTED INTERVENTION, Vol. 3216*, 2004, pp. 51–59.

[231] A. Nussbaum, “Ueber das gefassystem des Herzens,” *Archiv fur mikroskopische Anatomie*, vol. 80, pp. 450–477, 1912.

[232] J. F. O’Brien and N. F. Ezquerra, “Automated Segmentation of Coronary Vessels in Angiographic Image Sequences Utilizing Temporal, Spatial and Structural Constraints,” in *SPIE Conference Visualization in Biomedical Computing, Vol. 2359*, 1994, pp. 25–37.

[233] T. O’Donnell and T. E. Boult, “The extruded generalized cylinder: A deformable model for object recovery,” in *IEEE Conference on Computer Vision and Pattern Recognition*, 1994, pp. 174–181.

[234] A. Ofer, S. S. Nitecki, S. Linn, M. Epelman, D. Fischer, T. Karram, D. Litmanovich, H. Schwartz, A. Hoffman, and A. Engel, “Multidetector CT Angiography of Peripheral Vascular Disease: A Prospective Comparison with Intraarterial Digital Subtraction Angiography,” *American Journal of Roentgenol*, vol. 180, no. 3, pp. 719–724, Mar. 2003.

[235] E. S. Ofjord, G. Clausen, and K. Aukland, “Skimming of microspheres in vitro: implications for measurement of intrarenal blood flow.,” *The American journal of physiology*, vol. 241, no. 3, pp. H342–7, Sep. 1981.

[236] T. Olofsson, “Deconvolution and Model-Based Restoration of Clipped Ultrasonic Signals,” *IEEE Transactions on Instrumentation and Measurement*, vol. 54, no. 3, pp. 1235–1240, Jun. 2005.

[237] M. S. Olufsen, C. S. Peskin, and W. Y. Kim, “Numerical simulation and experimental validation of blood flow in arteries with structured-tree outflow conditions,” *Annals of Biomedical Engineering*, vol. 28, no. 11, pp. 1281–99, 2000.

[238] M. Oshima, R. Torii, T. Kobayashi, N. Taniguchi, and K. Takagi, “Finite element simulation of blood flow in the cerebral artery,” *Computer Methods in Applied Mechanics and Engineering*, vol. 191, no. 6–7, pp. 661–671, Dec. 2001.

[239] N. Otsu, “A Threshold Selection Method from Gray-Level Histograms,” *IEEE Transactions on Systems, Man, and Cybernetics*, vol. 9, no. 1, pp. 62–66, 1979.

[240] M. K. Ozkan, A. M. Tekalp, and M. I. Sezan, “POCS-based restoration of space-varying blurred images,” *IEEE Transactions on Image Processing : A Publication of the IEEE Signal Processing Society*, vol. 3, no. 4, pp. 450–4, Jan. 1994.

[241] P. Pankajakshan, L. Blanc-Feraud, Z. Kam, and J. Zerubia, “Point-Spread Function retrieval for fluorescence microscopy,” *2009 IEEE International Symposium on Biomedical Imaging: From Nano to Macro*, pp. 1095–1098, Jun. 2009.

[242] T. N. Pappas and J. S. Lim, “A new method for estimation of coronary artery dimensions in angiograms,” *IEEE Transactions on Acoustics, Speech, and Signal Processing*, vol. 36, no. 9, pp. 1501–1513, 1988.

[243] Pedersen L., Grunkin M., Ersboll B., Madsen K., Larsen M., Christoffersen N., and Skands U., “Quantitative measurement of changes in retinal vessel diameter in ocular fundus images,” *Pattern Recognition Letters*, vol. 21, no. 13, p. 9, 2000.

[244] E. M. Pedersen, A. P. Yoganathan, and X. P. Lefebvre, “Pulsatile flow visualization in a model of the human abdominal aorta and aortic bifurcation,” *Journal of Biomechanics*, vol. 25, no. 8, pp. 935–944, Aug. 1992.

[245] K. Perktold and G. Rappitsch, “Computer simulation of local blood flow and vessel mechanics in a compliant carotid artery bifurcation model,” *Journal of Biomechanics*, vol. 28, no. 7, pp. 845–856, Jul. 1995.

[246] R. R. Petrocelli, J. L. Elion, and K. M. Manbeck, “A new method for structure recognition in unsubtracted digital angiograms,” in *Proceedings of the IEEE Computers in Cardiology, Issue 11-14*, 1992, pp. 207–210.

[247] R. R. Petrocelli, K. M. Manbeck, and J. L. Elion, “Three dimensional structure recognition in digital angiograms using Gauss-Markov methods,” in *Proceedings of the IEEE Computers in Cardiology, Issue 5-8*, 1993, pp. 101–104.

[248] M. Pilz, S. Honold, and A. Kienle, “Determination of the optical properties of turbid media by measurements of the spatially resolved reflectance considering the point-spread function of the camera system.,” *Journal of Biomedical Optics*, vol. 13, no. 5, p. 054047, Jan. 2008.

[249] F. Plouraboue, P. Cloetens, C. Fonta, A. Steyer, F. Lauwers, and J. P. Marc-Vergnes, “X-ray high-resolution vascular network imaging,” *Journal of Microscopy*, vol. 215, no. Pt 2, pp. 139–48, Aug. 2004.

[250] A. J. Pope, G. B. Sands, B. H. Smaill, and I. J. LeGrice, “Three-dimensional transmural organization of perimysial collagen in the heart,” *American Journal of Physiology. Heart and Circulatory Physiology*, vol. 295, no. 3, pp. H1243–H1252, Sep. 2008.

[251] A. R. Pries, T. W. Secomb, P. Gaehtgens, and J. F. Gross, “Blood flow in microvascular networks. Experiments and simulation,” *Circulation Research*, vol. 67, no. 4, pp. 826–34, Oct. 1990.

[252] A. R. Pries, T. W. Secomb, T. Gessner, M. B. Sperandio, J. F. Gross, and P. Gaehtgens, “Resistance to blood flow in microvessels in vivo,” *Circulation Research*, vol. 75, no. 5, pp. 904–15, Nov. 1994.

[253] A. R. Pries, T. W. Secomb, and P. Gaehtgens, “Biophysical aspects of blood flow in the microvasculature,” *Cardiovascular Research*, vol. 32, no. 4, pp. 654–667, Oct. 1996.

[254] V. Prinet, O. Mona, and J. M. Rocchisani, “Multi-dimensional vessels extraction using crest lines,” in *Proceedings of 17th International Conference of the Engineering in Medicine and Biology Society*, 1997, vol. 1, p. 393—394.

[255] F. W. Prinzen and J. B. Bassingthwaighte, “Blood flow distributions by microsphere deposition methods,” *Cardiovascular Research*, vol. 45, no. 1, pp. 13–21, Jan. 2000.

[256] F. W. Prinzen and R. W. Glenny, “Developments in non-radioactive microsphere techniques for blood flow measurement,” *Cardiovascular Research*, vol. 28, no. 10, pp. 1467–75, Oct. 1994.

[257] M. Prokop, “Multislice CT angiography,” *European Journal of Radiology*, vol. 36, no. 2, pp. 86–96, 2000.

[258] C. Pudney, “Distance-ordered Homotopic Thinning: a Skeletonization Algorithm for 3D Digital Images,” *Computer Vision and Image Understanding*, vol. 72, no. 3, pp. 404–413, 1998.

[259] A. J. Pullan, N. P. Smith, and P. J. Hunter, “An Anatomically Based Model of Transient Coronary Blood Flow in the Heart,” *SIAM Journal on Applied Mathematics*, vol. 62, no. 3, pp. 990–1018, Jan. 2002.

[260] S. Raab, E. Thein, A. G. Harris, and K. Messmer, “A new sample-processing unit for the fluorescent microsphere method,” *The American Journal of Physiology*, vol. 276, no. 5 Pt 2, pp. H1801–6, May 1999.

[261] T. Ragan, J. D. Sylvan, K. H. Kim, and H. Huang, “High-resolution whole organ imaging using two-photon tissue cytometry,” *Journal of Biomedical Optics*, vol. 12, no. 1, 2007.

[262] A. N. Rajagopalan and S. Chaudhuri, “An MRF model-based approach to simultaneous recovery of depth and restoration from defocused images,” *IEEE Transactions on Pattern Analysis and Machine Intelligence*, vol. 21, no. 7, pp. 577–589, Jul. 1999.

[263] K. Rakusan, N. Cicutti, and M. F. Flanagan, “Changes in the microvascular network during cardiac growth, development, and aging,” *Cellular & Molecular Biology Research*, vol. 40, no. 2, pp. 117–22, Jan. 1994.

[264] K. Rakusan and P. Wicker, “Morphometry of the small arteries and arterioles in the rat heart: effects of chronic hypertension and exercise.,” *Cardiovascular Research*, vol. 24, no. 4, pp. 278–84, Apr. 1990.

[265] S. Ramcharitar, Y. Onuma, J.-P. Aben, C. Consten, B. Weijers, M.-A. Morel, and P. W. Serruys, "A novel dedicated quantitative coronary analysis methodology for bifurcation lesions," *EuroIntervention : Journal of EuroPCR in Collaboration with the Working Group on Interventional Cardiology of the European Society of Cardiology*, vol. 3, no. 5, pp. 553–7, Mar. 2008.

[266] B. Randoux, B. Marro, F. Koskas, M. Duyme, M. Sahel, A. Zouaoui, and C. Marsault, "Carotid artery stenosis: prospective comparison of CT, three-dimensional gadolinium-enhanced MR, and conventional angiography," *Radiology*, vol. 220, no. 1, pp. 179–85, Jul. 2001.

[267] A. Restivo, A. Smith, J. L. Wilkinson, and R. H. Anderson, "The medial papillary muscle complex and its related septomarginal trabeculation. A normal anatomical study on human hearts," *Journal of Anatomy*, vol. 163, pp. 231–42, Apr. 1989.

[268] H. T. Robertson and M. P. Hlastala, "Microsphere maps of regional blood flow and regional ventilation," *Journal of Applied Physiology*, vol. 102, no. 3, pp. 1265–72, Mar. 2007.

[269] G. Roditi and D. Kusumawidjaja, "Magnetic resonance angiography and computed tomography angiography for peripheral arterial disease," *Imaging*, vol. 21, no. 2, pp. 85–108, Aug. 2009.

[270] M. Rolf, "Three-Dimensional Coronary Tree Vessel Diameter Measurements, Masters Thesis," Biophysical Engineering, Applied Physics, University of Twente, 2005.

[271] M. P. Rolf, R. ter Wee, T. G. van Leeuwen, J. A. E. Spaan, and G. J. Streekstra, "Diameter measurement from images of fluorescent cylinders embedded in tissue," *Medical & Biological Engineering & Computing*, vol. 46, no. 6, pp. 589–96, Jun. 2008.

[272] J. Rosenthal, V. Mangal, D. Walker, M. Bennett, T. J. Mohun, and C. W. Lo, "Rapid high resolution three dimensional reconstruction of embryos with episcopic fluorescence image capture," *Birth Defects Research. Part C, Embryo Today: Reviews*, vol. 72, no. 3, pp. 213–23, Sep. 2004.

[273] D. Roy, M. Breen, O. Salvado, M. Heinzel, E. McKinley, and D. Wilson, "Imaging System for Creating 3D Block-Face Cryo-Images Of Whole Mice," *Proceedings - Society of Photo-Optical Instrumentation Engineers*, vol. 6143, p. nihpa112282, Jan. 2006.

[274] D. Roy, G. J. Steyer, M. Gargesha, M. E. Stone, and D. L. Wilson, "3D cryo-imaging: a very high-resolution view of the whole mouse," *Anatomical Record (Hoboken, N.J. : 2007)*, vol. 292, no. 3, pp. 342–51, Mar. 2009.

[275] T. J. Ryan, “The coronary angiogram and its seminal contributions to cardiovascular medicine over five decades,” *Transactions of the American Clinical and Climatological Association*, vol. 113, pp. 261–71, Jan. 2002.

[276] G. B. Sands, D. A. Gerneke, D. A. Hooks, C. R. Green, B. H. Smaill, and I. J. Legrice, “Automated imaging of extended tissue volumes using confocal microscopy.,” *Microscopy Research and Technique*, vol. 67, no. 5, pp. 227–39, Aug. 2005.

[277] G. B. Sands, B. H. Smaill, and I. J. LeGrice, “Virtual sectioning of cardiac tissue relative to fiber orientation,” *Annual International Conference of the IEEE Engineering in Medicine and Biology Society. IEEE Engineering in Medicine and Biology Society*, vol. 2008, pp. 226–9, Jan. 2008.

[278] A. Sarantopoulos, G. Themelis, and V. Ntziachristos, “Imaging the bio-distribution of fluorescent probes using multispectral epi-illumination cryoslicing imaging.,” *Molecular iIaging and Biology : MIB : the Official Publication of the Academy of Molecular Imaging*, vol. 13, no. 5, pp. 874–85, Oct. 2011.

[279] A. Sarwal and A. P. Dhawan, “3-D reconstruction of coronary arteries,” in *Proceedings of 16th Annual International Conference of the IEEE Engineering in Medicine and Biology Society*, 1994, pp. 504–505.

[280] Y. Sato, T. Araki, M. Hanayama, H. Naito, and S. Tamura, “A viewpoint determination system for stenosis diagnosis and quantification in coronary angiographic image acquisition,” *IEEE Transactions on Medical Imaging*, vol. 17, no. 1, pp. 121–37, Feb. 1998.

[281] Y. Sato, S. Nakajima, H. Atsumi, T. Koller, G. Gerig, S. Yoshida, and R. Kikinis, “3D Multi-scale line filter for segmentation and visualization of curvilinear structures in medical images,” *IEEE Medical Image Analysis*, vol. 2, no. 2, pp. 143–168, Mar. 1998.

[282] J. Sauvola and M. Pietikäinen, “Adaptive document image binarization,” *Pattern Recognition*, vol. 33, no. 2, pp. 225–236, 2000.

[283] R. W. Schafer, R. M. Mersereau, and M. A. Richards, “Constrained iterative restoration algorithms,” *Proceedings of the IEEE*, vol. 69, no. 4, pp. 432–450, Apr. 1981.

[284] S. J. Schambach, S. Bag, L. Schilling, C. Groden, and M. A. Brockmann, “Application of micro-CT in small animal imaging,” *Methods (San Diego, Calif.)*, vol. 50, no. 1, pp. 2–13, Jan. 2010.

[285] J. M. Schmitt, “Restoration of optical coherence images of living tissue using the CLEAN algorithm,” *Journal of Biomedical Optics*, vol. 3, no. 1, p. 66, Jan. 1998.

[286] R. Sedgewick, *Algorithms in C*, 3rd ed. Addison-Wesley, 1998, pp. 11–20.

[287] S. I. Seldinger, "Catheter replacement of the needle in percutaneous arteriography; a new technique," *Acta Radiologica*, vol. 39, no. 5, pp. 368–76, May 1953.

[288] M. I. Sezan and A. M. Tekalp, "Adaptive image restoration with artifact suppression using the theory of convex projections," *IEEE Transactions on Acoustics, Speech, and Signal Processing*, vol. 38, no. 1, pp. 181–185, 1990.

[289] J. Shen and T. Chan, "Variational Restoration of Nonflat Image Features: Models and Algorithms," *SIAM Journal on Applied Mathematics*, vol. 61, no. 4, pp. 1338–1361, Jan. 2001.

[290] K. Shimizu, K. Tochio, and Y. Kato, "Improvement of transcutaneous fluorescent images with a depth-dependent point-spread function.," *Applied Optics*, vol. 44, no. 11, pp. 2154–61, Apr. 2005.

[291] R. Shingrani, G. Krenz, and R. Molthen, "Automation process for morphometric analysis of volumetric CT data from pulmonary vasculature in rats.," *Computer Methods and Programs in Biomedicine*, vol. 97, no. 1, pp. 62–77, Jan. 2010.

[292] L. D. G. Sigalotti, J. Klapp, E. Sira, Y. Meleán, and A. Hasmy, "SPH simulations of time-dependent Poiseuille flow at low Reynolds numbers," *Journal of Computational Physics*, vol. 191, no. 2, pp. 622–638, Nov. 2003.

[293] P. O. Sjöquist, G. Duker, and O. Almgren, "Distribution of the collateral blood flow at the lateral border of the ischemic myocardium after acute coronary occlusion in the pig and the dog," *Basic Research in Cardiology*, vol. 79, no. 2, pp. 164–75, 1984.

[294] C. Smets, G. Verbeeck, P. Suetens, and A. Oosterlinck, "A knowledge-based system for the delineation of blood vessels on subtraction angiograms," *Pattern Recognition Letters*, vol. 8, no. 2, pp. 113–121, Sep. 1988.

[295] N. P. Smith and G. S. Kassab, "Analysis of coronary blood flow interaction with myocardial mechanics based on anatomical models," *Philosophical Transactions of the Royal Society A: Mathematical, Physical and Engineering Sciences*, vol. 359, no. 1783, pp. 1251–1262, Jun. 2001.

[296] N. P. Smith, A. J. Pullan, and P. J. Hunter, "Generation of an Anatomically Based Geometric Coronary Model," *Annals of Biomedical Engineering*, vol. 28, no. 1, pp. 14–25, 2000.

[297] P. Soille, *Morphological image analysis : principles and applications*. Berlin ;;New York: Springer, 1999.

[298] P. Soille, *Morphological Image Analysis: Principles and Applications*. Springer, 2002, p. 392.

[299] J. A. E. Spaan, ter R. Wee, van J. W. G. E. Teeffelen, G. J. Streekstra, M. Siebes, C. Kolyva, H. Vink, D. S. Fokkema, and van E. T. Bavel, "Visualisation of intramural coronary vasculature by an imaging cryomicrotome suggests compartmentalisation of myocardial perfusion areas," *Medical & Biological Engineering & Computing*, vol. 43, no. 4, pp. 431–435, 2005.

[300] J. A. E. Spaan, *Coronary Blood Flow: Mechanics, Distribution, and Control (Google eBook)*. Springer, 1991, p. 389.

[301] J. Spaan, C. Kolyva, J. van den Wijngaard, R. ter Wee, P. van Horssen, J. Piek, and M. Siebes, "Coronary structure and perfusion in health and disease," *Philosophical Transactions. Series A, Mathematical, Physical, and Engineering Sciences*, vol. 366, no. 1878, pp. 3137–53, Sep. 2008.

[302] W. Spalteholz, "Die koronararterien des Herzens," *Verb. Anat. Ges.*, vol. 21, pp. 141–162, 1907.

[303] C. Srinivas and M. D. Srinath, "Stochastic model-based approach for simultaneous restoration of multiple misregistered images," *Proceeding SPIE Vol. 1360*, vol. 1360, pp. 1416–1427, 1990.

[304] G. J. Steyer, D. Roy, and O. Salvado, "Removal of out-of-plane fluorescence for single cell visualization and quantification in cryo-imaging," *Annals of Biomedical Engineering*, vol. 37, no. 8, pp. 1613–1628, 2009.

[305] D. D. Streeter, H. M. Spotnitz, D. P. Patel, J. Ross, and E. H. Sonnenblick, "Fiber orientation in the canine left ventricle during diastole and systole," *Circulation Research*, vol. 24, no. 3, pp. 339–47, Mar. 1969.

[306] D. D. Streeter and D. L. Bassett, "An engineering analysis of myocardial fiber orientation in pig's left ventricle in systole," *The Anatomical Record*, vol. 155, no. 4, pp. 503–511, Aug. 1966.

[307] J. S. Stroud, S. A. Berger, and D. Saloner, "Numerical Analysis of Flow Through a Severely Stenotic Carotid Artery Bifurcation," *Journal of Biomechanical Engineering*, vol. 124, no. 1, p. 9, 2002.

[308] G. R. Stuhne and D. A. Steinman, "Finite-Element Modeling of the Hemodynamics of Stented Aneurysms," *Journal of Biomechanical Engineering*, vol. 126, no. 3, p. 382, 2004.

[309] M. Tadjfar, "Branch Angle and Flow Into a Symmetric Bifurcation," *Journal of Biomechanical Engineering*, vol. 126, no. 4, p. 516, 2004.

[310] A. D. Talenfeld, R. B. Schwope, H. J. Alper, E. I. Cohen, and R. A. Lookstein, "MDCT angiography of the renal arteries in patients with atherosclerotic renal artery stenosis: implications for renal artery stenting with distal protection.," *American Journal of Roentgenology*, vol. 188, no. 6, pp. 1652–8, Jun. 2007.

[311] J.-P. Tarel and N. Hautiere, “Fast visibility restoration from a single color or gray level image,” in *2009 IEEE 12th International Conference on Computer Vision*, 2009, pp. 2201–2208.

[312] C. A. Taylor, T. J. R. Hughes, and C. K. Zarins, “Finite element modeling of blood flow in arteries,” *Computer Methods in Applied Mechanics and Engineering*, vol. 158, no. 1–2, pp. 155–196, May 1998.

[313] B. D. Thackray and A. C. Nelson, “Semi-automatic segmentation of vascular network images using a rotating structuring element (ROSE) with mathematical morphology and dual feature thresholding,” *IEEE Transactions on Medical Imaging*, vol. 12, no. 3, pp. 385–92, Jan. 1993.

[314] K. E. Thompson and H. S. Fogler, “Modeling flow in disordered packed beds from pore-scale fluid mechanics,” *AIChE Journal*, vol. 43, no. 6, pp. 1377–1389, Jun. 1997.

[315] G. Tian, B. Xiang, G. Dai, G. Li, J. Sun, R. Summers, and R. Deslauriers, “Retrograde cardioplegia,” *J. Thorac. Cardiovasc. Surg.*, vol. 125, no. 4, pp. 872–880, Apr. 2003.

[316] R. Toledo and X. Orriols, “Tracking Elongated Structures using Statistical Snakes,” in *Proceedings IEEE Conference on Computer Vision and Pattern Recognition. CVPR 2000*, 2000, pp. 157–162.

[317] Y. A. Tolias and S. M. Panas, “A fuzzy vessel tracking algorithm for retinal images based on fuzzy clustering,” *IEEE Transactions on Medical Imaging*, vol. 17, no. 2, pp. 263–73, Apr. 1998.

[318] T. Tommasi, A. Diaspro, and B. Bianco, “3-D reconstruction in optical microscopy by a frequency-domain approach,” *Signal Processing*, vol. 32, no. 3, pp. 357–366, Jun. 1993.

[319] E. Toyota, K. Fujimoto, Y. Ogasawara, T. Kajita, F. Shigeto, T. Matsumoto, M. Goto, and F. Kajiya, “Dynamic changes in three-dimensional architecture and vascular volume of transmural coronary microvasculature between diastolic- and systolic-arrested rat hearts.,” *Circulation*, vol. 105, no. 5, pp. 621–6, Feb. 2002.

[320] T. Traupe, S. Gloekler, S. F. de Marchi, G. S. Werner, and C. Seiler, “Assessment of the human coronary collateral circulation.,” *Circulation*, vol. 122, no. 12, pp. 1210–20, Sep. 2010.

[321] S. E. Umbaugh, *Computer Imaging: Digital Image Analysis and Processing*. Taylor & Francis, 2005, p. 688.

[322] E. van Bavel and J. A. Spaan, “Branching patterns in the porcine coronary arterial tree. Estimation of flow heterogeneity.,” *Circulation research*, vol. 71, no. 5, pp. 1200–12, Nov. 1992.

[323] J. P. H. M. van den Wijngaard, P. Horssen, R. D. Wee, M. Siebes, H. Schulten, M. J. Post, and J. A. E. Spaan, "Identification of coronary collaterals in imaging cryomicrotome datasets," in *4th European Conference of the International Federation for Medical and Biological Engineering*, 2009, pp. 768–770.

[324] J. P. H. M. van den Wijngaard, C. Kolyva, M. Siebes, J. Dankelman, M. J. C. van Gemert, J. J. Piek, and J. A. E. Spaan, "Model prediction of subendocardial perfusion of the coronary circulation in the presence of an epicardial coronary artery stenosis.," *Medical & Biological Engineering & Computing*, vol. 46, no. 5, pp. 421–32, May 2008.

[325] J. P. H. M. van den Wijngaard, P. van Horssen, R. ter Wee, R. Coronel, J. M. de Bakker, N. de Jonge, M. Siebes, and J. A. E. Spaan, "Organization and collateralization of a subendocardial plexus in end-stage human heart failure," *American Journal of Physiology. Heart and Circulatory Physiology*, vol. 298, no. 1, pp. H158–62, Jan. 2010.

[326] J. P. H. M. van den Wijngaard, H. Schulten, P. van Horssen, R. D. Ter Wee, M. Siebes, M. J. Post, and J. A. E. Spaan, "Porcine coronary collateral formation in the absence of a pressure gradient remote of the ischemic border zone," *American Journal of Physiology. Heart and Circulatory Physiology*, vol. 300, no. 5, pp. H1930–7, May 2011.

[327] P. Van der Zee, *Measurement and modelling of the optical properties of human tissue in the near infrared*. 1992.

[328] P. van der Zee and D. T. Delpy, "Computed point spread functions for light in tissue using a measured volume scattering function," *Advances in Experimental Medicine and Biology*, vol. 222, pp. 191–7, Jan. 1988.

[329] P. van der Zee and D. T. Delpy, "Simulation of the point spread function for light in tissue by a Monte Carlo method," *Advances in Experimental Medicine and Biology*, vol. 215, pp. 179–91, Jan. 1987.

[330] P. van Horssen, J. van den Wijngaard, F. Nolte, I. Hoefer, R. Haverslag, J. A. E. Spaan, and M. Seibers, "Extraction of coronary vascular tree and myocardial perfusion data from stacks of cryomicrotome images," *Functional Imaging and Modeling of the Heart*, vol. 5528, pp. 486–494, 2009.

[331] P. van Horssen, M. Siebes, I. Hoefer, J. A. E. Spaan, and J. P. H. M. van den Wijngaard, "Improved detection of fluorescently labeled microspheres and vessel architecture with an imaging cryomicrotome.," *Medical & Biological Engineering & Computing*, vol. 48, no. 8, pp. 735–44, Aug. 2010.

[332] P. van Horssen, J. P. H. M. Wijngaard, M. Siebes, and J. A. E. Spaan, "Improved regional myocardial perfusion measurement by means of an imaging cryomicrotome," *4th European Conference of the International Federation for Medical and Biological Engineering*, vol. 22, pp. 771–774, 2009.

[333] T. G. van Leeuwen, D. J. Faber, and M. C. Aalders, “Measurement of the axial point spread function in scattering media using single-mode fiber-based optical coherence tomography,” *IEEE Journal of Selected Topics in Quantum Electronics*, vol. 9, no. 2, pp. 227–233, Mar. 2003.

[334] M. F. van Oosterhout, F. W. Prinzen, S. Skurada, R. W. Glenny, and J. R. Hales, “Fluorescent microspheres are superior to radioactive microspheres in chronic blood flow measurements.,” *The American Journal of Physiology*, vol. 275, no. 1 Pt 2, pp. H110–5, Jul. 1998.

[335] L. J. van Vliet and P. W. Verbeek, “Edge localization by MoG filters: Multiple-of-Gaussians,” *Pattern Recognition Letters*, vol. 15, no. 5, pp. 485–496, May 1994.

[336] M. Vendelin and R. Birkedal, “Anisotropic diffusion of fluorescently labeled ATP in rat cardiomyocytes determined by raster image correlation spectroscopy.,” *American journal of physiology. Cell physiology*, vol. 295, no. 5, pp. C1302–15, Nov. 2008.

[337] P. J. Verveer, M. J. Gemkow, and T. M. Jovin, “A comparison of image restoration approaches applied to three-dimensional confocal and wide-field fluorescence microscopy,” *Journal of Microscopy*, vol. 193, no. 1, pp. 50–61, Jan. 1999.

[338] M. Viceconti, “The virtual physiological human: challenges and opportunities,” in *3rd IEEE International Symposium on Biomedical Imaging: Nano to Macro*, 2006, pp. 812–815.

[339] I. E. Vignon-Clementel, C. Alberto Figueroa, K. E. Jansen, and C. A. Taylor, “Outflow boundary conditions for three-dimensional finite element modeling of blood flow and pressure in arteries,” *Computer Methods in Applied Mechanics and Engineering*, vol. 195, no. 29–32, pp. 3776–3796, Jun. 2006.

[340] M. A. Vincent, S. Rattigan, M. G. Clark, S. L. Bernard, and R. W. Glenny, “Spatial distribution of nutritive and nonnutritive vascular routes in perfused rat hindlimb muscle using microspheres,” *Microvascular Research*, vol. 61, no. 1, pp. 111–21, Jan. 2001.

[341] R. A. Waltz, J. L. Morales, J. Nocedal, and D. Orban, “An interior algorithm for nonlinear optimization that combines line search and trust region steps,” *Mathematical Programming*, vol. 107, no. 3, pp. 391–408, 2006.

[342] S. Y. Wan, A. P. Kiraly, E. L. Ritman, and W. E. Higgins, “Extraction of the hepatic vasculature in rats using 3-D micro-CT images,” *IEEE transactions on medical imaging*, vol. 19, no. 9, pp. 964–71, Sep. 2000.

[343] C. Y. Wang, J. B. Bassingthwaighte, and L. J. Weissman, “Bifurcating distributive system using Monte Carlo method,” *Mathematical and Computer Modelling*, vol. 16, no. 3, pp. 91–98, Mar. 1992.

[344] L. V. Wang and H. Wu, *Biomedical optics: principles and imaging*, vol. 3. Nature Publishing Group, a division of Macmillan Publishers Limited. All Rights Reserved., 2007, p. 928.

[345] L. Wang, S. L. Jacques, and L. Zheng, "MCML--Monte Carlo modeling of light transport in multi-layered tissues.," *Computer Methods and Programs in Biomedicine*, vol. 47, no. 2, pp. 131–46, Jul. 1995.

[346] R. K. Wang, X. Xu, V. V. Tuchin, and J. B. Elder, "Concurrent enhancement of imaging depth and contrast for optical coherence tomography by hyperosmotic agents," *Journal of the Optical Society of America B*, vol. 18, no. 7, p. 948, Jul. 2001.

[347] Y. M. Wang, B. Judkewitz, C. A. Dimarzio, and C. Yang, "Deep-tissue focal fluorescence imaging with digitally time-reversed ultrasound-encoded light.," *Nature communications*, vol. 3, p. 928, Jan. 2012.

[348] Z. Wang and Y. Fu, "Frequency-domain Regularized Deconvolution for Images with Stripe Noise," in *Fourth International Conference on Image and Graphics (ICIG 2007)*, 2007, pp. 110–115.

[349] M. Watanabe, K. Yokoyama, and E. Okada, "Estimation of point spread function for scattering effect on cortical tissue image - Proc. SPIE," in *Photon Migration and Diffuse-Light Imaging*, 2003, vol. 5138, p. 5138_239.

[350] J. T. Wearn, "The extent of the capillary bed of the heart," *The Journal of Experimental Medicine*, vol. 47, no. 2, pp. 273–90, Jan. 1928.

[351] M. E. Weaver, G. A. Pantely, J. D. Bristow, and H. D. Ladley, "A quantitative study of the anatomy and distribution of coronary arteries in swine in comparison with other animals and man," *Cardiovascular Research*, vol. 20, no. 12, pp. 907–17, Dec. 1986.

[352] R. D. ter Wee, H. Schulten, M. J. Post, and J. A. E. Spaan, "Localization and visualization of collateral vessels by means of an imaging cryomicrotome," *Vascular Pharmacology*, vol. 45, no. 3, pp. e63–e64, Mar. 2006.

[353] F. C. White and C. M. Bloor, "Coronary collateral circulation in the pig: correlation of collateral flow with coronary bed size," *Basic Research in Cardiology*, vol. 76, no. 2, pp. 189–96, 1981.

[354] N. Wiener, *Extrapolation, interpolation, and smoothing of stationary time series*. New York: Wiley, 1964, p. 176.

[355] G. C. Willis, A. W. Light, and W. S. Gow, "Serial arteriography in atherosclerosis," *Canadian Medical Association Journal*, vol. 71, no. 6, pp. 562–8, Dec. 1954.

[356] B. C. Wilson and S. L. Jacques, “Optical reflectance and transmittance of tissues: principles and applications,” *IEEE Journal of Quantum Electronics*, vol. 26, no. 12, pp. 2186–2199, 1990.

[357] D. E. Wilson, “Added mass and damping coefficients fora hexagonal cylinder,” *Journal of Fluids and Structures*, vol. 5, no. 5, pp. 503–519, Sep. 1991.

[358] D. Wilson, D. Roy, G. Steyer, M. Gargesha, M. Stone, and E. McKinley, “Whole Mouse Cryo-Imaging,” in *Proceedings - Society of Photo-Optical Instrumentation Engineers*, 2008, vol. 6916, p. 69161I–69161I9.

[359] T. Wischgoll, J. S. Choy, and G. S. Kassab, “Extraction of morphometry and branching angles of porcine coronary arterial tree from CT images.,” *American journal of physiology. Heart and circulatory physiology*, vol. 297, no. 5, pp. H1949–55, Nov. 2009.

[360] T. Wischgoll, J. S. Choy, E. L. Ritman, and G. S. Kassab, “Validation of image-based method for extraction of coronary morphometry.,” *Annals of Biomedical Engineering*, vol. 36, no. 3, pp. 356–68, Mar. 2008.

[361] T. Wischgoll, J. Meyer, B. Kaimovitz, Y. Lanir, and G. S. Kassab, “A novel method for visualization of entire coronary arterial tree,” *Annals of Biomedical Engineering*, vol. 35, no. 5, pp. 694–710, May 2007.

[362] H. S. Wong and L. Guan, “A neural learning approach for adaptive image restoration using a fuzzy model-based network architecture,” *IEEE Transactions on Neural Networks / A Publication of the IEEE Neural Networks Council*, vol. 12, no. 3, pp. 516–31, Jan. 2001.

[363] J. Woods, J. Biemond, and A. Tekalp, “Boundary value problem in image restoration,” in *ICASSP ’85. IEEE International Conference on Acoustics, Speech, and Signal Processing*, 1985, vol. 10, pp. 692–695.

[364] P. D. Woolliams, R. A. Ferguson, C. Hart, A. Grimwood, and P. H. Tomlins, “Spatially deconvolved optical coherence tomography,” *Applied Optics*, vol. 49, no. 11, p. 2014, Apr. 2010.

[365] C. Wu, J. J. K. Derwent, and P. Stanchev, “Retinal vessel radius estimation and a vessel center line segmentation method based on ridge descriptors,” *Journal of Signal Processing*, vol. 55, no. 1–3, pp. 91–102, 2009.

[366] X. Wu, V. Luboz, K. Krissian, S. Cotin, and S. Dawson, “Segmentation and reconstruction of vascular structures for 3D real-time simulation,” *Medical Image Analysis*, vol. 15, no. 1, pp. 22–34, Feb. 2011.

[367] J. Yi and J. B. Ra, “A locally adaptive region growing algorithm for vascular segmentation,” *International Journal of Imaging Systems and Technology*, vol. 13, no. 4, pp. 208–214, Dec. 2003.

[368] A. A. Young, I. J. Legrice, M. A. Young, and B. H. Smaill, “Extended confocal microscopy of myocardial laminae and collagen network,” *Journal of Microscopy*, vol. 192, no. 2, pp. 139–50, Nov. 1998.

[369] J. Zhang, “The mean field theory in EM procedures for blind Markov random field image restoration.,” *IEEE Transactions on Image Processing : a Publication of the IEEE Signal Processing Society*, vol. 2, no. 1, pp. 27–40, Jan. 1993.

[370] H. Zhonghai and Z. Guangshuai, “Study on airway resistance based on lung fractal structure,” in *2010 International Conference On Computer Design and Applications*, 2010, pp. V1–431–V1–434.

[371] L. Zhou, M. S. Rzeszotarski, L. J. Singerman, and J. M. Chokreff, “The detection and quantification of retinopathy using digital angiograms.,” *IEEE transactions on medical imaging*, vol. 13, no. 4, pp. 619–26, Jan. 1994.

[372] Y. Zhou and A. W. Toga, “Efficient Skeletonization of Volumetric Objects,” *IEEE Transactions on Visualization and Computer Graphics*, vol. 5, no. 3, pp. 196–209, Jan. 1999.

[373] F. Zijlstra, J. H. Reiber, and P. W. Serruys, “Does intracoronary papaverine dilate epicardial coronary arteries? Implications for the assessment of coronary flow reserve.,” *Catheterization and cardiovascular diagnosis*, vol. 14, no. 1, pp. 1–6, Jan. 1988.

Appendix A: Monte Carlo Simulations

A.1 Comparison of Monte Carlo and PSF Models at Shallow Depths

In Fig. A.1, the tissue PSF model presented in sections 2.2.1-2 (Rolf et al. 2008) is compared to the Monte Carlo photon transport simulation at shallow depths. The PSF closely follows the Monte Carlo random walk simulation at depths < 5 voxels or 250 micrometers (each voxel is 50 microns cubed).

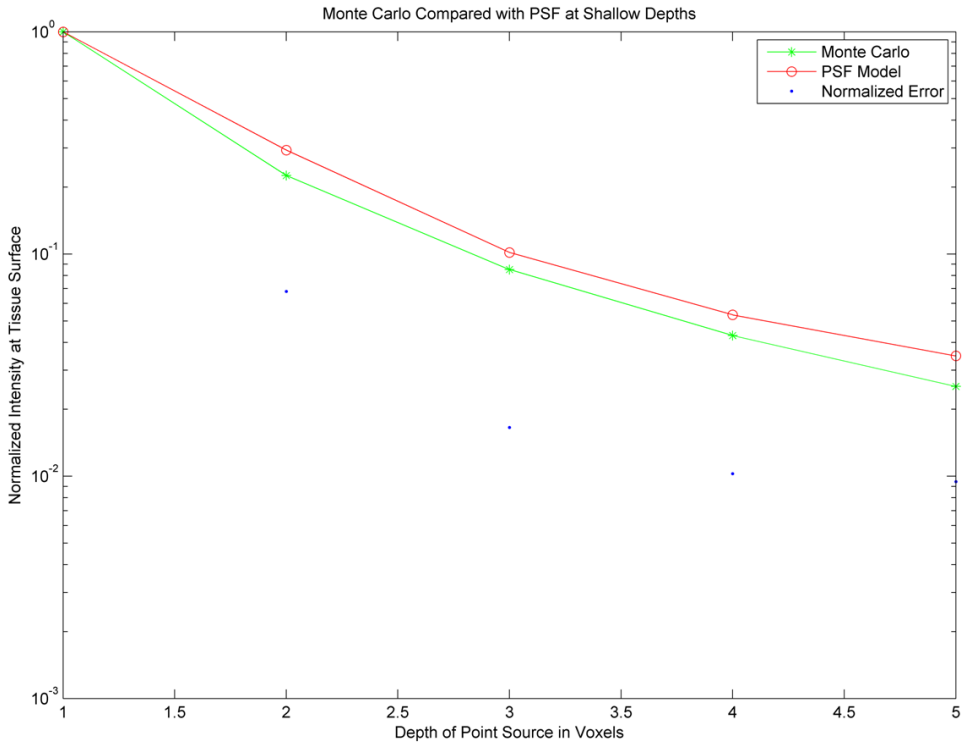


Figure A.1: Semilog plot of the normalized surface intensity of a simulated point source (embedded in a slab of tissue) against the depth of the point source for both Monte Carlo and the PSF models.

Since the cryomicrotome can only image fluorescent objects embedded in tissue at shallow depths (less than 200 micrometers), the PSF is an approximate but valid model for this study. Figs. A.2 and A.3 show the images of and line intensity profiles across the intensity distribution on the tissue surface emitted from the point source placed at shallow depths ranging from 25 – 225 micrometers. Unscattered direct light from the point source is observed when the point source is at shallow depths, but when the point source is located at larger depths, its emitted fluorescence reaching the surface is

primarily diffused having undergone much more scattering. Thus the intensity of light observed at the surface drops rapidly as the point source is placed progressively deeper in the tissue.

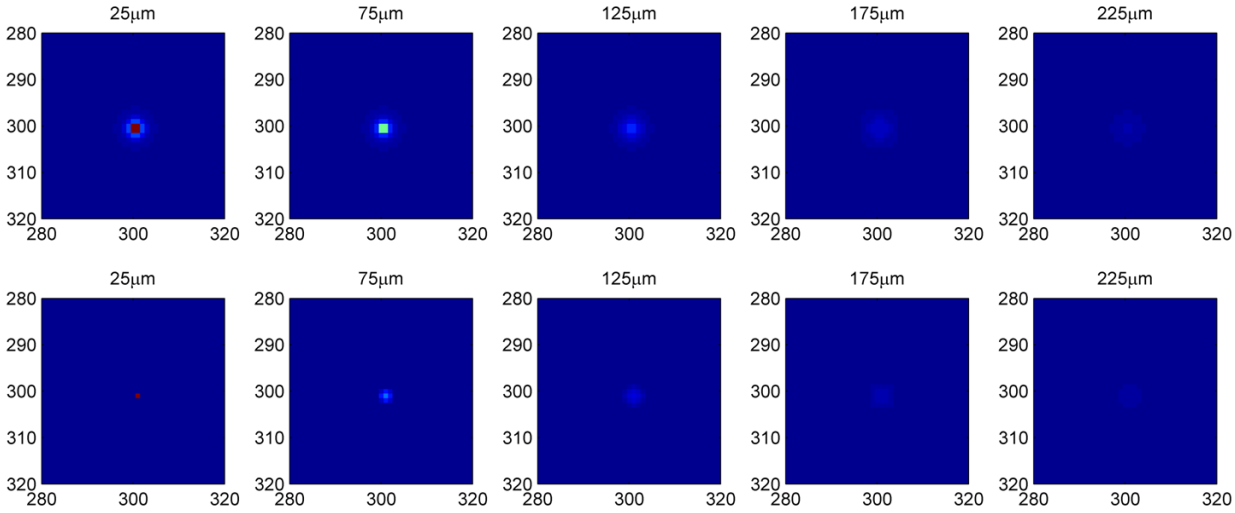


Figure A.2: Intensity distribution images at the tissue surface from fluorescence emitted by a point source placed at progressively larger depths (depths are printed in each plot's title). The tissue PSF model surface images are in the top row and Monte Carlo random walk (50 million photon packets) simulation surface images are in the bottom row. Colormap is the same for all the images. The intensity range is 0 – 1.

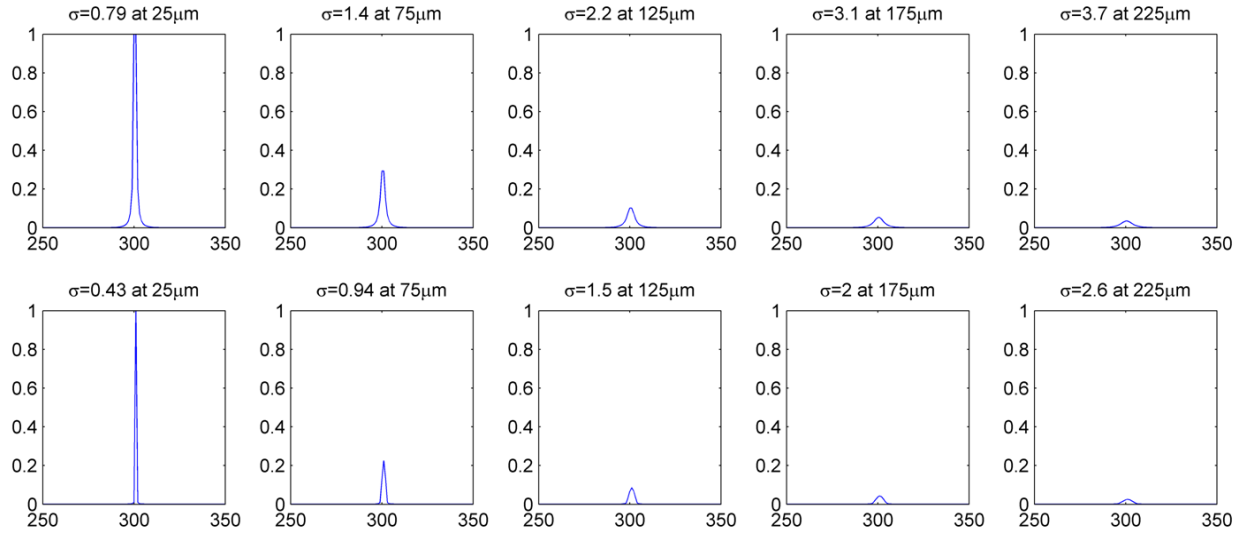


Figure A.3: Line intensity profiles across the centre of each surface image intensity distribution emitted from the point source at each progressively larger depth in tissue (depth is printed in plot titles). The tissue PSF model's line intensity profiles are in the top row, and Monte Carlo simulation's line intensity profiles are in the bottom row. The intensity distribution of light emitted by the point source when it is very near the surface approaches a Dirac delta function, but as the depth of the point source increases, the distribution broadens (σ increases) and there is a steep drop in intensity. The intensity ranges from 0 – 1.

A.2 Phantom Based Evaluation of PSF Model Validity

A vessel phantom image (see Fig. A.4) was simulated with varying sizes and angles using the 100-million photon-packet Monte Carlo and PSF models (specified in Chapter 2) of light transport in tissue. The vessel axis angles were varied from 0 to 90 degrees, i.e. completely parallel to completely perpendicular to the image plane.

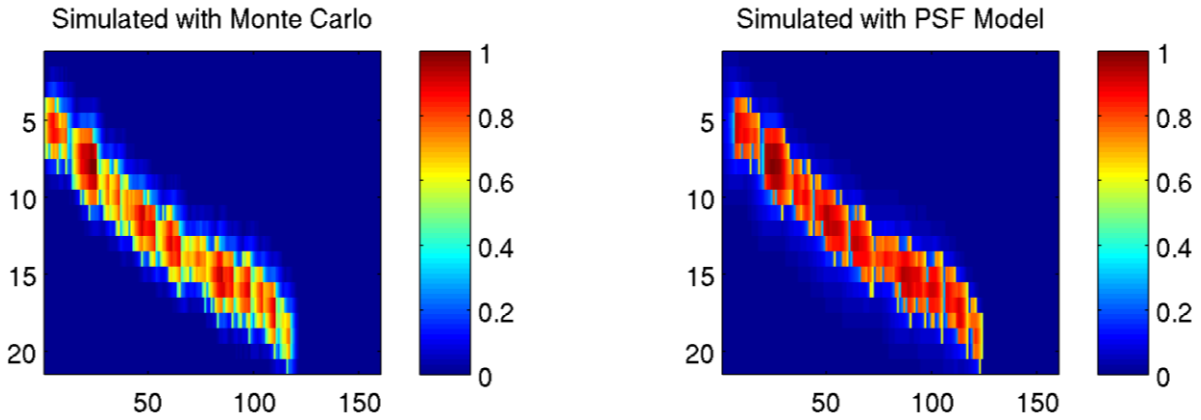


Figure A.4: Maximum intensity projections (along *x* dimension) of a 3D image volume of a phantom vessel simulated with Monte Carlo and PSF models. Phantom vessel size is 1.7 voxels radius. Excitation and emission attenuation coefficients are 23.52 mm^{-1} and 21.90 mm^{-1}, as specified in chapter 2.

Error in the model-based vessel radius estimation due to using a PSF versus the Monte Carlo model of light transport was found to be 0.08 ± 0.01 voxels, which is negligible for blood flow simulations. Section 5.3.7 in chapter 5 tests the sensitivity of blood flow simulations to the vessel radii estimates in the reconstructed vasculature model by perturbing the radius with the larger error of 0.25 voxel (0.25 voxels > 0.01 voxels) standard deviation. Error in blood flow simulations due to this error in radii is negligible compared to the error between the flow model and microsphere perfusion measurements. Thus the PSF model is a valid approximate model of light transport in tissue for estimating vessels from the cryomicrotome images.

Appendix B: Optical Parameter Estimates

B.1 Unconstrained Unbounded Variable Estimates

Microspheres (micrometer size fluorescent beads) embedded in porcine cardiac tissue are used in this study as point sources to estimate the point spread function of the cryomicrotome images. The point spread function, parameterized by optical excitation and emission attenuation coefficients, is fitted to the microsphere images to estimate the optical parameters. The emission attenuation coefficient is optimized as a separate variable than the excitation attenuation coefficient. The optimization is constrained such that $\mu_{ex} \geq \mu_{em}$ and bounded such that $0.01 < \mu_{ex} < 0.05$ and $0.01 < \mu_{em} < 0.05$. To assess the effect of these constraints and bounds on the optical parameter estimation, the optimization was performed with varying starting point and without constraints and bounds. The results of this unconstrained unbounded parameter estimation are shown in Figure B.1.

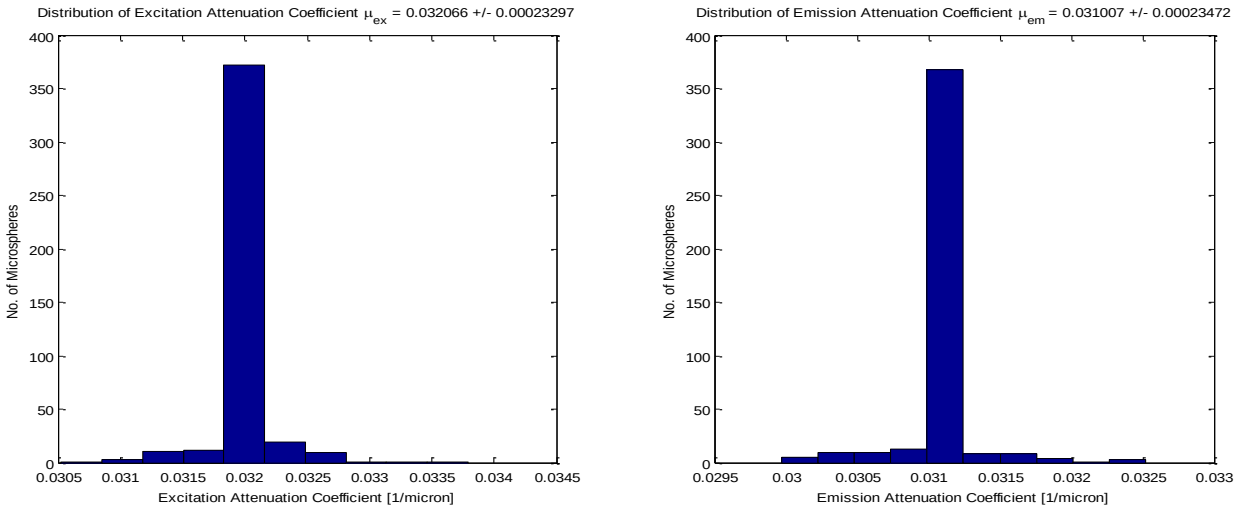


Figure B.1: Probability distributions (titles give mean ± standard deviation) of μ_{ex} and μ_{em} [1/μm] for porcine cardiac tissue. Optical parameter estimation was performed with unconstrained and unbounded optimization.

The results of the unconstrained and unbounded parameter estimation are similar to those of the constrained and bounded parameter estimation in that the mean of the two are both close to $\mu_{ex} = 0.032$ and $\mu_{em} = 0.031$. The standard deviation in the unconstrained and unbounded

parameter estimation was also less than in the constrained and bounded parameter estimation, thus showing that removing constraints and bounds still results in only a small variation in optical parameters estimated from microspheres embedded in porcine cardiac tissue.

B.2 Partial Volume Effect on Microsphere Optical Parameter Estimation

In order to determine the sensitivity of the optical parameter estimation from microspheres to partial volume effect, a microsphere image volume of size 7x7x4 voxels extracted from the porcine coronary cryomicrotome dataset (of the pig in Fig. 3.3) was downsampled to 5x5x3 voxels, about 2/3 of the original size in each dimension (see Fig. B.2).

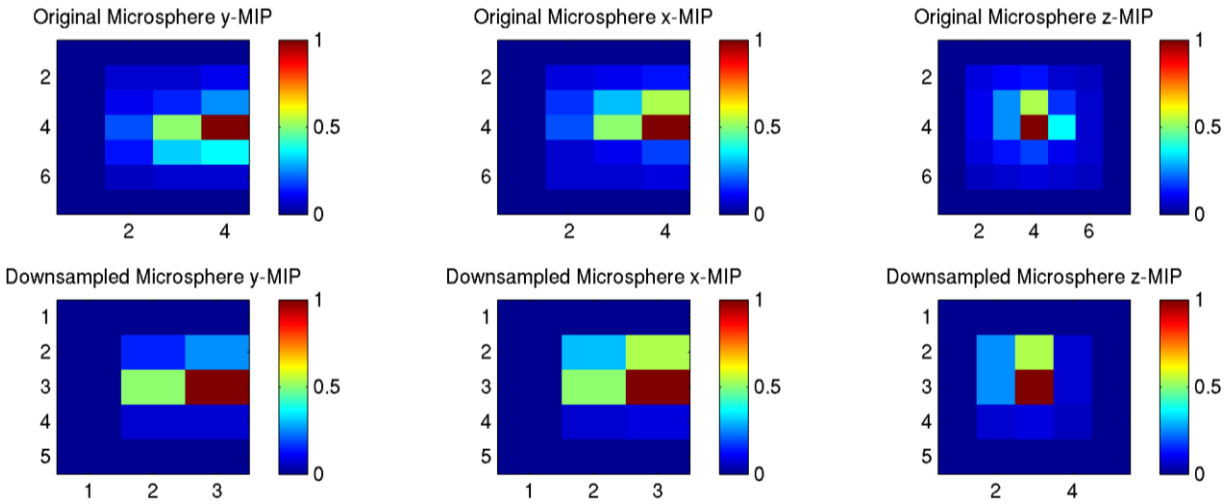


Figure B.2: Original and downsampled microsphere image volumes shown as maximum intensity projections (MIPs).

The excitation attenuation coefficient measured to be 0.0362 [μm^{-1}] from the full original resolution microsphere image volume, and it measured to be 0.0334 [μm^{-1}] from the downsampled microsphere image. This results in a distribution of μ_{ex} = 0.0348 ± 0.0019 μm^{-1}. This standard deviation in the uncertainty in parameter estimation due to resolution is negligibly small compared to the standard deviation of 0.0049 [μm^{-1}] in the intramural spatial attenuation coefficient variation (see Fig. 3.7 (c)-(d) titles) over the entire heart. Thus the microsphere parameter estimation is robust to partial volume effect.

Appendix C: Deconvolution Tests

C.1 Phantom Based Evaluation of Deconvolution

To test the effect of the obliqueness of vessels to the image plane and pixel saturation on deconvolution techniques, 3D vessel phantoms of 5-voxel and 10-voxel radii were simulated with the long axis at two angles (90° and 45°) from the imaging (*x*-*y*) plane and convolved with the analytical theoretical PSF model (with and without saturation). The PSF was parameterized with μ_{ex} = 0.032 [μm^{-1}] and μ_{em} = 0.031 [μm^{-1}] (these values were measured from images of microspheres embedded in porcine cardiac tissue in chapter 3 of this study and are used as the PSF parameters for basis of comparison between the deconvolution methods). Using the same PSF, the deconvolution techniques were tested to de-blur the blurred phantom, i.e. restore the original vessel from the degraded image. The original vessel, a binary image, when convolved with the PSF creates a blurred image with values in the range 0-10 because of the convolution, which simulates the intensity distribution. Saturation of voxel intensity in the captured images was simulated by restricting the range from 0-1 (in this simulation, 1 is assumed to be both the illumination intensity level of the original vessel and also the maximum intensity that can be recorded by the camera's sensors).

Fig. C.1 shows the original, blurred, and deconvolved (with the three methods) vessel phantoms for both unsaturated and saturated vessel images. Fig. C.2 shows the original, blurred, and deconvolved (with the three methods) vessel phantoms for both a vessel oriented orthogonal (90°) and tilted (45°) with respect to the imaging plane. Line intensity profiles across the vessel phantom cross-sections are shown in both figures. As tabulated in Table C.1, the mean square error between the original phantom and the deconvolved vessel phantom was used as the criterion to judge which of the deconvolution techniques performs best for restoring vessel data. For saturated vessel images, Richardson-Lucy results in the least mean

square error for the vessel at both 90° and 45° angles, and is thus more effective at vessel image restoration than Wiener and regularized filtering.

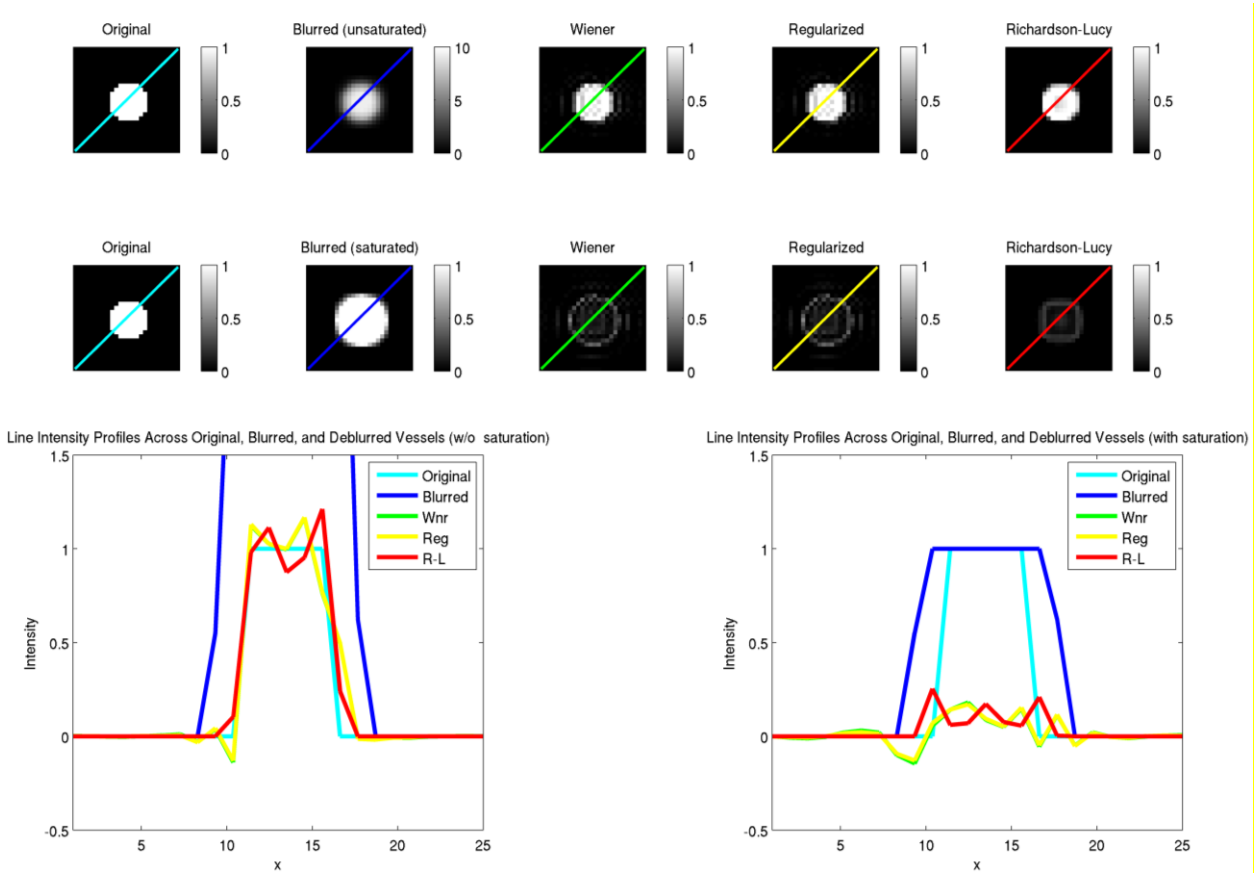


Figure C.1: Compares deconvolution on unsaturated versus saturated images. 3D phantom (25 voxel)3 of a 5-voxel-radius vessel at an angle of 90° (from the imaging plane) which was blurred with a PSF and deblurred with the same PSF using Wiener, regularized, and Richardson-Lucy deconvolution methods. The original blurred image was first deconvolved without simulating the effects of saturation (top row of images) and then deconvolved after pixel saturation was simulated in it (bottom row of images). The original image ranged from 0-1 but after convolution with the PSF, the blurred imaged ranges from 0-10 (unsaturated image). The deconvolved images again range from 0-1 as they try to restore an estimate of the original. The first two columns are the vessel phantom, original and blurred with PSF, respectively. The last three columns are the deblurred vessel phantom after being deconvolved with Wiener, regularized, and Richardson-Lucy deconvolution, respectively. The plots show the line intensity profiles across cross-sections of the original (cyan) vessel phantom, blurred with the PSF (blue), and deconvolved with Wiener (green), regularized (yellow), and Richardson-Lucy deconvolution, respectively. The plots show the line intensity profiles across cross-sections of the original (cyan) vessel phantom, blurred with the PSF (blue), and deconvolved with Wiener (green), regularized (yellow), and Richardson-Lucy (red). Left and right plots are for the blurred image without and with saturation simulated, respectively. Lines across which the intensity profiles were calculated are shown as colored lines across the vessel cross-sections in the original, blurred, and deblurred images.

As can be seen in the line intensity profile plots of Figures C.1-2, Richardson-Lucy deconvolution performed best in restoring the phantom, with the least ringing and oscillation in the restored estimate. The line intensity profiles of the results of the Wiener and regularized filtering are plotted in green and yellow, respectively. As observed in the bottom plots of Figs. C.1-2, the green and yellow lines (Wiener and regularized filtering results) oscillate around zero at the edge of the intensity profile, whereas the red line (Richardson-Lucy) does not. Richardson-Lucy resulted in the most accurate deblurring for the vessel both without and with saturation, and was thus used for testing vessel image restoration in the artificial vessel phantoms in the next section C.2.

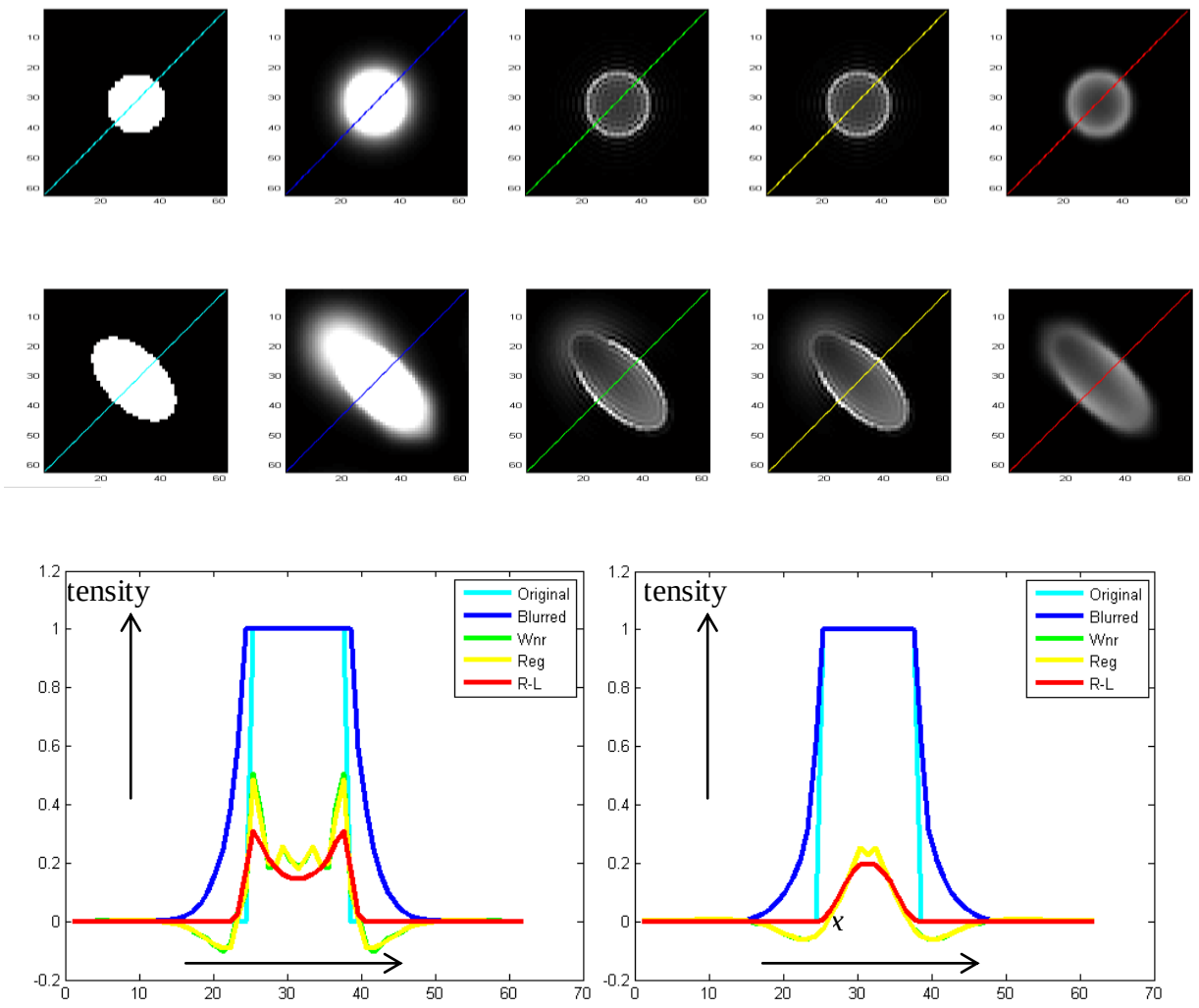


Figure C.2: This figure compares deconvolution of an orthogonal versus tilted vessel. 3D phantom (62x62x62 voxel^3) of a 10-voxel-radius vessel at an angle of 90° (top row) and 45° (bottom row) to the imaging (*x*-*y*) plane. The first two columns are the vessel phantom, original and convolved with PSF, respectively. The last three columns are the blurred vessel phantom deconvolved with Wiener, regularized, and Richardson-Lucy deconvolution, respectively. For all the images, the grayscale colormap ranges from 0 (black) to 1 (white) in intensity. The plots show the line intensity profiles across cross-sections of the original (cyan) vessel phantom, blurred with the PSF (blue), and deconvolved with Wiener (green), regularized (yellow), and Richardson-Lucy (red), which has the least ringing or oscillation in the restored estimate. Left and right plots are for the vessel angled at 90° and 45°, respectively, from the imaging plane. Lines across which the intensity profiles were calculated are shown as colored lines across the vessel cross-sections in the original, blurred, and deblurred images.

Deconvolution	Wiener	Regularized	Richardson-Lucy
Vessel angled 90°	0.0386	0.0380	0.0362
Vessel angled 45°	0.0811	0.0806	0.0800

Table C.1: Mean square error between the original and deblurred vessel phantom (oriented at 90° and 45° angles to the imaging plane, respectively) with Wiener, regularized, and Richardson-Lucy deconvolution. Richardson-Lucy consistently results in the least error between the original and deblurred vessel phantoms. The small differences in error between the Richardson-Lucy versus the prior two approache is because noise was not simulated. The primary degradation is not noise but optical blurring which increases as the vessel axis angle from the image plane decreases (this is the effect we focus our analysis on herein).

In Figs. C.1-2, the line intensity profiles across the vessel phantom deblurred with Wiener and regularized filtering seem to be practically the same. The small difference between the two methods is due to the fact that the Wiener filter uses a constant approximation for the signal to noise ratio, whereas regularized constrained least squares filtering uses the noise mean and variance. These parameters can generally be determined from the Fourier or power spectrum of the image. The regularized constrained least squares filter simply replaces the signal to noise ratio in the Wiener filter with a frequency variant function (Umbaugh 2007, Gonzalez et al. 2002), and this change does not seem to have much effect on vessel image restoration, according to this study. The small differences in error between the methods are because noise was not simulated. The primary degradation is not noise but optical blurring, which increases as the vessel axis angle from the image plane decreases (this is the effect we focus our analysis on herein).

Additionally, Figs. C.1-2 demonstrate the large amount of ringing or oscillation in intensity in the deconvolved vessel phantom's cross-sections. This undesired effect of ringing occurs near object boundaries and at steep intensity transitions at edges and bright point sources, both of which are found in vessel images. Ringing is caused by the sharp intensity gradients at the boundaries of the saturated vessels, which result in high frequencies in the Fourier domain. Deconvolution in the Fourier domain amplifies these high frequencies, thus introducing the ringing phenomenon in the image when it is inverted back to the spatial domain (Woods et al.

1985, Lagendijk et al. 1988). And finally, it can be observed from Figs. C.1-2 that deconvolution darkens the vessel images, decreases the voxel intensity, and creates dark holes in the vessel center elaborated in section C.2, when the vessel image data is saturated. This is because the PSF assumes a Gaussian profile for the vessel cross-sections, but the saturation results in data loss in the pixels near the vessel centre and cuts off the Gaussian peak, resulting in a non-Gaussian profile of the vessel cross-section. Standard deconvolution methods are affected by pixel saturation and hence the need to model the image acquisition process.

C.2 Ground Truth Based Evaluation of Deconvolution

Cryomicrotome images of three embedded fluorescent cylinders (Rolf et al. (2008)) of known diameter (measured through a microscope) were used to evaluate the improvement in vessel cross-sectional boundaries after image restoration. Deconvolution with the Richardson-Lucy method performed on the images of the artificial vessels embedded in tissue-mimicking gel and imaged by the cryomicrotome is shown in Fig. C.3. The PSF model used is specified in equation (2.6) and the attenuation coefficient used was taken from Rolf et al. (2008), who measured the parameter from microspheres embedded in the same gel as the artificial vessels. Note: for estimating radii of porcine coronary vessels, the optical tissue parameters are measured from microspheres embedded in the same porcine myocardium tissue as the coronary vessels. For estimating radii of the ground-truth artificial vessel phantoms, the optical parameters are measured from microspheres embedded in the same gel as the artificial vessel phantoms. The microspheres from which the optical parameters are measured are in both cases embedded in the same material as the vessels. The *hole-effect* is evident in the deconvolved image due to the saturated vessel centre in the original image.

Fig. C.3 shows the vessel boundary delineation using geodesic level sets (Li et al. 2005) on raw and deconvolved vessel cross-sectional images of the three artificial vessels of diameters 510, 300, and 170 μm, respectively. In Fig. C.3, the green circle is an approximate contour (each point of which is at an average distance of the level sets boundary points from centerpoint) that would represent the vessel cross-section, assuming the cross-section is close to circular (the cross-section is generally elliptical for vessels angled obliquely to the imaging plane). The green circle is shown in the images to visually demonstrate how the halo can bias the zero level sets contour to be off-centre.

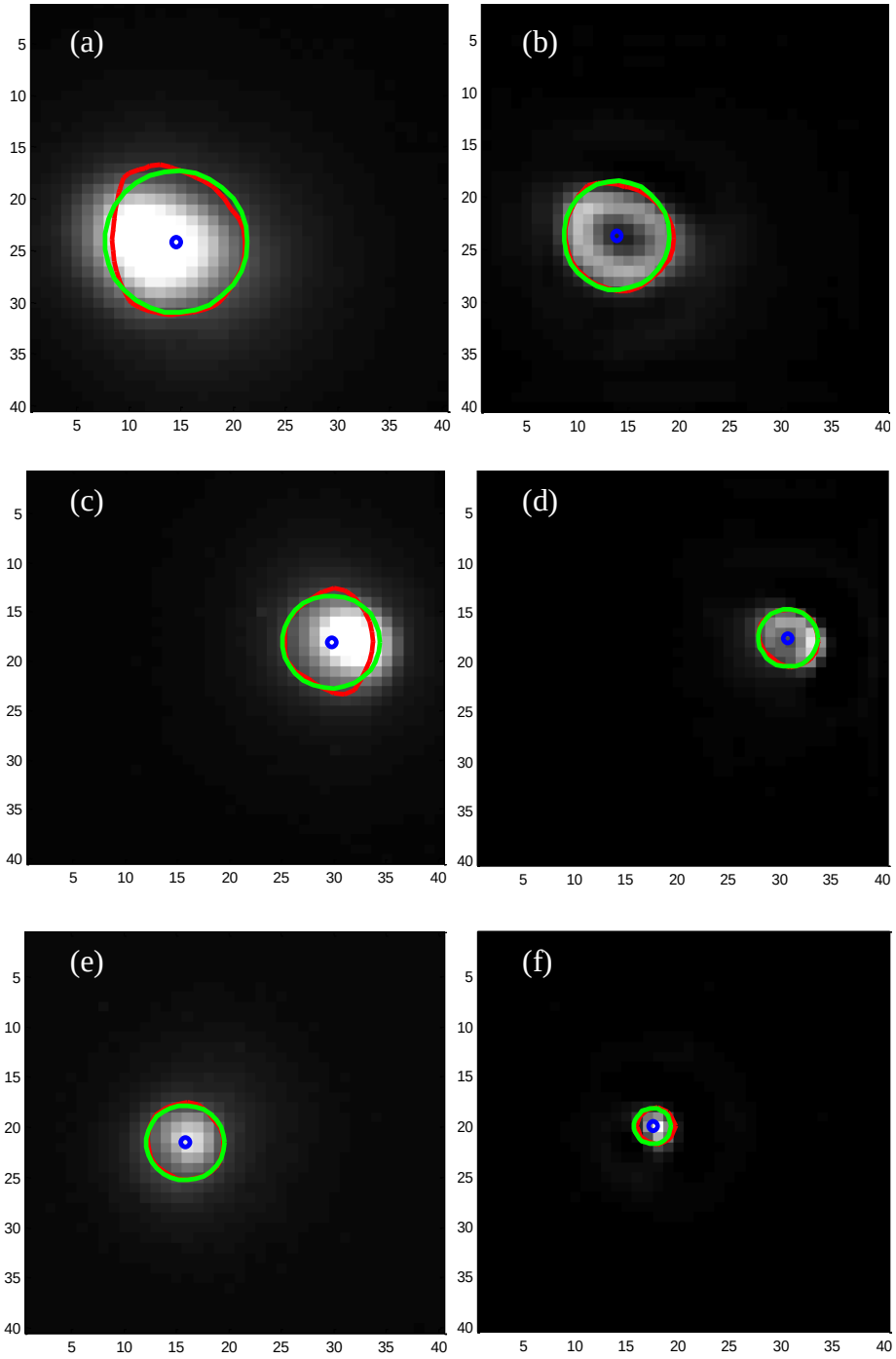


Figure C.3: Level sets segmentation on vessel cross-sectional raw (a) and deconvolved (b) images of a 510μm diameter vessel, raw (c) and deconvolved (d) images of a 300μm diameter vessel, and raw (e) and deconvolved (f) images of a 170μm diameter vessel. The blue dot is the centerpoint, the red contour is the final evolution of the level set, and the green circle is the approximate contour. Image dimensions are 40x40 pixel^2 (2 mm)^2 where the voxel resolution is (50μm)^3. The images were deconvolved with 20 iterations of Richardson-Lucy using the PSF in equation (2.6) with $\mu_{ex} = \mu_{em} = 0.0022$ μm-1, which was measured from microspheres embedded in the same gel as the vessel (Rolf et al. 2008). The number of evolutions of the deformable contour was 300 (parameters listed in Table C.2). The grayscale intensity ranges from 0 (black) to 255 (white).

The real contour of the vessel boundaries cannot be determined, since these cryomicrotome images are distorted by out-of-focus light. Li et al. (2005) was used to evolve the level set curves towards the vessel boundaries:

$$\frac{\partial \phi}{\partial t} = \mu\left[\Delta\phi - \nabla\cdot\left(\frac{\nabla\phi}{|\nabla\phi|}\right)\right] + \lambda\delta(\phi)\nabla\cdot\left(g\frac{\nabla\phi}{|\nabla\phi|}\right) + \nu g\delta(\phi)$$

$$g = \frac{1}{1+\left|\nabla G_\sigma * I\right|^2} \qquad \text{(C.1)}$$

$$\delta(\phi) = \begin{cases} 0 & |\phi| > \varepsilon \\ \frac{1}{2\varepsilon}\left[1+\cos\left(\frac{\pi\phi}{\varepsilon}\right)\right] & |\phi| \le \varepsilon \end{cases}$$

where g is the edge indicator function, G_σ is the Gaussian kernel, I is the image, $\delta(\phi)$ is the smoothed Dirac delta function, $\phi(t)$ is the level set function, t is time, k is the iteration, and i,j denote a pixel in the image (or in the discrete level set function). The Laplacian operator (Δ), gradient operator (∇), and the divergence operator ($\nabla\cdot$), and convolution ($*$) are used. The parameters σ, ε, μ, λ, ν, and τ are defined in Table C.2.

$\sigma = 1.5$	scale of the Gaussian kernel that is convolved with the image
$\varepsilon = 1.5$	the width of the regularized Dirac delta function
$\tau = 5$	time step; the condition $\tau\mu$ < 0.25 must be met for stable level set evolution
$\mu = 0.04$	coefficient that controls the effect of penalizing the deviation of the level set function from a sign distance function
$\lambda = 5$	coefficient of the weighted length of the zero level curve
$\nu = 1.5$	coefficient of the weighted area of the zero level curve; $\nu > 0$ if initial contour outside object shrink contour, and $\nu < 0$ if initial contour inside object to expand contour

Table C.2: Parameter values for level sets implementation of Li et al. (2005).

The level sets are solved in practice, using a direct Euler approach, as shown in equation (C.2):

$$\phi_{i,j}^{k+1} = \phi_{i,j}^{k} + \tau\frac{\partial\phi}{\partial t} \qquad \text{(C.2)}$$

It is important to note that the deconvolution (see Fig. C.3) process only suppressed but did not fully remove the halo and transparency artifacts. Furthermore, as a side-effect it darkened the images and created holes in the vessels. The holes are due to the fact that the deconvolution

does not incorporate the saturation in the centre of the vessel (nonlinear response of the CCD sensor to overexposure); i.e. the *hole-effect* is caused because a Gaussian vessel intensity profile is assumed. In summary, we opted to not use deconvolution to remove the blurring in the vessel images because:

- Deconvolution can never perfectly restore the raw observed image to the actual vessel because of the unknown noise component of the imaging modality. It can at best only restore a noise-distorted estimate of the original vessel. No restoration procedure can perfectly restore in the situation of noise and saturation. However, a model-based approach is better suited for saturated images as it can model and simulate the image acquisition in the vessel measurement.
- Deconvolution darkens the saturated vessel images because it does not remove, but only reduces the intensity of the out-of-focus light emitted from fluorescent dye in the vessels below the surface (especially those that are at an oblique angle to the imaging surface). Thus it is not robust to the nonlinear effect of CCD sensor blooming and pixel saturation.
- Deconvolution creates holes in the vessel centre due to not accounting for intensity saturation of voxels in the vessel centre. The saturation in the vessel centre causes the cross-section to be non-Gaussian and thus renders vessel radius estimation difficult with the FWHM method (discussed earlier in the beginning of chapter 3), which assumes a 2D Gaussian profile for the vessel cross-section. The FWHM vessel radius estimation method is evaluated on vessel image data in Chapter 4 by fitting a Gaussian to the non-saturated voxels of the vessel. As discussed earlier in introduction section 1.4.6.9, the model-based approach that can incorporate nonlinearity is more suitable for cryomicrotome data than linear deconvolution.

For segmentation of the vascular images of this study, voxel classification approaches would not be suitable. Gradient-based vessel voxel labelling would not work since the transition from vessel to non-vessel is indistinct, and intensity-based vessel voxel labelling would not work since the voxels inside the vessels are darkened and comparable in intensity to the non-vessel background. The level sets method was used herein as a state-of-the-art example of geometric deformable model methods applied to vessel boundary delineation. Vessel boundary delineation is not a viable approach to segmenting vessels in the deconvolved images because the vessel boundary is obscured by a darkened halo. Also, the evolution of the deformable contour is highly sensitive to the smoothing parameter, the scale of the Gaussian kernel used to smooth the images, degraded by out-of-focus artefacts. The obscuring halo and dark *hole-artefacts* are dependent on both the size and orientation of the vessel, and thus it is not possible to develop a single algorithm for segmentation unless it includes a model of the vessel itself, as proposed in Chapter 4.

Appendix D: Comparison of Image Processing Algorithms

D.1 Constant Versus Variable Step Size Multi-scale Filtering

One of the approaches to multi-scale filtering is to use a variable step size between the scales, e.g., the scales could be varied such that each scale is a proportion of the previous scale. This approach assumes that larger vessels can be detected within a larger range of scales and thus the step size at larger scales does not need to be as fine as at smaller scales. The results of the multi-scale vesselness output of this variable step size approach were compared with the constant step size approach employed in this study. The multi-scale vesselness filtering was performed on the same block of the porcine coronary vasculature data with both the constant and variable step sizes approaches. In the constant step size approach, the scales were varied from [0.1 – 1] voxels with a step size of 0.1 voxel for smaller vessels and they were varied from [1 – 5] voxels with a step size of 1 voxel for larger vessels. For the variable step size approach the scale was initialized at 0.1 and was doubled each time until it reached a value greater than 5 voxels. A manual segmentation of the same vasculature data block was used as the gold standard. Of the 1287 centreline voxels that were labelled as belonging to a vessel in the manual segmentation, the constant step size filtering detected 1286 of them whereas the variable step size filtering detected only 1281. Although this difference may seem trivial, even a single centreline voxel missed may result in a disconnected branch and loss of an entire subtree in the vessel data. Additionally, the total sum of all the normalized vesselness at all the centerline voxels of the manual segmentation with the constant step size approach was 103.25, whereas the sum was only 94.34 with the variable step size approach. In other words, the constant step size approach resulted in 8.6% higher vesselness detection than the variable step size approach. In the cryomicrotome image data, the vessel intensity and detection is sensitive to vessel size. Therefore, to capture the smallest possible vessels for extraction of the whole-

organ coronary network down to microvasculature, we chose the constant step size approach to multi-scale vesselness filteringto ensure we detected maximum vesselness from the images especially for small vessel sizes. The variable filtering can potentially miss some vessels, especially at the smaller sizes, since they are responsive only at a certain scale, i.e. they can be missed if the scale is not exactly comparable to their size. To visually compare the vesselness responses of the constant and variable step size approaches, we calculated the percent error between the manual segmentation (1 = vessel, 0 = not vessel) and the normalized vesselness filtering responses of the constant and variable approaches at the skeletonized centerline voxels. The centerline voxels of the skeletonized manual segmentation were used in the error calculation because they are the most fundamental in the vessel branch definition. The normalized vesselness responses ranged from 0 – 1, where the vesselness of each voxel was given a value between 0 (definitely not a vessel) and 1 (definitely a vessel). Fig. D.1 shows the skeletonized centreline voxels of the manual segmentation of the pig coronary vascular data block colored by the difference between the percent errors in the normalized vesselness responses of the constant and variable step size multi-scale filtering. As observed in Fig. D.1, at some of the voxels, the constant step size method had 18.5% lower error than the variable step size method.

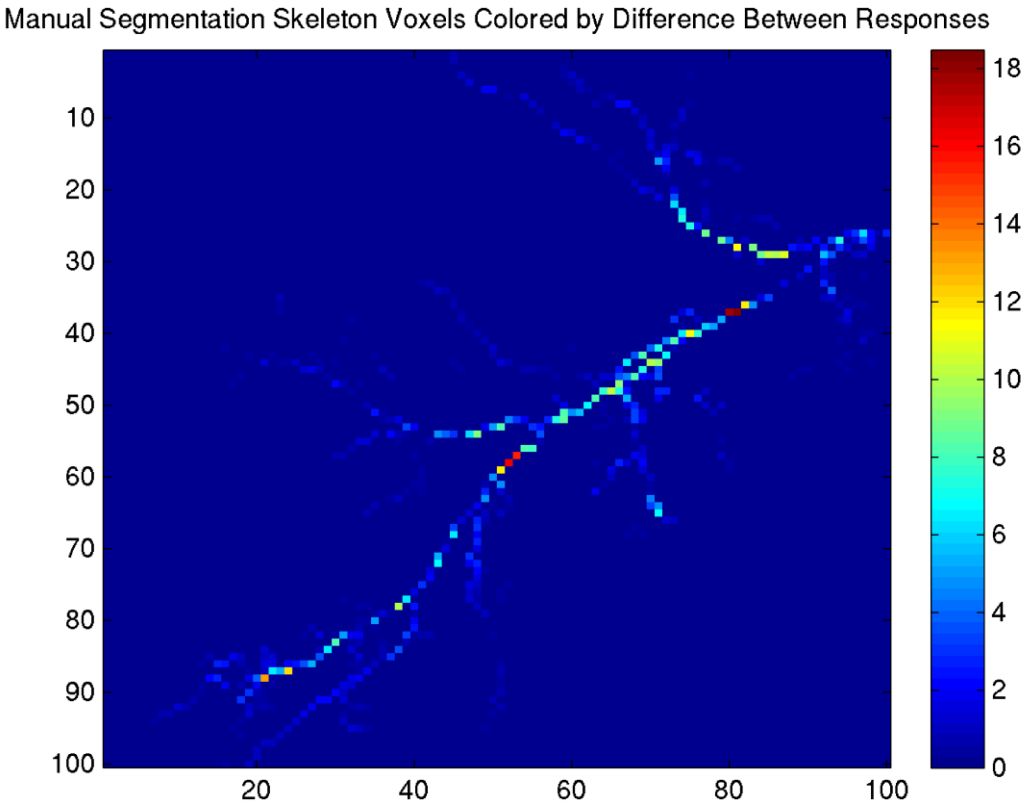


Figure D.1: Skeletonized centreline voxels of the manual segmentation of the pig coronary vascular data block colored by the difference between the percent errors in the normalized vesselness responses of the constant and variable step size multi-scale filtering.

Regarding how small a step size is required in the multi-scale filtering, we compared the small-scales filtering response on the pig vascular block with a step size of 0.1 and with a step size of 0.05. The same number of voxels was detected. Additionally, the total sum of vesselness was the same with both step sizes, indicating that 0.1 voxels was a sufficiently fine step size and a smaller step size would not increase the vesselness detected.

D.2 Comparison of Local Adaptive Otsu and Sauvola Thresholding

One of the most common methods of binarizing images is the Otsu technique (Otsu 1979), which is used for thresholding the large scale vesselness ouput in this work because the large vessels are clearly distinguished from the background and show consistency in the vessel voxel intensity (small variation), thus not requiring local adaptive thresholding. However, in

this work, we employed Sauvola local adaptive thresholding (Sauvola and M. Pietikäinen, 2000) on the small-scale output of the multi-scale vesselness filtering. This is because Otsu local thresholding resulted in disconnected branches since it missed the voxels of small vessels at junctions when performed on a block of pig coronary vasculature data. This is clearly illustrated in Fig. D.2, where the Sauvola and Otsu local threshold outputs are shown along with the manual thresholding output. The manually skeletonized centreline voxels were chosen to compare the Otsu and Sauvola techniques because these are the voxels that determine if a vessel is connected to the main tree, i.e. they are most fundamental to detecting and defining vessel branching.

Otsu local thresholding was performed by dividing the image into blocks and computing the local threshold that maximally separated and classified the voxel values in each local block into background and the foreground, i.e. vessels. Sauvola's method was performed by dividing the image into blocks and choosing the threshold close to the mean of the voxel values in high contrast blocks and choosing a threshold below the mean at a value proportional to the normalized local standard deviation in low contrast blocks. The same block window size of 10x10 voxels was used for performing the Otsu and Sauvola local thresholding.

Otsu local thresholding fails for small vessels because of the large intensity variation in the small vessels. The vesselness output cannot optimally be divided into foreground and background because there is no clear divide or high contrast between background and vessels in the small-scale vesselness output, but rather a wide distribution (large standard deviation) of vesselness detected for the small-scale vessels. As evident by the results tabulated in Table D.1, Sauvola's method is much more sensitive to vessel detection in the cryomicrotome image data because it employs the local standard deviation of the distribution of vesselness values in the local block to adapt the threshold.

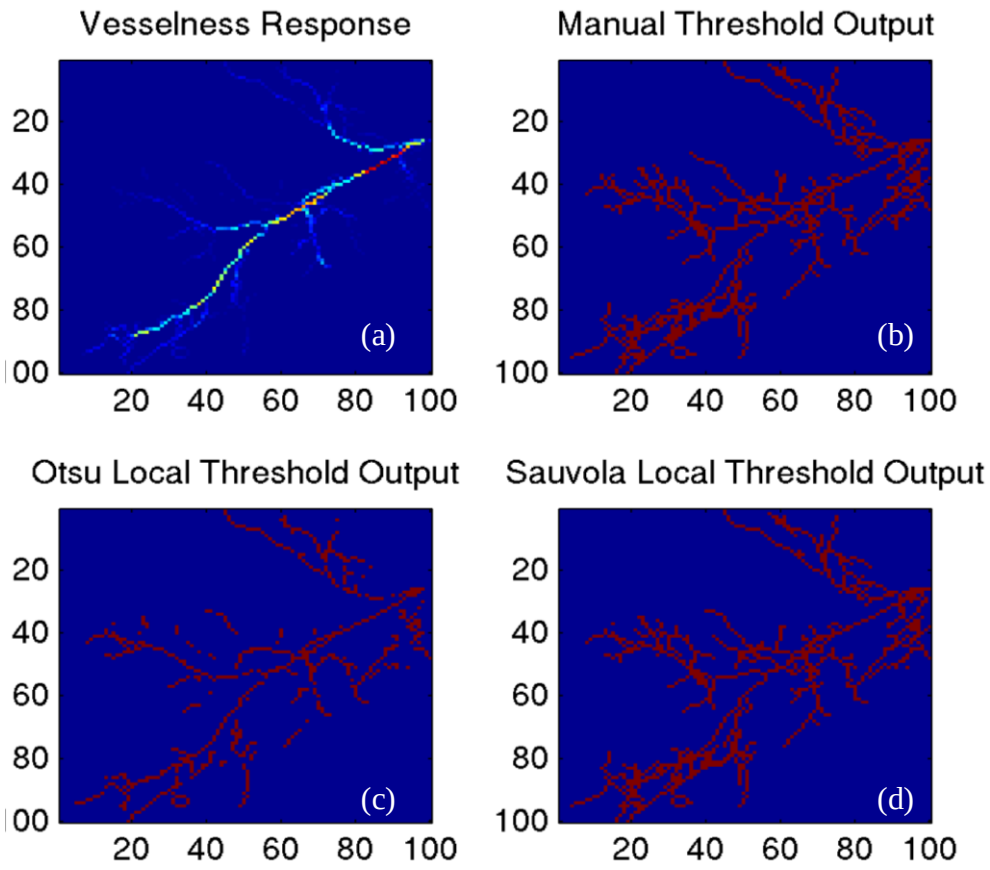


Figure D.2: Results are shown for binarization of the multi-scale vesselness response (a) thresholded manually (b) and with Otsu (c) and Sauvola (d) local adaptive methods. The values are only shown for the manually segmented skeleton centreline voxels because these are the voxels most important for vessel delineation.

	Otsu Local Thresholding	Sauvola Local Thresholding
Number of false negatives	611	95
Number of true positives	676	1192
Accuracy	0.9990	0.9998
Sensitivity	0.5253	0.9262

Table D.1: Comparison of local adaptive thresholding performed with Otsu and Sauvola methods on a block of the pig coronary vasculature data. The manual segmentation was used as the gold standard.

Appendix E: Unconstrained Unbounded Radius Estimation

The model-based method incorporates the optical tissue properties and their intramural spatial variation in the measurement of vessels embedded in the myocardium. This method optimizes the optical attenuation coefficients using fluorescent microsphere beads embedded in tissue. The emission attenuation coefficient is optimized as a separate variable than the excitation attenuation coefficient. The optimization is constrained such that $\mu_{ex} \geq \mu_{em}$ and bounded such that $0.01 < \mu_{ex} < 0.05$ and $0.01 < \mu_{em} < 0.05$. To assess the effect of these constraints and bounds on the model-based method, both the attenuation coefficient and radius estimation were performed with unbounded and unconstrained optimization. The constraints and bounds were removed and a single attenuation coefficient $\mu_t = \mu_{ex} = \mu_{em}$ was used in the constant optical parameter model-based method. In Fig. E.1, the radii estimates from the unconstrained and unbounded model-based method with constant and varying optical parameters are compared directly with each other for two pig hearts. Just as in the constrained and bounded optimization, the estimated radius still differed much more between the constant and varying parameter cases for smaller vessels in the unconstrained and unbounded optimization. In the unconstrained and unbounded model-based method, smaller vessel radius estimation is also more sensitive to spatially varying optical tissue parameters, just as in the constrained and bounded model-based method. This suggests the need to measure spatial variation in optical tissue parameters for accurate radius estimation of small vessels (< 1 mm in radius).

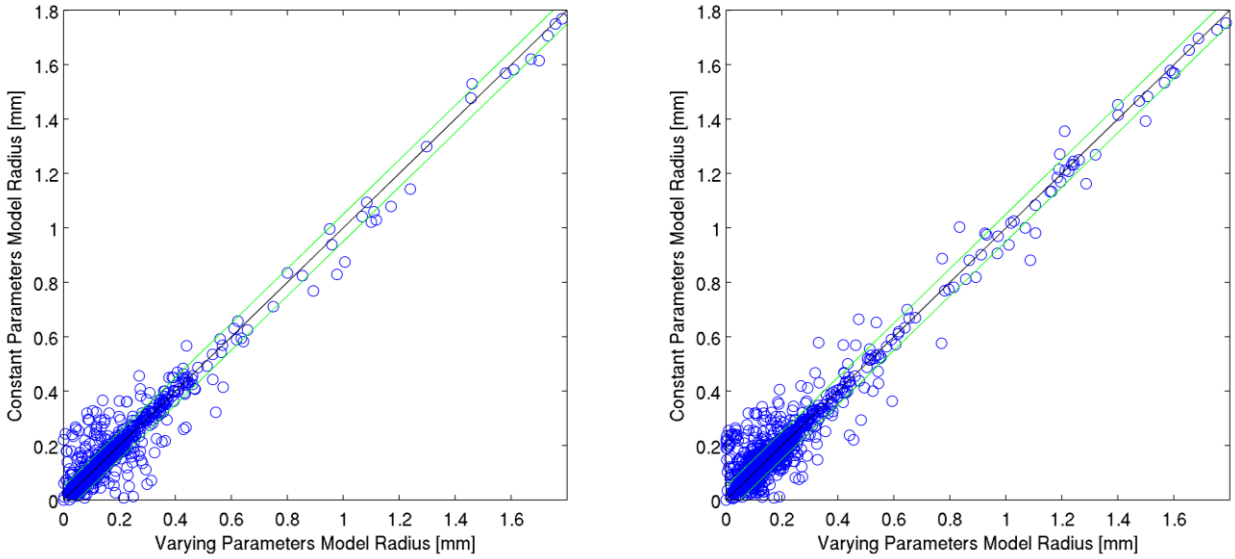


Figure E.1: The two plots (of two distinct pig heart coronary vasculatures) compare unconstrained and unbounded model-based radius estimation performed with varying optical parameters to unconstrained and unbounded model-based radius estimation performed with constant ($\mu_t = \mu_{ex} = \mu_{em}$) optical parameters. The radii are plotted in millimetres and the green lines enclose a difference of one voxel (0.05 mm). Note: only differences between methods are shown, not which is more accurate.